2013 NCREE Research Programs and Accomplishments

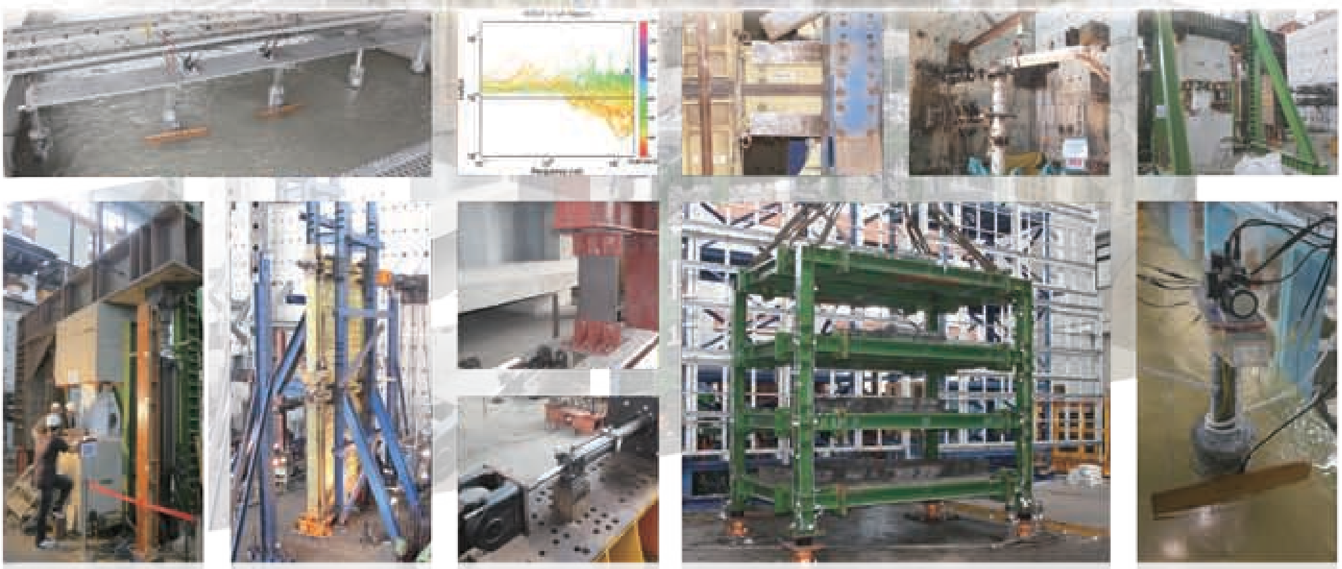

National Center for Research on Earthquake Engineering

2013 NCREE

Research Programs and Accomplishments

Contents

Medium-Range Improvement for Performance-Based Seismic Design of Buildings in Taiwan (II)

Tsung-Jen Teng [1]、Yuan-Tao Weng [2]、Juin-Fu Chai[1]、Shyh-Bin Chiou[3] and Wen-I Liao[4]

鄧崇任 [1]、翁元滔 [2]、柴駿甫 [1]、邱世彬 [3]、廖文義 [4]

Abstract

The objective of this study is to review the background material regarding the probabilistic performance-based design of structures. Based on such a review, a design procedure is recommended in order to make a medium-range improvement for the performance-based seismic design of buildings in Taiwan.

Keywords: probabilistic performance-based design, demand hazard curve

Introduction

Seismic performance can be quantified in terms of the following: (a) seismic demand; (b) seismic damage; (c) seismic consequences including direct repair costs, casualties, and indirect business disruption. Although the latter two metrics provide a more explicit measure of seismic performance, they are currently hindered by less available data and greater uncertainty in comparison to metrics based on seismic demand. As a result, many seismic design guidelines use seismic demand as explicit seismic performance criteria. The seismic demand hazard analysis recommended for quantifying seismic performance and the probabilistic checking schemes for the desired performance objectives are described as follows.

Seismic Predictive Equations and Correlation Coefficient

There are two major predictive equations used in performance-based earthquake engineering. Due to the aleatory randomness, the residual of the predictive value is treated as random variable. The equations are illustrated as follows:

1. Predictive equation for the ground motion models: For a given scenario and location, the univariate distribution of $S_a(T)$ is lognormal, and the ground motion predictive equation for $\ln S_a(T)$ takes the following form: $\ln S_a(T) = \overline{\ln S_a(T)} + \varepsilon(T)\sigma(T) \cdot \ln S_a(T)$ denotes the logarithmic spectral acceleration at period T. $\overline{\ln S_a(T)}$ denotes the mean predicted logarithmic spectral acceleration, which depends on the given scenario and local site condition $\varepsilon(T)$ denotes the normalized residual and $\sigma(T)$ denotes the logarithmic standard deviation that is estimated as part of the ground motion predictive equation. The ground motion predictive equations are fitted using large databases, such as PEER NGA (Nest Generation Attenuation) database.
2. Predictive equation for the structural response model: we assume that given the level of S_a , the predicted median value of the engineering demand parameter $\hat{\mu}_{EDP}$ can be represented approximately by the form $\hat{\mu}_{EDP} = a(S_a)^b$. In order to complete this probabilistic representation of drift with the given S_a, we assume that the engineering demand parameters (EDPs) are distributed lognormally about the median $\hat{\mu}_{EDP}$ with the standard deviation of the natural logarithm (i.e., dispersion), $\beta_{DR|S_a}$.

The predictive equations for ground motion

[1] Research Fellow, National Center for Research on Earthquake Engineering, chai@ncree.org.tw
[2] Research Fellow, National Center for Research on Earthquake Engineering, tjteng@ncree.org.tw
[3] Assistant Researcher, National Center for Research on Earthquake Engineering
[4] Professor, Department of Civil Engineering, NTUT

models can address the probability distribution of spectral acceleration at an individual period, given a set of predictor variables such as magnitude and distance. However, they do not address the correlation between spectral acceleration values at multiple periods. Those correlations are required for several calculations related to seismic hazard analysis and ground motion selection. Jayaram and Baker（2008） studied the jointed distribution of spectral accelerations using recorded time histories. They concluded that it is reasonable to assume a multivariate normal distribution for logarithmic spectral accelerations at multiple periods for a specified location during a given earthquake. Using the NGA ground motion library and the new NGA ground motion models, Baker and Jayaram（2008） measured these correlations, and presented predictive equations to provides correlations between logarithmic spectral acceleration at two periods. These correlation equations are applicable for use with any of the NGA ground motion models, at periods between 0.01 seconds and 10 seconds. The predicted correlation coefficient is given by

$$\begin{cases} \text{if } T_{max} < 0.109\,; & \rho_{\ln S_a(T_1),\ln S_a(T_2)} = C_2 \\ \text{else if } T_{min} > 0.109\,; & \rho_{\ln S_a(T_1),\ln S_a(T_2)} = C_1 \\ \text{else if } T_{max} < 0.2\,; & \rho_{\ln S_a(T_1),\ln S_a(T_2)} = \min(C_2, C_4) \\ \text{else}\,; & \rho_{\ln S_a(T_1),\ln S_a(T_2)} = C_4 \end{cases} \tag{1}$$

Where $T_{min} = \min(T_1, T_2)$ and $T_{max} = \max(T_1, T_2)$; and

$$C_1 = 1 - \cos\left(\frac{\pi}{2} - 0.366\ln\left(\frac{T_{max}}{\max(T_{min}, 0.109)}\right)\right) \tag{2}$$

$$C_2 = \begin{cases} 1 - 0.105\left(1 - \frac{1}{1 + e^{100T_{max} - 5}}\right)\left(\frac{T_{max} - T_{min}}{T_{max} - 0.0099}\right); & \text{if } T_{max} < 0.2 \\ 0; & \text{otherwise} \end{cases} \tag{3}$$

$$C_3 = \begin{cases} C_2; & \text{if } T_{max} < 0.109 \\ C_1; & \text{otherwise} \end{cases} \tag{4}$$

$$C_4 = C_1 + 0.5\left(\sqrt{C_3} - C_3\right)\left(1 + \cos\left(\frac{\pi T_{min}}{0.109}\right)\right) \tag{5}$$

Simulation of Target Conditional Spectra and Selection of Recorded Ground Motions

The approach used for simulating logarithmic spectral acceleration at multiple periods $[\ln S_a(T_a), \ldots, \ln S_a(T_n)]$ conditioned on $\ln S_a(T_0)$ for a given earthquake scenario is described as follows:

The unconditional marginal distribution of $\ln S_a(T_0)$ is specified by the ground motion prediction equation through $\overline{\ln S_a(T_0)}$ and $\sigma(T_0)$. On the basis of the properties of the multivariate normal distribution, it can be concluded that the distribution of $\ln S_a(T)$ for a given earthquake will also follow a multivariate normal distribution with the following mean (μ) and covariance matrices(Σ):

$$\mu = \begin{bmatrix} \mu_{\ln S_a(T_a)} + \varepsilon(T_a)\sigma_{\ln S_a(T_a)} \\ \vdots \\ \mu_{\ln S_a(T_n)} + \varepsilon(T_n)\sigma_{\ln S_a(T_n)} \end{bmatrix} = \begin{bmatrix} \mu_{\ln S_a(T_a)} + \rho(T_a, T_0)\varepsilon(T_0)\sigma_{\ln S_a(T_a)} \\ \vdots \\ \mu_{\ln S_a(T_n)} + \rho(T_n, T_0)\varepsilon(T_0)\sigma_{\ln S_a(T_n)} \end{bmatrix} \tag{6}$$

Where $\varepsilon(T_0) = \left(\ln S_a(T_0) - \overline{\ln S_a(T_0)}\right)/\sigma(T_0)$, and $\rho(T_i, T_j)$ denotes the correlation between $\ln S_a(T_i)$ and $\ln S_a(T_j)$ provided by, for example, Baker & Jayaram（2008）.

Let Σ denote the covariance matrix of $[\ln S_a(T_a), \ldots, \ln S_a(T_n)]$ conditioned on $\ln S_a(T_0)$.Let Σ_0 denote the unconditional covariance matrix of $[\ln S_a(T_a), \ldots, \ln S_a(T_n)]$ and Σ_1 denote the covariance between $[\ln S_a(T_a), \ldots, \ln S_a(T_n)]$ and $\ln S_a(T_0)$.

$$\Sigma_0 = \begin{bmatrix} \sigma^2_{\ln S_a(T_a)} & \cdots & \rho(T_a, T_n)\sigma_{\ln S_a(T_a)}\sigma_{\ln S_a(T_n)} \\ \vdots & \ddots & \vdots \\ \rho(T_n, T_a)\sigma_{\ln S_a(T_n)}\sigma_{\ln S_a(T_a)} & \cdots & \sigma^2_{\ln S_a(T_n)} \end{bmatrix} \tag{7}$$

$$\Sigma_1 = \begin{bmatrix} \rho(T_a, T_0)\sigma_{\ln S_a(T_a)}\sigma_{\ln S_a(T_0)} \\ \vdots \\ \rho(T_n, T_0)\sigma_{\ln S_a(T_n)}\sigma_{\ln S_a(T_0)} \end{bmatrix} \tag{8}$$

Σ can be computed as follows：

$$\Sigma = \Sigma_0 - \frac{1}{\sigma^2_{\ln S_a(T_0)}}\Sigma_1\Sigma_1^T \tag{9}$$

where Σ_1^T denotes the transpose of Σ_1.

For any given event and location, $[\ln S_a(T_a), \ldots, \ln S_a(T_n)]$ values can be simulated as conditioned on $\ln S_a(T_0)$ by sampling from a multivariate normal distribution with the above mean (μ) and covariance matrices (Σ). Jayaram et al.（2011）proposed conditional spectrum (CS) algorithm to select ground motion that matches the target response spectrum mean and variance. The selection algorithm probabilistically generates multiple response spectra from the given distribution, and then selects recorded ground motions whose response spectra individually matches the simulated response spectra. A greedy optimization technique further improves the math between the target and the sample means and variances.

Quantification of Seismic Performance and Demand Hazard

The seismic demand obtained from an intensity -based assessment utilizes the distribution of seismic demand from ground motions. A specific value of some conditioning intensity measure and the mean of this distribution are conventionally used in design verification. Bradley（2013）shows that the seismic demands from an intensity-based assessment: (a) are not unique, with different values obtained using different conditioning intensity measures; and (b) do not consider the possibility that the demand value could be exceeded from different intensity ground motions. That study also shows that the mean seismic demand from an intensity-based assessment almost always underestimates the demand hazard value for the exceedance rate considered, on average by 17% and with a large variability. Therefore, the seismic demand hazard is a more robust metric for quantifying seismic performance.

In order to produce a drift demand hazard curve $\lambda_D(d)$, it must convolve the S_a hazard and drift demand conditional on S_a.The drift demand hazard curve $\lambda_D(d)$ provides the annual frequency that the drift demand D exceeds any specific value d. Using the total probability theorem (Benjamin and Cornell, 1970), $\lambda_D(d)$ becomes in an integral form

$$\lambda_D(d) = \int P[D \ge d | S_a = x] |d\lambda(x)| \tag{10}$$

The second factor within the integral represents the likelihood of a given level of spectral acceleration; it can be easily obtained from the hazard curve $\lambda(x)$. The first factor $P[D \ge d | S_a = x]$ represents the likelihood that the drift exceeds d given that S_a is known. This factor can be provided by structural response analysis.

Assume that given the level of S_a, the predicted median drift demand $\hat{D}$ can be represented approximately by the form $\hat{D} = a(S_a)^b$. In order to complete this probabilistic representation of drift given S_a, we assume that the drift demands D are distributed lognormally about the median $\hat{D}$ with the standard deviation of the natural logarithm, $\beta_{D|S_a}$. The associated parameters can be estimated through conducting a number of nonlinear analyses, which are followed by a regression analysis of $\ln D$ on $\ln S_a$. With the drift prediction form $\hat{D} = a(S_a)^b$ and the D's lognormal distribution assumption, the first factor in Eq. (10) becomes

$$P[D \ge d | S_a = x] = 1 - \Phi\left(\frac{\ln[d / a(x)^b}{\beta_{D|S_a}}\right) \tag{11}$$

In which $\Phi(\ )$ is standardized Gaussian distribution function.

In principle, Eq. (10) can be solved numerically for any assumption about the form of probabilistic representation of the spectral acceleration as well as the displacement demand.

Assume that the site hazard curve can be approximated in the region around $S_a^{\lambda_0}$, i.e., in the range of values in the region of hazard level in the proximity of the performance objective λ_0 e.g. $1/2500$ per year (or 2% in 50 years) by the form

$$\lambda(S_a) \cong k_0 e^{-k_2 in^2 S_a - k_1 \ln S_a} \tag{12}$$

Using Eqs. (11) and (12), Eq. (10) for the drift hazard curve becomes, upon integration:

$$\lambda_D(d) = P[D \ge d] = \sqrt{q} \times k_0^{1-q} \times \left[\lambda(S_a^d)\right]^q \times \exp\left[\frac{k_1^2}{4k_2}(1-q)\right] \tag{13}$$

$$q = \frac{1}{1 + 2k_2 \beta_{D|S_a}^2 / b^2} \tag{14}$$

And $S_a^d \equiv (d/a)^{1/b}$ is defined as the spectral acceleration corresponding to the drift level d, that is, the inverse of $\hat{D} = a(S_a)^b$.

Eq.(13) can be used to find the annual likelihood of exceeding any specific displacement demand, recognizing that the dynamic behavior may be highly nonlinear and that for any specific ground motion there will typically be large variability ($\beta_{DR|S_a}$) in the dynamic response. This implies that even ground motion intensity levels less than S_a^d may cause drift d or more. All possibilities have been included via the integration in Eq. (10).

Probabilistic Performance Objective and Checking Schemes

Cornell el al.(2002)have developed a probabilistic framework for the design and assessment of structures. This framework was based on realizing a performance objective that is expressed as the probability of exceeding a specified performance level for the structure in question. Our goal is to provide criteria based on the desired performance objectives that are defined as the specified annual frequency of exceeding the performance level such as collapse-prevention damage state and lift safety damage state. Therefore, the probabilistic checking schemes for the desired performance objectives can be defined as that the annual frequency λ_{PL} of the performance level not being met (capacity side) must be less than or equal to he performance objective λ_0 (demand side):

$$\lambda_{PL} \le \lambda_0 \tag{15}$$

In order to produce the annual frequency λ_{PL} of the performance level not being met, it must combine the hazard curve $\lambda_D(d)$ with the drift capacity representation. Using the total probability theorem again, λ_{PL} becomes in integral form

$$\lambda_{PL} = \int P[C \le d | D = d] |d\lambda_D(d)| \tag{16}$$

The second factor, the likelihood of a given displacement demand level, can be determined from the drift hazard curve derived in Eq. (10) or Eq. (13). The first factor is the likelihood that the drift capacity is less than a specified value d, given that the drift demand is equal to that value,

The drift capacity C denotes the drift level at which the performance level will be exceeded (e.g., structure collapse will occur). The drift capacity is assumed to have a median value $\hat{C}$ and to be lognormally distributed with dispersion β_{CR}. With this assumption, it follows that the first factor in Eq. (16) is $P[C \le d | D = d] = \Phi(\ln[d/\hat{C}] / \beta_{CR})$. Substituting this result and Eq. (13) into Eq. (16) and carrying out the integration in Eq. (16), one find the primary result similar to that of Eq. (13) (Vamvatsikos, 2013):

$$\lambda_{PL} = \sqrt{\phi} \times k_0^{1-\phi} \times [\lambda(S_a^{\hat{C}})]^{\phi} \times \exp\left[\frac{k_1^2}{4k_2}(1-\phi)\right] \quad (17)$$

$$\phi = \frac{1}{1 + 2k_2\left(\beta_{DR|S_a}^2 + \beta_{CR}^2\right)/b^2} \quad (18)$$

and $S_a^{\hat{C}} \equiv \left(\hat{C}/a\right)^{1/b}$ is defined as the spectral acceleration corresponding to the drift capacity $\hat{C}$.

Introducing epistemic uncertainty involves using the mean hazard value $\bar{\lambda}(S_a^{\hat{C}})$ and the updated value of ϕ' for estimating the overall mean annual frequency of the performance level not being met via Eq. (17).

$$\phi' = \frac{1}{1 + 2k_2\left(\beta_{DR|S_a}^2 + \beta_{CR}^2 + \beta_{DU}^2 + \beta_{CU}^2\right)/b^2} \quad (19)$$

In which β_{DU} and β_{CU} are the demand and capacity dispersions that are due to epistemic uncertainty.

Consideration of epistemic uncertainty in the probabilistic modeling of demand and capacity are allowed for the definition confidence statements for the likelihood performance objective being achieved. If instead a certain mean annual frequency value is required, reflecting, e.g., the x=90% confidence level, the associated dispersion in the mean annual frequency of the performance level not being met due to epistemic uncertainty is defined as

$$\beta_{TU} = \sqrt{\beta_{DU}^2 + \beta_{CU}^2}\,\phi\left(k_1 + 2k_2 \ln s_a^{\hat{C}}\right)/b \quad (20)$$

Then, let K_x be the standard normal variate corresponding to the desired x confidence level. For example, if x=90% confidence, K_x needs to be $K_{90\%} = \Phi^{-1}(90\%) = 1.28$. The corresponding mean annual frequency of the performance level not being met becomes

$$\lambda_{PL}^{x} = \sqrt{\phi} \times k_0^{1-\phi} \times \left[\bar{\lambda}(s_a^{\hat{C}})\right]^{\phi} \times \exp\left[\frac{k_1^2}{4k_2}(1-\phi) + K_x\beta_{TU} - \gamma_{UT_x}\right] \quad (21)$$

where a skewness correction factor is employed for additional accuracy:

$$\gamma_{UT_x} = k_2\left(\beta_{DU}^2 + \beta_{CU}^2\right)\frac{\phi}{b}\cdot\frac{(1-2x)^2}{(1-x)^{0.4}} \quad (22)$$

For one to set the criterion that the confidence is at least 90% and the actual probability of the limit state is no more than the objective λ_0, the original checking schemes (Eq. (15)) may be modified as

$$\lambda_{PL}^{X} \le \lambda_0 \quad (23)$$

Both the demand and the capacity sides of the modified probabilistic checking schemes (i.e. Eq. (23)) need to be converted into a convenient, more conventional checking schemes. For the demand side, , we firstly convert the target annual frequency λ_0 of being exceeded into an intermediate form in terms of the ground motion intensity $S_a^{\lambda_0}$, which is defined as the S_a level with λ_0. This can be achieved through setting the annual being-exceeded frequency $\lambda(S_a)$ of the site hazard curve (See Eq.(12)) to be equal to λ_0. And then we convert this intermediate form further into a final form in terms of the median drift demand $\hat{D}^{\lambda_0}$ under a given ground intensity $S_a^{\lambda_0}$ ($S_a^{\lambda_0} = \left(\hat{D}^{\lambda_0}/a\right)^{1-b}$). This can be achieved through solving the inverse of the relationship $\hat{D}^{\lambda_0} \equiv a(S_a^{\lambda_0})^b$. For the capacity side, we have already expressed the mean annual frequency λ_{PL}^{x} of the performance level not being met in terms of the site hazard value $\bar{\lambda}\left(S_a^{\hat{C}}\right)$ under a given spectral acceleration level $S_a^{\hat{C}}$, which is defined in terms of the drift capacity $\hat{C}$ as $S_a^{\hat{C}} \equiv \left(\hat{C}/a\right)^{1/b}$. Finally, both the demand and the capacity sides of the probabilistic checking schemes (Eq. (23)) have been converted into a format with demand and capacity. At the same time, an explicit quantification of the confidence level at which the objective has been achieved.

Conclusions

In this study, we review the background material in the probabilistic performance-based design of structures. From such a background review, a design procedure is recommended for the current medium-range improvement for performance-based seismic design of buildings in Taiwan. However, some issues still have to be worked out in the implementation of seismic design guidelines: (a) for each seismic zone , the control earthquakes (magnitude, distance), which can be obtained from PSHA disaggregation at short period and period of one second for each ground shaking level, need to be tabulated; (b) the regression parameters of the predictive equations for the ground motion models need to be tabulated; (c) for each seismic zone, the shape parameters (k_0, k_1, k_2) in the approximation of the seismic zone hazard curves at short periods and the period of one second need to be tabulated.

References

Baker, J. W., and Jayaram, N. (2008), "Correlation of spectral acceleration values from NGA ground motion models." *Earthquake Spectra*, 24(1), 299-317.

Benjamin, J. R. and Cornell, C. A. (1970), *Probability, Statistics, and Decision for Civil Engineers*, New York: McGraw-Hill.

Bradley, BA. (2013) , "A comparison of intensity-based demand distributions and the seismic demand hazard for seismic performance assessment." *Earthquake Engineering & Structural Dynamics*, 42(15):2235–2253.

Cornell, CA, Jalayer, F, Hamburger, R, and Foutch, DA. (2002) , "Probabilistic basis for 2000 SAC federal emergency management agency steel moment frame guidelines." *J. Struct. Eng.*, 128(4):525–33.

Energy Dissipation of a Suspension-Type Tuned Mass Damper by Varying Pendulum Length

Kuan-Hua Lien[1], Yong-An Lai[2], Walter Chuang-Sheng Yang[3], Lap-Loi Chung[4] and Lai-Yun Wu[5]

連冠華[1]、賴勇安[2]、楊創盛[3]、鍾立來[4]、吳賴雲[5]

Abstract

In this paper, an optimal energy dissipation algorithm is proposed for a semi-active suspension-type tuned mass damper (SA-STMD) by varying the pendulum length. The SA-STMD mechanism consists of a mass block, a suspension rope, and a movable fulcrum. The fulcrum is similar to a short tube that is actuated by a linear motor on a track in a vertical direction. As the fulcrum goes up, the pendulum length extends and the stiffness of the SA-STMD decreases. On the other hand, as the fulcrum goes down, the pendulum length shortens and the stiffness of the SA-STMD increases. By varying the fulcrum position, the SA-STMD restoring force can be adjusted. When the energy dissipated by the suspension-type tuned mass damper (STMD) is insufficient, the stiffness of the SA-STMD varies according to the optimal energy dissipation algorithm to provide a controllable restoring force that is designed to act as a viscous damper that can make up the lack of dissipated energy. By numerical verification, the optimal energy dissipation algorithm can produce a variable restoring force with a hysteresis loop in a butterfly shape. Therefore, the SA-STMD using the optimal energy dissipation algorithm can supply enough damping to match the demand.

Keywords: suspension-type tuned mass damper, variable stiffness, semi-active control, structural control

Introduction

Semi-active suspension-type tuned mass dampers (SA-STMD) with variable stiffness have mostly been studied to overcome the detuning problem (Chu et al. 2005). In this paper, an optimal energy dissipation algorithm is proposed for a SA-STMD to solve the problem where the energy dissipation of a suspension-type tuned mass damper (STMD) is insufficient.

The restoring force of a SA-STMD can be adjusted by varying the pendulum length. When the energy dissipated by a STMD is insufficient, the SA-STMD stiffness varies according to the optimal energy dissipation algorithm to provide a controllable restoring force that is designed to act as a linear or non-linear viscous damper that can make up the lack of dissipated energy. By numerical verification, the optimal energy dissipation algorithm produces a variable restoring force to dissipate vibration energy. Therefore, the SA-STMD using the optimal energy dissipation algorithm supplies enough damping to match demand.

Equation of Motion

A semi-active control mechanism of a suspension-type tuned mass damper is shown in Fig. 1. The SA-STMD consists of a mass block, a suspension rope, and a movable fulcrum. The fulcrum is similar to a tube that is actuated by a linear motor on the track

[1] Ph.D.
[2] Graduate Student
[3] Research Engineer & Lecturer
[4] Research Fellow and Professor
[5] Professor

in a vertical direction. As the fulcrum goes up, the pendulum length extends and the stiffness of the SA-STMD decreases. On the other hand, as the fulcrum goes down, the pendulum length shortens and the stiffness of the SA-STMD increases.

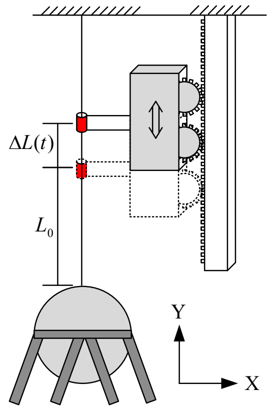

Fig. 1. Mechanism of SA-STMD.

A primary structure is modeled as a single-degree-of-freedom (SDOF) structure with mass m_s, damping coefficient c_s and stiffness k_s. A SA-STMD is attached to the SDOF structure. The mass, damping coefficient and stiffness of the SA-STMD are m_d, c_d and $k_d(t)$, respectively. The stiffness of the SA-STMD $k_d(t)$ is variable due to the change of the fulcrum position and the pendulum length and is expressed as:

$$k_d(t) = m_d g / L(t) \tag{1}$$

where g is the gravitational acceleration and $L(t)$ is the pendulum length which varies with the fulcrum position.

In order to increase the stability of dynamic analysis, the stiffness of the SA-STMD, $k_d(t)$ is divided into two parts:

$$k_d(t) = k_{d0} + k_{d1}(t) \tag{2}$$

where $k_{d0} = m_d g / L_0$ is the constant stiffness of the SA-STMD with constant pendulum length L_0 and $k_{d1}(t)$ is the variable stiffness of the SA-STMD due to the variable pendulum length and is given by:

$$k_{d1}(t) = \frac{m_d g}{L(t)} - \frac{m_d g}{L_0} = \frac{-m_d g \Delta L(t)}{L_0\left[L_0 + \Delta L(t)\right]} \tag{3}$$

When a SDOF structure is subjected to an external disturbance $w(t)$ and connected with a SA-STMD, the model obtained is as shown in Fig. 2 and the equation of motion can be written as:

$$\mathbf{M}\ddot{\mathbf{x}}(t) + \mathbf{C}\dot{\mathbf{x}}(t) + \mathbf{K}\mathbf{x}(t) = \mathbf{b}f_r(t) + \mathbf{e}w(t) \tag{4}$$

where $\mathbf{x}(t) = \begin{bmatrix} x_d(t) \\ x_s(t) \end{bmatrix}$ is the displacement vector, $x_d(t)$ and $x_s(t)$ are the displacements of the SA-STMD and the structure, respectively; $\mathbf{M} = \begin{bmatrix} m_d & 0 \\ 0 & m_s \end{bmatrix}$ is the mass matrix; $\mathbf{C} = \begin{bmatrix} c_d & -c_d \\ -c_d & c_d + c_s \end{bmatrix}$ is the damping matrix; $\mathbf{K} = \begin{bmatrix} k_d & -k_d \\ -k_d & k_d + k_s \end{bmatrix}$ is the stiffness matrix; $\mathbf{b} = \begin{bmatrix} -1 \\ 1 \end{bmatrix}$ and $\mathbf{e} = \begin{bmatrix} 0 \\ 1 \end{bmatrix}$ are the location vectors of the controllable restoring force and the structural external loading, respectively; $w(t)$ is the external disturbance; and $f_r(t)$ is the controllable restoring force of the SA-STMD provided by the controllable stiffness of the SA-STMD $k_{d1}(t)$ and can be expressed as:

$$\begin{aligned} f_r(t) &= k_{d1}(t)[x_d(t) - x_s(t)] \\ &= \frac{-m_d g \Delta L(t)}{L_0\left[L_0 + \Delta L(t)\right]}[x_d(t) - x_s(t)] \end{aligned} \tag{5}$$

Represented in the state-space form, the second-order differential equation (4) is changed to a first-order differential equation as:

$$\dot{\mathbf{z}}(t) = \mathbf{A}\mathbf{z}(t) + \mathbf{b}f_r(t) + \mathbf{e}w(t) \tag{6}$$

where $\mathbf{z}(t) = \begin{bmatrix} \mathbf{x}(t) \\ \dot{\mathbf{x}}(t) \end{bmatrix}$ is the state vector; $\mathbf{A} = \begin{bmatrix} \mathbf{0} & \mathbf{I} \\ -\mathbf{M}^{-1}\mathbf{K} & -\mathbf{M}^{-1}\mathbf{C} \end{bmatrix}$ is the system matrix; and $\mathbf{B} = \begin{bmatrix} \mathbf{0} \\ \mathbf{M}^{-1}\mathbf{b} \end{bmatrix}$ and $\mathbf{E} = \begin{bmatrix} \mathbf{0} \\ \mathbf{M}^{-1}\mathbf{e} \end{bmatrix}$ are the location vectors of the controllable restoring force and the structural external loading in state-space, respectively.

Under the assumption that the controllable restoring force and the structural external disturbance are piecewise constant, Equation (6) can be expressed in a discrete-time fashion as a first-order difference equation:

$$\mathbf{z}[n+1] = \mathbf{A}_d\mathbf{z}[n] + \mathbf{b}_d f_r[n] + \mathbf{e}_d w[n] \tag{7}$$

where $\mathbf{A}_d = e^{\mathbf{A}\Delta t}$ is the discrete-time system matrix; and $\mathbf{B}_d = \mathbf{A}^{-1}(\mathbf{A}_d - \mathbf{I})\mathbf{B}$ and $\mathbf{E}_d = \mathbf{A}^{-1}(\mathbf{A}_d - \mathbf{I})\mathbf{E}$ are the location vectors of the controllable restoring force and the structural external loading in discrete-time state space, respectively. From Equation (5), the discrete-time controllable restoring force $f_r[n]$ can be expressed in terms of the discrete-time state vector as:

$$\begin{aligned} f_r[n] &= k_{d1}[n](x_d[n] - x_s[n]) \\ &= k_{d1}[n]\mathbf{d}_1^{\mathrm{T}}\mathbf{z}[n] \\ &= \frac{-m_d g \Delta L[n]}{L_0\left(L_0 + \Delta L[n]\right)}\mathbf{d}_1^{\mathrm{T}}\mathbf{z}[n] \end{aligned} \tag{8}$$

where $\mathbf{d}_1^{\mathrm{T}} = \begin{bmatrix} 1 & -1 & 0 & 0 \end{bmatrix}^{\mathrm{T}}$ is the output vector of the stroke (relative displacement) of the SA-STMD with respect to the structure.

When the disturbance is known, the state vector $\mathbf{z}[n+1]$ at the (n+1) step can be calculated from Equation (7). Through step by step, the state vectors are obtained. Furthermore, the structural acceleration can be obtained from the motion equation in the configuration space (Equation (4)). Therefore, all the time-histories of the structural responses can be obtained.

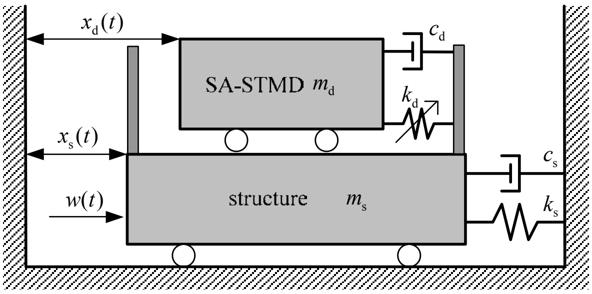

Fig. 2. Model of a SDOF structure with a SA-STMD

Control Algorithm

In order to assign the controllable restoring force $f_r[n]$ as a damping force to dissipate vibration energy, the controllable restoring force must be related to the power-law exponent of the SA-STMD relative velocity. Therefore, from Equation (8), the controllable pendulum length $\Delta L[n]$ is assigned as:

$$\begin{aligned}\Delta L[n] &= G(x_d[n]-x_s[n])\left|\dot{x}_d[n]-\dot{x}_s[n]\right|^{\gamma}\operatorname{sgn}(\dot{x}_d[n]-\dot{x}_s[n]) \\ &= G\mathbf{d}_1^{\mathrm{T}}\mathbf{z}[n]\left|\mathbf{d}_2^{\mathrm{T}}\mathbf{z}[n]\right|^{\gamma}\operatorname{sgn}(\mathbf{d}_2^{\mathrm{T}}\mathbf{z}[n])\end{aligned} \tag{9}$$

where G is the gain parameter which is determined to minimize the structural response; $\mathbf{d}_2^{\mathrm{T}}=\begin{bmatrix}0 & 0 & 1 & -1\end{bmatrix}^{\mathrm{T}}$ is the output vector of the relative velocity of the SA-STMD with respect to the structure; and γ is the power-law exponent of the SA-STMD relative velocity.

Substituting the controllable pendulum length $\Delta L[n]$ from Equation (9) to Equation (8) leads to the following equation:

$$\begin{aligned}f_r[n] = &\left\{\frac{-Gm_d g(\mathbf{d}_1^{\mathrm{T}}\mathbf{z}[n])^2}{L_0\left(L_0+G(\mathbf{d}_1^{\mathrm{T}}\mathbf{z}[n])\left|\mathbf{d}_2^{\mathrm{T}}\mathbf{z}[n]\right|^{\gamma}\operatorname{sgn}(\mathbf{d}_2^{\mathrm{T}}\mathbf{z}[n])\right)}\right\}\times \\ &\left|\mathbf{d}_2^{\mathrm{T}}\mathbf{z}[n]\right|^{\gamma}\operatorname{sgn}(\mathbf{d}_2^{\mathrm{T}}\mathbf{z}[n])\end{aligned} \tag{10}$$

From the above equation, the controllable restoring force $f_r[n]$ is related to the power-law exponent of the SA-STMD relative velocity and it becomes a nonlinear damping force with exponent γ. The gain parameter G must be negative to ensure that the term inside the curly brackets is positive. This term inside the brackets becomes the damping coefficient which is time-varying. As a whole, the controllable restoring force is designed such that it is a nonlinear damping force with a time-varying damping coefficient.

To achieve the maximum efficiency of the SA-STMD, the gain parameter G must be optimized. In order to determine the optimal gain parameter, the sum of the square of the structural displacement response is employed as an appropriate performance index J in the optimization procedure:

$$J=\sum_{n=0}^{n_1}\mathbf{d}_y^{\mathrm{T}}\mathbf{z}[n]\mathbf{z}[n]\mathbf{d}_y^{\mathrm{T}} \tag{11}$$

where n_1 is the instant at which external loading is terminated and $\mathbf{d}_y^{\mathrm{T}}=\begin{bmatrix}0 & 1 & 0 & 0\end{bmatrix}$ is the output vector of structural displacement.

The state vector $\mathbf{z}[n]$ in the above equation should satisfy the state equation (7) which becomes the equality constraint to the performance index J. After incorporation of the equality constraint with a time-varying Lagrange multiplier vector $\boldsymbol{\lambda}[n+1]$, the augmented performance index $\bar{J}$ is obtained as:

$$\begin{aligned}\bar{J} &= J+\sum_{n=0}^{n_1}\left\{\begin{matrix}\boldsymbol{\lambda}^{\mathrm{T}}[n+1]\times \\ (\mathbf{A}_d\mathbf{z}[n]+\mathbf{b}_d f_r[n]+\mathbf{e}_d w[n]-\mathbf{z}[n+1])\end{matrix}\right\} \\ &= \sum_{n=0}^{n_1}\left\{\begin{matrix}\mathbf{z}^{\mathrm{T}}[n]\mathbf{d}_y\mathbf{d}_y^{\mathrm{T}}\mathbf{z}[n]+\boldsymbol{\lambda}^{\mathrm{T}}[n+1]\times \\ (\mathbf{A}_d\mathbf{z}[n]+\mathbf{b}_d f_r[n]+\mathbf{e}_d w[n]-\mathbf{z}[n+1])\end{matrix}\right\}\end{aligned} \tag{12}$$

where $\boldsymbol{\lambda}[n+1]$ is the 4×1 Lagrange multiplier vector.

Since the augmented performance index $\bar{J}$ is a function of the co-state vector $\boldsymbol{\lambda}[n+1]$, the state vector $\mathbf{z}[n]$, and the gain parameter G, the sufficient and necessary conditions for the minimization of the augmented performance index are derived such that the first variation $\delta\bar{J}$ is zero. Therefore, the first condition is:

$$\mathbf{z}[n+1]=\mathbf{A}_d\mathbf{z}[n]+\mathbf{b}_d f_r[n]+\mathbf{e}_d w[n]\,,\quad \mathbf{z}[0]=\mathbf{z}_0 \tag{13}$$

where $\mathbf{z}[0]=\mathbf{z}_0$ is the initial condition for the state equation.

The second condition $\dfrac{\partial\bar{J}}{\partial\mathbf{z}^{\mathrm{T}}[n]}=\mathbf{0}$ is:

$$\begin{aligned}\boldsymbol{\lambda}[n] = &\, 2\mathbf{d}_y\mathbf{d}_y^{\mathrm{T}}\mathbf{z}[n]+\mathbf{A}_d^{\mathrm{T}}\boldsymbol{\lambda}[n+1]+ \\ &\left(\mathbf{d}_1 k_{d1}[n]+\mathbf{z}^{\mathrm{T}}[n]\mathbf{d}_1\frac{-m_d g(\frac{\partial\Delta L[n]}{\partial\mathbf{z}^{\mathrm{T}}[n]})}{(L_0+\Delta L[n])^2}\right)\times \\ &\mathbf{b}_d^{\mathrm{T}}\boldsymbol{\lambda}[n+1]\,,\quad \boldsymbol{\lambda}[n_1+1]=\mathbf{0}\end{aligned} \tag{14}$$

where

$$\frac{\partial\Delta L[n]}{\partial\mathbf{z}^{\mathrm{T}}[n]}=G\mathbf{d}_1\left|\mathbf{d}_2^{\mathrm{T}}\mathbf{z}[n]\right|^{\gamma}\operatorname{sgn}(\mathbf{d}_2^{\mathrm{T}}\mathbf{z}[n])+G(\mathbf{d}_1^{\mathrm{T}}\mathbf{z}[n])\gamma\left|\mathbf{d}_2^{\mathrm{T}}\mathbf{z}[n]\right|^{\gamma-1}\mathbf{d}_2$$

and the terminal condition for the co-state equation $\boldsymbol{\lambda}[n_1+1]=\mathbf{0}$.

The third condition $\frac{\partial \bar{J}}{\partial G} = 0$ is:

$$\sum_{n=0}^{n_1} \left\{ \begin{array}{l} \boldsymbol{\lambda}^{\mathrm{T}}[n+1]\mathbf{b}_{\mathrm{d}}\mathbf{z}^{\mathrm{T}}[n]\mathbf{d}_1 \times \\ \dfrac{-m_{\mathrm{d}} g \mathbf{d}_1^{\mathrm{T}}\mathbf{z}[n] \left|\mathbf{d}_2^{\mathrm{T}}\mathbf{z}[n]\right|^{\gamma} \operatorname{sgn}(\mathbf{d}_2^{\mathrm{T}}\mathbf{z}[n])}{(L_0 + \Delta L[n])^2} \end{array} \right\} = 0 \qquad (15)$$

The sufficient and necessary conditions represented by Equations (13) to (15) for the optimal gain parameter G^{opt} are nonlinear and very complex, thus a closed-form solution cannot be obtained. Therefore, a numerical iteration method is adopted. Under a specific external disturbance, the initial guess for the gain parameter $G^{(0)}$ is assigned as 0. The time varying restoring force, pendulum length and variable stiffness can be calculated from Equations (10), (9) and (3), respectively. The state vector $\mathbf{z}[n]$ can then be solved from Equation (13). The co-state vector $\boldsymbol{\lambda}[n]$ can be solved backwards by Equations (14) in sequence. The state vector and co-state vector can be substituted into Equation (15) to check whether it is vanishing or not, and if not, the gain parameter can be updated until the tolerance of the vanishing Equation (15) is acceptable.

Numerical Verification

A simplified Taipei 101 SDOF structure model with structural frequency of 0.1245 Hz and structural damping ratio ζ_s of 0.02, (Chung et al., 2013), is installed with a SA-STMD or an optimal passive tuned mass damper (P-TMD), separately, and subjected to a design wind force. The SA-STMD and P-TMD have the same design parameters but the SA-STMD with zero damping is simulated for comparison.

Design wind force

The Taipei 101 SDOF structural responses with tuned mass dampers (TMDs) under the design wind force are shown in Fig. 3. The SA-STMD can reduce the structural response almost the same with the optimal P-TMD, only about 104.97 % of the optimal P-TMD. The hysteresis loops of the SA-STMD and the P-TMD are shown in Fig. 4.

Conclusions

In this paper, an optimal energy dissipation algorithm for a semi-active suspension-like tuned mass damper with a variable pendulum length is presented. According to the results of numerical simulations, the main conclusions of this study are summarized as follows:

1. The optimal energy dissipation algorithm leads to the adjusted pendulum length being equal to the product of the gain parameter, the relative displacement and the relative velocity of the SA-STMD. It can offer a controllable restoring force which is similar to a damping force to make up the required energy dissipation.

2. The function of the SA-STMD using the optimal energy dissipation algorithm can be achieved when the damping of the TMD system is insufficient. The energy dissipated by the SA-STMD can be supplemented up to the optimal damping. Therefore the problem of the lack of dissipation energy can be solved. In addition, the installation space and funding can be reduced because the viscous damper is not necessary.

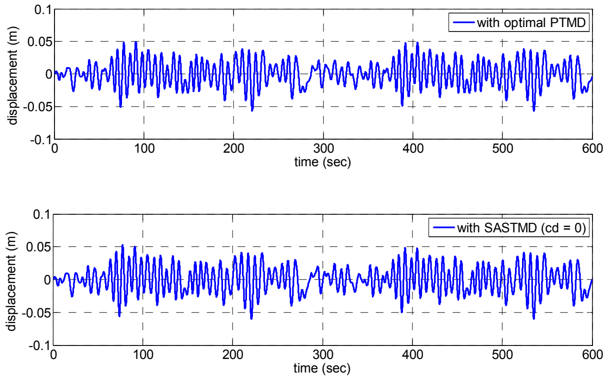

Fig. 3. Time histories of structural displacement.

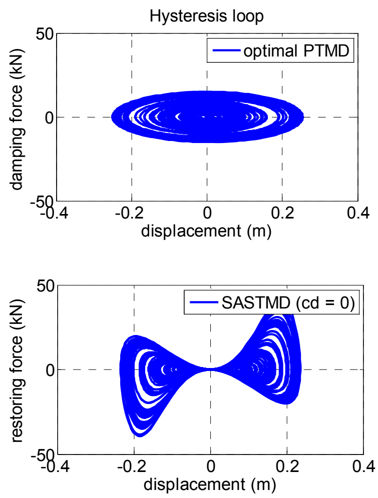

Fig. 4. Hysteresis loops of TMD

References

Chu, S.Y., Soong, T.T. and Reinhorn, A.M. (2005), Active, Hybrid and Semi-Active Structural Control. Wiley, New York.

Chung, L.L., Wu, L.Y., Yang, C.S, Lien, K.H., Lin M.C. and Huang H.H. (2013), “Optimal design formulas for viscous tuned mass dampers in wind-excited structures”, Structural Control and Health Monitoring 20, 320–336.

Response Spectrum Analyses of Non-Proportionally Damped Multi-Story Asymmetric-Plan Buildings

Jui-Liang Lin [1] and Keh-Chyuan Tsai [2]

林瑞良 [1]、蔡克銓 [2]

Abstract

It is essential to characterize the supplemental damping in buildings so that practicing engineers can understand the resultant effects of the additional damping. It is straightforward to characterize the overall system parameters representing the amount and the plan-wise distribution of the supplemental damping in a single-story asymmetrical building. Nevertheless, this becomes a difficult task in multi-story asymmetrical buildings. For this reason, this study first develops the effective one-story building (EOSB) that retains the characteristics of the two dominant vibration modes of the original non-proportionally damped multi-story asymmetrical building. By using the EOSB, the supplemental damping in the original multi-story asymmetrical building can be conveniently characterized. The relationships between the roof displacements of the original building and those of the EOSB are established. This enables the application of the response spectra constructed from EOSBs to estimate the peak roof displacements of the original multi-story asymmetrical buildings.

Keywords: response spectrum analysis; non-proportional damping; asymmetric-plan buildings; viscous dampers; effective one-story building

Introduction

Various types of dampers have been developed for earthquake engineering in order to suppress structural responses due to seismic loads. Therefore, in order to conduct response spectrum analysis on buildings with viscous dampers, model building codes (IBC 2000) stipulate how to compute the equivalent damping ratio resulting from the supplemental dampers. Obviously, both the amount of supplemental damping and the plan-wise placement of the viscous dampers, such as the dispersion of the viscous dampers and the distance between the center of supplemental damping (CSD) and the center of mass (CM), greatly influence the seismic responses of asymmetric-plan buildings. In fact, the damping effects of the viscous dampers on the seismic responses of elastic single-story asymmetric-plan buildings have been extensively studied (Goel 1998). Although complex eigenvalue analyses provide exact information about the modal properties of non-proportionally damped buildings, the overall system parameters representing the amount and the plan-wise distribution of the added viscous dampers cannot be obtained from conducting this type of analysis. The overall system parameters are useful in developing a fundamental understanding of the resultant effects of the added viscous dampers. Hence, Goel (1998) characterized the supplemental damping in single-story asymmetric-plan buildings with linear viscous dampers by using three overall system parameters. These three overall system parameters are (1) the supplemental damping ratio ξ_{sd} ; (2) the normalized supplemental damping eccentricity $\bar{e}_{sd}$; and (3) the normalized supplemental damping radius of gyration $\bar{\rho}_{sd}$. Goel (1998) also conducted a parametric study on these three parameters, and provided insights into the effects of the amount, the resultant location, and the dispersion of the added dampers. Thus, practicing engineers can effectively

[1] Research Fellow, National Center for Research on Earthquake Engineering, jllin@ncree.narl.org.tw.

[2] Professor, Department of Civil Engineering, National Taiwan University, kctsai@ntu.edu.tw

gain a physical interpretation of all installed viscous dampers in terms of these three overall system parameters for a single story asymmetrical building. Goel (1998) concluded that multi-story asymmetrical buildings with supplemental viscous dampers were worthy of further investigation.

The response spectra constructed from non-proportionally damped single-story asymmetrical buildings have been used extensively to investigate the effects of the supplemental damping on their seismic responses. However, there is no quantitative relationship between the seismic responses of these single-story buildings and those of general multi-story non-proportionally damped buildings. Thus, even though much research has investigated this type of response spectra (Tso and Sadek 1985), it seems difficult to apply this type of response spectra to estimate the seismic responses of the general multi-story non-proportionally damped building.

It has been found that each vibration mode of multi-story one-way asymmetrical buildings can be effectively represented by using a two-degree-of-freedom (2DOF) modal system (Lin and Tsai 2007). Because the characterization of the supplemental damping in single-story asymmetrical buildings is straightforward, this study first develops the effective one-story building (EOSB) associated with the original multi-story asymmetrical building. The EOSB uses the subspace spanned by the 1st undamped translational-dominant mode and the 1st rotational-dominant mode, accounting for damping coupling. Thus, one can then use the EOSB to estimate peak response. The concept and the application of the EOSB are shown schematically in Fig. 1.

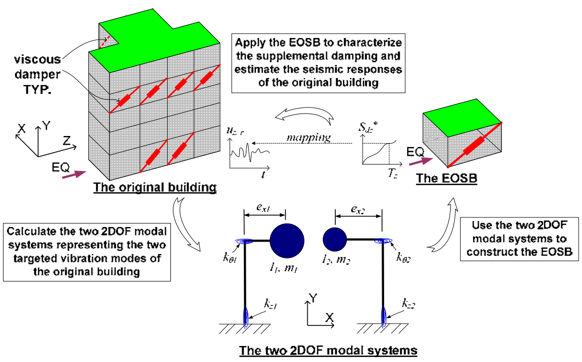

Figure 1. Sketch of the concept of the EOSB and its application

The effective one-story building (EOSB)

The two horizontal axes of the coordinate system used in this study are the X- and the Z- axes. The direction of the Y-axis is opposite the direction of gravity. For the sake of simplicity, the original N-story asymmetrical building is only symmetric about the X-axis and the ground motion is applied along the Z-axis. The first translational-dominant and the first rotational-dominant vibration modes of the original building are chosen as the two targeted vibration modes to form the EOSB. That is to say, the two 2DOF modal systems representing the two vibration modes of the EOSB are the same as those representing the two targeted vibration modes of the original building. The mass, damping, and stiffness matrices of the EOSB are respectively denoted as

$$\mathbf{M}^* = \begin{bmatrix} m^* & 0 \\ 0 & I^* \end{bmatrix}, \quad \mathbf{C}^* = \begin{bmatrix} c_{zz}^* & c_{z\theta}^* \\ c_{\theta z}^* & c_{\theta\theta}^* \end{bmatrix}, \quad \mathbf{K}^* = \begin{bmatrix} k_{zz}^* & k_{z\theta}^* \\ k_{\theta z}^* & k_{\theta\theta}^* \end{bmatrix} \tag{1}$$

and its mode shapes are denoted as $\begin{bmatrix} \phi_{zi}^* & \phi_{\theta i}^* \end{bmatrix}^T$, i=1, 2. The superscript * used in Eq. 1 denotes the quantities belonging to the EOSB in order to differentiate those notations from the commonly used notations for the original building. Because the EOSB and the original multi-story building have two 2DOF modal systems in common, the following equalities should exist:

$$\phi_{zi}^* m^* \phi_{zi}^* : \phi_{\theta i}^* I^* \phi_{\theta i}^* = m_i : I_i, \quad i = 1,2 \tag{2}$$

where m_i, I_i , i = 1, 2, are the properties of the two 2DOF modal systems representing the two targeted vibration modes of the original multi-story building—computed as follows (Lin and Tsai 2007):

$$m_i = \boldsymbol{\varphi}_{zi}^T \mathbf{m} \boldsymbol{\varphi}_{zi}, \quad I_i = \boldsymbol{\varphi}_{\theta i}^T \mathbf{I} \boldsymbol{\varphi}_{\theta i}, \quad i = 1,2 \tag{3}$$

—**m**, **I** are the N×N mass and mass moment of inertia matrices of the original N-story one-way asymmetrical building, respectively; and $\boldsymbol{\varphi}_{zi}$, $\boldsymbol{\varphi}_{\theta i}$ are the N×1 sub-vectors of the i-th undamped mode shape of the original building. Note that the values 1 and 2 for subscript i (Eq. 2) for the quantities related to the original building respectively represent the lower and the higher vibration modes between the two targeted vibration modes. On the other hand, the values 1 ad 2 for subscript i (Eq. 2) for the quantities related to the EOSB respectively represent the first and the second vibration modes of the EOSB. Equation 2 indicates that

$$\frac{\phi_{z1}^*}{\phi_{\theta 1}^*} = \pm\sqrt{\frac{m_1 I^*}{I_1 m^*}}, \quad \frac{\phi_{z2}^*}{\phi_{\theta 2}^*} = \pm\sqrt{\frac{m_2 I^*}{I_2 m^*}} \tag{4}$$

From Eq. 4, we have the mode shape matrix of the EOSB as

$$\boldsymbol{\Phi}^* = \begin{bmatrix} \phi_{z1}^* & \phi_{z2}^* \\ \phi_{\theta 1}^* & \phi_{\theta 2}^* \end{bmatrix} = \begin{bmatrix} 1 & \alpha \\ s_1\sqrt{\dfrac{I_1 m^*}{m_1 I^*}} & \alpha s_2\sqrt{\dfrac{I_2 m^*}{m_2 I^*}} \end{bmatrix} \tag{5}$$

where α is an arbitrary constant, and s_1 and s_2 may equal 1 or -1. The transformed mass matrix of the EOSB is computed as

$$\bar{\mathbf{M}}^* = \mathbf{\Phi}^{*T}\mathbf{M}^*\mathbf{\Phi}^* = \begin{bmatrix} m^* + \dfrac{m^* I_1}{m_1} & \alpha m^* + s_1 s_2 \alpha m^* \sqrt{\dfrac{I_1 I_2}{m_1 m_2}} \\ \alpha m^* + s_1 s_2 \alpha m^* \sqrt{\dfrac{I_1 I_2}{m_1 m_2}} & \alpha^2 m^* + \alpha^2 \dfrac{m^* I_2}{m_2} \end{bmatrix} \quad (6)$$

Since the off-diagonal terms of the transformed mass matrix (Eq. 6) should be equal to zero, it yields

$$s_1 s_2 = -1, \quad I_1 I_2 = m_1 m_2 \quad (7)$$

In addition, because $m_1+I_1 = m_2+I_2 = 1$ and we choose $\alpha = \sqrt{m_2/m_1}$, Eq. 6 can be simplified as

$$\bar{\mathbf{M}}^* = \frac{m^*}{m_1}\begin{bmatrix} 1 & 0 \\ 0 & 1 \end{bmatrix} \quad (8)$$

and Eq. 7 yields $m_1 = I_2$ and $m_2 = I_1$. Thus, the stiffness matrix of the EOSB is obtained as

$$\mathbf{K}^* = \left(\mathbf{\Phi}^{*T}\right)^{-1} \mathbf{\Lambda}\bar{\mathbf{M}}^* \left(\mathbf{\Phi}^*\right)^{-1} = m^* \begin{bmatrix} m_1\omega_1^2 + m_2\omega_2^2 & sym. \\ -r^*\sqrt{m_1 m_2}\left(s_2\omega_1^2 + s_1\omega_2^2\right) & r^{*2}\left(I_1\omega_1^2 + I_2\omega_2^2\right) \end{bmatrix} \quad (9)$$

where

$$\mathbf{\Lambda} = \begin{bmatrix} \omega_1^2 & 0 \\ 0 & \omega_2^2 \end{bmatrix} \quad (10)$$

and $r^* = \sqrt{I^*/m^*}$; ω_1 and ω_2 are the undamped vibration frequencies of the two targeted vibration modes of the original building. The values of s_1 and s_2, which may be 1 or -1, are determined by investigating the two targeted undamped mode shapes of the original building. For example, if the signs of $\boldsymbol{\varphi}_{zn}$ and $\boldsymbol{\varphi}_{\theta n}$, n=1, 2, are the same, s_n is equal to 1. Conversely, if the signs of $\boldsymbol{\varphi}_{zn}$ and $\boldsymbol{\varphi}_{\theta n}$, n=1, 2, are opposite, s_n is equal to -1. The damping matrix of the EOSB is assumed to be positively associated with the 2DOF modal damping matrix of the lower vibration mode among the two targeted vibration modes of the original building. Thus, the damping matrix of the EOSB can be expressed as:

$$\mathbf{C}^* = \begin{bmatrix} c_{zz}^* & c_{z\theta}^* \\ c_{\theta z}^* & c_{\theta\theta}^* \end{bmatrix} = m^* \begin{bmatrix} \dfrac{c_{z1}}{m_1} & \dfrac{s_1 r^* c_{z\theta 1}}{\sqrt{m_1 I_1}} \\ \dfrac{s_1 r^* c_{z\theta 1}}{\sqrt{m_1 I_1}} & \dfrac{r^{*2} c_{\theta 1}}{I_1} \end{bmatrix} \quad (11a)$$

where

$$c_{z1} = \boldsymbol{\varphi}_{z1}^T \mathbf{c}_{zz} \boldsymbol{\varphi}_{z1}, \quad c_{\theta 1} = \boldsymbol{\varphi}_{\theta 1}^T \mathbf{c}_{\theta\theta} \boldsymbol{\varphi}_{\theta 1}, \quad c_{z\theta 1} = \boldsymbol{\varphi}_{z1}^T \mathbf{c}_{z\theta} \boldsymbol{\varphi}_{\theta 1} \quad (11b)$$

and $\mathbf{c}_{zz}$, $\mathbf{c}_{\theta\theta}$, $\mathbf{c}_{z\theta}$ are the $N\times N$ damping sub-matrices of the original multi-story building. The equation of motion of the EOSB becomes:

$$\begin{bmatrix} 1 & 0 \\ 0 & 1 \end{bmatrix}\begin{bmatrix} \ddot{u}_z^* \\ r^*\ddot{u}_\theta^* \end{bmatrix} + \begin{bmatrix} \dfrac{c_{z1}}{m_1} & \dfrac{s_1 c_{z\theta 1}}{\sqrt{m_1 I_1}} \\ \dfrac{s_1 c_{z\theta 1}}{\sqrt{m_1 I_1}} & \dfrac{c_{\theta 1}}{I_1} \end{bmatrix}\begin{bmatrix} \dot{u}_z^* \\ r^*\dot{u}_\theta^* \end{bmatrix} + \begin{bmatrix} m_1\omega_1^2 + m_2\omega_2^2 & sym. \\ -\sqrt{m_1 m_2}\left(s_2\omega_1^2 + s_1\omega_2^2\right) & I_1\omega_1^2 + I_2\omega_2^2 \end{bmatrix}\begin{bmatrix} u_z^* \\ r^* u_\theta^* \end{bmatrix} = -\begin{bmatrix} 1 \\ 0 \end{bmatrix}\ddot{u}_g(t) \quad (12)$$

If the inherent damping matrix is neglected, the parameters ξ_{sd}, $\bar{e}_{sd}$, and $\bar{\rho}_{sd}$ of EOSB can be expressed as:

$$\xi_{sd} = \frac{c_{z1}}{2m_1\omega^*} = \frac{c_{z1}}{2m_1\sqrt{m_1\omega_1^2 + m_2\omega_2^2}}$$
$$\bar{e}_{sd} = \frac{s_1 c_{z\theta 1}}{c_{z1}}\sqrt{\frac{m_1}{I_1}} \quad (13)$$
$$\bar{\rho}_{sd} = \sqrt{\frac{m_1}{I_1 c_{z1}}\left(c_{\theta 1} - \frac{c_{z\theta 1}^2}{c_{z1}}\right)}$$

Response spectrum analyses

In order to apply the response spectra constructed from the EOSBs to predict the peak responses of the original multi-story building, Lin and Tsai (2013) find the relationship between the peak responses of the EOSB and those of the original multi-story building. The displacement spectra, denoted as S_{dz}^* and $S_{d\theta}^*$, constructed from the EOSBs can be used to predict the peak roof displacements, denoted as $S_{dz,r}$ and $S_{d\theta,r}$, of the original non-proportionally damped multi-story asymmetrical building:

$$S_{dz,r} \approx \eta_z S_{dz}^*, \quad S_{d\theta,r} \approx \eta_\theta S_{d\theta}^* \quad (14a)$$

where

$$\eta_z = \frac{\mathbf{h}^T\mathbf{m1}}{\mathbf{h}^T\mathbf{mh}}, \quad \eta_\theta = \frac{\mathbf{h}^T\mathbf{m1}}{\sqrt{\mathbf{h}^T\mathbf{mhh}^T\mathbf{Ih}}}$$
$$\mathbf{h} = \begin{bmatrix} 1 & \dfrac{N-1}{N} & \cdots & \dfrac{1}{N} \end{bmatrix}^T, \quad n = 1 \sim 2 \quad (14b)$$

Buildings TS, TSS, and TF were used as the example buildings to verify the accuracy of applying the response spectra constructed from the EOSB to estimate their peak roof responses (Lin and Tsai 2013). The selected ground motion records are the set of 20 ground motions records with a return period of 475 years, which was used in the SAC steel research project for buildings located in Los Angeles. The properties of the EOSBs for Buildings TS, TSS, and TF are shown in Lin and Tsai (2013). The response spectra of the EOSBs constructed are shown in Fig. 2. The spectral values S_{dz}^* and $S_{d\theta}^*$ (Fig. 2), corresponding to the translational vibration periods of buildings TS, TSS, and TF, multiplied by η_z and η_θ, respectively, and the estimation errors are shown in Lin and Tsai (2013). It is found that the means of the estimation errors are between 3.8% and 13.4%; the coefficients of variation for the estimation errors are between 0.23 and 1.61. In addition, most of the estimations are on the conservative side. Fig. 3 shows the comparison of the estimated and the exact peak roof responses. The aforementioned estimation results confirm that the peak roof displacements of these three 8-story example buildings can be satisfactorily estimated using the proposed approach.

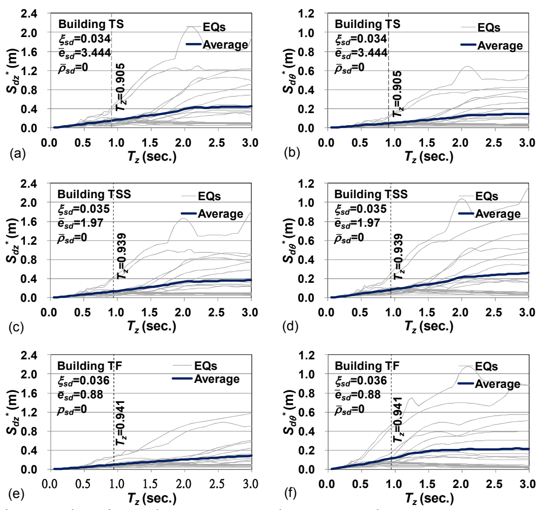

Figure 2. The displacement response spectra for Building (a) and (b) TS $(\xi = 0.02, \quad \bar{e} = 1.3, \quad \Omega = 1.794)$; (c) and (d) TSS $(\xi = 0.02, \quad \bar{e} = 0.738, \quad \Omega = 1.098)$; (e) and (f) TF $(\xi = 0.02, \quad \bar{e} = 0.331, \quad \Omega = 0.492)$ subjected to the selected set of 20 seismic ground motions.

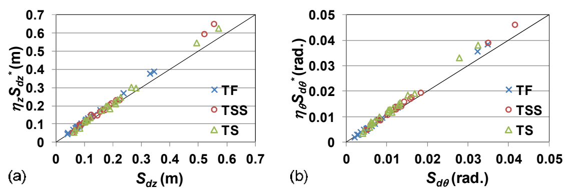

Figure 3. The comparison of the estimated (a) roof translations and (b) roof rotations with the corresponding exact responses for Buildings TS, TSS, and TF subjected to the selected set of 20 seismic ground motions.

Conclusions

Evidently, besides the equivalent damping ratio, there should be other overall system parameters for characterizing the plan-wise distribution of added viscous dampers in multi-story asymmetrical buildings. In this study, there were three proposed supplemental damping characteristics for multi-story asymmetrical buildings with linear viscous dampers, which are the same as those stated in other literature focusing on single-story asymmetrical buildings. These three supplemental damping characteristics are the equivalent supplemental damping ratio ξ_{sd}, the normalized equivalent supplemental damping eccentricity $\bar{e}_{sd}$, and the normalized equivalent supplemental damping radius of gyration $\bar{\rho}_{sd}$. This study first constructed the EOSB as the vehicle for characterizing the supplemental damping in multi-story asymmetrical buildings. These overall system parameters enable practicing engineers to understand and quantitatively describe the resultant effects of the added viscous dampers in multi-story asymmetrical buildings. Second, this study showed that the roof displacement responses of the original multi-story building could be estimated by mapping the displacement responses of the EOSB. The response spectra constructed from the EOSBs were satisfactorily applied to estimate the peak roof displacements of three non-proportionally damped 8-story example buildings subjected to 20 seismic ground motions.

References

Goel, R.K. (1998), “Effects of supplemental viscous damping on seismic response of asymmetric-plan systems”, *Earthquake Engineering and Structural Dynamics*, 27: 125-41.

IBC (2000), International building code, *International Conference of Building Officials*, Whittier, CA.

Lin, J.L., Tsai, K.C. (2007), “Simplified seismic analysis of asymmetric building systems”, *Earthquake Engineering and Structural Dynamics*, 36: 459-79.

Lin, J.L., Tsai, K.C. (2013), “Application of supplemental damping characteristics to response spectrum analyses of non-proportionally damped multistory asymmetric-plan buildings”, *Earthquake Spectra*, 29: 207-232.

Tso, W.K., Sadek, A.W. (1985), “Inelastic seismic response of simple eccentric structures”, *Earthquake Engineering and Structural Dynamics*, 13: 255-269.

The Study of the Seismic Assessment Parameters of a New Seismic-design Building

Te-Kuang Chow [1] and Yeong-Kae Yeh [2]

周德光 [1]、葉勇凱 [2]

Abstract

At present, the commonly used method in earthquake engineering for new building design is based on the current seismic design specifications, according to seismic requirements and the allowable ductility capacity, which provides designers with a minimum design horizontal force, which is then combined with the response spectrum to complete the elastic design. The current seismic assessment procedures use nonlinear pushover analysis to achieve this result. The performance target ground acceleration of a structure is compared with the site peak ground acceleration of a design earthquake with a 475-year return period to evaluate whether the seismic capacity of the structure is adequate. This article explores the parameters and discusses the differences between seismic design specifications and seismic evaluation by pushover analysis. The initial yield lateral force and the ductility capacity from pushover analysis are all higher than those of the current seismic design specifications. The results of this study indicate that the current seismic design specifications have conservative design lateral force and ductility capacity requirements.

Keywords: new design, seismic design specification, seismic evaluation, nonlinear pushover analysis

Introduction

A detailed seismic evaluation procedure is often used to confirm the seismic capacity of existing buildings. Currently, the most widely used detailed evaluation method is nonlinear pushover analysis to obtain the capacity curves of structures: that is to establish the relationship curve of the base shear and roof displacement. Then based on the building's performance needs, a performance point is set on the capacity curve through a specific procedure in order to find a design earthquake that can cause the desired performance roof displacement. This performance target earthquake is presented in terms of its associated 475-year design response spectrum and maximum ground acceleration. The specifics for the above procedures fall into two methodologies: one is the capacity spectrum method suggested by ATC 40 [1]; another is the coefficient method suggested by FEMA 356 [2].

In Taiwan, the most popular detailed seismic evaluation methods are “Seismic Evaluation of Reinforced Concrete Structure with Pushover Analysis” developed by the National Center for Research on Earthquake Engineering (NCREE) [3, 4] and “Seismic Evaluation of RC Buildings (SERCB) [5]” developed by the team of Prof. I-Chau Tsai from National Taiwan University. Both of these two methods are based on the capacity spectrum method of ATC-40. The capacity spectrum method has been widely used in the seismic evaluation and retrofitting of existing buildings in Taiwan. It is necessary to explore the differences between related parameters in pushover analysis and the new seismic-design procedure. A building that were designed according to the latest seismic design specifications [6] had seismic evaluation conducted using nonlinear pushover analysis to explore differences in their parameters and conservative factors. In the new seismic-design procedure, structures are treated as elastic structures, whereas in pushover analysis, they are treated as nonlinear structures. Both procedures have corresponding parameters such as the design seismic force, yield seismic force, ultimate seismic force, ductility capacity, and allowable ductility capacity. Design specification sets the related values according to the structure of the system. Pushover analysis can obtain the same corresponding

[1] Assistant Technologist, National Center for Research on Earthquake Engineering, tkchow@ncree.narl.org.tw

[2] Research Fellow, National Center for Research on Earthquake Engineering, ykyeh@ncree.narl.org.tw

parameter values through structural analysis, and then both procedures can be compared.

In this paper, the example structure of the Civil 404-100 report was used to demonstrate the new seismic-design procedure. For the nonlinear pushover analysis, the third version of the technology handbook [4] of NCREE was adopted to define the nonlinear hinges of the structure, and the software package ETABS is used as the tool.

New Seismic-Design Building Case

The following are the summarized structural data of the new seismic-design building case of the Civil 404-100 report:

1. The structure is located in Taichung City, Central District, and its site soil is classified as Site Class 1.
2. The building includes two basement stories, ten stories, and two convex layer stories. The 1st floor has a height of 4.5 m, the 2nd~10th floors are 3.2 m in height, the convex layer floors are 3 m in height each, and the basement floors are 3.2m in height each. The structural analysis model is shown in Figure 1.

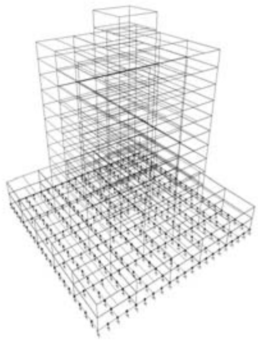

Figure 1. 3D Structural analysis model

3. A raft foundation is adopted and soil springs are used for the interaction between soil and foundation.
4. The structural system is a dual system in the X-direction, which contains ductile moment-resisting frames and shear walls to resist horizontal forces; in the Y-direction, the structural system is a ductile moment-resisting frame system.
5. Material strength (kgf/cm^2): Concrete: 280, main bar: 4200, and stirrup: 2800.
6. Member size:
   Columns: 80×80 cm square section;
   Girders: 40×70, 50×75, 50×80, 60×75 and 60×80 cm rectangular section;
   Beams: 30×60 cm rectangular section;
   Shear walls: 30 cm below the 2nd floor,
   25 cm for the 3rd~4th floors, and
   20 cm above the 5th floor;
   Slabs: 20 cm in the interior of the 1st floor,
   24 cm in exterior of the 1st floor and
   15 cm for all other slabs.
7. For the vertical loading analysis, calculations included the weight for each floor as shown in Table 1.
8. For the seismic loading analysis, calculations included the vertical distribution of the minimum horizontal design force on each floor as shown in Table 2.
9. The parameters obtained from the results of the new seismic-design procedure, shown in Table 3, can be compared with those from the pushover analysis.
10. For the design results for reinforcement, the reader is referred to report NCREE-13-041.

Table 1. Floor weights by floor

Floor	Weight(*tf*)
PRFL	65.82
R2FL	102.85
R1FL	545.45
10FL	667.74
9FL	667.74
8FL	667.74
7FL	667.74
6FL	693.32
5FL	694.79
4FL	697.56
3FL	699.02
2FL	775.3
1FL	1927.44
B1FL	1767.53
B2FL	4462.91
Sum	15102.95

Table 2. Vertical distribution of lateral force by floor

X Direction			Y Direction		
Floor	Lateral Force(*tf*)	Scale	Floor	Lateral Force(*tf*)	Scale
PRFL	30.04	0.177	PRFL	21.6	0.177
R2FL	22.44	0.132	R2FL	16.14	0.132
R1FL	169.67	1	R1FL	122.01	1
10FL	143.77	0.847	10FL	91	0.746
9FL	128.49	0.757	9FL	81.32	0.666
8FL	113.2	0.667	8FL	71.65	0.587
7FL	97.92	0.577	7FL	61.98	0.508
6FL	85.8	0.506	6FL	54.31	0.445
5FL	70.08	0.413	5FL	44.35	0.363
4FL	54.39	0.321	4FL	34.42	0.282
3FL	38.5	0.227	3FL	24.37	0.200
2FL	24.96	0.147	2FL	15.8	0.129
1FL	192.74	1.136	1FL	192.74	1.580
B1FL	162.61	0.958	B1FL	162.61	1.333
B2FL	0	0	B2FL	0	0

Table 3. Parameters in the seismic-design procedire

	X Direction	Y Direction
T_{dyn}(sec)	0.7592	1.2544
0.4S_{DS}(g) (PGA)	0.32	
Seismic force magnification of initial yielding α_y	1	
Ductility capacity of the structural system R	4	
Allowable ductility capacity of the structural system R_a	3	
The minimum horizontal design force	0.141W 979.26*tf*	0.092W 638.95 *tf*

Pushover Analysis for Seismic Evaluation

First, nonlinear hinges are added to the previously described structural model; the loading includes dead load and 1/2 design live load. Two different lateral force distributions for the seismic force are considered: dominant modal distribution and design lateral force distribution. Three structural models are considered: the original design model, the X-direction pushover analysis model (using the equivalent column model to simulate shear walls), and the Y-direction pushover analysis model (using the original ductile moment resistant frame structure model). The compared modal periods are shown in Table 4.

Table 4. Comparison of modal periods

Direction	Dominant Mode	T_{dyn} (sec)			
		404-100 model example	Origin design model	X direction pushover analysis model	Y direction pushover analysis model
X-Translation	3	0.7592	0.7792	0.8398	---
Y-Translation	1	1.2544	1.2528	---	1.2861
Z-Rotation	2	---	---	---	---

As shown in Table 4, the modal periods of the 404-100 model and the original design model are extremely close. The modal periods of X- and Y-direction pushover analysis models are larger than the modal period of the 404-100 model because of the reduced stiffness of beams and columns in the pushover models.

The capacity curve of the pushover analysis comes from the whole structure. The capacity curve of the whole structure is the relationship curve of B2FL base shear and R1FL roof mass center displacement. The capacity curve of the whole structure needs to be converted to the capacity curve of the superstructure, which is the relationship curve of 1FL floor base shear and R1FL floor mass center displacement. With the reference modal shape of the superstructure, the superstructure's capacity curve can be transformed to the capacity spectrum and the performance curve. The reference modal shape of the pushover model in the X-direction is shown in Table 5. From the results of pushover analysis in the X- and Y- directions, the seismic capacity of the CP (Collapse Prevention) point can be compared with the 2500-year return period seismic demand. The CP point is located at the final point of the capacity curve. The parameters of pushover analyses are summarized in Table 6. It can be seen that the seismic capacities for CP points of the X- and Y-direction pushover analyses are higher than the current seismic specification requirements, and that the ductility capacity R is higher than the new design specification value 4, which means that the current seismic design specification includes a considerable degree of safety.

Parameter Comparison

From the capacity curve of pushover analysis, the ductility capacity of the structural system R, design seismic force P_d, yield seismic force P_y, and ultimate seismic force P_u can be obtained to compare with the values of the new seismic-design procedure. The analysis results in X-direction are shown in Figure 2, Figure 3, and Table 7. The analysis results in the Y-direction are shown in Figure 4, Figure 5, and Table 8.

Table 5. Reference modal shape
(X-direction pushover model)

Floor	Whole structure		Superstructure	
	Modal shape	Nomalized modal shape	Modal shape	Nomalized modal shape
PRFL	0.0215	1.000	-	-
R2FL	0.0198	0.921	-	-
R1FL	0.0181	0.842	0.0172	1.000
10FL	0.0163	0.758	0.0154	0.895
9FL	0.0144	0.670	0.0135	0.785
8FL	0.0126	0.586	0.0117	0.680
7FL	0.0107	0.498	0.0098	0.570
6FL	0.0089	0.414	0.0080	0.465
5FL	0.0071	0.330	0.0062	0.360
4FL	0.0054	0.251	0.0045	0.262
3FL	0.0039	0.181	0.0030	0.174
2FL	0.0025	0.116	0.0016	0.093
1FL	0.0009	0.042	0.0000	0.000
B1FL	0.0004	0.019	-	-
B2FL	0	0.000	-	-

Table 6. Parameters of pushover analyses

	Dominant mode distribution		Design specifications lateral force distribution	
	X	Y	X	Y
Performance target ground acceleration	0.736g	0.824g	0.701g	0.799g
Ductility capacity	5.07	4.88	5.50	5.07
Seismic capacity	0.736g		0.701g	
Seismic demand $0.4S_{MS}$	0.4 g			

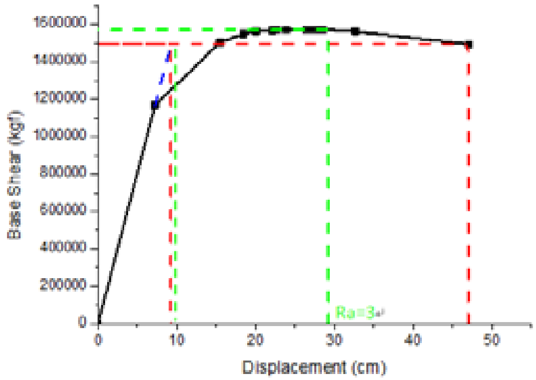

Figure 2. Ductility capacity diagram in X-direction
(dominant mode distribution)

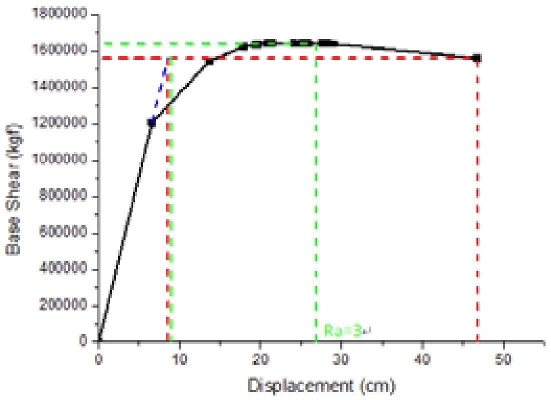

Figure 3. Ductility capacity diagram in X-direction (design specifications lateral force distribution)

Table 7. Parameter comparison for X-direction analysis

	Seismic design	Dominant mode distribution	Design specifications lateral force distribution
Ultimate seismic force P_u (tf)	1371	1494	1561
Yield (design) seismic force P_y (tf)	979	1167	1206
Ultimate ductility capacity R	4	5.07	5.50
Performance target ground acceleration (allowable ductility capacity R_a=3) (g)	0.32	0.571	0.522
Performance target ground acceleration (CP point) (g)	0.40	0.736	0.701

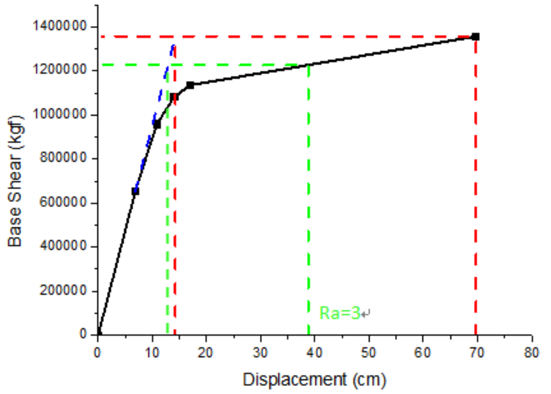

Figure 4. Ductility capacity diagram in Y-direction (dominant mode distribution)

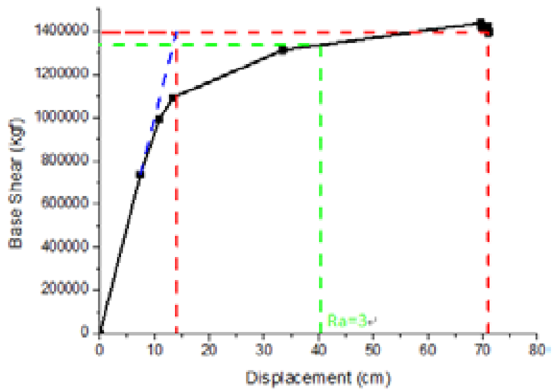

Figure 5. Ductility capacity diagram in Y-direction (design specifications lateral force distribution)

Table 8. Parameter comparison for Y-direction analysis

	Seismic design	Dominant mode distribution	Design specifications lateral force distribution
Ultimate seismic force P_u (tf)	895	1357	1396
Yield (design) seismic force P_y (tf)	639	652	736
Ultimate ductility capacity R	4	4.88	5.06
Performance target ground acceleration (allowable ductility capacity R_a=3) (g)	0.32	0.578	0.567
Performance target ground acceleration (CP point) (g)	0.40	0.824	0.797

According to the comparisons, the seismic forces and ductility capacities of pushover analyses are all higher than the new seismic-design requirements. The results indicate that the new seismic specification is more conservative than pushover analysis and the pushover analysis will provide higher seismic capacity.

Conclusions

This study shows that the load distribution mode affects the result of pushover analysis. It also indicates that the actual seismic capacity of the building is larger than the current seismic design specification. The current seismic design specification retains a considerable degree of safety..

References

[1] Applied Technology Council (ATC) (1996), "ATC-40 Seismic Evaluation and Retrofit of Concrete Buildings", prepared by the Applied Technology Council, Redwood City, Calif.

[2] Federal Emergency Management Agency (FEMA) (2000), "Prestandard and Commentary for the Seismic Rehabilitation of Buildings (FEMA Publication 356)", prepared by the American Society of Civil Engineers, Washington, D.C.

[3] 「Seismic Evaluation of Reinforced Concrete Structure with Pushover Analysis」 NCREE 09-015，Taipei，2009。

[4] 「Technology Handbook for Seismic Evaluation and Retrofit of School Buildings - Third Edition」 NCREE 13-023，Taipei，2013。

[5] Architecture and Building Research Institute, (Ministry of the Interior), 「Technology Handbook for Seismic Evaluation of RC Buildings - Window assisted analysis system」Taipei，2005。

[6] Construction and Planning Agency Ministry of the Interior，「Building Seismic Design Specification and Commentary」，Taipei，July 2011。

Verification of Simplified Pushover Analysis of School Buildings with Brick Walls by In-Situ Tests

Lap-Loi Chung[1], Chun-Ting Huang[2], Yao-Sheng Yang[2], Sheng-Xue Lin[2]
Yong-An Lai[2], and Lai-Yun Wu[3]

鍾立來[1]、黃鈞鼎[2]、楊耀昇[2]、林聖學[2]、賴勇安[2]、吳賴雲[3]

Abstract

Based on the capacity spectrum method from ATC-40, a seismic evaluation method by using pushover analysis is developed by the National Center for Research on Earthquake Engineering (NCREE). In civil engineering, ETABS and SAP2000 are used for pushover analysis to analyze the seismic capacity of existing buildings. However, for some people, this software may be too expensive therefore, a simple method called simplified pushover analysis is developed. This method can help engineers obtain preliminary analysis results of the seismic capacity for existing buildings without using software. The method of seismic evaluation for existing buildings needs to be confirmed. In the past, NCREE has conducted in-situ tests of school buildings. The capacity curve of a school building with brick walls has been established from the experimental results. The simplified pushover analysis is verified by comparing the results obtained with the experimental ones. The comparison indicates that the proposed analysis method can be used for low-rise buildings and is beneficial for engineers performing seismic evaluations for low-rise buildings.

Keywords: brick wall, school building, simplified pushover analysis,

Introduction

In Taiwan, school buildings are reinforced concrete (RC) buildings that can be used as emergency shelters during an earthquake. However, during the Chi-Chi Earthquake in Taiwan, a total of 829 school buildings were damaged and collapsed. Unfortunately, elementary and junior high schools were subject to the majority of the damage. Solving the problem of a lack of knowledge about the seismic capacity of existing school buildings becomes a stringent issue, and in order to realize the seismic capacity of school buildings, seismic evaluation methods are proposed by the National Center for Research on Earthquake Engineering (NCREE) to select which existing school buildings need to be retrofitted.

The best way to verify the reasonableness of existing seismic evaluation methods is by using in-situ pushover tests results. For this reason, in-situ pushover tests of school buildings that were subjected to lateral forces have been carried out in Taiwan by the NCREE. The reasonable results can provide engineers with a way to perform detailed seismic evaluations.

For existing low-rise school buildings in Taiwan, there is another seismic evaluation method that can analyze the seismic capacity of existing school buildings without using a software package. This method is called simplified pushover analysis. It can not only calculate the seismic capacity by hand, but also help engineer check the software package results.

Since the displacements of all vertical members in a single story are consistent, the lateral force of the story is obtained by superimposing the lateral forces of all vertical members in that story. According to the distribution of earthquake forces based on the seismic code in Taiwan, the story drift corresponding to the story lateral force of each story can be found. Finally, the seismic capacity curve of the structure, which is the relationship between the base shear versus roof

[1] Research Fellow, National Center for Research Earthquake Engineering. chung@ncree.org.tw.
[2,3]Department of Civil Engineering, NTU. d00521023@ntu.edu.tw

displacement, can be obtained.

The simplified pushover analysis was verified by in-situ pushover tests of school buildings (only columns are considered). The result of the simplified pushover analysis shows that the analytical pushover curve shows conservative agreement with in-situ pushover tests of school buildings and it is beneficial for engineers in checking the results of seismic evaluation methods.

In this study, the reasonableness of simplified pushover analysis for school buildings with brick walls is investigated. Brick walls confined on three sides are very common in school buildings in Taiwan because of the requirements for ventilation and natural light in a classroom. Brick wall is also considered to be a vertical member in the simplified pushover analysis, which is verified by in-situ pushover tests of a school building in Kou-hu Elementary School. The capacity curves from a simplified pushover analysis and in-situ pushover tests are compared.

Lateral Force-Displacement Curve of Vertical Members

In the typical school buildings damaged by the Chi-Chi Earthquake, the failure behavior of the buildings was weak-column and strong-beam. Therefore, vertical members played the main role in resisting the earthquake. Not only are the columns vertical members, but also the confined brick walls restrained on three sides, which are very common in school buildings in Taiwan, are vertical members. Thus, in this study, there are two types of vertical members to be considered. The nonlinear behavior of typical school buildings is established by the nonlinear behavior of RC columns and brick walls restrained on three sides. From previous research studies, column behaviors are categorized into three different column failure conditions: flexural failure, shear failure, and flexural-shear failure (Sezen & Moehle, 2004). In our study, the failure condition of all columns is flexural-shear failure, and the lateral force-displacement curve of a column found in Elwood & Moehle (2005) is defined in Fig. 1.

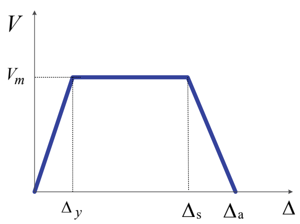

Fig. 1 Lateral force-displacement curve of flexural-shear failure of a column

In Fig.1, V_m is the nominal shear strength calculated as in eq. (1):

$$V_m = 2M_n / H_n \tag{1}$$

where M_n is the nominal flexural strength; and H_n is the clear height of the RC column. When a column undergoes yielding, the lateral displacement (Δ_y) can be calculated using eq. (2):

$$\Delta_y = V_m / k \tag{2}$$

where k is the lateral stiffness of a column that can be calculated using eq. (3).

$$k = 0.35 \times 12(E_c I_g) / H_n^3 \tag{3}$$

where E_c is the modulus of elasticity of concrete; and I_g is the moment of inertia of the gross concrete section. When a column undergoes shear failure, the lateral displacement (Δ_s) can be calculated using eq. (4):

$$\frac{\Delta_s}{H_n} = \left[\frac{3}{100} + 4\rho'' - \frac{1}{133}\frac{v_m}{\sqrt{f_c'}} - \frac{1}{40}\frac{P}{A_g f_c'}\right] \geq \frac{1}{100} \tag{4}$$

where ρ'' is the ratio of transverse reinforcement and is defined as $\rho'' = A_{st} / (b \times s)$; A_{st} is area of transverse reinforcement; b is the column section width; s is the tie spacing; v_m is the maximum nominal shear stress and is defined as $v_m = V_m / bd$; d is the depth to centerline of tension reinforcement; f_c' is the compressive strength of concrete; and P and A_g are the axial force and the gross area of the RC column, respectively. When a column undergoes axial failure, the lateral displacement (Δ_a) can be calculated using eq. (5):

$$\Delta_a = H_n \left[\frac{4}{100} \frac{1 + (\tan\theta)^2}{\tan\theta + P \dfrac{s}{A_{st} f_{yt} d_c \tan\theta}}\right] \tag{5}$$

where θ is the angle from the horizontal to the critical plane due to shear failure (assumed to be 65 degrees); s is the transverse reinforcement spacing; f_{yt} is the specified yield strength of the transverse reinforcement; and d_c is the depth of the column core from the center line to the center of the ties.

From the Design and Construction Specifications of Brick Structures for Buildings, in Taiwan, the lateral force-displacement curve for brick walls confined on three sides is as shown in Fig. 2.

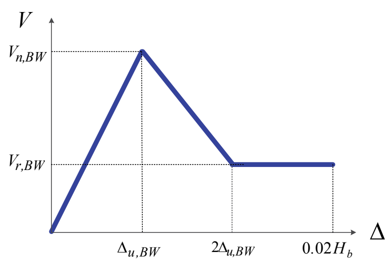

Fig. 2 Lateral force-displacement curve of brick wall

In Fig. 2, the ultimate strength $V_{n,BW}$ can be calculated using eq. (6):

$$V_{n,BW} = T_b \times (W_b \times \tau_f + H_2 \times 0.45 f_{mbt}) \tag{6}$$

where T_b and W_b are the thickness and width of a brick wall, respectively; and τ_f is the friction strength between the brick and mortar and is calculated using eq. (7):

$$\tau_f = 0.0337(f_{mc})^{0.885} \quad (7)$$

where f_{mc} is the compressive strength of mortar; and f_{mbt} is the splitting tensile strength between the brick and mortar and is calculated using eq. (8):

$$f_{mbt} = 1.079(f_{mc})^{0.338} \quad (8)$$

H_2 is the effective height of brick wall calculated using eq. (9):

$$H_2 = 0.5W_b \tan\theta_c \le H_b \quad (9)$$

where H_b is the height of the brick wall; and θ_c is the crack angle of the brick wall and is calculated using eq. (10):

$$\theta_c = \tan^{-1}\left(\frac{2(h_b+g_h)}{w_b+l_b+2g_v}\right) \quad (10)$$

where h_b is the height of a brick; w_b is the width of a brick; l_b is the length of a brick; and g_h and g_v are the horizontal and vertical thicknesses of mortar between the brick, respectively.

The ultimate displacement $\Delta_{u,BW}$ of a brick wall can be calculated using eq. (11):

$$\Delta_{u,BW} = \lambda\frac{V_{n,BW}}{E_u \times T_b} \quad (11)$$

where E_u is the elastic modulus and is calculated using eq. (12):

$$E_u = 61.29\eta_1\eta_2 f_{bc}^{0.7} f_{mc}^{0.3} \quad (12)$$

where η_1 and η_2 are the modification factors where $\eta_1 = 1.67 - 0.64(H_b/W_b)$, $0.5 \le H_b/W_b \le 2.0$; and $\eta_2 = 0.367$; f_{bc} is the compressive strength of brick; and λ is defined by eq. (13)

$$\lambda = \left[\left(\frac{5}{4}+\frac{3}{2}\nu\right)\frac{W_b}{H_b}+\left(2+\frac{7}{4}\nu\right)\frac{H_b}{W_b}+\left(2+\frac{3}{2}\nu\right)\frac{H_b^3}{W_b^3}\right] \quad (13)$$

where $0.5 \le H_b/W_b \le 2$; $\nu = 0.15$.

When the displacement of the brick walls is equal to $2\Delta_{u,BW}$, the lateral force will reduce to a residual strength $V_{r,BW}$, which can be calculated using eq. (13):

$$V_{r,BW} = \tau_f \times T_b \times W_b \le 0.6V_{n,BW} \quad (13)$$

Simplified Pushover Analysis

In this study, the specimen used was a 2-story school building and its seismic capacity was calculated by a simplified pushover analysis using the following procedure:

1. The lateral force-displacement curves of all vertical members for the first and second story were established.
2. The lateral force-displacement curves of the first and second stories were established. It should be noted that the lateral forces of each story were obtained by superimposing the lateral forces of all vertical members in the respective story by a consistent displacement.
3. Based on the seismic code in Taiwan, when a building is subjected to a lateral earthquake load, the distribution of the lateral force of the first and second story can calculated by eq. (14):

$$V_{2F} = \frac{W_{RF}h_{RF}}{W_2h_2 + W_{RF}h_{RF}} \times V_{1F} \quad (14)$$

   where $V_{1F} = V_{bs}$ is the base shear; W_{RF} and W_2 are the weights of the roof floor and the second floor, respectively; and h_{RF} and h_2 are the height of the roof floor and the second floor, respectively.
4. Based on eq. (14) and the lateral force-displacement curves of the first and second story, the corresponding lateral displacement of the first story (Δ_1) and the second story (Δ_2) were obtained. The roof displacement can be calculated by eq. (15):

$$\Delta_{RF} = \Delta_1 + \Delta_2 \quad (15)$$

5. Finally, the base shear versus the roof displacement curve determining the seismic capacity of the 2-story school building was obtained.

Data of Kou-hu Elementary School

The data of the school building subjected to in-situ tests in Kou-hu Elementary School are summarized as follows:

Kou-hu Elementary School is a 2-story RC building with brick walls located in Yunlin, Taiwan. There are two classrooms in each story and the heights of the first and second story are 3.32m and 3.40m, respectively, as show in Fig 3.

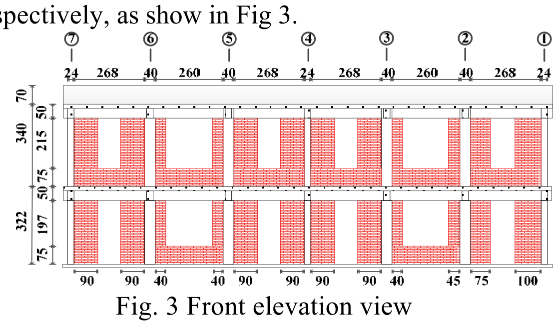

Fig. 3 Front elevation view

The total length and width of each classroom are 9m and 9.3m, respectively, as show in Fig 4.

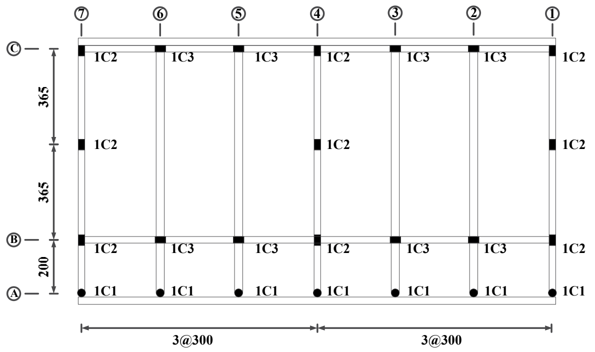

Fig. 4 Plan view

There are 24 columns and 24 brick walls confined with concrete columns in the first story and 21 columns and 24 brick masonry walls confined with concrete columns in the second story.

The material strengths are $f_c' = 281.35\,kgf/cm^2$, $f_{yt} = 3537.21\,kgf/cm^2$, $f_{mc} = 265.30\,kgf/cm^2$, and $f_{bc} = 221.20\,kgf/cm^2$. They are the average values of the samples taken from the building. In this study, the value of θ_c is equal to 20.7°.

Analysis Results

Fig. 4 presents the lateral force-displacement curve of the first and second story. The maximum lateral forces of the first and second story are 206tf and 180tf, respectively.

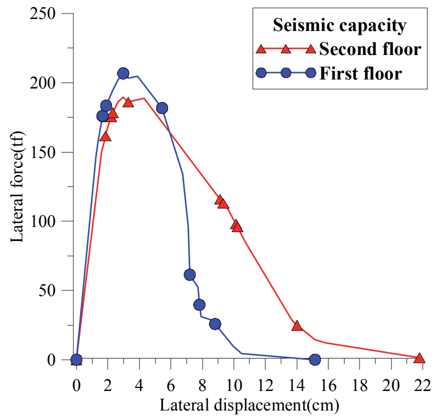

Fig. 4 Lateral force-displacement curve of first and second story

Fig. 5 presents the comparison of pushover curves between the in-situ tests and the simplified pushover analysis. The maximum base shears from the simplified pushover analysis and in-situ tests were 206tf and 286tf as the roof displacement reached 3.88cm and 2.99cm, respectively. The initial stiffness values from analysis and tests were 76.98tf/cm and 266.67tf/cm, respectively.

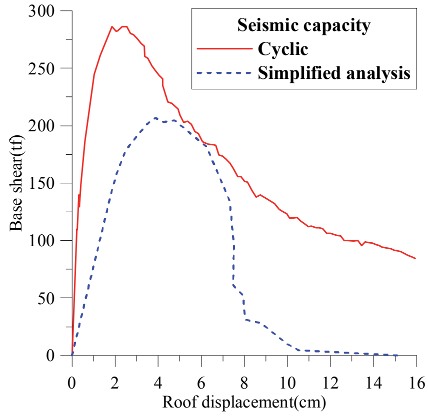

Fig. 5 Comparison between in-situ tests and the simplified pushover analysis

Conclusions

Seismic capacity from the simplified pushover analysis obtained by superimposing the lateral force-displacement curves of vertical members was verified with the in-situ pushover tests of Kou-hu Elementary School in Taiwan. The verification indicates the following:

1. The results of analysis provide conservative predictions in base shear and stiffness. The base shear prediction is 72.3% of the test result while the initial stiffness is 29% of the test result.
2. The simplified pushover analysis is an effective analytical tool to obtain the seismic capacity of shear buildings.

References

Sezen H. and Moehle, J.P., “Shear Strength Model for Lightly Reinforced Columns,” ASCE Journal of Structural Engineering, Vol. 130, No: 11, pp. 1692-1703, 2004.

Elwood, K.J. and Moehle, J.P., “Drift Capacity of Reinforced Concrete Columns with Light Transverse Reinforcement,” Earthquake Spectra, Vol. 21, No. 1, pp. 71-89, 2005.

Elwood, K.J. and Moehle, J.P., “Axial Capacity Model for Shear-Damaged Columns,” ACI Structural Journal, Vol. 102, No. 4, pp. 578-587, 2005.

Simplified Pushover Analysis for School Building Retrofitted with Reinforced Concrete Jacketing

Lap-Loi Chung[1,2], Yu-Cheng Li[3], Wei-Bin Weng[4], Yao-Sheng Yang[4], Te-Kuang Chow[5], Chiung-Shiann Huang[6], Chein-Shan Liu[2]

鍾立來[1,2], 黎育誠[3], 翁緯彬[4], 楊耀昇[4], 周德光[5], 黃炯憲[6], 劉進賢[2]

Abstract

Many elementary and secondary school buildings were damaged by the devastating 921 Chi-Chi earthquake, which led many researchers to propose retrofitting methods to improve the seismic performance of school buildings. Retrofitting with reinforced concrete jacketing at columns can increase the ductility and strength of buildings. After this procedure, a simplified pushover analysis can be performed to understand the behavior of the structure, and this is an easy way to allow young engineers to analyze structures by hand instead of using software like ETABS. The method used for analysis is called *slope-deflection pushover*. It is based on the slope-deflection method but includes some additional assumptions. Because of this, it is not only suitable for weak-column strong-beam buildings but also strong-column weak-beam buildings. Compared with experimental results, the slope-deflection pushover analysis underestimates the strength and deformation capacity, but overestimates the stiffness of a building. Compared with ETABS analysis, the strength and stiffness of the building estimated by the slope-deflection pushover analysis are higher than those determined by the ETABS analysis. Furthermore, the mode and sequence of failure of the building determined by the slope-deflection pushover analysis are also very similar to those determined by ETABS analysis.

Keywords: school buildings, retrofitted, reinforced concrete jacketing, seismic evaluation, strong-column weak-beam, pushover analysis

Assumptions of slope-deflection pushover analysis

Conventional pushover analysis is only suitable for weak-column strong-beam buildings. After retrofitting with jacketing columns, the performance of a structure can change from weak-column strong-beam to strong-column weak-beam characteristics. The ductility and strength of buildings are overestimated by a conventional pushover analysis. Therefore, a slope-deflection pushover analysis is proposed in this paper. It extends the structural analysis from only weak-column strong-beam buildings to include strong-column weak-beam buildings as well. Before using the slope-deflection pushover, we make the following assumptions:

1) It is limited to low-rise reinforced concrete buildings.
2) The lateral displacement of every column is the same on the same floor.
3) There are no walls, *i.e.*, the strength provided by walls is negligible.
4) Rotation angles at the two ends of the beam are the same.

Slope-deflection pushover analysis

[1] Research Fellow, National Center for Research on Earthquake Engineering, chung@ncree.narl.org.tw
[2] Professor, Department of Civil Engineering, National Taiwan University
[3] Graduate Student, Department of Civil Engineering, National Chiao Tung University
[4] Graduate Student, Department of Civil Engineering, National Taiwan University, r01521240@ntu.edu.tw
[5] Research Assistant, National Center for Research on Earthquake Engineering
[6] Professor, Department of Civil Engineering, National Chiao Tung University

Figure 1 shows a specimen from Hou-Jia Junior High School that was retrofitted with reinforced concrete jacketing. Based on Assumption 4, the structure can be decomposed into four independent unit column lines. Taking column line C11 (Fig. 2(a)) as an example, the moments at the column and beam-ends are expressed by the slope-deflection formulas:

$$M_{c,bot,1F} = \frac{2(EI)_{c,1F}}{H_{c,1F}}(\theta_{b,1F} - 3\frac{\Delta_{1F}}{H_{c,1F}}) \tag{1}$$

$$M_{c,top,1F} = \frac{2(EI)_{c,1F}}{H_{c,1F}}(2\theta_{b,1F} - 3\frac{\Delta_{1F}}{H_{c,1F}}) \tag{2}$$

$$M_{b,1F} = \frac{6(EI)_{b,1F}}{L_{b,1F}}\theta_{b,1F} = k_{b,1F}\theta_{1F} \tag{3}$$

$$M_{c,bot,2F} = \frac{2(EI)_{c,2F}}{H_{c,2F}}(2\theta_{b,1F} + \theta_{b,2F} - 3\frac{\Delta_{2F}}{H_{c,2F}}) \tag{4}$$

$$M_{c,top,2F} = \frac{2(EI)_{c,2F}}{H_{c,2F}}(\theta_{b,1F} + 2\theta_{b,2F} - 3\frac{\Delta_{2F}}{H_{c,2F}}) \tag{5}$$

$$M_{b,2F} = \frac{6(EI)_{b,2F}}{L_{b,2F}}\theta_{b,2F} = k_{b,2F}\theta_{2F} \tag{6}$$

Here, $M_{c,bot,1F}$ and $M_{c,top,1F}$ are respectively the bottom and top moments of the first-floor column; $M_{c,bot,2F}$ and $M_{c,top,2F}$ are respectively the bottom and top moments of the second-floor column; $M_{b,1F}$ and $M_{b,2F}$ are respectively the moments of the first and second-floor beams; $H_{c,1F}$ and $H_{c,2F}$ are respectively the effective heights of the first and second-floor columns; $\theta_{b,1F}$ and $\theta_{b,2F}$ are respectively the rotation angles of the first and second-floor joints; Δ_{1F} and Δ_{2F} are respectively the lateral displacements of the first and second floors; $k_{b,1F}$ and $k_{b,2F}$ are respectively the stiffnesses of the first and second-floor beams modeled as springs (Fig. 2(b)). Meanwhile, $(EI)_c$ is the flexural stiffness of the concrete cracked cross-section of the column ($0.35E_cI_g$ for columns without retrofit and $0.7E_cI_g$ for columns with reinforced concrete jacketing as per FEMA 273 and ATC-40), where E_c is Young's modulus for concrete and I_g is the moment of inertia of the cross-section of the column; and $(EI)_b$ is the flexural stiffness of the concrete cracked cross-section of the beam ($0.35E_cI_g$).

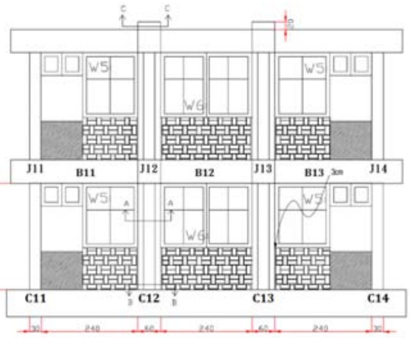

Fig. 1 The specimen from Hou-Jia Junior High School

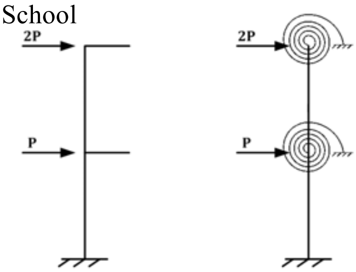

(a) (b)

Fig. 2 Column line C11

Linear elastic section of the capacity curve

In Eqs. (1) to (6), there are four degrees of freedom, Δ_{1F}, Δ_{2F}, $\theta_{b,1F}$, and $\theta_{b,2F}$, and an unknown force, P. By using the four conditions that the summation of the moments of the first-floor joint is equal to zero, summation of the moments of the second-floor joint is equal to zero, the shear force of the first-floor column is equal to 3P, and the shear force of the second-floor column is equal to 2P, we can derive the relationship between these four degrees of freedom and the force P.

The base shear–roof displacement curve does not rise without limit. If one of the components yields, then a turning point appears on the capacity curve, making the slope of the curve decrease. Component yielding is the fifth condition required to obtain a unique solution, *i.e.*, a turning point of the curve. Assuming that one of the components yields first, then after obtaining a solution, we must check the relationship between the four degrees of freedom, the force P, and the moments. If it is meaningful, then this solution is the correct point of the curve; if not, then another component is assumed to have yielded instead. After obtaining the turning point, the moment of the yielding component has to be fixed to the yielding moment. Next, it is assumed that an additional component yields and then the second meaningful turning point is found. Following these steps, we can find every point of the curve. When the solution diverges, this means that the maximum force P has been found, and the curve will not rise any further.

Cracked section of the capacity curve

When a component enters the plastic region, we cannot assume that the moment is fixed in order to determine the cracked curve point, and so we must calculate the cracked displacement Δ_s and the rotation angle $\theta_{b,s}$ first, and then use them to find the turning point of the descendant part of the curve. Normally, when a component cracks, it does not lose all its resistance instantly; however, to simplify the calculation, we assume that a component loses its resistance instantly when it reaches Δ_s or $\theta_{b,s}$. This means that the moment becomes zero. The cracked displacement Δ_s and the rotation angle $\theta_{b,s}$ can be calculated by:

$$\frac{\Delta_s}{H} = 0.03 + 4\rho'' - \frac{1}{133}\frac{v_m}{\sqrt{f_c'}} - \frac{1}{40}\frac{N}{A_g f_c'} \geq \frac{1}{100} \quad \text{and} \tag{7}$$

$$\theta_{b,s} = a + \theta_{b,y}\,. \tag{8}$$

Equation (7) is taken from the research of Elwood and Moehle, where $\rho'' = A_{st} / bs$ is the volume ratio of the shear stirrup; $v_m = V_m / bd$ is the shear stress; f_c' is the resisting concrete compression strength; N is the axial force; A_g is the cross-sectional area of the column; A_{st} is the total cross-sectional area of the shear stirrup in a spacing interval; b is the column width; s is the spacing interval; and d is the effective cross-section depth. Equation (8) is taken from ASCE 41-06, where $\theta_{b,s}$ is the angle of rotation when the beam cracks; $\theta_{b,y}$ is the angle of rotation when the beam yields; and a is the increment between $\theta_{b,s}$ and $\theta_{b,y}$, and is equal to 0.02.

The calculation of the descendant part of the curve is similar to the ascendant part, the only difference being that the cracked displacement and rotation angle are assumed instead of the component moment. That is to say, it is assumed that one component cracks, and then a solution is obtained and checked. If it is meaningful, then it is considered to be a turning point of the descendant part of the curve. In the next calculation, we set the cracked component moment to zero, and then the next point at which another component cracks is obtained. The above steps are repeated to find every point of the curve until the base shear equals zero (Figure 3).

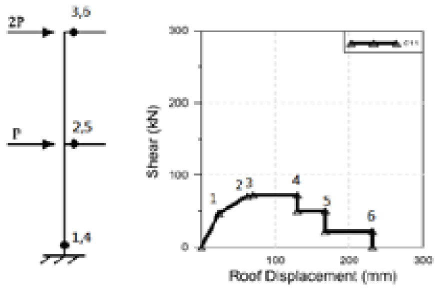

Fig. 3 The sequences of yielding and failure of C11

Capacity curve of the structure

The force–displacement curves of the four column lines are calculated and drawn (Figure 4). According to Assumption 2, we can superpose these four curves to represent the capacity curve of the structure (Figure 5).

The roof displacement of the test was 170.93 mm with a maximum base shear strength of 882.26 kN. The roof displacement of the slope-deflection (SD) pushover was 96.73 mm with a maximum strength of 686.36 kN. This shows that the SD pushover analysis underestimates strength by approximately 22% (Figure 5).

Where the curve decreases to 0.8 times the maximum strength, the strength of the test is 705.81 kN with a roof displacement of 380.41 mm and the strength estimated by the SD pushover is 549.09 kN with a roof displacement of 130.01 mm. This shows that the deformation capacity of the test is better than that of the SD pushover (Figure 5).

From the ETABS analysis results, the roof displacement is 107.83 mm with a maximum strength of 617.77 kN. The strength is obviously lower than those obtained by the test and SD pushover analysis. The initial stiffness of ETABS is more conservative than that of SD pushover, but closer to the test curve. Where strength decreases to 0.8 times the maximum strength, the strength of ETABS is 494.22 kN with a roof displacement of 132.90 mm. Its deformation capacity is similar to that of SD pushover.

From the behavior illustrated by the curves, the strength and ductility of both SD pushover and ETABS are conservative compared with those found from testing, but the stiffness is higher.

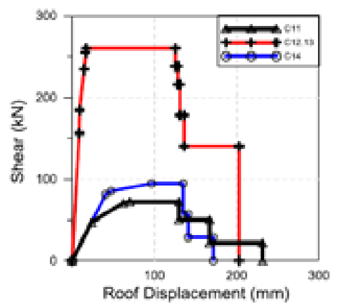

Fig. 4 Capacity curves of four unit columns

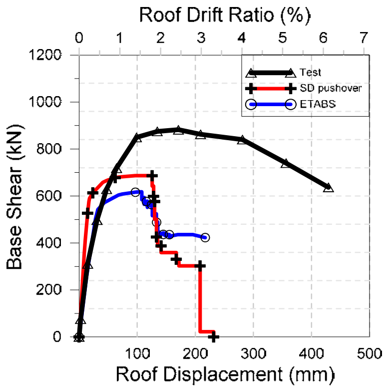

Fig. 5 Capacity curves

The sequence of failure

For the sequence of failure, the two ends of the inner beam in the SD pushover and ETABS analysis first generated a bending plastic hinge. Next, the bottom of the inner jacketed column generated a bending plastic hinge, and then the bottom of the outer jacketed column generated a bending plastic hinge. This shows that the behavior of the structure is characteristic of a strong-column weak-beam building when retrofitted with jacketed columns. Furthermore, for these two kinds of analysis all the plastic beam hinges occurred on the first floor only.

When the test generated maximum strength, not only the beams, but also the bottoms of the jacketed columns generated plastic hinges (Figure 6). This means that the bottoms of the columns fully developed their strength. For SD pushover (Figure 7) and ETABS analysis (Figure 8), when generating maximum strength, the bottoms of the jacketed columns had already generated plastic hinges. This validates the SD pushover and ETABS analysis.

Conclusions

Compared with the results of testing, the strength and ductility estimated by the slope-deflection (SD) pushover analysis were rather conservative; however, the stiffness was overestimated because the structure without retrofitting was tested to failure and repaired with reinforced concrete jacketing. Therefore, we conclude that SD pushover is a good way to analyze structures.

SD pushover is a simple way to analyze structures by assuming the position of the inflection point is located at the middle of the beam. In fact, it is closer to the weaker joint in the elastic part of the curve. When the two ends of the beam yield, the position of the inflection point is distributed by the magnitude of the positive and negative yielding moments of beam. If there is a simple way to define the actual position of the inflection point, then the result of the SD pushover analysis will be that much closer to that of the actual test results.

References

FEMA 273, "NEHRP Guidelines for the Seismic Rehabilitation of Buildings," Federal Emergency Management Agency, Washington, D.C., 1997.

ATC-40, Seismic evaluation and retrofit of concrete buildings. Report No. SSC 96-01, Applied Technology Council, 1996.

Elwood, K.J. and Moehle, J.P., "Drift Capacity of Reinforced Concrete Columns with Light Transverse Reinforcement," Earthquake Spectra, Vol. 21, No. 1, pp. 71-89, 2005.

American Society of Civil Engineers (ASCE),Seismic Rehabilitation of Existing Buildings,Report No. ASEC/SEI 41-06, Virginia, USA, 2007.


Fig. 6 Failure of test when generating maximum strength

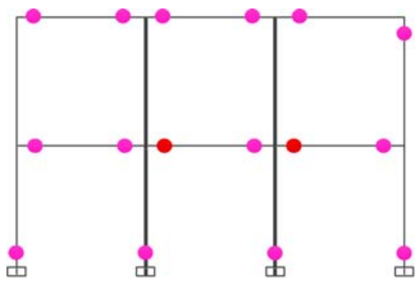
Fig. 7 Failure of SD pushover when generating maximum strength

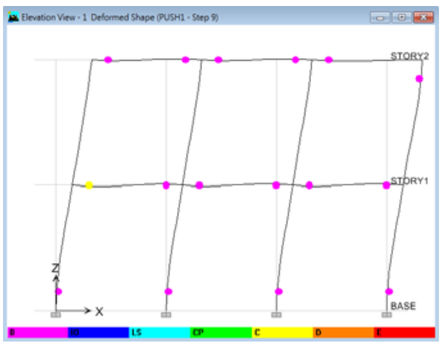

Fig. 8 Failure of ETABS when generating maximum strength

Shear Strength Prediction of Reinforced Concrete Deep Beams with Web Openings

Chien-Chuang Tseng [1] and Shyh-Jiann Hwang [2]

曾建創 [1]、黃世建 [2]

Abstract

This paper presents a new method for predicting the shear strength and failure mechanisms, which include concrete crushing and steel yielding, of reinforced concrete deep beams with web openings. The proposed method is derived from the concept of struts and ties, and also satisfies the equilibrium, compatibility, and constitutive laws of cracked reinforced concrete. The proposed method can accurately predict the following parameters: the ratio of horizontal and vertical reinforcement, the location and size of web openings, concrete strength, the shear span-depth ratio, and flexural steel. The shear strength predictions of the proposed method, the strut-and-tie model of Tan *et al.*, and the empirical formula of Kong and Sharp are compared with the available experimental data. The comparison shows that both the proposed method and the strut-and-tie model of Tan *et al.* can accurately predict all the parameters under comparison. The empirical formula of Kong and Sharp, on the other hand, cannot satisfactorily predict their behavior.

Keywords: reinforced concrete deep beams, web openings, shear strength, strut-and-tie model

Introduction

Reinforced concrete deep beams have to be provided with web openings for service and access. If the openings interrupt the load paths joining the loading and reaction points, the simple load paths will naturally become more complex and the shear capacity of the beam will be reduced.

Research into deep beams with web openings was begun by Kong and Sharp (1973, 1977) [1], who used a series of empirical methods. According to their experimental results, the location and size of the opening affects the shear strength. Kong and Sharp published an empirical equation in 1978 [2] that can predict the shear strength of deep beams with web openings. The parameters of the equation are: the location of the opening, the size of the opening, allocation of the reinforcement, the strength of the reinforcement, and the rupture strength of the concrete. However, based on experimental observation, a possible failure mode is diagonal crushing of the concrete, rather than concrete rupture.

Thus, in recent years, the methods for reasonable deep beam analysis, such as the strut-and-tie model, have been developed. Tan *et al.* (2003) [3] have accurately predicted the shear strengths of reinforced concrete deep beams with web openings. Nevertheless, their calculation process involves an iterative method and is particularly complex. It is also unable to predict the failure mode.

This study follows Hwang's concepts (2000) [4] and we propose an analytical method for shear strength of deep beams with web openings. This proposed model can make precise and reasonable predictions of the shear strength and failure mode. Its parameters include ratios of the horizontal and vertical reinforcement, the location and size of the web openings, concrete strength, the shear span-depth ratio, and flexural steel. This proposed model can predict shear strength directly without employing an iterative method, and can also indicate failure mode and failure location.

---

[1] Assistant Technician, National Center for Research on Earthquake Engineering, cctseng@ncree.narl.org.tw

[2] Deputy Director General, National Center for Research on Earthquake Engineering, sjhwang@ncree.narl.org.tw

Proposed Model Macromodel

Due to the opening in a deep beam, the shear force will separate into two load paths across four nodes, as shown in Fig. 1. Force equilibrium is satisfied at each node.

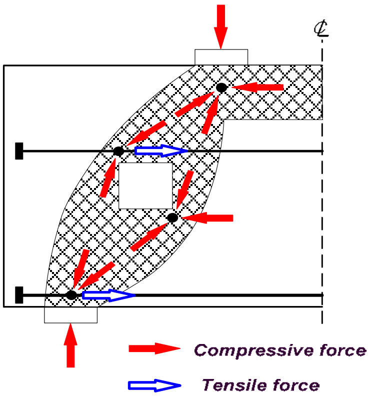

Fig. 1. The strut-and-tie model for deep beams with web openings.

We should define the locations of node 1, node 2, node 3, and node 4 clearly, as shown in Fig. 2. The locations of node 1 and node 2 depend on the depth of the compression zone for each respective section. The depth of the compression zone can be calculated by:

$$k_1 d_1 = \left(\sqrt{\left(n\frac{A_s}{bd_1} \right)^2 + 2n\frac{A_s}{bd_1}} - n\frac{A_s}{bd_1} \right) \cdot d_1 \qquad (1a)$$

$$k_2 d_2 = \left(\sqrt{\left(n\frac{A_s}{bd_2} \right)^2 + 2n\frac{A_s}{bd_2}} - n\frac{A_s}{bd_2} \right) \cdot d_2 \qquad (1b)$$

where $k_1 d_1$ and $k_2 d_2$ (Figs. 2(b) and (c)) are the depths of the compression zone at section 1 and section 2, respectively; d_1 and d_2 are the effective depths of the deep beam at section 1 and section 2, respectively; n is the modular ratio of elasticity ($n = E_s / E_c$); E_s is the elastic modulus of the steel; E_c is the elastic modulus of the concrete; A_s is the area of the flexural steel; and b is the width of the deep beam. Finally, we can define the location of the four nodes as shown Fig. 2.

Load Distribution

Deep beams with web openings are a kind of squat member in which shear force can be transmitted directly via a strut, and the failure mode is similar to that of deep beams, as it is easy to cause concrete crushing as a result of concrete softening. Because this failure behavior is classified as brittle, we can assume that the behavior is linear before failure. Therefore, we can calculate the load distribution of the upper load path and the lower load path based on the respective distributions of shear stiffness. This is the main concept behind the proposed model.

First, the shear stiffness of each element should be defined. We take shear element 14 as an example. Assume that its shear stresses are uniformly distributed throughout its entire volume. Then the shear force equals the shear stress multiplied by the area of the plane (Fig. 3(c)). The vertical displacement is $\Delta_{14} = x_{14}\gamma_{14}$. Therefore, the shear stiffness of shear element 14 is:

$$k_{14} = \frac{V_{14}}{\Delta_{14}} = \frac{b\, y_{14}\, \tau_{14}}{x_{14}\gamma_{14}} = \frac{b\, y_{14} G}{x_{14}} \propto \frac{y_{14}}{x_{14}} = \tan\theta_{14} \qquad (2)$$

where V_{14} is the shear force, y_{14} is the height, x_{14} is the width, τ_{14} is the shear stress, γ_{14} is the shear strain, G is the shear modulus, and θ_{14} is the inclined angle of shear element 14.

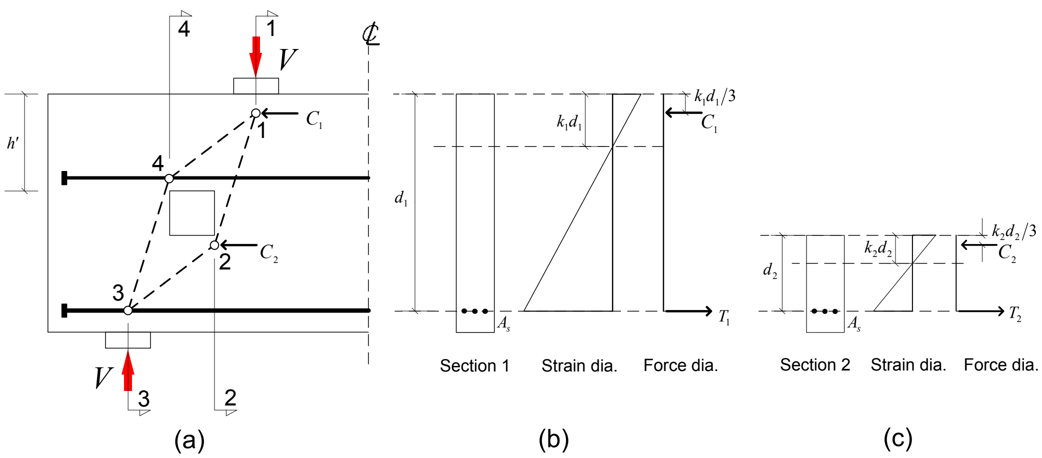

Fig. 2. Geometric selection of (a) each node, (b) section 1, and (c) section 2

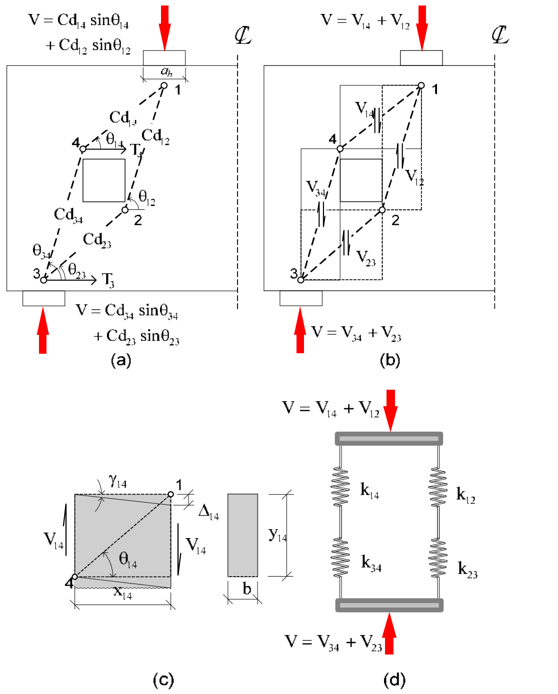

Fig. 3. Load distribution: (a) diagonal compression strength, (b) vertical shear strength, (c) shear element 14 subjected to shear force, and (d) load distribution by shear stiffness.

Referring to the concept of stiffness distribution illustrated in Fig. 3(d), we only need to determine the shear stiffness of each shear element, and then we can obtain the stiffness ratio of the upper load path and lower load path, as shown in Fig. 3:

$$\begin{aligned} k_{143} : k_{123} &= \frac{1}{1/k_{14} + 1/k_{34}} : \frac{1}{1/k_{12} + 1/k_{23}} \\ &= \frac{1}{1/\tan\theta_{14} + 1/\tan\theta_{34}} : \frac{1}{1/\tan\theta_{12} + 1/\tan\theta_{23}} \end{aligned} \qquad (3)$$

Finally, we can obtain the relationship between the shear strengths of the upper load path and the lower load path:

$$\frac{V_{14}}{V_{12}} = \frac{V_{34}}{V_{23}} = \frac{k_{143}}{k_{123}} \qquad (4)$$

Shear Strength Prediction

The proposed method can accurately predict different failure modes, calculate the corresponding shear strength, and then determine the failure mechanism and shear strength. The process is as follows:

1. Crushed Concrete at Node 1: Under the condition of load distribution, the upper and lower load distributions of shear stiffness must be satisfied when concrete at node 1 is being crushed. This is caused by the resultant force of $Cd_{14,1c}$ and $Cd_{12,1c}$.

2. Crushed Concrete at Node 2: When concrete is being crushed at node 2, we can obtain the shear strength of the lower load path and also the shear strength of the upper load path under the condition of load distribution. The upper and lower load distributions of shear stiffness must be satisfied.

3. Steel Yielding at Node 3: When the flexural steel yields at node 3 ($T_3 = T_{3y}$), the equilibrium requirement of the vertical forces must be satisfied at node 3. The upper load and lower load distributions of shear stiffness must also be satisfied.

4. Steel Yielding at Node 4: When steel yields at node 4, we can obtain the shear strength of the upper load path. Then, the shear strength of the lower load path will increase continually until failure occurs. We can calculate the minimum value of the shear strength out of node 1, node 2, and node 3, to find the failure location and the corresponding shear strength of the lower load path.

Finally, we can calculate the minimum value of the shear strength out of node 1, node 2, node 3, and node 4, to find the failure location and corresponding shear strength of a deep beam with web openings.

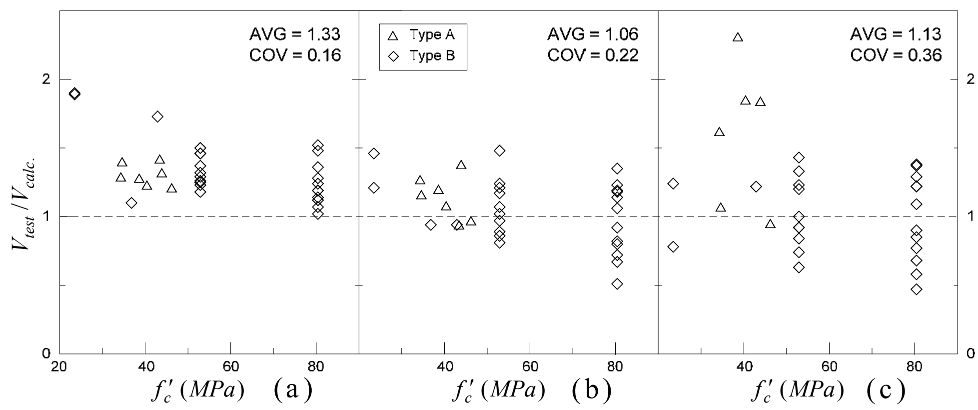

Fig. 4. Effects of concrete strength on shear strength predictions: (a) This study, (b) Tan *et al.*, and (c) Kong *et al.*

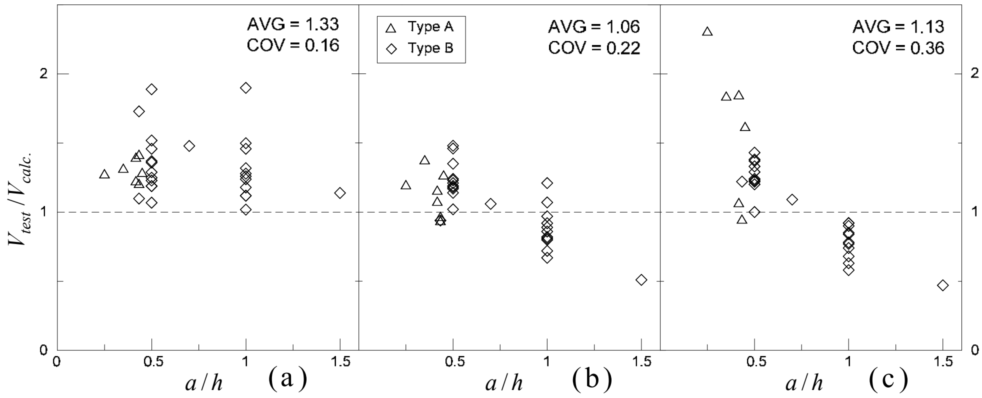

Fig. 5. Effects of shear span-depth ratio on shear strength predictions:
(a) This study, (b) Tan *et al.,* and (c) Kong *et al.*

Results and Conclusions

The shear strength predicted by the proposed method, the strut-and-tie model of Tan *et al.* (2003), and the empirical formula of Kong and Sharp (1977) are compared with the available specimens. These 33 specimens have been tested previously by Kong *et al.* (1978), Kong and Kubik (1979), Guan and Kong (1994), and Yang *et al.* (2006). These 33 specimens were selected according to the following rules:

1. Specimens with incline web reinforcement were excluded.
2. Specimens that were not reinforced with horizontal tension steel or horizontal stirrups above the openings were excluded.
3. Specimen NW5-0.3/4 was excluded owing to uncertainty in the allocation or reinforcement around its opening.

Referring to Fig. 4 and Fig. 5, the proposed method shows more consistency in the measured-to-calculated strength ratio across the parameters of concrete strength (f_c') and shear span-depth ratio (a/h). However, for predictions made by the methods of Tan *et al*. (2003) and Kong *et al*. (1978), the measured-to-calculated strength ratio decreased as the concrete strength (f_c') and shear span-depth ratio (a/h) increased. When the concrete strength was more than 50 MPa or the shear span-depth ratio was more than 0.5, the prediction of the shear strength was not very conservative ($V_{test}/V_{calc.} < 1$).

The proposed method can simulate the effects of varying several parameters on the shear strength of reinforced concrete deep beams with web openings more accurately (the coefficient of variation was 0.16) and conservatively than competing methods, and furthermore, this proposed method can also indicate the failure mode and failure location.

References

Kong, F. K., and Sharp, G. R., 1977, "Structural idealization for deep beams with web openings," Magazine of Concrete Research, Vol. 29, No. 99, pp. 81-91.

Kong, F. K., and Sharp, G. R., Appleton, S. C., Beaumont, C. J., and Kubik, L. A., 1978, "Structural idealization for deep beams with web openings: Further Evidence," Magazine of Concrete Research, Vol. 30, No. 103, pp. 89-95.

Tan, K. H., Tong, K., and Tang, C. Y., 2003, "Consistent strut-and-tie model of deep beams with web openings," Magazine of Concrete Research, Vol. 55, No. 1, pp. 65-75.

Hwang, S. J., Lu, W. Y., and Lee, H. J., 2000, "Shear strength prediction for deep beams," ACI Structural Journal, Vol. 97, No. 3, pp. 367-376.

Hwang, S. J., and Lee, H. J., 2002, "Strength prediction for discontinuity regions failing in diagonal compressions by softened strut-and-tie model," Journal of Structural Engineering, ASCE, Vol. 128, No. 12, pp. 1519-1526.

Kong, F. K., and Kubik, L. A., 1979, "A large scale tests on reinforced concrete deep beams with web openings," University of Cambridge, Project Report CUED/C-Strut./TR. 80.

Yang, K. H., Eun, H. C., and Chung, H. S., 2006, "The influence of web openings on the structural behavior of reinforced high-strength concrete deep beams," Engineering Structures, Vol. 28, pp. 1825-1834.

Stability Analyses of Cross-river Bridges under Flood Water and Debris Loads (III)

Hsiao-Hui Hung [1] , Hao-Han Lee [2] and Chang-Wei Huang[3]

洪曉慧 [1]、李昊翰 [2]、黃仲偉 [3]

Abstract

The purpose of the present study was to investigate the stability of cross-river bridges subject to hydraulic loads and debris accumulation during extreme flood events. According to past reconnaissance reports on typhoons and floods, the collapse of many bridges can be attributed to debris accumulation. The debris not only increases the effective area of the substructure components, but also reduces the flow area resulting in backwater upstream and increased velocities flowing through the bridge opening. The effect of debris accumulation, however, is not included in the current bridge design code in Taiwan. In order to gain a better understanding of bridge behavior in an extreme flood event, the hydraulic loads have to be calculated precisely, especially the hydraulic loads under the condition of debris accumulation. Therefore, a series of small scale hydraulic model tests for a single pier and large scale hydraulic model tests for a continuous bridge under floodwater and debris loads were conducted.

Keywords: debris forces, scour, hydraulic loads

Introduction

The rivers in Taiwan have the common characteristics of a steep riverbed and rapid flow. The heavy rain brought about by typhoons often induces local scouring around bridge foundations, and makes the exposure of foundations a serious problem. In addition, high velocity water flow and drifting wood also induce large lateral forces that act on the bridge piers and the exposed foundations, jeopardizing the safety and stability of the bridges. According to past reconnaissance reports on typhoons and floods, the collapse of many bridges can be attributed to debris accumulation. The debris not only increases the effective area of the substructure components, but also increases floodwater elevations and the potential for scour. For bridge sites where the foundation soil and sediments are susceptible to scour, the resistance of the bridges to lateral loads can be reduced by exposure of the foundations. The combination of debris forces, the increased area of the pier that is subjected to pressure and reduced foundation resistance is highly likely to affect the stability of a bridge. For instance, Typhoon Morakot on August 8th, 2009 destroyed many bridges in Taiwan. By observing these bridges after the typhoon, it was noted that there was a lot of debris, including floating trees and trash, accumulating around some of the bridge piers. Therefore, many experts believe that one of the causes of the large number of bridge failures during this typhoon was the combined effect of scouring and flow discharge loss blocked by debris accumulation. In practical situations, the effect of debris accumulation interacts with scour depth and flood velocity. The quantitative relationship between these three variables has to be investigated through experimental methods. Therefore, the purpose of the current study is to clarify the effect of debris accumulation and flood velocity on debris force and scour depth through a series of small-scale tests on a single pier, and also large scale hydraulic model tests on a continuous bridge under flood water and debris loads.

Experimental Setup

[1] Associate Researcher, National Center for Research on Earthquake Engineering, hhung@narlabs.org.tw.

[2] Graduate Student, Chung Yuan Christian University,

3 Associate Professor, Chung Yuan Christian University

A series of small-scale tests for a single pier and a large-scale hydraulic model test for a continuous bridge under floodwater and debris loads were conducted. In these experiments, rectangular wooden boards of different sizes were used to simulate debris accumulation of different levels. A load cell installed between the board and model pier was used to measure the forces applied by the stream flow through the accumulated debris. Micro-seismographs mounted on the piers were used to record the vibration of the piers or bridges under the flow. In addition, the scouring depth was recorded by video cameras mounted inside the test pier.

The small-scale test was conducted in the test flume at the hydraulic laboratory of NTU (Fig. 1). The total length of the flume was 13 m, including a movable bed of 3 m. The width and the height of the flume was 60 cm and 1 m, respectively. To monitor the variation of the scouring depth during the test, the test model, a hollow single-pier model, was made of transparent acrylic to allow cameras to be installed inside. The total height of the 1/54 scaled single-pier model was 53 cm, including the height of the pier (15 cm), cap beam (7 cm), and caisson (48 cm). The diameters of the pier and caisson were 4.6 cm and 10 cm, respectively. Four different sizes of wooden boards were used to simulate debris accumulation of different levels. The purpose of the single pier test was to investigate the effect of debris accumulation on the behavior of the bridge pier under a simple experimental condition. Therefore, the effect of the slope of the bed and flow direction was neglected.

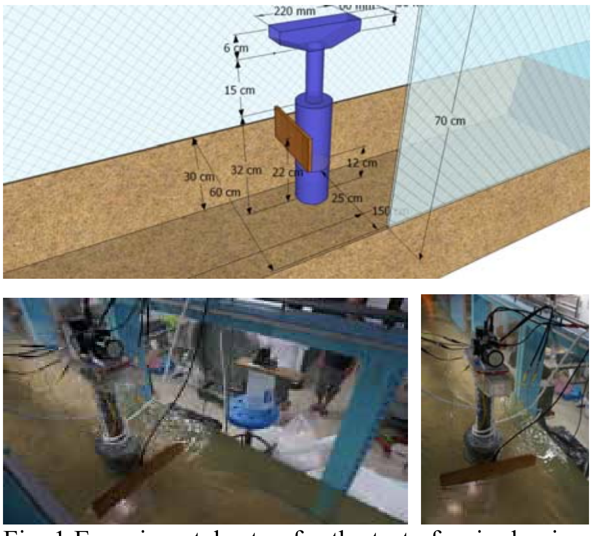

Fig. 1 Experimental setup for the test of a single pier

During the test, the flow velocity was controlled by adjusting the angle of the tail water plate and the motor frequency of the pump. Experiments were conducted under three different flow velocities, 14.36 cm/s, 28.49 cm/s and 40.53 cm/s, and four different sizes of wooden boards, 10×15 cm^2, 10×20 cm^2, 10×25 cm^2 and 10×30 cm^2. Cases without debris accumulation were also conducted. Thus, the total number of small-scale tests conducted was 15. In the initial state, the caisson was embedded in the sand about 12 cm deep, and the center of the wooden board was mounted on the caisson at a distance 22 cm upward from the base of the foundation. The steady flow depth was 15 cm.

The large-scale hydraulic model test for a continuous bridge was conducted at the hydraulic laboratory of the Water Resources Planning Institute located in New Taipei city. The test flume was constructed to simulate the riverbed of the Daja River at the site of the Daja river bridge. The experimental setup is shown in Fig. 2, where the model bridge was a 4-span continuous bridge with five piers. The span length was 1 m, the total height of each of the 1/36 scaled pier models was 77 cm, including the height of the pier (22 cm), cap beam (7 cm), and caisson (48 cm). Two of the test models (Pier 2 and Pier 3), which were made of transparent Acrylic, had cameras installed inside to monitor the variation in scouring depth during the test. The steady flow level was kept constant at 15 cm for the test and the initial embedded depth of the caisson was 21.5 cm. To simulate debris accumulation of different levels, a total of four different sizes of wooden boards, 10×30 cm^2, 10×50 cm^2, 10×70 cm^2 and 10×130 cm^2, were installed on the upstream side of the caissons. The board with a size of 10×130 cm^2 was installed on both the upstream side of pier 2 and pier 3 to simulate the case where the debris covers a whole span. Tests under two different flow velocities were conducted to observe the influence of the flow condition. Thus, a total of 10 tests were performed, including the cases without the obstruction of the wooden boards.

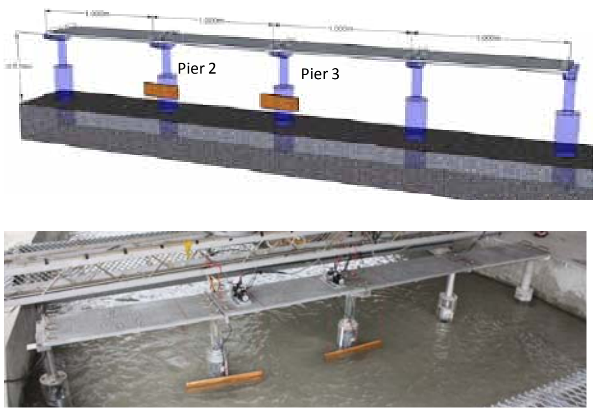

Fig. 2 Experimental setup for the test of multiple piers

Test Results of the Single Pier

Fig. 3 presents the time histories of the applied forces measured from the load cell mounted between the wooden board and the bridge caisson under different flow velocities for the single-pier test. It shows that the applied force increases as the size of the board and flow velocity increase; however, the applied loading declines with time. This is probably due to the fact that scour occurred at the foundation, and the scour depth increased with time. As the scour depth increased, the area of the local discharge section increased too. This change slowed down the local flow velocity and thereby reduced the drag force applied to the wooden boards.

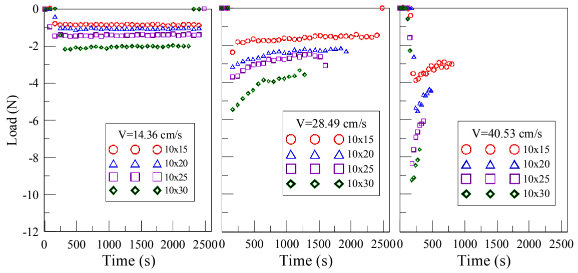

Fig. 3 Time histories of the measured loadings

The corresponding time histories of the observed residual depth under different flow velocities are given in Fig. 4. The residual depth in the vertical axis represents the remaining embedded depth of the caisson in the soil. When the residual depth reached zero, the pier toppled. Table 1 gives the duration before the pier toppled. As can be seen in Fig. 4 and Table 1, the scour depth increased with increasing flow velocity. For instance, under low flow velocity (V= 14.36 cm/s), the scour depth ranged from 1 cm to 4 cm. For the cases under the flow velocity of 28.49 cm/s, the scour depth varied from 7 cm to 12 cm. As the flow velocities increased to 40.53 cm/s, the range of the scour depth increased to over 10 cm. The increase in the size of the wooden board also resulted in the increase in the scour depth. In addition, the scour process becomes faster making the pier topple earlier, as can be observed in Table 1. This observation confirms that the debris accumulation on the pier or foundation can not only increase the drag force applied on the bridge components, it can also make the scouring even more serious. The effect also becomes more significant as the flow velocity increases.

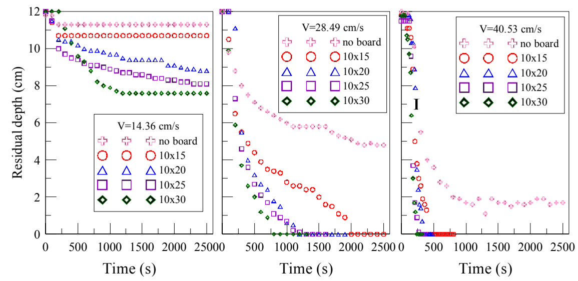

Fig. 4 Time histories of the observed residual depth

The time histories of the predominant frequency along the transverse direction (y-direction), which was obtained by performing the short-time Fast Fourier Transform on the vibration data recorded from the pier top, are given in Fig. 5. By comparing Fig. 5 with Fig. 4, it can be found that the dominant frequency declined rapidly as the residual depth deceased. In addition, the declining speed increased with the increase in wooden board size. This is because as the blocked area increased, the scouring situation became worse and therefore the pier stiffness decreased, as did the predominant frequency. This observation implies that the instant frequency calculated from the vibration signal recorded during the flood can be an alternative index to judge the seriousness of the scouring situation. This is useful because the actual scour depth is not easy to measure in practice.

Table1 Stability condition of the test pier

velocity / board	14.36 cm/s	28.49 cm/s	40.53 cm/s
w/o board	-	-	-
10×15 (cm^2)	-	-	toppled (14m 44s)
10×20 (cm^2)	-	toppled (32m 20s)	toppled (08m 19s)
10×25 (cm^2)	-	toppled (27m 00s)	topple (06m 15s)
10×30 (cm^2)	-	toppled (22m 35s)	toppled (05m 19s)

Ps: the time given in parentheses represents the time when the pier toppled.

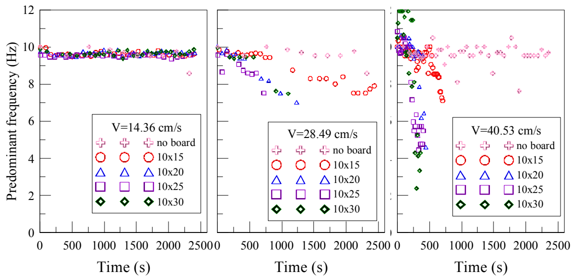

Fig. 5 Time histories of the predominant frequency along y-direction

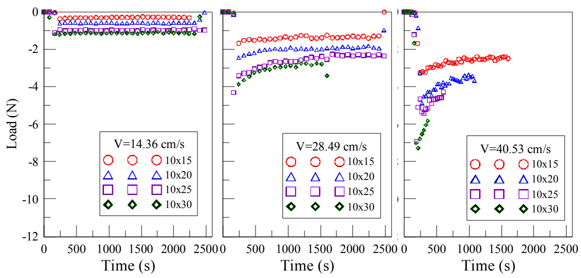

Fig. 6 Time histories of the measured loadings (cases with a penetration rate of 15%)

To investigate the effect of debris accumulation for different penetration rates, similar small-scale experiments using wooden boards with drilled holes to simulate the debris were conducted. Fig. 6 shows the Time histories of the measured forces for the case with a penetration rate of 15%. By comparing Fig. 3 and Fig. 6, one can note that the measured loading for the cases with a penetration of 0% (w/o drilled holes) was lower than for those with a penetration rate of

15%. Since most accumulated debris has some level of penetration (Parola 2000), the results indicate that the measured forces for the cases using the idealized wooden board to simulate debris represents the upper limit value for more practical situations.

Test Results of the Continuous Bridge

The large-scale model tests of the continuous bridge were conducted under two different flow conditions. One had an average flow velocity of 104 cm/s, the other had an average flow velocity of 34 cm/s. For the case of V= 104 cm/s, the approach-flow velocities, which were measured at 0.7 m upstream from the pier centerline, were 113.2 cm/s for pier 2 and 102.4 cm/s for pier 3. For the case of V = 34 cm/s, the approach-flow velocities for pier 2 and pier 3 were 38.9 cm/s and 34 cm/s, respectively.

Figs. 7 to 10 show the time histories of the measured forces and the observed residual depth for pier 2 and 3 under different flow velocities. Due to the hydraulic model having a curved shape, the local velocities at different locations can be very different and the flow distribution can be complicated. The fluctuation of the measured data was significant; however, in an overall sense, the scouring at the foundation got worse as the blockage area increased due to the existence of the wooden board. In addition, the forces applied on the pier increased with the increasing size of the board. At the same time, the measured forces decreased as the scour depth increased, which is similar to what was observed in the small-scale tests. In addition, from the photos taken after the test, one can observe that the extent of the scour hole increases with the increase in the width of the wooden board. Therefore, even though the increase in the scour depth results in a decline of the drag force, the loss of the soil support due to scour would reduce the bearing forces of the soil around the bridge pier and endanger the stability of the bridge. The debris accumulation would not only induce higher drag forces on the pier, but also make the scouring even worse.

Conclusions

In this study, debris accumulation around a bridge pier was simulated by rectangular wooden boards attached to the upstream side of the piers. The effect of the debris accumulation on the behavior of the pier under water flow was investigated by tests conducted at the test flume and a riverbed model. Load cells, micro-seismometers and video cameras were installed to measure the forces and to record the vibration frequency and the scour process. The experimental results confirm that debris accumulation not only induces a larger drag force on the bridge components, it also increases the scouring speed and depth. Therefore, the consequence of debris accumulation on a bridge pier cannot be ignored. The potential influence of debris accumulation has to be taken into account in the design of new bridges and for the safety evaluation of existing bridges.

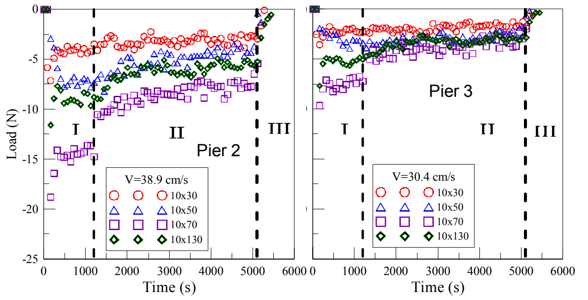

Fig. 7 Time history of the measured forces
(Average flow velocity = 34.06 cm/s)

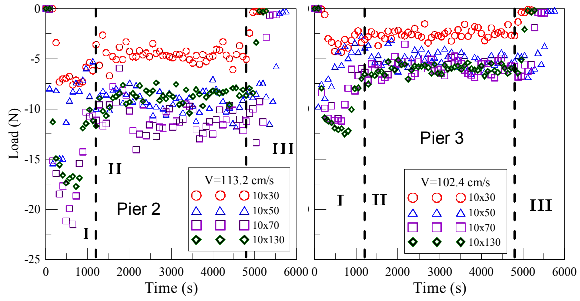

Fig. 8 Time history of the measured forces
(Average flow velocity = 104.35 cm/s)

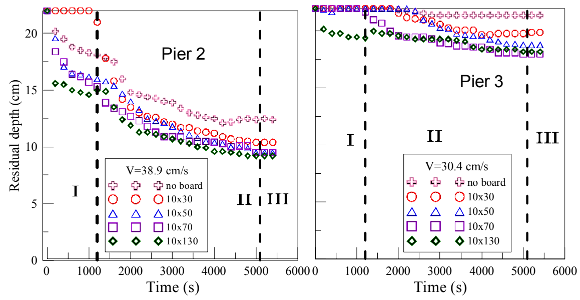

Fig. 9 Time history of the residual depth
(Average flow velocity = 34.06 cm/s)

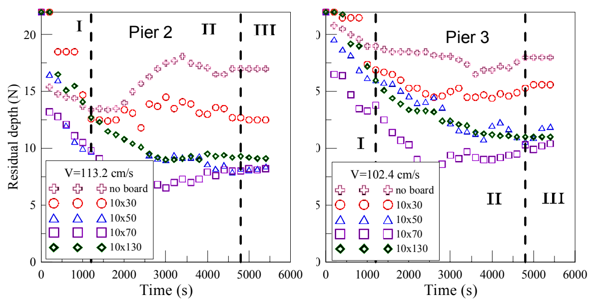

Fig. 10 Time history of the residual depth
(Average flow velocity = 104.35 cm/s)

References

Parola, A.C., 2000, Debris Forces on Highway Bridges, NCHRP 445, National Cooperative Highway Research Program.

Inspecting and Monitoring the Safety of Bridge on the Wu-Yang C907 Viaduct of National Highway 1

Lu-Sheng Lee [1], Zheng-Kuan Lee [2], Jingo Chen[2]

Abstract

Because of wrong construction procedure, some of the newly bridge, Wu-Yang C907 Viaduct of National Highway 1, crack on the surface of the girders. Therefore the bridge owner, Taiwan Area National Expressway Engineering Bureau, entrusts NCREE with a long tern bridge-monitoring project. This paper will introduce the project as well as the sensors to be applied on the girder. If the deflection of the girder exceeds the allowable limit, the bridge owner will be informed with the new measurement.

Keywords: Optic fiber sensor, bridge health monitoring

Introduction

This study was conducted to solve national bridge-building project issues and encourage future relevant studies. Sub-project C907 of the Wu-Yang Viaduct Widening Project involved the construction of the Luzhu section and the airport interchange in Taoyuan of National Highway 1, specifically, along the girders P19N-P20N, and P21S-P22S and P31S-P32S, which are located on the main route directing toward northern and southern Taiwan, respectively. However, during construction, because the concrete was not tamped after the cement was poured, honeycomb deficiencies occurred. Although concrete reinforcement was performed, because this highway is crucial in Taiwan, the safety of the national highway bridge must be attentively focused on. Therefore, our center developed fiber optic sensors that enabled long-term monitoring and synchronized vertical displacement and physical crack detecting and recording to ascertain bridge conditions and protect driver safety.

Bridge Health Monitoring

Because of Taiwan's unique geographical environment and because drivers have varying driving habits, immediate monitoring of highway changes and data analysis and interpretation are required to obtain immediate feedback regarding bridge conditions when sudden changes, such as earthquakes, overloaded vehicles, speeding, and heavy traffic occur. This information is transmitted promptly and accurately to the bridge-management authorities to ensure that the bridges are fully functional. The remote, real-time monitoring system can be used to evaluate and diagnose bridge conditions based on bridge usage, thereby providing a favorable monitoring and warning system.

Because bridge conditions change over time, bridge designs and construction quality inevitably deteriorate, despite receiving perfection and high safety factor scores. In addition, because of damage caused by sudden activities, such as heavy traffic, vehicle overloads, and earthquakes, bridge safety monitoring and inspections must be implemented to protect driver safety.

Fig. 1 Visual inspection of bridge

Visual Inspecting

We marked on an optimal spot under girders P19N and P20N, P21S and P22S, and P31S and P32S. Next,

[1] Technologist, National Center for Research on Earthquake Engineering

[2] Associate Researcher, National Center for Research on Earthquake Engineering

we fixed the target outside the fence and under the girders to distinctly indicate the target positions, which were subsequently recorded. We inspected the reinforced areas (where honeycomb deficiency occurred) and used the first images of the bridge as the baseline values (Fig. 1).

We will perform an inspection under favorable weather conditions. In addition to capturing images of the girders, we visually examined and recorded the physical conditions of the entire bridge. We then compared these images with old images to determine whether new cracks had developed. Finally, we archived the images to determine the physical condition of girders in various road sections.

Bridge Loading Test

The girders examined in this study underwent manual load testing on February 7, 2013 and March 13, 2013, and manual leveling measurements to obtain deflection responses (Fig. 2). The deflection responses can be used as parameters for establishing safety indicators. We used fiber optic leveling to conduct regular measurements and inform owners of girder deflection changes.

Fig. 2 Bridge Loading Test and Manual Leveling on March 13, 2013

Long-Term Deflection Measurement

In the project, for the long term deflection measurement, we will place a fiber optic leveling sensor in the box girders of the bridge sections. Next, we used a laser-leveling scanner to delineate a reference point before stabilizing the fiber optic leveling sensor. We then fused optical fiber lead wires to the tubes and the P19N–P20N, P21S–P22S, and P31S–P32S sensors and connected the tubes using fiber optic connectors to the instrument box under the bridge pillars.

We collected the data at the site and determined the displacement by conducting data analysis. If the results show that changes in girder deflection had reached a critical value, this value can be assumed to be half of the maximum deflection value that was obtained through the load testing (Table 1) as the abnormal value.

Table 1 The maximum deflection values obtained through load testing

Girders P19N~P20N	Girders P21~P22S	Girders P31~ P32S
16 dump trucks Each dump truck = 20 tf	28 dump trucks Each dump truck = 20 tf	12 dump trucks Each dump truck = 20 tf
2.6 cm	4.4 cm	1.0 cm

Our achievements in the study and development of the optical fiber bridge sensors and software can be applied to instantaneously monitor the structural safety of the bridge. When changes occur, warning signals are activated, thereby providing bridge-management authorities with accurate and reliable information, which can be used as a reference for determining the bridge maintenance cycle and evaluating bridge durability.

Introduction to Optic fiber Bragg Sensor

Optic fiber applies total internal reflection principle of light to transmit signal or energy. The commercial single mode optic fiber is with the loss rate of 0.2 dB per kilometer. On the other hand, the sensing fiber bragg grating (FBG) is an artificial segment which can reflect specific wavelength of a broadband spectrum, as shown in Fig.3.

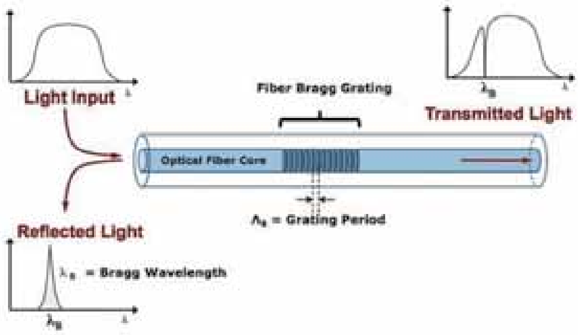

Fig. 3 The filter and the constitution of a FBG

After transmitting a wide broadband spectrum signal into the left hand side of the fiber, the FBG will reflect a specific narrow spectrum (with central wavelength λ_b) according to the grating period of the FBG. If the FBG is subject to a stress, then the central wavelength will change to be $\lambda_b + \Delta\lambda_b$, where $\Delta\lambda_b$ positive for tensile stress and negative of compressive stress. To include both the stress effect and the thermal effect, the mathematical relationship in the first order could be written as followed:

$$\frac{\Delta\lambda_B}{\lambda_B} = C_S\Delta\varepsilon + C_T\Delta T \qquad (1)$$

Where $\Delta\varepsilon$ is the strain induced by the stress, and ΔT is the difference in temperature. C_S and C_T is the correspondent constant. Strictly speaking, to distinguish the contribution by the stress from the contribution by the thermal, it takes two FBGs in need. In practice, in order to reduce the quantity of FBGs, it is possible to apply only one FBG for estimating the stress contribution if a specified uncertainty is allowed (for example: 10 %) through the design of a sensor.

In sensor design, FBGs and glue are applied as strain sensors as well as sensor in most literature; however in this study, the FBG is the force detector as well as the sensor through the joint: the hot shrink tubes. As shown in Fig.4, a basic element is setup to easily establish the force-and-strain relationship. With the basic element, one can make up displacement sensors, level sensor, and etc.

In fig.4, since the basic element could not subjected to compressive force, the pre-stress tensile force must be applied in advance to shit the origin of the coordinate.

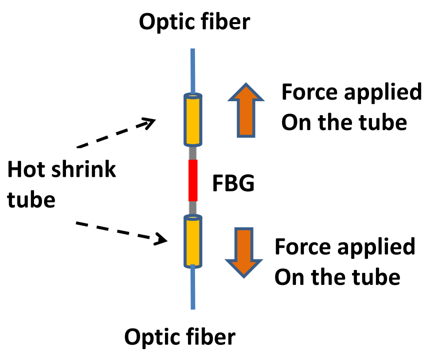

Fig.4 Force detector through the tubes

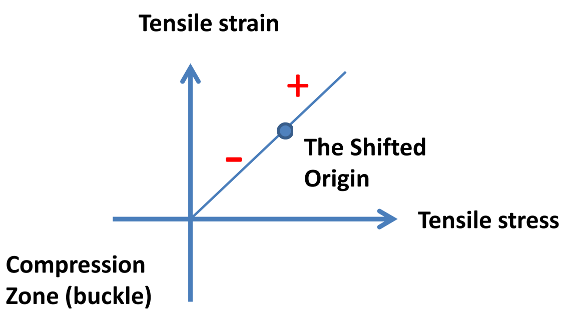

Fig.5 The basic element subjected to the pre-stress tensile force and the origin of the coordinate is shifted

Fiber Optic Leveling Measurement

Fiber optics leveling measurement is an application involving the principles of leveling pipes (Fig. 6). When a bottle rises up or settles down (caused by the vertical girder displacement), the vertical level changes, causing water to flow from one bottle to the others, creating the optical fiber strain. This informs technicians that the deflection of the bridge girder is changing. Once the change in girder deflection falls below the safety value, an immediate warning is activated to notify the bridge-management authorities.

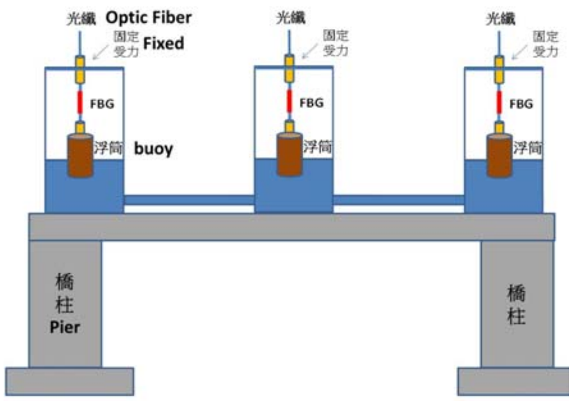

Fig. 6 Fiber optic leveling sensors

Sensor Layout on Bridge

Figure 6 presents the sensor layout on the bridge, the pillars and girders of P21S–P22S and P31S–P32.

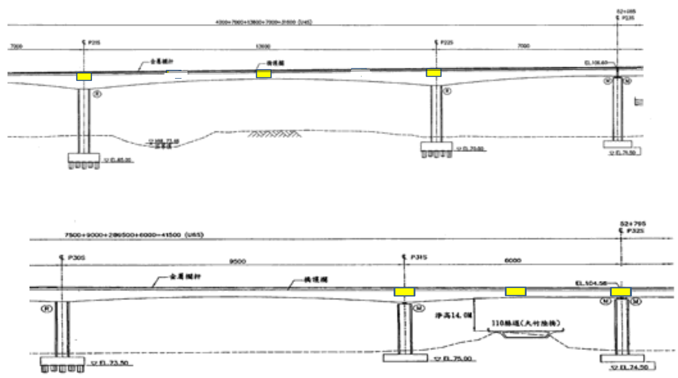

Fig. 6 Schematic diagram of the sensor layout

Conclusion and Future Prospects

1. This study implemented the bridge-inspection and monitoring technology on the bridge C907 on the Wu-Yang Viaduct of National Highway 1 and gained insight regarding experiences in system maintenance. The system not only provides safety warnings, but also protects driver safety; thus, our research results contributed to industries and societies.
2. In addition to verifying immediate measurement data, the fiber optic sensor system could transmit

quick and accurate warnings to bridge-management authorities, thereby allowing them to instantly activate emergency responses.

3. We combined the fiber optic sensor with monitoring software technology, both of which were developed by our research team, and anticipated that this innovative technology will provide industries with an easy, user-friendly, and economical measurement technique.
4. By using the on-site assessment records and fiber optic monitoring technology, we developed a bridge safety evaluation system and bridge safety warning standards, which facilitate the prevention of property loss and casualties caused by bridge accidents, thereby emphasizing the concept that an ounce of prevention is worth a pound of cure.
5. By using lengthy multi-span bridges and combining fiber grating sensors and communication technology with bridge construction projects, we verified the durability of the disaster-prevention monitoring system.

An Experimental Study on the Equivalent Load Effect of Bridge Scour

Chun-Chung Chen[1], Kuo-Chun Chang[2], Chi-Ying Lin[3], Chih-Hao Chen[4]

陳俊仲 [1]、張國鎮 [2]、林其穎 [3]、陳志豪 [4]

Abstract

In recent times, scour has become the major cause of failure for cross-water bridges owing to frequently occurring hydraulic hazards such as typhoon-induced flood. Although the scour phenomenon has been studied for a long time by hydraulic researchers, its effect on a bridge structure has still not been clarified sufficiently for use in engineering design. Although current bridge design does consider the scour effect for bridge safety, it is merely used to verify stability under scour and is not actually a design factor that influences bridge structure design. This is because the result of scour is not an additional external force but a reduction in resistance. This paper discusses an innovative idea that transforms the reduction in the soil bearing capacity of the bridge pier foundation into a load effect on the structure. In order to verify the proposed method for evaluating the reduction in soil bearing capacity that comes with decreasing embedded depth of the pile, a series of lateral bearing capacity tests were conducted with a model pier under controlled conditions to establish the relationship between the scour depth and the soil bearing capacity of the pier model. This study verifies the proposed methodology used for converting the scour depth, the soil bearing capacity reduction, into the equivalent scour load. When the expected scour depth is known, the calculated corresponding equivalent scour load can be used to design a bridge structure with suitable lateral loading capacity. In order to more generally apply the equivalent scour load to design specifications, the scale effect of the bridge pier should be further investigated.

Keywords: scour, equivalent load effect, pile foundation, lateral capacity

Introduction

The escalating scale of natural disasters associated with global climate change and the growing world population increasingly threatens civil infrastructure. In particular, flooding is a major disaster that can result in damage to or failure of cross-water bridge structures. Floating or submerged debris induced by flooding may deepen the scour depth of bridge foundations, and result in a reduction of an affected bridge's structural capacity. In the United States, as discussed by Reddy (2006), there are currently more than 482,000 bridges that span waterways, and the total number of bridge failures caused by earthquakes, wind, corrosion, structural issues, accidents, and construction problems combined, are less than the failures caused by scouring. The total scour consists of three primary components: the long-term degradation of the riverbed, contraction scour at the bridge, and local scour at the piers or abutment (FHWA, 2012). As the overburden depth grows shallower, the pile capacity increases owing to the decrease in the effective stress, resulting in reduction of both the point and frictional resistance. Then, in the most common cases, the bridge fails as a result of bearing capacity failure, column tilt due to an overturning moment, or pile buckling due to insufficient support from the surrounding sediment.

Current bridge design codes consider separately

[1] Associate Researcher, National center for Research on Earthquake Engineering, jingochen@narlabs.org.tw
[2] Director, National Center for Research on Earthquake Engineering, kcchang@ncree.org.tw
[3] Research Assistant, Department of Civil Engineering, National Taiwan University, R98521219@ntu.edu.tw
[4] Graduate Student, Department of Civil Engineering, National Taiwan University, R01521210@ntu.edu.tw

the scour effect and the other regular load effects, since the scour effect only causes a reduction of soil capacity but does not increase the load of the bridge structure. Liang and Lee (2013) proposed an approach for converting the resistance reduction into an equivalent load effect and offered models of different failure modes, including vertical settlement and instability failure of the pile foundation; however, some inconsistency exists across the two methods. The equivalent scour load model of the settlement failure is based on a direct approach but the equivalent scour load model of the instability failure is based on an indirect approach. Thus, complementary approaches using both failure modes were established.

This study mainly focuses on verifying the method of the instability failure mode. Furthermore, a revised equivalent scour load model of the instability failure mode based on the direct approach was developed. To test the validity of each approach, and to understand how the scour depth affects bridge pier stability, the lateral bearing capacity of the pile foundation was investigated. By controlling the relative density of the soil, altering the pile embedded depth, and assuming rigid body motion of the pile foundation, an empirical formula for the reduction of lateral bearing capacity under scour can be drawn though regression. The test results were compared with LPILE analysis, with the revised equivalent scour load employed. Although a complicated scale effect still exists, the equivalent scour load and the trend of resistance reduction under scour can be used as a reference to indicate the safety and stability of a bridge pier.

Equivalent Scour Load

Liang and Lee (2008) proposed that multi-hazard must be integrated into the Load and Resistance Factor Design (LRFD). Design procedures for extreme and time-dependent load effects, such as earthquakes, scour, and truck loads, are established separately. Liang and Lee (2013) offered several original ideas to solve the problems related to these types. The major concern in this study is scour, and Liang and Lee have provided an applicable approach that considers the scour effect as an equivalent load effect. The effect of the resistance reduction is converted into an equivalent load effect, and the scour phenomenon can then be combined with other load effects and considered in the design procedure. This study reviews the method proposed by Liang and Lee (2013), utilizing an equivalent scour load, and how it relates to instability failure.

The concept proposed by Liang and Lee can be schematically shown as in Fig. 1. The reaction force is calculated by assuming the modulus of subgrade reaction is proportional to the depth x (*i.e.*, $k(x) = n_h x$, where n_h is a constant of the modulus of horizontal subgrade reaction related to the pile diameter) and is replaced by an equivalent stiffness on the surface of the sediment. The equivalent scour load can be expressed as:

$$S = \frac{n_h \Delta}{12}\left[\frac{(H_0 + H_a)^4}{H + H_a} - \frac{H_0^4}{H}\right], \qquad (1)$$

where H_0 is the pile embedded depth without scour; H is the total length of the pile; and H_a is the additional length needed to balance the reduction of soil capacity, where H_a can be approximated by:

$$H_a = \frac{4H}{4H - H_0} d_S . \qquad (2)$$

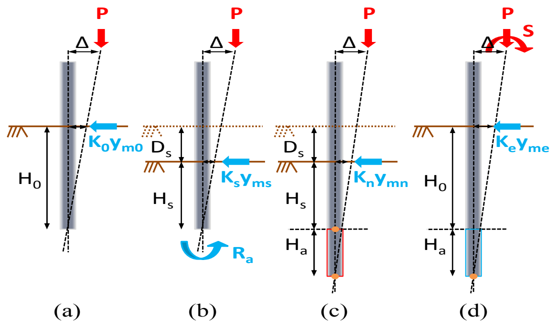

Fig. 1. Illustration of the equilibrium states of pile instability failure (a) before scour, (b) with scour, (c) with scour and additional pile length, and (d) the equivalent structure without scour.

Complementary Equivalent Scour Load Model due to Instability

Liang and Lee have established a method for investigating the scour effect via the equivalent scour load that incorporates two failure modes, including vertical displacement and instability. However, these methods for determining the equivalent scour load are based on two different approaches. In the vertical displacement failure mode, the resistance difference due to the scour effect is directly transformed into the equivalent scour load. On the other hand, in the instability mode, instead of applying the resistance difference, a circuitous method assuming pile elongation equivalent to the additional resistance is required to recompense the scour effect is used. The equivalent scour load for the instability case is equal to the resistance difference of the original structure and the equivalent structure (*i.e.*, the structure with an elongated pile and without the scour effect). Due to this inconsistency, corresponding approaches must be found and discussed. In Fig. 1(b), applying the direct method to the instability failure mode, by making the resistant moment of the sediment lost during the scouring process equal to the equivalent scour load, the equivalent scour load can be calculated as:

$$\begin{aligned} S = R_a &= y_{m0} k_0 H_0 - y_{mS} k_S H_S \\ &= \frac{n_h \Delta}{12H}\left[H_0^4 - (H_0 - d_S)^4\right] \end{aligned} \qquad (3)$$

Based on the calculation results, the trends of these equivalent scour loads can be seen. For the first approach, with additional length, the equivalent scour loads show an upward concave trend. On the other hand, for the second approach, with direct transformation of the resistance reduction, the equivalent scour loads show a downward concave trend. Further evidence is required to verify which approach is superior. The single pile bearing capacity test was conducted to confirm the supposed method for instability failure modes.

Lateral Capacity Test

The specimen used in the experimental test can be seen in Fig. 2(a), and the experimental sand box used as the soil container is shown in Fig. 2(b). The soil sediment used in this experiment was quartz sand; its friction angle was 29° and its relative density was controlled to 50%.

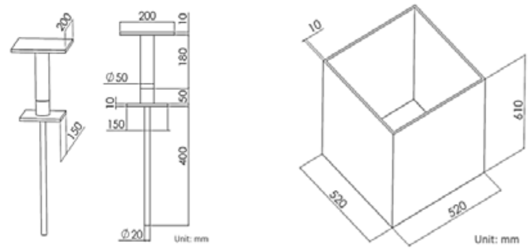

(a) (b)

Fig. 2. Schematic view of (a) the pile specimen and (b) the sand box.

The resistance reductions corresponding to different pile lateral displacements are shown in Fig. 3. By defining the failure criterion of lateral displacement for the pile as 10 mm, the relationship between resistance reduction and the normalized scour depth can be regarded as the relationship between equivalent scour load and normalized scour depth. In Fig. 4, both the indirect and direct methods can be seen to overestimate the resistance reduction; however, the equivalent scour load constructed by the direct method seems closer to the experiment result. For this reason, the revised equivalent load model developed in the next section was derived based on the direct method.

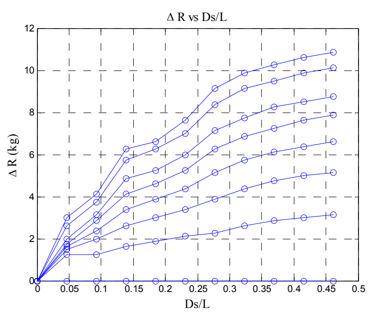

Fig. 3. Resistance reduction vs. normalized scour depth for different pile displacements.

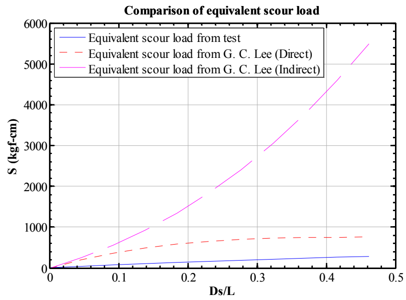

Fig. 4. Comparison of lateral capacity test results for equivalent scour loads derived from the direct and indirect methods.

Revised Equivalent Scour Load Model and LPILE Analysis

In Fig. 4, it can be seen that the equivalent scour load model based on the direct method still overestimates the resistance reduction of the scour effect. One probable reason is that the resistance of the surrounding sediment is overestimated. In addition, in the static pushover analysis, which is based on the LPILE analysis, the rotation point of the pile is located at one-fourth of the embedded depth from the bottom for each case of scour depth. Thus, for the revised model, it is supposed that the rotation point is located at one-fourth of the embedded depth from the bottom, as in Fig. 5.

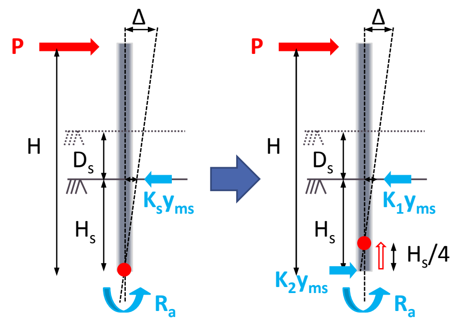

Fig. 5. Illustration of the equilibrium state of pile instability failure for the revised equivalent scour load model.

Following the same assumption, except for the location of the rotation point, the equivalent stiffnesses of the sediment for the revised model can be derived as:

$$k_1 = \frac{2}{45} n_h H_0^2 \tag{4}$$

and:

$$k_2 = \frac{1}{10} n_h H_0^2 \, . \tag{5}$$

Applying the direct approach, the resistance comes from the upper and lower parts of the equivalent soil spring, and the equivalent scour load equals the difference between the resistances before and with scour. The revised equivalent scour load can be expressed as:

$$S = \frac{n_h \Delta}{8}\left(\frac{H_0^4}{4H - H_0} - \frac{H_S^4}{4H - H_S}\right). \tag{6}$$

A comparison of the revised equivalent scour load, the original equivalent scour load based on the direct method, and the test result is shown in Fig. 6. Furthermore, comparisons of the test result and LPILE analysis results are shown in Fig. 7. In the LPILE analysis, each case is based on the revised equivalent scour load being applied to the structure without scour to then compare it with the test result for the same scour depth.

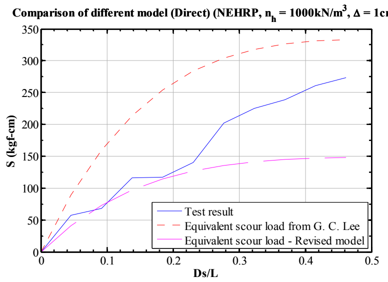

Fig. 6. Comparison of the equivalent scour load of the direct method and the revised model for the lateral capacity test.

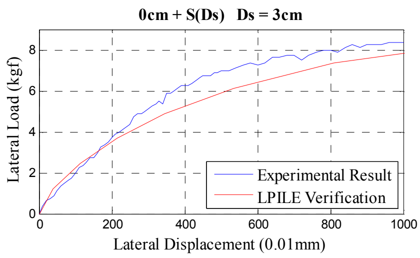

(a)

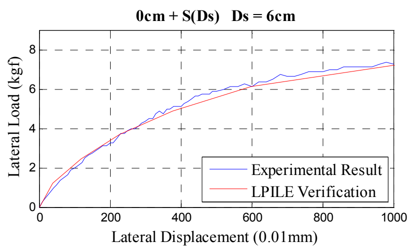

(b)

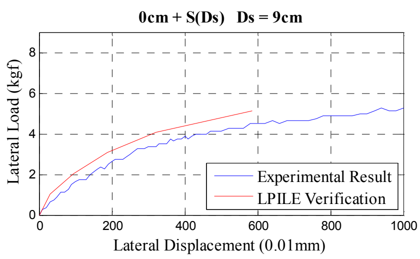

(c)

Fig. 7. Comparisons of test results and LPILE analysis results by applying the equivalent scour load to a structure without scour.

Discussion and Summary

In Fig. 6, the revised equivalent model can be seen to be closer to the test result; however, with the increase in scour depth, the revised model underestimates the effect of resistance reduction. Thus, the displacement in Fig. 7 is underestimated in the case of larger scour depth. The relationship between resistance reduction and normalized scour depth is approximately linear, and it is neither concave-up nor concave-down. Further investigation is required to explain this phenomenon and to help revise the model. Furthermore, the test result may contain the scale effect and it should be considered in the future revised equivalent scour load model.

The equivalent scour load model converts the scour effect, which is a result of increasing scour depth, to an equivalent scour load, which is a load effect, which can then be further combined with the LRFD procedure once the loading probability model is built. Due to the complexity of the scour phenomenon, however, the failure modes of the bridge and pile foundation are much more complicated. As such, compound failure modes also need to be studied.

References

FHWA. (2012), Evaluating Sour at Bridges. 5th edition, Federal Highway Administration (FHWA), Hydraulic Engineering Circular No.18 (HEC-18). U.S. Department of Transportation, Washington, DC.

Lee, G. C., Tong, M., and Yen, W. P. (2008), Design of highway bridges against extreme hazard events: issues, principles and approaches, Report No. MCEER-08-SP06, the State University of New York at Buffalo, NY.

Liang, Z., Lee, C. G. (2013), Bridge pier failure probabilities under combined hazard effects of scour, truck and earthquake. Part I: occurrence probabilities, Earthquake Engineering and Engineering Vibration, Volume 12, Issue 2, pp 229-240

Liang, Z., Lee, C. G. (2013), Bridge pier failure probabilities under combined hazard effects of scour, truck and earthquake. Part II: failure probabilities, Earthquake Engineering and Engineering Vibration, Volume 12, Issue 2, pp 241-250

Reddy, D. R. (2006), Bridge Scour Detection. National Conference on Advances in Bridge Engineering (ABE), IIT Roorkee, Roorkee, March 24-25

Experimental Study on Seismic Behavior of a Typical Sprinkler Piping System in Hospitals

Juin-Fu Chai[1], Kuo-Chun Chang[2], Fan-Ru Lin[3], Zen-Yu Lin[4] and Jhen-Gang Huang[5]

柴駿甫 [1]、張國鎮 [2]、林凡茹 [3]、林震宇 [4]、黃振綱 [5]

Abstract

It is evident from the past earthquake experiences of hospitals that damaged sprinkler piping systems heavily impact the functionality of the hospital and take a long time to rehabilitate the operation. An example of this was observed in a responsibility hospital during the Taiwan Jiashian earthquake in 2010, when a broken sprinkler piping system caused serious flooding that reduced medical functionality.

To ensure that the immediate needs of emergency medical services provided by hospitals after strong earthquakes are not interrupted, this paper introduces a research program on assessment and improvement strategies for typical configurations of sprinkler piping systems in hospitals. A horizontal piping subsystem with an original configuration of the aforementioned seismically damaged sprinkler piping system is duplicated for shaking table tests. Furthermore, piping subsystems with a variety of seismic-resistant devices, such as braces, flexible pipes, and mechanical couplings, are tested. The test results show that the main cause of damage is the poor shear capacity of the screwed fitting of the small-bore tee branch. The optimum improvement strategy to achieve higher nonstructural performance for the piping subsystem is to strengthen the main pipe with braces and to decrease shear demands on the tee branch by the use of flexible pipes.

Keywords: hospital sprinkler piping systems; shaking table testing; horizontal piping systems.

Introduction

Based on the lessons learned from the 1999 Chi-Chi earthquake, the Taiwan government promoted a scheme for the seismic evaluation and retrofit of buildings, including a comprehensive review of the seismic capacity of public buildings and critical facilities, such as main hospitals. The purpose of this scheme is to improve the seismic performance of buildings in order to maintain the safety of general buildings and retain the functionality of critical facilities during and after earthquakes. It is recognized that the immediate operation and safety of such critical facilities after earthquakes relies heavily on the performance of associated nonstructural components. Hence, the capability of water supply, power supply and fire suppression systems in the critical facilities should be especially taken into account. However, taking hospitals as an example, even though the building structures of the main hospitals have all been evaluated and parts of them have been strengthened seismically by 2014, the mechanical /electrical systems have yet to be evaluated or retrofitted owing to a lack of mature evaluation methods and approved codes of practice for seismic upgrading.

Among the numerous problems due to seismic damage of nonstructural components, water leaks or flooding resulting from broken sprinkler piping systems is an important issue for hospitals because of

[1] Research Fellow, National Center for Research on Earthquake Engineering
[2] Professor, Department of Civil Engineering, National Taiwan University
[3] Assistant Researcher, National Center for Research on Earthquake Engineering
[4] Research Assistant, National Center for Research on Earthquake Engineering
[5] Graduate Student, Department of Civil Engineering, National Taiwan University

the effect of water damage on the room fixtures below and the relationship between this damage and medical functionality. Such damage occurred at the Olive View Medical Center, the Holy Cross Medical Center, and Northridge Hospital in the San Fernando Valley during the 1994 Northridge earthquake [1]. From a literature review of earthquake damage, common failures of sprinkler piping systems occur at the screwed fittings, anchorages, and sprinkler heads. Another example was observed in a designated hospital during the 2010 Jiashian earthquake in Taiwan (Fig. 1), where a reduction of medical functionality was caused by serious flooding due to a broken small-bore pipe in the sprinkler system.

NFPA 13 [2] provides a common code of practice for seismic installation of fire sprinkler systems in general buildings. Instead of stress analysis, a rule-based approach is proposed by the NFPA standard. However, its effectiveness in seismic upgrading needs to be verified through more extensive studies. In view of the immediate needs of emergency medical services provided by hospitals after strong earthquakes, an ongoing research program on assessment and improvement strategies for typical configurations of sprinkler piping systems in hospitals was organized by the National Center for Research on Earthquake Engineering (NCREE). Based on the typical damage states observed from previous earthquakes, this paper focuses on the study of the seismic behavior of a typical subsystem of a horizontal sprinkler piping through shaking table tests.

Fig. 1 Flooding at a hospital during the 2010 Jiashian earthquake.

In Situ Investigation

In order to realize the configuration of a typical sprinkler piping system of a hospital, an *in situ* investigation was conducted at a hospital building where the sprinkler piping system was damaged during the 2010 Jiashian earthquake. As shown in Fig. 2, the broken segment of the piping system is located in a patient room on the top floor of the 6-story building. Restricted by the confined space above the suspended ceiling system, four pipes along the corridor, with diameters of 6″, 2-1/2″, 6″, and 4″ (from left to right), are carried together by trapeze frame supports, where the left 6″-diameter pipe is the main pipe of the sprinkler piping system (Fig. 3). From the results of ambient vibration tests and impact hammer tests, the fundamental frequency of the building structure was identified to be approximately 2.0 Hz in both horizontal directions, while that of the piping system was 5.37 Hz in the transverse direction of the main pipe.

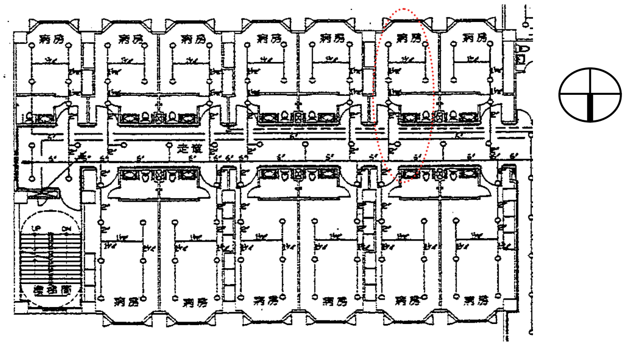

Fig. 2 Plan drawing of the sprinkler system including the part damaged in the 2010 Jiashian earthquake.

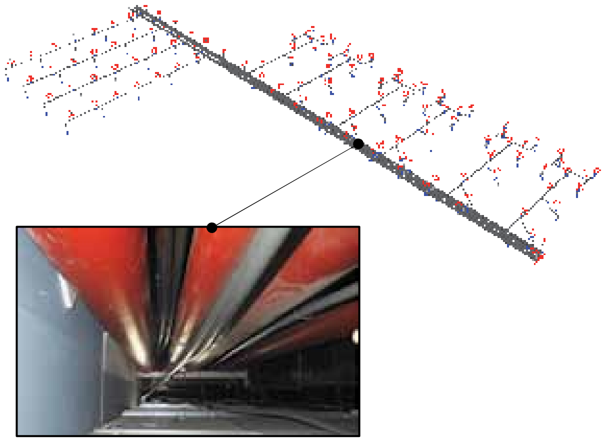

Fig. 3 The numerical model of the horizontal piping system.

The experimental setup was limited by the size of the shaking table at the NCREE. Therefore, only a typical sprinkler piping unit for one patient room, together with the adjacent part of main pipe, was duplicated in the laboratory (Fig. 4). To determine reasonable boundary conditions for the tested segment of the main pipe in the shaking table tests, preliminary FEM models of both the complete horizontal piping system and the test specimen were established and verified with the system identification results according to the *in situ* investigation of the configuration and restraints of the horizontal piping system on the 6th floor.

Fig. 4 The numerical model of the test specimen.

Test Setup

The objective of this test is to identify the failure modes of a typical sprinkler piping system in a hospital and to propose appropriate improvement strategies for greater seismic performance (Fig. 5 and Fig. 6(a)). The same damage as occurred in the 2010 Jiashian earthquake was planned to be reproduced for the test with the original configuration of screwed fittings. In addition, the modified configurations with the proposed seismic restraint devices, including braces, flexible hoses, and couplings, were arranged at the proper positions to verify their respective improvement efficiencies as well (Table 1 and Fig. 6).

Table 1 Testing configurations

OC	Original configuration
CT	Coupling near the tee branch
DB	Double braces
FH	Flexible hose
CB	Coupling between the tee branch and partition
DBF	Double braces with flexible hose

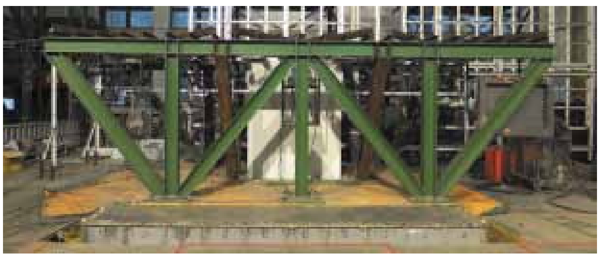

Fig. 5 Shaking table test for the sub-system.

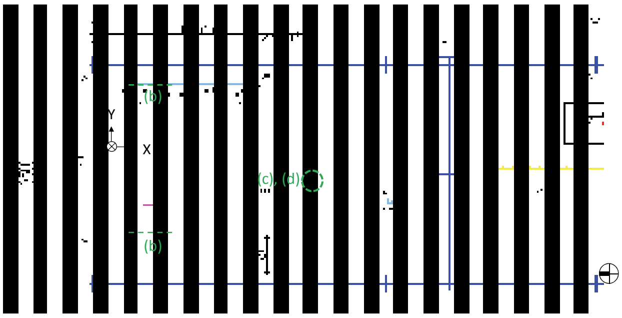

(a) Basic test configuration

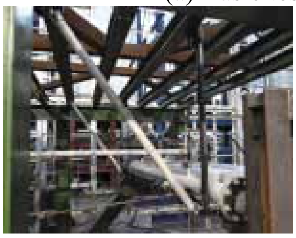

(b) Braces

(c) Flexible hose

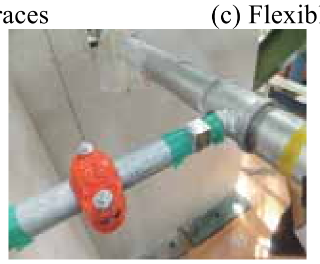

(d) Coupling

Fig. 6 Test configuration and seismic restraint devices.

The tested piping sub-system was hung from a rigid steel frame, which was designed to be stiff enough to transfer the motion of the shaking table without any significant effects. Figures 7 and 8 depict the two types of horizontal motions measured at the steel frame. The purpose of the Type A input motion was to verify whether the seismic restraint devices satisfy the requirements of the building codes in Taiwan [3], while the purpose of the Type B input motion was to simulate the floor response of the hospital during the 2010 Jiashian earthquake.

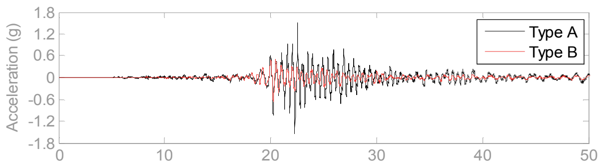

(a) X-axis peak values: 0.67g (A) 1.56g (B)

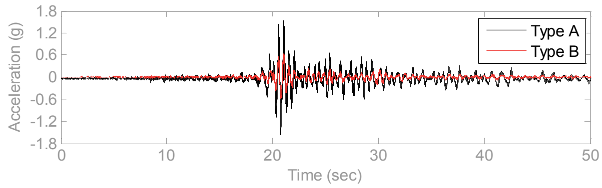

(b) Y-axis peak values: 0.63g (A) 1.56g (B)

Fig. 7 Acceleration time series of input motions.

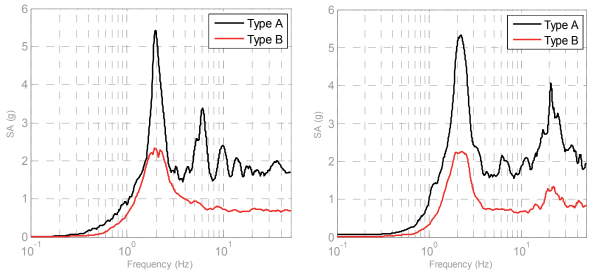

(a) X-axis (b) Y-axis

Fig. 8 Response spectra of input motions.

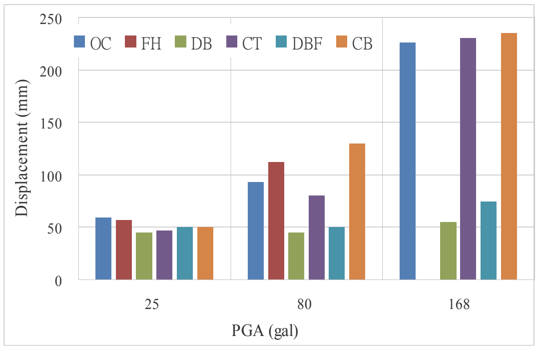

Fig. 9 Diameter of the reaming on the ceiling board in the Type B tests.

Test Results

Table 2 depicts the identified natural frequencies of each test configuration from the results of the resonant frequency survey tests. The first mode of the original configuration of the sub-system was translation along the X-axis. It can be seen that the braces increased the natural frequencies significantly, while the couplings and flexible hoses decreased the natural frequencies and changed the stress distribution of local segments. In order to observe leakage of the specimen and the associated damage to adjacent architectural components due to seismic interaction, three performance indexes were examined during and after each test: (1) the damage of the piping segments, (2) the enlarged diameters of the reaming on the ceiling boards and partition walls due to impacts caused by sprinkler heads and piping segments, and (3) the leakage of contained water (Fig. 9 and Fig. 10). The test results of the original configuration showed that the screwed fitting of the small-bore piping at the tee branch was the most vulnerable part of the tested piping system and was damaged at the 100% intensity level of the Type B test (Fig. 11). The optimum improvement strategy is to not only strengthen the main pipe with braces but also use flexible hoses near the tee branch to decrease both the shear and displacement demands on the screwed fittings. Owing to the brittle failure caused by the screwed fitting and couplings, the mechanical behavior of both devices should be further studied.

Table 2 Natural frequencies of the piping system (Hz)

Test	1st mode	2nd mode	3rd mode
OC	1.95 (X)	5.91 (Y)	10.3 (Y)
CT	1.95 (X)	5.27 (Y)	8.15 (Y)
CB	1.66 (X)	4.30 (Y)	6.74 (Y)
FH	2.15 (X)	2.78 (X)	11.5 (Y)
DB	5.52 (Y)	7.13 (X)	10.21 (Y)
DBF	4.79 (Y)	5.32 (X)	8.50 (X)

Fig. 10 Damaged small-bore piping at the tee branch.

Conclusions

In view of the immediate needs of emergency medical services provided by hospitals after strong earthquakes, an ongoing research program on assessment and improvement strategies for typical configurations of sprinkler piping systems in hospitals was implemented by the NCREE. From the results of shaking table tests, the main cause of damage was found to be the poor shear capacity of the screwed fitting of the small-bore tee branch. The optimum improvement strategy for achieving a higher nonstructural performance of the piping subsystem is to strengthen the main pipe with braces and to decrease shear demands on the tee branch with the use of a flexible hose. Owing to the brittle failure caused by the screwed fitting and couplings, the mechanical behaviors of both devices will be investigated in future studies.

References

1. G&E Engineering Systems Inc., "Fragility of Non-Structural Components: A.1 fire sprinkler systems", FEMA P-58/BD-3.9.12, 2009.
2. "Standard for the Installation of Sprinkler Systems", NFPA 13, 2010.
3. Ministry of the Interior, "Seismic Design Specifications and Commentary of Buildings", 2011.

Study on Smart Carbon Fiber Reinforced Concrete for Structural Monitoring-I

Fang-Yao Yeh[1], Kuo-Chun Chang[2], Wen-Cheng Liao[3] and Wan-Yu Lien[4]

葉芳耀 [1]、張國鎮 [2]、廖文正 [3] 連婉佑 [4]

Abstract

Structural monitoring systems are important in civil engineering. Traditional structural monitoring systems have some disadvantages such as a shorter sensor life span than the structures. This research uses CFRC (Carbon Fiber Reinforced Concrete) as a structural monitoring sensor to extend the life of the sensor to match that of the structure. There are some known advantages of carbon fiber reinforced concrete, such as high tensile strength and high ductility which increases the seismic capacity and security of structures. However, CFRC has functionality similar to piezoresistive materials which can be used as a self-sensing material for strain measurement and damage detection. This property is based on the reversible effect of the strain on the volume of electrical resistivity and the irreversible effect of material damage on its resistivity. The strain sensing behavior is such that the resistivity decreases reversibly upon compression due to the slight inward push of crack-bridging fibers and the consequent decrease in the contact electrical resistivity of the fiber-cement interface. Similarly, the resistivity increases reversibly upon tension due to the slight outward pull of crack-bridging fibers and the consequent decrease in the contact resistivity. To consider the economic benefits, the fiber content is only 0.2 vol. % which is less than half of the amount used in other references (0.48 vol. %). The experimental results show that the conductivity of current materials is significantly improved by CFRC and that it can be used for strain measurement and damage detection with fiber content of 0.2 vol. %. Moreover, the experimental results of CFRC coated beams can be kept in a database for applications in the future.

Keywords: CFRC, Self-sensing, Strain measurement, Damage detection

Introduction

This article shows that once carbon fiber is added to concrete to become carbon fiber reinforced concrete (CFRC) it has functionality similar to piezoresistive materials that can be used as self-sensing materials for strain measurement and damage detection. This functionality is based on pairing the reversible effect of strain on the volume's electrical resistivity with the irreversible effect of damage to the resistivity. The strain sensing behavior is such that the resistivity decreases reversibly upon compression due to the slight inward push of crack-bridging fibers and the consequent decrease in the contact electrical resistivity of the fiber-cement interface. Similarly, the resistivity increases reversibly upon tension due to the slight outward pull of crack-bridging fibers and the consequent decrease in the contact resistivity [Wen and Chung, 2007; Han and Ou, 2007]. The self-sensing ability of CFRC cement-based composites has been well demonstrated under compression and under flexure. Using the electrical resistance change of CFRC and the appearance of structural cracks, we are able to integrate sensors which possess the material smartness quotient of self-sensing, stability, and repetitiveness.

[1] Research Fellow, National Center for Research on Earthquake Engineering, fyyeh@ncree.narl.org.tw
[2] Director, National Center for Research on Earthquake Engineering, kcchang@ncree.narl.org.tw
Professor, Department of Civil Engineering, National Taiwan University, ciekuo@ntu.edu.tw
[3] Assistant Professor, Department of Civil Engineering, National Taiwan University, wcliao@ntu.edu.tw
[4] Master, Department of Civil Engineering, National Taiwan University, quietskycrystal@gmail.com

Experimental Investigations

Preparation of Materials

The design concrete strength for CFRC was set as 500 kgf/cm^2. The cement was a blended Portland cement and the specimens were made from a mix with the following ratios: water-cement ratio (w/c) = 0.4; sand-cement ratio (s/c) = 0.75; silica fume 15 % by weight of cement; methylcellulose 0.4 % by weight of cement and carbon fiber 0.2 % by of total volume. The fiber diameter was 7 μm. The nominal fiber length was 15 mm. A standard mixing procedure was used. A rotary mixer with flat beater was used for mixing. After pouring the mix into oiled molds, an external electric vibrator was used to facilitate compaction and decrease the amount of air bubbles.

Specimens and Test Setup

From the aforementioned concrete mixture, 8 different styles of CFRC beams and CFRC for coating on RC portal frame type bridge piers produced for testing at 28 days of age. The concrete beams had dimensions of 550×150×150 mm and were prepared for three-point bending test. The portal frame type bridge piers had cross section dimensions of 60×60 cm and net high and net span of 400 cm and were prepared for pushover test. The test setups are shown in Fig. 1and Fig. 2.

Three-point Bending Test of CFRC Beams

Cyclical loading was applied on the CFRC beam specimen shown in Fig. 1(b). The dynamic strain of the CFRC beam was measured by the strain gauge, the central deformation was measured by LVDT, and the electrical resistance was measured by Keithley 2000 digital multimeter under a gauge length equal to 120mm (Fig. 1(a)).

Pushover Test of Portal Frame Type Bridge Piers

An axial loading of 1,500 kN was applied to the top of each pier, and lateral loading was applied to the top of the pier by displacement control using drift ratios (ratios of lateral displacement to story height) with representatives of the order of plus or minus 0.25, 0.5, 0.75, 1.0, 1.5, 2, 3, 4, 5, 6, 7, 8 %. The end of each experiment was taken to be when fractures in the longitudinal reinforcement of the pier occurred. Each cycle of target displacement was set to three laps before 3% of drift ratio and 2 laps from 4% of drift ratio until the end of the experiment (Fig. 2(b)).

Select bottom of P1 column as the region for strain measurement by using CFRC, the area was set to 600×600 mm. A CFRC coating of thickness of 12 mm was coated on the surface of this region. Three distributed electrodes were provided and three strain gages CH-1, CH-2 and CH-3 were also set at the same region, in order to compare the measurement results, respectively. The dynamic strain of the portal frame type bridge pier was measured by the strain gauge, and the electrical resistance was measured by Keithley 2000 digital multimeter under a gauge length equal to 120 mm, the same electrode configuration as in three-point bending test (Fig. 2(a)).

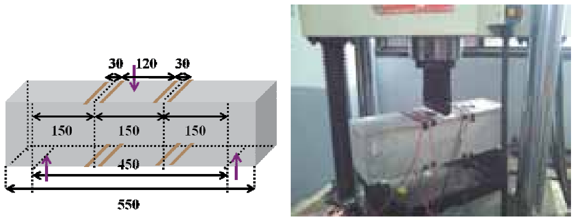

(a) (b)

Fig. 1 Bending test of concrete beams, (a) electrode configuration, (b) test setup

(a) (b)

Fig. 2 Pushover test of RC portal frame type bridge piers, (a) electrode configuration, (b) test setup

Results and Discussion

Three-point Bending Test of CFRC Beams

The test results of 28 day old three-point bending specimens are shown in Table 1. The different types of specimen shown in Table 1 include a pure CFRC beam without steel reinforcement (P), a pure CFRC beam with steel reinforcement (PS), a concrete beam coated with a CFRC layer without steel reinforcement (Co) and a concrete beam coated with a CFRC layer with steel reinforcement (CoS).

Fig. 3(a) and Fig. 3(b) show the loading protocol, fractional change in electrical resistance, and strain measured by strain gauge at top and bottom of CoS3 specimen. Fig. 3(c) and Fig. 3(d) show the relationships between fractional change in electrical resistance of CFRC and strain measured by strain gauge at top and bottom of CoS3 specimen. These data existed linear relation-ship between fractional change in electrical resistance of CFRC and strain measured by strain gauge before proportional limit. If exceed the proportional limit, the fractional change in electrical resistance increases (tension side) or decreases (compression side) due to the increase of electrical resistance in CFRC specimen caused by the microstructure changes, micro crack density increases and damage occurrences.

From Table 1, the following results were observed: (1) from a comparison of the two pure CFRC beams, the strain in both the tension and compression side of the P specimens are found to be smaller than the PS specimens, but the electrical resistance (Ro) and gauge factor (GF) are found to be larger in the P specimens; (2) from a comparison of the two CFRC coated beams, the gauge factor of the CoS specimens are found to be greater than the Co specimens; (3) from a comparison between the pure CFRC beams and the CFRC coated beams, the gauge factor of the CFRC coated beams (Co and CoS) are found to be larger in the pure CFRC beams (P and PS). Generally, the CoS specimens were found to have the greater gauge factor.

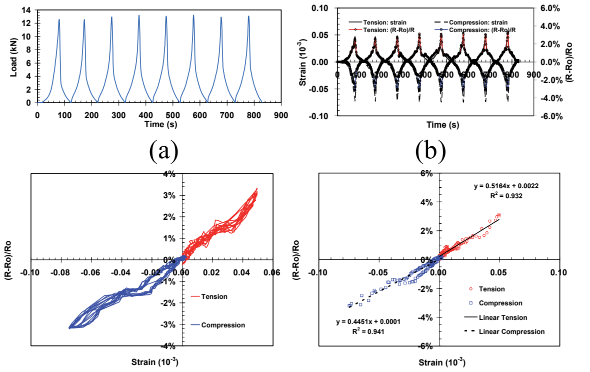

(a) (b) (c) (d)

Fig. 3 Test results of CoS3 specimen, (a) variation of load with time, (b) variation of fractional change in electrical resistance and strain measured by strain gauge with time, (c) comparison between fractional change in electrical resistance and strain measured by strain gauge, (d) comparison between fractional change in electrical resistance and strain measured by strain gauge in linear region

Pushover Test of Portal Frame Type Bridge Piers

The beginning of strain measurement was start at lateral displacement of bridge pier approach 5 mm (t = 0). The test results of strain measured by three strain gauges and fractional change of electrical resistance with time are shown in Fig. 4(a). The variation of strain measured by strain gauge with time is very similar to the variation of fractional change in electrical resistance with time. The response of fractional change of electrical resistance of CFRC is earlier than the strain measured by strain gauge and represented the ability to predict the occurrence of deformation.

The bending test results in Table 1 show that average gauge factors of CoS specimens are 693 on compression side and 619 on tension side. Base on this two gauge factors, the fractional change of electrical resistance are converted to resistance strain and the variation of strain measured by fractional change in electrical resistance and by strain gauge with time are shown in Fig. 4(b).

Fig. 4(b) shows the compressive strain measured by the strain gauge CH-3 is similar to strain measured by fractional change in electrical resistance under displacement of 20 mm. At bottom of the column, under compressive loading and at 5, 10 and 20 mm of displacement of the loop, strain can be measured by both CFRC and strain gauges, but the fractional change of electrical resistance of CFRC is more sensitive than strain changes measured by strain gauge. The maximum compressive strain of approximately 5.9×10^{-4} measured at displacement of 20 mm among three loops of measurement. At bottom of the column, under tensile loading, strain gauge measurement of tensile strain appears to be inaccurate, probably due to the strain gauge affixed position is not the position of the maximum tensile strain occurs, and therefore the loss of sensitivity to measure tensile strain. The fractional change of electrical resistance of CFRC has higher strain sensitivity. In the displacement of 20 mm in all three loops can amount to a maximum tensile strain, estimate the maximum tensile strain of approximately 1.7×10^{-4}.

When the lateral displacement of bridge pier continues to increase to 30 mm, there are some cracks occurred between CFRC layer and the surface of bridge pier, as shown in Fig. 5(a). At this moment, the electrical resistance change will be stop, and CFRC loss of function of strain measurement. When displacement of bridge pier continues to increase, resulting in the stripping and collapse between CFRC coating layer and the surface of bridge pier, as shown in Fig. 5(b). A subsequent CFRC strain measurement applications, coating and bonding between CFRC and tested structures issues CFRC for structural health monitoring, and will be the focus of research must be overcome.

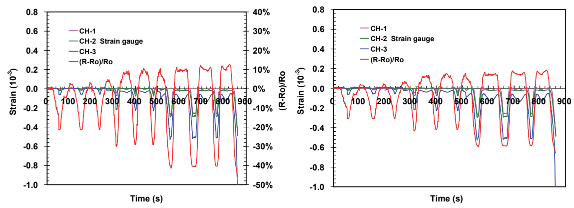

(a) (b)

Fig. 4 Results of pushover test, (a) variation of fractional change in electrical resistance and strain measured by strain gauge with time, (b) variation of strain measured by fractional change in electrical resistance and by strain gauge with time

(a) (b)

Fig. 5 Failure mode of CFRC coating on surface of bridge pier, (a) delamination between CFRC coating and bridge pier, (b) stripping and collapse of CFRC coating from surface of bridge pier

Summary and Discussion

To consider the economic benefits, the fiber content of the CFRC is only 0.2 vol. % which is less than half the amount used in other references (0.48 vol. %). The experimental results of three-point bending tests of CFRC beams and pushover tests of portal frame type bridge piers show that the conductivity of materials significantly improved and that CFRC can be used for strain measurement and damage detection at a fiber content of 0.2 vol.%.

From the tension tests, we observed that due to the similarity between the fractional change in electrical resistance and tensile strain under uniaxial tension testing, the material can be used as a self-sensing material for strain measurement within the proportional limit. The slope of the fractional change against tensile strain curve is a good indicator for damage detection under tensile loading.

From the compression tests, we also observed that due to the similarity between the fractional change in electrical resistance and compressive strain under uniaxial compression testing, the material can be used as a self-sensing material for strain measurement within the proportional limit. The slope of the fractional change against compressive strain curve is a good indicator for damage detection under compressive loading.

From the three-point bending tests, the gauge factor of the concrete beams coated with a CFRC layer with steel reinforcement was found to be greater than that of a concrete beam coated with a CFRC layer but without steel reinforcement and pure CFRC beams with or without steel reinforcement. Moreover, the experimental results of the coated beams can be kept in the database for applications in the future.

From the pushover tests, at bottom of the column, under compressive loading, strain can be measured by both CFRC and strain gauges, but the fractional change of electrical resistance of CFRC is more sensitive than strain changes measured by strain gauge. At bottom of the column, under tensile loading, strain gauge measurement of tensile strain appears to be inaccurate, probably due to the strain gauge affixed position is not the position of the maximum tensile strain occurs, and therefore the loss of sensitivity to measure tensile strain. The fractional change of electrical resistance of CFRC has higher strain sensitivity.

When the lateral displacement of bridge pier continues to increase to 30 mm, there are some cracks occurred between CFRC layer and the surface of bridge pier. At this moment, the electrical resistance change will be stop, and CFRC loss of function of strain measurement. When displacement of bridge pier continues to increase, resulting in the stripping and collapse between CFRC coating layer and the surface of bridge pier. A subsequent CFRC strain measurement applications, coating and bonding between CFRC and tested structures issues CFRC for structural health monitoring, and will be the focus of research must be overcome.

Self-sensing of the tensile strain, compressive strain, and damage detection was found to be effective in CFRC under cyclic loading. The self-sensing ability of CFRC, as shown in the sensing of strain and damage detection, is demonstrated in this paper.

References

Sihai Wen and D. D. L. Chung “Piezoresistivity-based strain sensing in carbon fiber-reinforced cement”, *ACI Materials Journal,* Vol. 104, No. 2, pp 171-179, 2007.

Baoguo Han and Jinping Ou “Embedded piezoresistive cement-based stress/strain sensor”, *Sensors and Actuator*, A138, pp 294-298, 2007.

Table 1 Results of the three-point bending tests

Bending		Specimen	Strain (10^{-3})		Ro (Ω)		GF		R^2		Force
			c	t	c	t	c	t	c	T	kN
CFRC	w/o Rebar	P1	-0.08	0.040	36.8	53.3	175	220	0.97	0.81	7
	w Rebar	PS1	-0.17	0.075	14.7	18.9	52	87	0.96	0.90	10
		PS2	-0.15	0.075	15.3	15.9	78	89	0.92	0.89	10
Coated	w/o Rebar	Co1	-0.11	0.075	54.1	51.1	252	160	0.97	0.91	8.5
		Co2	-0.15	0.060	31.9	35.7	49	78	0.88	0.95	8.5
	w Rebar	CoS1	-0.15	0.060	81.9	49.7	1031	497	0.95	0.94	13
		CoS2	-0.06	0.045	40.6	84.3	603	844	0.98	0.93	13
		CoS3	-0.08	0.050	31.8	47.8	445	516	0.94	0.93	13

Feasibility Study on Performance-Based Sloped Rolling-Type Isolation Devices

Wang-Chuen Lin [1], Yin-Han Yang [2], Chia-Yi Shiau [3], Jia-Xiang Hong [4], Shiang-Jung Wang [5] and Jenn-Shin Hwang [6]

林旺春 [1]、楊印涵 [2]、蕭佳益 [3]、洪家翔 [4]、汪向榮 [5]、黃震興 [6]

Abstract

It has been demonstrated from previous studies that sloped rolling-type isolation devices possess steady transmitted acceleration responses in horizontal directions and excellent self-centering capabilities. In addition, built-in damping mechanisms can effectively suppress excessive displacement responses and stop rolling motions during and after excitations. This study aims to derive the generalized equations of motion for sloped rolling-type isolation devices in which the rollers move between two arbitrary sloping surfaces. Moreover, by taking a performance-based design concept into consideration, an isolation device designed with variable-damping and multi-slope mechanisms is proposed and its advantages are numerically verified by using the derived generalized analytical model.

Keywords: seismic isolation, sloped rolling-type isolation device, twin-flag hysteretic model, performance-based design, numerical verification

Introduction

A sloped multi-roller isolation device was theoretically and experimentally investigated by Wang et al. (2013). It was indicated that the simplified twin-flag hysteretic model, which can be easily applied in SAP2000, could not exactly reflect the influence of vertical excitations on horizontal transmitted acceleration responses. Therefore, to consider such an influence, this study derives generalized equations of motion for a sloped rolling-type isolation device in which the rollers move between two V-shaped surfaces with arbitrary sloping angles θ_1 and θ_2 . Moreover, by involving a performance-based design concept, an isolation device designed with variable-damping and multi-slope mechanisms is then proposed. Its advantages in displacement response reduction and self-centering improvement are further discussed based on the derived generalized analytical model.

Generalized equations of motion for sloped rolling-type isolation devices

In this study, the two design conditions (Wang et al., 2013) for the sloped rolling-type isolation device are incorporated into the theoretical derivation. It is assumed that the dynamic behavior of rollers is ideal pure rolling motion. Based on the dynamic force equilibrium and dynamic moment equilibrium, several free body diagrams can be separated to describe the tangential force, normal force, and sliding friction damping force. A simplified model in which the roller is sandwiched between the superior and inferior bearing plates is presented in Figure 1. Two opposite rolling motion directions are identified by $\mathrm{sgn}(x_1)=\mathrm{sgn}(x_2)=1$ and $\mathrm{sgn}(x_1)=\mathrm{sgn}(x_2)=-1$ corresponding to the rightward movement ($\mathrm{sgn}(\dot{x}_1)=\mathrm{sgn}(\dot{x}_2)=1$) and leftward movement ($\mathrm{sgn}(\dot{x}_1)=\mathrm{sgn}(\dot{x}_2)=-1$) of the superior bearing plate (or the roller) relative to the inferior bearing plate.

---

[1] Assistant Researcher, National Center for Research on Earthquake Engineering, wclin@narlabs.org.tw
[2] Research Assistant, National Center for Research on Earthquake Engineering, yinhanyang@narlabs.org.tw
[3] Assistant Researcher, National Center for Research on Earthquake Engineering, cyshiau@narlabs.org.tw
[4] Graduate Student, National Taiwan Univ. of Sci. and Tech., m10005303@mail.ntust.edu.tw
[5] Associate Researcher, National Center for Research on Earthquake Engineering, sjwang@narlabs.org.tw
[6] Division Director, National center for Research on Earthquake Engineering, jshwang@narlabs.org.tw

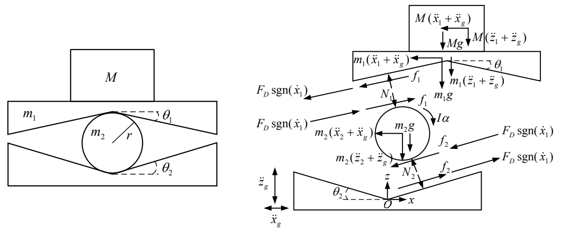

Figure 1. Simplified models and free body diagrams

The free body diagrams for one of the four situations are shown in Figure 1, in which $\ddot{x}_g\,(\ddot{z}_g)$ represents the horizontal (vertical) acceleration excitations; M, m_1 and m_2 are the seismic reactive masses of the protected object, the superior bearing plate and the roller, respectively; θ_1 and θ_2 are the sloping angles of the superior and inferior bearing plates, respectively; r is the radius of the roller; I is the moment of inertia of the roller; α is the angular acceleration of the roller; g is the acceleration of gravity; $x_1\,(z_1)$, $\dot{x}_1\,(\dot{z}_1)$, and $\ddot{x}_1\,(\ddot{z}_1)$ are the horizontal (vertical) displacement, velocity, and acceleration responses of the protected object and superior bearing plate relative to the origin O, respectively; $x_2\,(z_2)$, $\dot{x}_2\,(\dot{z}_2)$ and $\ddot{x}_2\,(\ddot{z}_2)$ are the horizontal (vertical) displacement, velocity, and acceleration responses of the roller relative to the origin *O*, respectively; the positive directions of x and z are correspondingly defined to be rightward and upward; $f_1\,(f_2)$ and $N_1\,(N_2)$ represent the rolling force and the normal force acting between the superior bearing plate and the roller (between the roller and the inferior bearing plate), respectively; and F_D is the build-in damping force.

By considering the free body diagrams of the superior bearing plate and the protected object, two equilibrium equations are obtained:

$$\begin{aligned}\sum F_x &= (M+m_1)(\ddot{x}_1+\ddot{x}_g)\\ &= -f_1\cos\theta_1 - \operatorname{sgn}(x_1)N_1\sin\theta_1\\ &\quad -\operatorname{sgn}(\dot{x}_1)F_D\cos\theta\end{aligned} \tag{1}$$

$$\begin{aligned}\sum F_z &= (M+m_1)(\ddot{z}_1+\ddot{z}_g) =\\ &= -f_1\sin\theta_1 + \operatorname{sgn}(x_1)N_1\cos\theta_1\\ &\quad -\operatorname{sgn}(\dot{x}_1)F_D\sin\theta - (M+m_1)g\end{aligned} \tag{2}$$

Moreover, by considering the free body diagram of the roller, three equilibrium equations are obtained:

$$\begin{aligned}\sum F_x &= m_2(\ddot{x}_1+\ddot{x}_g)\\ &= f_1\cos\theta_1 - f_2\cos\theta_2 + \operatorname{sgn}(x_1)N_1\sin\theta_1\\ &\quad -\operatorname{sgn}(x_1)N_2\sin\theta_2 + \operatorname{sgn}(\dot{x}_1)F_D\cos\theta_1\\ &\quad -\operatorname{sgn}(\dot{x}_1)F_D\cos\theta_2\end{aligned} \tag{3}$$

$$\begin{aligned}\sum F_z &= m_2(\ddot{z}_2+\ddot{z}_g)\\ &= \operatorname{sgn}(x_1)f_1\sin\theta_1 - \operatorname{sgn}(x_1)f_2\sin\theta_2\\ &\quad +\operatorname{sgn}(\dot{x}_1)F_D\sin\theta_1 - \operatorname{sgn}(\dot{x}_1)F_D\sin\theta_2\\ &\quad -N_1\cos\theta_1 + N_2\cos\theta_2 - m_2 g\end{aligned} \tag{4}$$

$$\sum M = I\alpha = f_1 r + f_2 r \tag{5}$$

Four compatibility conditions can be obtained from the relative motion between the superior bearing plate and the roller:

$$\ddot{x}_2 = r\alpha\cos\theta_2 \tag{6}$$

$$\ddot{z}_2 = r\alpha\sin\theta_2 \tag{7}$$

$$\ddot{x}_1 = \ddot{x}_2 + r\alpha\cos\theta_1 = r\alpha\cos\theta_2 + r\alpha\cos\theta_1 \tag{8}$$

$$\ddot{z}_1 = \ddot{z}_2 + r\alpha\sin\theta_1 = r\alpha\sin\theta_2 + r\alpha\sin\theta_1 \tag{9}$$

With reasonable ignorance of higher order terms of sloping angles (i.e. $\cos^2\theta_1$, $\cos^2\theta_2 \approx 1$, $\sin^2\theta_1$ and $\sin^2\theta_2 \approx 0$) and the mass of the roller, and substituting $I=(1/2)m_2r^2$, a total of nine variables, including α, f_1, f_2, N_1, N_2, $\ddot{x}_1$, $\ddot{x}_2$, $\ddot{z}_1$, and $\ddot{z}_2$, can be solved by using Equations (1) to (9). The horizontal and vertical acceleration responses for the superior bearing plate (or the protected object) and the roller relative to the origin *O* are listed below:

$$\begin{aligned}\ddot{x}_1 &= \frac{(\cos\theta_1+\cos\theta_2)}{2(M+m_1)(1+\cos(\theta_1-\theta_2))}\Big\{-\operatorname{sgn}(\dot{x}_1)2F_D\\ &\quad -(M+m_1)\big[\ddot{x}_g(\cos\theta_1+\cos\theta_2)\\ &\quad +\operatorname{sgn}(x_1)(g+\ddot{z}_g)(\sin\theta_1+\sin\theta_2)\big]\Big\}\end{aligned} \tag{10}$$

$$\begin{aligned}\ddot{x}_2 &= \frac{\cos\theta_2}{2(M+m_1)(1+\cos(\theta_1-\theta_2))}\Big\{-\operatorname{sgn}(\dot{x}_1)2F_D\\ &\quad -(M+m_1)\big[\ddot{x}_g(\cos\theta_1+\cos\theta_2)\\ &\quad +\operatorname{sgn}(x_1)(g+\ddot{z}_g)(\sin\theta_1+\sin\theta_2)\big]\Big\}\end{aligned} \tag{11}$$

$$\begin{aligned}\ddot{z}_1 &= \frac{-(\sin\theta_1+\sin\theta_2)}{2(M+m_1)(1+\cos(\theta_1-\theta_2))}\Big\{\operatorname{sgn}(\dot{x}_1)2F_D\\ &\quad +(M+m_1)\big[\ddot{x}_g(\cos\theta_1+\cos\theta_2)\\ &\quad +\operatorname{sgn}(x_1)(g+\ddot{z}_g)(\sin\theta_1+\sin\theta_2)\big]\Big\}\end{aligned} \tag{12}$$

$$\begin{aligned}\ddot{z}_2 &= \frac{\sin\theta_2}{2(M+m_1)(1+\cos(\theta_1-\theta_2))}\Big\{\operatorname{sgn}(\dot{x}_1)2F_D\\ &\quad +(M+m_1)\big[\ddot{x}_g(\cos\theta_1+\cos\theta_2)\\ &\quad +\operatorname{sgn}(x_1)(g+\ddot{z}_g)(\sin\theta_1+\sin\theta_2)\big]\Big\}\end{aligned} \tag{13}$$

The generalized equations given in Equations (10) to (13) can also be applied to describe the dynamic responses of the two different design conditions, as shown in Figure 2, which were discussed in Wang's study (2013).

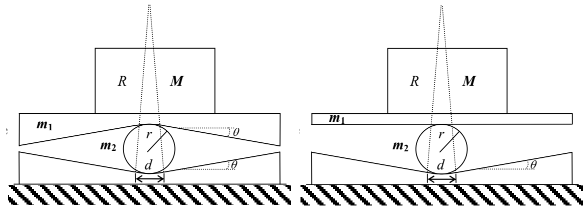

(a) Type A device (b) Type B device

Figure 2. Simplified models of two different design conditions

Type A device: roller sandwiched between two v-shaped sloped surfaces

Assuming the sloping angles of the superior and inferior bearing plates are θ in Equation (10), then

$$\begin{aligned}\ddot{x}_1+\ddot{x}_g &= \frac{1}{2}(g+\ddot{z}_g)\sin 2\theta\,\mathrm{sgn}(x_1)\\ &+\frac{F_D}{M+m_1}\cos\theta\,\mathrm{sgn}(\dot{x}_1)\end{aligned} \tag{14}$$

Type B device: roller sandwiched between a flat surface and a v-shaped sloped surface

Assuming the sloping angles of the superior and inferior bearing plates are zero and θ, respectively, in Equation (10), then

$$\begin{aligned}\ddot{x}_1+\ddot{x}_g &= -\frac{1}{2}(g+\ddot{z}_g)\sin\theta\,\mathrm{sgn}(x_1)\\ &-\frac{F_D}{M+m_1}\mathrm{sgn}(\dot{x}_1)\end{aligned} \tag{15}$$

Moreover, it is reasonable to assume that $\cos\theta \approx 1$ and $\sin\theta \approx x_1/2R$ when the roller moves within the fixed curvature range (d). Thus, the horizontal transmitted acceleration response of Type A device can be obtained by:

$$\ddot{x}_1+\ddot{x}_g = \frac{x_1}{2R}(g+\ddot{z}_g)\,\mathrm{sgn}(x_1)+\frac{F_D}{M+m_1}\mathrm{sgn}(\dot{x}_1) \tag{16}$$

Similarly, for Type B device:

$$\ddot{x}_1+\ddot{x}_g = \frac{x_1}{4R}(g+\ddot{z}_g)\,\mathrm{sgn}(x_1)-\frac{F_D}{M+m_1}\mathrm{sgn}(\dot{x}_1) \tag{17}$$

Verification of the generalized analytical model

Herein, the dynamic behavior of the sloped rolling type isolation device is numerically predicted by the simplified twin-flag hysteretic model (Equations (14) to (17)) and the analytical model derived from the generalized equations of motion (Equation (10)). Figure 3 shows the simplified twin-flag hysteretic model consisting of "Multi-Linear Link" and "Plastic Link (Wen, 1976)" in SAP2000.

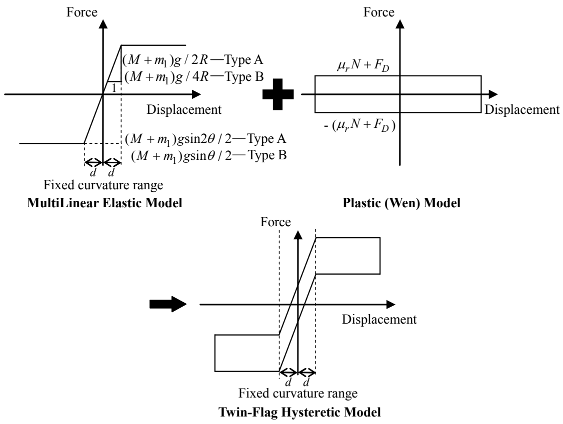

Figure 3. The simplified twin-flag hysteretic model in SAP2000

As an example, Type B device subjected to the uniaxial and biaxial Kobe earthquakes is considered. The sum of the masses of the superior bearing plate and the protected object, the built-in damping force, and the fixed curvature radius are designed to be 500kg, 250N, and 100mm, respectively. The design parameters of different analysis cases are detailed in Table 1.

Table 1. Design parameters of analytical studies

Analysis case	Sloping angle of V-shaped surface	Excitation direction	Input peak acceleration (g)
Case 1	6°	Uniaxial (X)	0.821
Case 2	6°	Biaxial (X/Z)	0.821/0.343
Case 3	12°	Uniaxial (X)	0.821
Case 4	12°	Biaxial (X/Z)	0.821/0.343

It is observed from Figure 4(a) that the difference between the analysis results obtained by the simplified twin-flag hysteretic model and the generalized analytical model under horizontal excitations is insignificant. In addition, as shown in Figures 4(a) and 4(c), the larger the design sloping angle, the more significant the effect arising from the higher order terms of sloping angles is. From the comparisons of Figures 4(a) and 4(b) as well as Figures 4(c) and 4(d), it is revealed that the vertical excitations will cause noticeable fluctuations when the rollers move apart from the fixed curvature range. This phenomenon cannot be appropriately reflected in the numerical results by using the simplified twin-flag hysteretic model. Therefore, the proposed generalized analytical model, when compared to the simplified twin-flag hysteretic model, can provide a more reliable, reasonable, and realistic dynamic behavior prediction for the sloped rolling type isolation device.

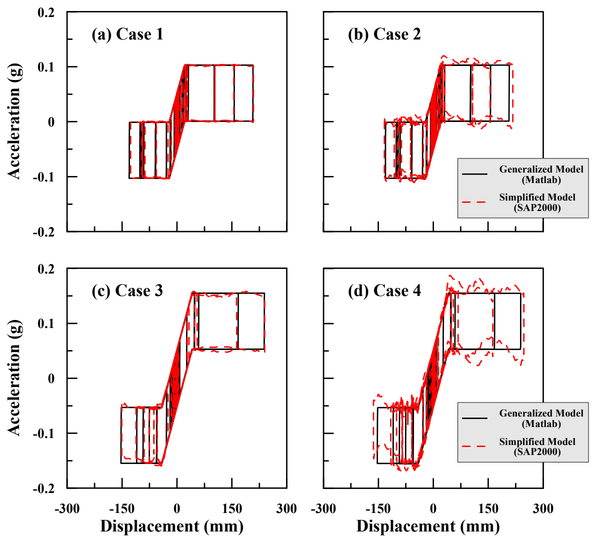

Figure 4. Comparison of hysteresis loops

Sloped rolling-type isolation devices with variable-damping and multi-slope design

To further achieve the performance-based design goal, variable-damping and multi-slope mechanisms are incorporated into the modified sloped rolling-type isolation device. To maintain a steady acceleration level (i.e. maximum transmitted acceleration response within a constant range) as shown in Figure 5, the first 25% range of the horizontal displacement capacity is designed with a larger sloping angle but with a smaller built-in damping force F_{D1}, which is beneficial for self-centering capability and frequent use. The remaining range is designed with a smaller sloping angle but with a larger built-in damping force F_{D2}, which can provide a better energy dissipation capability to suppress excessive displacement responses. To prevent undesired instant pounding, a transition range D_2 with an arc rolling range design is designed between the two ranges.

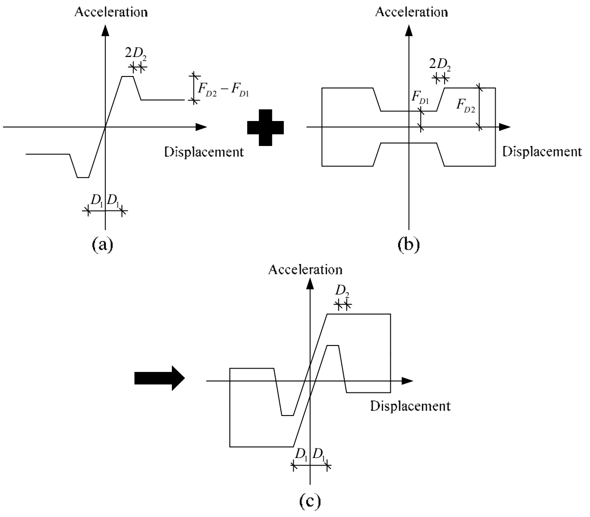

Figure 5. Performance-based design for sloped multi-roller isolation devices

Take Type B device is taken as an example. $M + m_1$ is assumed to be 500kg and the acceleration design target is intended to be less than 0.1g. After two sloping angles of the modified sloped rolling-type isolation device are determined to be 6 and 4 degrees, the corresponding built-in damping forces are calculated to be 235N and 320N by using Equation (15). The fixed curvature radius in the arc rolling range and transition range are designed to be 100mm. A counterpart (Type B) is designed with a constant sloping angle of 6 degrees and a constant built-in damping force of 235N. Under the uniaxial Kobe Earthquake and an artificial acceleration history (denoted as AC156-CHY009) compatible with AC156 (2007), the hysteresis loops obtained by the generalized analytical model are shown in Figure (6). Obviously, with the identical acceleration performance target, the modified sloped rolling-type isolation device with variable-damping and multi-slope mechanisms has better displacement control.

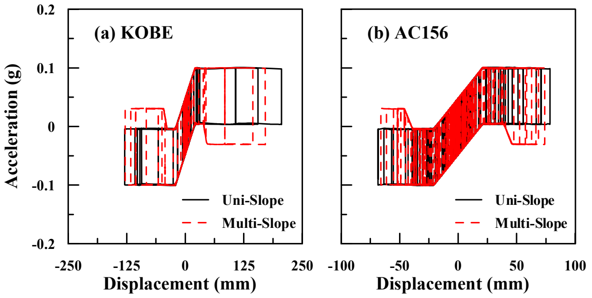

Figure 6. Comparison of hysteresis loops

Conclusions

In this study, the generalized equations of motion and a more accurate analytical model for a sloped rolling-type isolation device in which the rollers move between two arbitrary sloping surfaces are derived and proposed. As observed from the numerical comparisons, the proposed analytical model is more reasonable and reliable in characterizing the dynamic behavior of the sloped rolling-type isolation device than the simplified twin-flag hysteretic model. After considering different performance targets under small to severe earthquakes, an isolation device designed with variable-damping and multi-slope mechanisms is proposed. Under small and moderate earthquakes, a larger sloping angle and a smaller built-in damping can provide a better self-centering capability. Under severe earthquakes, a larger built-in damping force can provide a better energy dissipation capability to suppress excessive displacement responses. In order to further discuss a suitable performance-based design procedure for the sloped multi-rolling isolation device in engineering practice, a series of theoretical and experimental studies will be conducted.

References

Wang SJ, Hwang JS, Chang KC, Shiau CY, Lin WC, Tsai MS, Hong JX, Yang YH. Sloped multi-roller isolation devices for seismic protection of equipment and facilities. Earthq. Eng. and Struct. Dynam., 2013. DOI: 10.1002/eqe.2404.

Wen YK. Method for random vibration of hysteretic systems. J Eng. Mech., ASCE, 1976; 102(2): 249-263.

AC156. Acceptance criteria for seismic qualification by shake-table testing of nonstructural components and systems. ICC Evaluation Service, inc: 2007.

An Experimental Study of the Pseudo-local Flexibility Method for Damage Detection of Hyper-static Beams

Ting-Yu Hsu[1]、Wen-I Liao[2]、Shen-Yuan Shiao[3]、Chin-Hsiung Loh[4]

許丁友 [1]、廖文義 [2]、蕭勝元 [3]、羅俊雄 [4]

Abstract

Many vibration-based structural damage detection techniques that diagnose the damage imposed on a structure based on structural dynamic characteristic parameters have been proposed in the last two decades. One promising approach which has been proposed recently is the local flexibility method. The local flexibility method, which is based on virtual forces that cause nonzero stresses in a local part of the structure, can estimate the damage locations and local stiffness variations of beam structures. The structural modal parameters identified from the ambient vibration signals both before and after damage is the key information for the local flexibility method. In this study, non-local virtual forces which cause concentrated stresses in a local part and nonzero stresses in the other parts of a structure are utilized. The theoretical basis of the proposed method is derived, followed by validation of the method with a continuous steel beam experiment. The results illustrate that the non-local virtual forces can determine the local variations of stiffness for a beam more accurately with less identified modes. Therefore, the feasibility of the proposed method is higher because a limited number of high quality modes can be identified in real world applications.

Keywords: flexibility matrix, local flexibility method, damage detection, beam structures.

Introduction

The Local Flexibility Method (LFM) utilizes flexibility matrices of a beam structure constructed by structural modal parameters. When these matrices are combined with the designated local virtual forces, which cause stress fields restricted within a local region of the beam structure, the extent of the damage to the local region can be estimated. The structural modal parameters identified from the ambient vibration signals both before and after damage is the key information for the LFM. The number of modes required for the LFM is usually quite small, especially for a simply supported beam where only the first mode could be sufficient. However, for a hyperstatic beam, or for more complex structures, the number of modes required for the estimation of the damage may be much more. This makes the feasibility of the LFM much lower because in practice only the first few modes can be identified with high quality using ambient vibration signals. Therefore, in this study, non-local virtual forces which cause concentrated stresses in a local part and nonzero stresses in the other parts of a structure are employed. The proposed method is named as the pseudo local flexibility method (PLFM) and is explained and validated in the following sections. Firstly, the theoretical basis of the proposed method, which uses non-local virtual forces, is derived. Next, the effect of the number of modes on the damage detection results for damage scenarios involving both numerical and experimental hyperstatic beams is studied. Finally, the results are discussed and the advantage of the proposed PLFM is highlighted.

Methodology – The Pseudo Local Flexibility Method

[1] Associate Researcher, National Center for Research on Earthquake Engineering, dysheu@ncree.narl.org.tw
[2] Professor, Department of Civil Engineering, National Taipei University of Technology, wiliao@ncree.narl.org.tw
[3] Research Assistant, National Center for Research on Earthquake Engineering, shengyuan@ncree.narl.org.tw
[4] Professor, Department of Civil Engineering, National Taiwan University, lohc0220@ntu.edu.tw

The PLFM considers a structure with volume Ω and boundary $\boldsymbol{\Gamma}$, which is subject to the Dirichlet boundary conditions along part of its boundary (see Figure 1). A first load configuration f^1 is applied at a limited number of degrees of freedom (DOFs), r, where a response can be measured. The first load configuration for the PLFM is chosen such that the induced stress field $\boldsymbol{\sigma}^1$ consists of concentrated stresses in the local volume Ω_p and also a small stress outside Ω_p. Note that it is assumed that f^1 only causes non-zero stress within Ω_p for the LFM. The formula is based on the virtual work principle, with the strain energy of volume Ω_p neglected. For a beam structure, the damage detection equation can be obtained to estimate the rigidity reduction ratio within the local volume, denoted as R, when the shear deformation is neglected:

$$\frac{\sum_{j=1}^{r} f_j^2 x_j^1}{\sum_{j=1}^{r} f_j^2 x_{jd}^1} \cong \frac{\frac{1}{EI_p}\int_{\Omega_p} (\boldsymbol{\sigma}_p{}^2)^T \boldsymbol{\sigma}_p{}^1 d\boldsymbol{\Omega}_p}{\frac{1}{EI_p + \Delta EI_p}\int_{\Omega_p} (\boldsymbol{\sigma}_{pd}{}^2)^T \boldsymbol{\sigma}_{pd}{}^1 d\boldsymbol{\Omega}_p} = \frac{EI_p + \Delta EI_p}{EI_p} \equiv R \quad (1)$$

where EI_p is the bending rigidity within the local volume Ω_p. The virtual displacement vector x^1 under the first load configuration f^1 can be obtained using the following equation:

$$\boldsymbol{x}^1 = \boldsymbol{H}\boldsymbol{f}^1 \quad (2)$$

where H is the flexibility matrix. When a lumped and approximately equally distributed mass is assumed, the flexibility matrix can be estimated using the identified unscaled modal parameters as (Reynders & De Roeck, 2010) shown:

$$\boldsymbol{H} \cong \boldsymbol{H}^n = -\boldsymbol{\Phi}\boldsymbol{\Lambda}_c^{-1}(\boldsymbol{\Lambda}_c{}^H\boldsymbol{\Phi}^H\boldsymbol{\Phi}\boldsymbol{\Lambda}_c + \boldsymbol{\Phi}^H\boldsymbol{\Phi})^{-1}\boldsymbol{\Lambda}_c{}^H\boldsymbol{\Phi}^H \quad (3)$$

where $\boldsymbol{\Phi}$ is the matrix of mode shapes, $\boldsymbol{\Lambda}$c is the diagonal matrix of system poles and H is the Hermitian transpose. If only the first n modes are available, then the flexibility matrix is truncated, denoted as H^n. Note that, contradictory to the stiffness matrix, the contribution of the modes in the flexibility matrix is proportional to the inverse of the square of the system poles. The influence of higher modes on the flexibility matrix is much smaller than the influence of lower modes. As a result, the number of truncated modes needed to approximate a non-truncated flexibility matrix is much smaller than the ones needed to approximate a non-truncated stiffness matrix. This is beneficial to the practical cases where only a limited number of lower modes can be identified with acceptable accuracy, especially using ambient vibration signals.

The calculation of both the LFM and PLFM includes: using the identified modal parameters to construct the truncated flexibility matrix by Equation (3); multiplying the truncated flexibility matrix by the first load configuration to obtain the virtual displacement, as shown in Equation (2); and finally, multiplying the virtual displacement by the second load configuration both before and after damage, as shown in Equation (1). In fact, the truncated flexibility matrix and the second load configuration f^2 for the LFM and PLFM are identical. The only difference in the calculation between the LFM and PLFM is the first load configuration f^1.

Based on the theory above, the three main sources of theoretical error when estimating R using PLFM are: (1) the truncation error of the flexibility matrix due to the limited number of modes in Equation (3), denoted as ER_H; (2) the assumption that stress does not change due to damage for hyper-static structures, denoted as ER_σ; and (3) the neglect of virtual strain energy within Ω_q, denoted as ER_E. Note that for the LFM only ER_H and ER_σ exist. The determinant of the success of the PLFM is that if the non-local first load configuration f^1 can greatly reduce ER_H and at the same time induce a ER_E which is tolerable, then the total theoretical error of the PLFM has the potential to be smaller than that of the LFM. That is, the removal of the constraint in the LFM that f^1 only causes non-zero stress within Ω_p may benefit the damage detection results. Further discussion will be provided in the following sections.

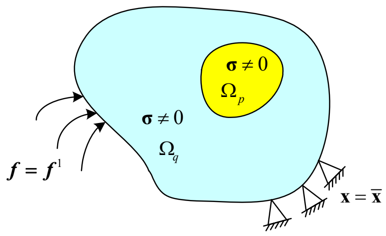

Fig. 1. A structure subjected to the first load configuration $\boldsymbol{f}^1$ that causes concentrated stress within the local region $\boldsymbol{\Omega}_p$.

Experimental Studies

A continuous steel beam of 2.4m length is designed and constructed to verify the proposed approach as shown in the left figure of Figure 2. The beam cross section is rectangular with a 5mm depth and 40mm width. The beam is supported at points 1, 5, and 13 with hinges and rollers as shown in Figure 3. Since the size of the specimen is quite small, the beam is excited by impact forces simulated using human fingers at several different points. The vertical acceleration response is measured at all the nodes except node 1, 5, and 13 because these nodes are supports.

Without loss of generality, the “damage” is simulated by increasing rigidity through the attachment of a small plate of length 50mm, with the same cross section as the beam as shown in the right figure of Figure 2. Three damage cases are considered as shown in Figure 3. The first damage case simulates the damage close to the middle of the long span, and the second case simulates the damage close to one of the supports. The third case simulates two damage locations at both the short span and the long span.

Fig 2. (Left) A continuous beam specimen with accelerometers; (Right) A typical example to increase the rigidity of the continuous beam by attaching a steel plate to simulate “damage”

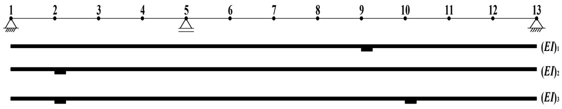

Fig 3. Measurement points and locations of stiffener for the three “damaged” cases of the continuous beam specimen.

In total, 4 modes with good quality can be identified from the output-only acceleration measurement using the stochastic subspace identification algorithm (Van Overschee & De Moor 1996). The modal frequencies and mode shapes typically identified when the beam is intact are shown in Figure 4. At each measurement point, the force configurations in the left part and right part of Figure 5 are applied as f^1 for the PLFM and LFM, respectively. The corresponding displacements x^1 at the measured DOFs are calculated using the truncated flexibility matrices constructed by a different number of modes and f^1. For both methods, the force configuration in Figure 5 is applied as f^2. The rigidity reduction ratio is estimated with Equation (1) using these identified modal parameters. The reference value of the rigidity reduction ratio is calculated using the flexibility matrix of a numerical beam model constructed by 48 beam elements.

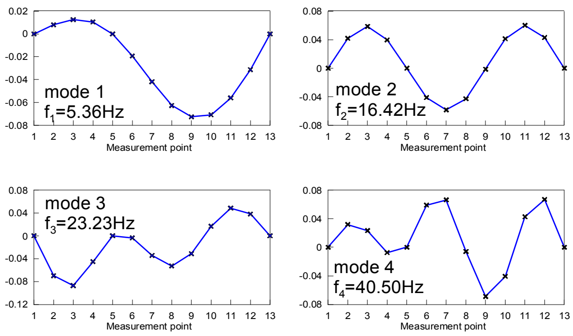

Fig 4. Typical mode shapes of the intact continuous beam specimen

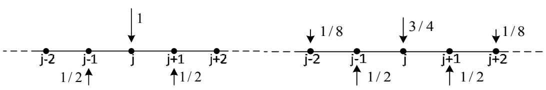

Fig. 5: A load configuration of a hyper-static beam structure that causes concentrated virtual stresses within the region between node j-1 to node j+1 (left figure) and that causes non-zero virtual stresses only within the region between node j-2 to node j+2 (right figure).

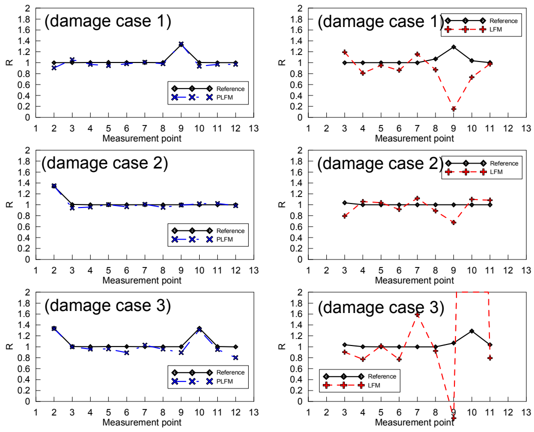

Fig 6. Estimated rigidity reduction ratio when using the first 2 unscaled modes with the PLFM (left) and the LFM (right).

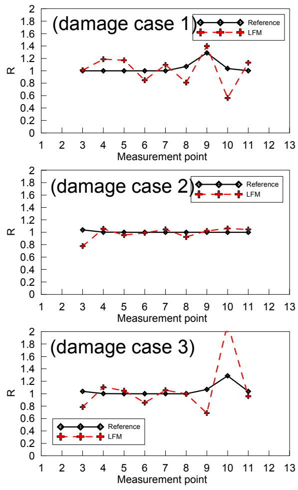

Fig. 7. Estimated rigidity reduction ratio when using the first 4 unscaled modes using the LFM: (a) damage case 1; (b) damage case 2; (c) damage case 3

For the proposed PLFM, the estimated rigidity reduction ratio at each measurement point using the first 2 modes is already rather close to the reference values for all three damage cases, as shown in the left part of Figure 6. Using more modes does not improve the results in all the cases, probably because the quality of the higher modes is not as good as that of the lower ones. On the other hand, for the original LFM, the estimated rigidity reduction ratio at most of the measurement points using the first 2 modes is not as close to the reference values when compared with using the PLFM, as shown in the right part of Figure 6. Some of the estimated rigidity reduction ratios are extremely big or small which implies that unreliable results are obtained. The estimated rigidity reduction ratio using the LFM becomes much better if all of the first 4 modes are employed, as shown in Figure 7. However, it is evident that the estimated rigidity reduction ratio using the PLFM is much closer to the reference values than the ratio estimated when using the LFM, even when only the first 2 modes are employed using the PLFM. This confirms again the superiority of the PLFM over the LFM, especially when fewer modes can be identified from measured signals.

Another interesting finding is that the increase in rigidity at node 2 in damage case 2 and damage case 3 cannot be easily discovered if the LFM is used, as shown through comparison with the reference values in Figure 6. The reference value at node 2 of these cases is only 1.038, which is very close to 1. Such a small change is not easily detected. The sensitivity to damage of the PLFM is higher than that of the LFM most likely for two main reasons. The first reason is because the non-zero stress induced by the first virtual load configuration using the LFM is between node 1 and node 5, while the region of concentrated stress induced by the first virtual load configuration using the PLFM is between node 1 and node 3. As shown by Equation (1), only the lump reduction ratio of the stiffness/rigidity can be estimated within the local region, therefore, the same extent of damage will induce a higher lump reduction ratio if a smaller local region is valid. That is, the PLFM is more sensitive to damage especially when the damage size or extent is smaller. Another reason for higher damage-sensitivity of PLFM is that the location of the damage within the local region also affects the value of the lump reduction ratio, due to the non-uniform moment induced by the applied virtual forces. The moment close to the center of the virtual forces is higher than the moment at the other parts in the local region. As a result, the closer the damage is to the center of the local region, the higher the lump reduction ratio will be. In this case, the non-zero stress induced by the first virtual load configuration using the LFM is between node 1 and node 5, while an increase in rigidity is caused at node 2. On the other hand, the region of concentrated stress induced by the first virtual load configuration using the PLFM is between node 1 and node 3, while the increase in rigidity is at the middle point. Therefore, the lump reduction ratio of the PLFM is much higher than the one of the LFM. This implies that when the damage is close to the support of a hyperstatic beam, the damage is more likely to be discovered using the PLFM. This displays another advantage of the PLFM; it is more sensitive to the damage close to the support than the LFM.

Conclusions and Discussions

In this paper, a PLFM to localize and quantify the damage of a hyperstatic beam structure is proposed. The PLFM breaks the constraint imposed in the original LFM that only virtual forces which cause nonzero local stress within a small part of a structure can be applied. That is, non-local virtual forces which cause a global but concentrated stress within the structure are valid for the PLFM. The release of the constraint on the virtual forces makes the virtual forces configuration simpler. The results of experimental studies on hyperstatic beams show that fewer modes are required for the PLFM to estimate the damage location and extent with acceptable accuracy. Note that the complexity of the intact and damaged structures increases the number of modes required to achieve acceptable damage detection results. Nevertheless, the feasibility of the PLFM is higher because a limited number of high quality modes can be identified in real world applications, especially for ambient vibration measurements where fewer modes can be identified due to lack of information about the excitation.

It was also found that the simplification of the first virtual force configuration in the PLFM makes it possible for the local region to be smaller. For the LFM, the local region is between 5 nodes while the local region for the PLFM is only between 3 nodes. Since the lump reduction ratio of the stiffness/rigidity can be estimated within the local region only, the same extent of damage will induce a higher lump reduction ratio if a smaller local region is valid. That is, the PLFM is more sensitive to damage especially when the size or extent of the damage is smaller. Furthermore, due to the fact that the moment close to the center of the virtual forces is higher than the moment at the other parts in the local region, the closer the damage is to the center of the local region, the higher the lump reduction ratio will be. Therefore, when the damage is close to the support, the damage is more likely to be discovered using the PLFM. This reveals another advantage of the PLFM because the PLFM is more sensitive to the damage close to the support than the LFM.

References

Toksoy, T. and Aktan, A. E. (1994), "Bridge-Condition Assessment By Modal Flexibility", *Experimental Mechanics*, Vol. 34, pp. 271–278.

Bernal D. (2002) , "Load Vectors for Damage Localization", *Journal of Engineering Mechanics*, Vol. 128, No. 1, pp. 7-14.

Reynders E. and De Roeck G. (2010), "A Local Flexibility Method for Vibration-based Damage Localization and Quantification", *Journal of Sound and Vibration*, Volume 329, Issue 12, pp. 2367-2383.

Van Overschee P. and De Moor B (1996), *Subspace Identification for Linear Systems: Theory - Implementation – Applications*. Kluwer Academic Publishers: Dordrecht, The Netherlands

Rehabilitation Objectives and Evaluation Criteria for Hospitals

Juin-Fu Chai[1], Jenn-Shin Hwang[2], Fan-Ru Lin[3], Kuang-Yen Liu[4] and Zen-Yu Lin[3]

柴駿甫[1]、黃震興[2]、林凡茹[3]、劉光晏[4]、林震宇[3]

Abstract

Based on the experiences learned from recent earthquakes, it is recognized that the earthquake resisting capacity of the responsibility hospitals with acute services should be upgraded. These hospitals assigned to provide emergency services after major earthquakes should remain functional for their engineering structures, medical facilities, electricity and water supply, and information services. However, in Taiwan, the medical equipment and supporting facilities have not been carefully inspected and seismically upgraded yet. Therefore, in order to facilitate the governmental political issuing and practical engineering services regarding the seismic upgrading of hospitals, the objective of this paper is to determine the seismic rehabilitation objectives and evaluation criteria of both building structures and essential medical equipment and nonstructural components in responsibility hospitals.

Keywords: hospital building structures; critical nonstructural components; medical equipment; seismic evaluation.

Introduction

The most important issue of a designated responsibility hospital with acute services is to maintain its emergency medical function all day long. In addition, due to the possible interruption of traffic after disaster earthquakes, it is necessary that medical equipment and medicine supplies of the designated hospital in the affected area should be self-sufficient for at least 72 hours. However, from the experiences of recent earthquakes, not only the hospital building structures but also the inside medical equipment (e.g. medicine cabinets and X-ray machines) were damaged seriously, and hence it resulted in significant shortage of emergency medical capacities of hospitals. It implies that the earthquake resisting capacity of the designated responsibility hospitals for emergency treatment should be upgraded to remain functional for the engineering structures, medical facilities, electricity and water supply, and information services after major earthquakes.

Nevertheless, in Taiwan, neither the building structures of major hospitals have been completely evaluated and retrofitted, nor the medical equipment and supporting facilities have been carefully inspected and seismically upgraded. Currently, most of the Ministry of Health and Welfare (MOHW) hospitals in Taiwan have completed the simplified evaluation of seismic capacity of building structures and the electrical and mechanical systems, some MOHW hospitals have finished the detailed seismic evaluation of building structures, but the specific seismic capacity of medical equipment and piping systems has not been considered. Therefore, in order to facilitate the governmental political issuing and practical engineering services regarding the seismic upgrading of hospitals, a 3-year project with the objective to develop a draft of “Seismic Evaluation and Strengthening Guidelines for Hospital Buildings” was organized by NCREE. As proposed, this guideline will consist of three major parts: (1) the upgrading strategy for seismic performance of hospitals, including the classification of building structures and

[1] Research Fellow, National Center for Research on Earthquake Engineering
[2] Professor, National Taiwan University of Science and Technology
[3] Assistant Researcher, National Center for Research on Earthquake Engineering
[4] Associate Researcher, National Center for Research on Earthquake Engineering

nonstructural components of hospitals, and the associated seismic rehabilitation objectives; (2) the seismic evaluation and strengthening guidelines for hospital building structures, and (3) the seismic evaluation and strengthening guidelines for critical medical equipment and nonstructural components in hospitals. This paper is focused on the seismic rehabilitation objectives and evaluation criteria of both building structures and essential medical equipment and nonstructural components in responsibility hospitals.

Rehabilitation Objectives

In Taiwan, the designated responsibility hospitals with acute service, MOHW or university hospitals, and those having essential facilities required for emergency treatment are defined as the Seismic Category I building with important factor I=1.5, and other hospitals not classified as Seismic Category I are defined as the Seismic Category III building with important factor I=1.25. In addition, the designated responsibility hospitals with acute services are classified into three levels as ‘severe’, ‘moderate’, and ‘general’ in consistence with their assigned capability for particular emergency treatment.

In general, as shown in Figure 1, the space in a hospital can be classified by human occupied area and non-human occupied area, or essential care area (including critical medical space and emergency exit access) and general area. For the nonstructural components in a hospital, the essential care areas and the supporting mechanical and electrical systems will be identified first according to the SB1953 [1] and the Hospital Safety Index developed by WHO. Then, inside the identified essential care areas, the architectural components necessary to meet “Life Safety” requirements and the critical medical equipment with higher seismic vulnerability will be chosen from criterion stated in ASCE7-05 [2] and the survey questionnaire answered by head nurses and facility managers.

The rehabilitation objective will be defined for the hospital to meet the specified rehabilitation goals. Each goal shall consist of a target performance level and an earthquake hazard level. There are three earthquake hazard levels EQL-1, EQL-2 and EQL-3 to be considered for the seismic evaluation of hospitals. Herein, EQL-1 is the frequently occurring small earthquake, EQL-2 is the design basis earthquake (DBE) level with a return period of 475 years (10% probability of exceedance within 50 years), and EQL-3 is the maximum considered earthquake (MCE) level with a hazard of 2%/50 years. The seismic demands (e.g. EPA) for the three earthquake hazard levels can be determined as specified by the Seismic Design Code for Buildings in Taiwan [3].

The target structural performance level of a hospital shall be selected from three discrete performance levels PLA, PLB and PLC, and the description of each structural performance level is listed in Table 1. In addition, the range of the three performance levels can be illustrated by the performance curve as shown in Figure 2. On the other hand, similar to SB1953, the target nonstructural performance level of a hospital shall be selected from 5 discrete performance levels NPL1, NPL2, NPL3, NPL4 and NPL5, and the description of each nonstructural performance level is listed in Table 2. Therefore, each nonstructural component can be tagged based on its particular characteristic and contribution in a hospital to meet the target performance level. The nonstructural components required to satisfy the performance level of NPL2 are tagged as NPL2, the additional nonstructural components required to satisfy the NPL3 are tagged as NPL3, and the more additional nonstructural components required to satisfy NPL4 are tagged as NPL4. In addition, the nonstructural components required to satisfy the performance level of NPL5, i.e. the electric and mechanical components used to support the components tagged by NPL3 to keep function without any interruption after strong earthquakes, are tagged as NPL5.

Based on the specified Seismic Category (I=1.0, 1.25 or 1.5) and the designated acute level (severe, moderate, or general) of an interested hospital, the rehabilitation objective of the nonstructural components can be determined by the performance matrix as shown in Table 3. It can be found by Table 3(a) for non-designated responsibility hospitals (I=1.25) that the nonstructural performance level is expected to be up to NPL4 under earthquake hazard level of EQL-1, NPL3 under EQL-2 (DBE) and NPL2 under EQL-3 (MCE), respectively, and the nonstructural performance level of NPL5 is not necessary for non-designated responsibility hospitals. In addition, the performance matrix also indicates that the nonstructural components tagged by NPL2 for a non-designated responsibility hospital should be designed for seismic retrofit under the earthquake hazard level of EQL-3 (MCE), the ones tagged by NPL3 should be designed by EQL-2 (DBE), and the ones tagged by NPL4 should be designed by EQL-1. For ‘moderate’ and ‘general’ designated responsibility hospitals (I=1.5), it is found from Table 3(a) that the associated rehabilitation objective are the same as that for non-designated responsibility hospitals (I=1.25) except that the performance level of NPL5 should be satisfied. It means that the nonstructural components tagged by NPL5 should be designed for seismic retrofit under the earthquake hazard level of EQL-2 (DBE), the same as that for components tagged by NPL3. Similarly, it can be found by Table 3(b) for university hospital (medical center) and ‘severe’ designated responsibility hospitals (I=1.5) that the nonstructural performance level is expected to be up to NPL4 under earthquake hazard levels of EQL-1 and EQL-2 (DBE), and NPL3 under EQL-3 (MCE), respectively. Moreover, the nonstructural components tagged by NPL5 should be designed for seismic retrofit under the earthquake hazard level of EQL-3 (MCE), the same as that for components tagged by NPL3.

Evaluation Criteria

For the interested hospital, the performance curve of the structure can be determined on the basis of the nonlinear static analysis (push-over analysis). Then, the limit point for each performance level can be defined according to the specified Seismic Category. As illustrated in Figure 2, the points A, B and C are the limit points of structural performance level PLA, PLB and PLC, respectively. Based on the seismic design code in Taiwan, the site-specific EPA= $0.4S_{MS}$, $0.4S_{DS}$ and $0.4S_{DS}/4.2$ can be determined at earthquake hazard levels EQL-3, EQL-2 and EQL-1, respectively, and the performance points associated with the three earthquake hazard levels can be determined. Therefore, based on the comparison of the performance point at each earthquake hazard level and the limit point corresponding to the particular structural performance level, the evaluation criteria for hospital building structure can be defined to meet the rehabilitation objective with triple rehabilitation goals.

For nonstructural components, each nonstructural component should be identified and tagged by NPL2, NPL3, NPL4 or NPL5 due to its particular characteristic and contribution in a hospital to meet the target performance level. The seismic capacity of the brace or anchorage system of these identified components shall be determined, and then compared with the seismic demands determined at the specified earthquake hazard levels to check the rehabilitation objective as define by Table 3 is satisfied or not.

Conclusions

In order to facilitate the governmental political issuing and practical engineering services regarding the seismic upgrading of hospitals, a 3-year project to develop the "Seismic Evaluation and Strengthening Guidelines for Hospital Buildings" was organized by NCREE. The preliminary achievements for the nonstructural components were presented in this paper. In the following, as planned, the seismic behavior of distribution system will be studied by experiment to support the proposed evaluation and strengthening guidelines, such as the fire protection sprinkler systems, post-installed anchorage attachment, and flexible mechanical coupling joints for piping systems. In addition, based on the MOU with cooperative hospitals, the detailed specification and the demonstration example of rehabilitation design will be performed.

References

1. SB 1953 Regulations (2001). Title 24, Part 1, California Building Standards Administrative Code, Chapter 6, OSHPD.
2. ASCE7-05 (2005). Minimum Design Loads for Buildings and Other Structures, American Society of Civil Engineers, Reston, VA.
3. Seismic Design Code and Commentary for Buildings (2011). Construction and Planning Agency, Ministry of Interior Affair, Taipei, Taiwan (in Chinese).

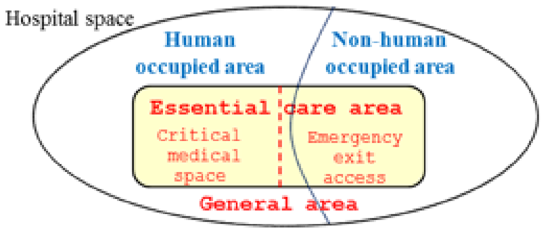

Figure 1. The classification of space in a hospital.

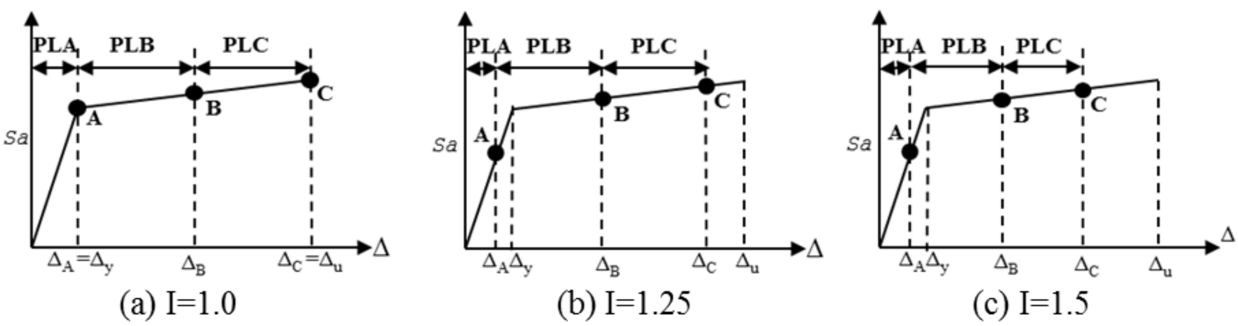

Figure 2. Seismic evaluation criteria for hospital building structure.

Table 1. Structural performance levels of a hospital.

Performance Level	Safety	Serviceability	Reparability	
			Short period	Long period
PLA	Structure remains elastic	Keep the same as prior to earthquake	Simply repaired	NA
PLB	Limited and repairable residual deformation	Return to the original after repair in short time	Emergency repair or replace of damaged members	Partially repaired or retrofitted
PLC	Collapse prevention	People exit safely	Additional vertical supporting	Partially rebuilt or retrofitted

Table 2. Nonstructural performance levels of a hospital.

Performance Level	Description
NPL5	Operational for essential care areas－ The building meets the criteria for NPL3, and further, on-site supplies of water and holding tanks for wastewater, sufficient for emergency operations in essential care areas without any interruption, are integrated into the building plumbing systems. An on-site emergency system is incorporated into the building electrical system for critical care areas. Additionally, the system shall provide for radiological service and an onsite fuel supply of acute care operation.
NPL4	Immediate Occupancy for human occupied areas－ The building meets the criteria for NPL3, and further, all architectural, mechanical, electrical systems, components and equipment, and hospital equipment in human occupied areas meet the bracing and anchorage requirements
NPL3	Immediate Occupancy for essential care areas－ The building meets the criteria for NPL2, and further, the critical components and equipment in essential care areas meet the bracing and anchorage requirements. ● critical care areas: including clinical laboratory service spaces, pharmaceutical service spaces, radiological service spaces, and central and sterile supply areas ● critical components: including elevator, communications systems, piping systems and tanks and vessel related to medical service; medical equipment; and potential falling or overturning architecture components.
NPL2	Life Safety－ the equipment related to emergency exit access are braced or anchored (e.g. communications systems, emergency power supply, bulk medical gas systems, fire alarm systems; and emergency lighting equipment and signs in the means of egress)
NPL1	Keep the existing building with the same performance, the equipment and systems may not meet the bracing and anchorage requirements.

Table 3. Nonstructural performance matrix

Earthquake Hazard Level	(a) For non-designated responsibility hospital (I=1.25) and 'moderate', and 'general' designated responsibility hospitals (I=1.5).				(b) For university hospital (medical center) and 'severe' designated responsibility hospitals (I=1.5)			
	NPL2	NPL3	NPL4	NPL5*	NPL2	NPL3	NPL4	NPL5*
EQL-1	○	○	◎	○	○	○	○	○
EQL-2 (DBE)	○	◎		◎	○	○	◎	○
EQL-3 (MCE)	◎				◎	◎		◎

* NPL5 is specified for designated responsibility hospitals only

Seismic Response Prediction of Base-Isolated Structures with High-Damping Rubber Bearings

Yin-Han Yang [1], Chia-Yi Shiau [2], Shiang-Jung Wang [3] and Jenn-Shin Hwang [4]

楊印涵 [1]、蕭佳益 [2]、汪向榮 [3]、黃震興 [4]

Abstract

To characterize the highly nonlinear hysteretic behavior of high-damping rubber (HDR) bearings, a previously developed mathematical hysteresis model, rather than the simplified bilinear hysteresis model, is adopted in this study. Unilateral and bilateral seismic simulation tests on a scaled-down multistory structure isolated with HDR bearings under three recorded earthquakes are conducted. Different sets of parameters for the mathematical hysteresis model are identified from the unilateral tests. A feasibility study on applying the identified parameters of the adopted hysteresis model to predict the bilateral seismic responses is performed. Moreover, the applicability of the adopted hysteresis model is investigated through a comparison of experimental measurement and analysis predictions using all sets of identified parameters. The noticeable influence ascribed to different earthquake characteristics such as the effect of near-field and far-field earthquakes on the modeling of HDR bearings is observed. Even though the prediction accuracy of the seismic responses is acceptable in both orthogonally horizontal directions, the bilateral hysteresis modeling of HDR bearings requires further study.

Keywords: high-damping rubber bearing; hysteresis model; base isolation; nonlinear seismic response analysis

Introduction

With regard to the analytical modeling of isolation bearings, the highly nonlinear hysteresis behavior of high-damping rubber (HDR) bearings may not be appropriately captured by the bilinear approximation (Naeim and Kelly, 1999) such that no specific model is currently available in most commercial tools for HDR bearings, even though a few analytical models have already been developed. In past research, several phenomenological models of elastomeric bearings have been provided by Bouc (1967) and Wen (1976) and by Özdemir (1976), and were subsequently adopted by Kikuchi and Aiken (1997) to describe hysteresis behavior at high shear strain levels, since the restoring force and damping force were experimentally found to be strongly related to shear strain magnitude. Moreover, Abe *et al.* (2004a, 2004b) derived a two-dimensional model on the basis of the Özdemir model (1976) using a three-dimensional constitutive law to study the multiaxial behavior of laminated rubber bearings. In addition to the phenomenological models, Pan and Yang (1996) proposed a mathematical hysteresis model that considers the shear force experienced by elastomeric bearings as a combination of the restoring force and damping force described by two mathematical equations. However, this mathematical model is unable to describe the Mullins and scragging effects (Mullins, 1969; Clark *et al*., 1997) on the hysteresis behavior of HDR bearings. Modified from Pan and Yang's model (1996), another mathematical model was proposed by Hwang *et al.* (2002) to further incorporate the prediction capability of cyclic softening and strain hardening behavior at high shear strain levels. The capability of the mathematical model has been verified through material tests of rubber layers, cyclic loading tests of HDR bearings, and unilateral shaking table tests of a rigid block

[1] Research Assistant, National Center for Research on Earthquake Engineering, yhyang@ncree.narl.org.tw
[2] Assistant Researcher, National Center for Research on Earthquake Engineering, cyshiau@ncree.narl.org.tw
[3] Associate Researcher, National Center for Research on Earthquake Engineering, sjwang@ncree.narl.org.tw
[4] Division Director, National Center for Research on Earthquake Engineering, jshwang@ncree.narl.org.tw

isolated by HDR bearings (Hwang *et al*., 2002).

In this study, unilateral and bilateral seismic simulation tests on a scaled-down base-isolated multistory structure with HDR bearings were conducted. To obtain the seismic responses of the base-isolated structure, an analytical structure model together with a mathematical model (Hwang *et al*., 2002) is established, and a state-space nonlinear dynamic analysis procedure is employed. The applicability of the mathematical model is investigated by comparing the results of analysis using the coefficients identified from the unilateral tests to the bilateral measured results of the HDR bearings.

Mathematical hysteresis model for HDR bearings

In the mathematical hysteresis model proposed by Hwang *et al*. (2000), the shear force experienced by elastomeric bearings is characterized as:

$$F(x(t),\dot{x}(t)) = K(x(t),\dot{x}(t))x(t) + C(x(t),\dot{x}(t))\dot{x}(t) \tag{1}$$

where $x(t)$ and $\dot{x}(t)$ are respectively the relative displacement and relative velocity of an elastomeric bearing at time t. The stiffness and damping coefficient at time t are given by

$$K(x(t),\dot{x}(t)) = a_1 + a_2 x^2(t) + a_3 x^4(t) + \frac{a_4 \exp\left[a_9 \int_0^t F(x(t),\dot{x}(t))dx(t)\right]}{\cosh^2(a_5 \dot{x}(t))} \tag{2}$$

and

$$C(x(t),\dot{x}(t)) = \frac{a_6 + a_7 x^2(t)}{\sqrt{a_8^2 + \dot{x}^2(t)}}\left\{1 + \exp\left[a_{10}\int_0^t F(x(t),\dot{x}(t))dx(t)\right]\right\} \tag{3}$$

where $a_1 \sim a_{10}$ are to-be-determined coefficients from cyclic loading reversals or dynamic tests. The cyclic softening behavior of elastomeric bearings can be regarded as a function of energy dissipation. Accordingly, the integral term $\int_0^t F(x(t),\dot{x}(t))dx(t)$ together with the to-be-determined coefficients were applied in Equations (2) and (3) to respectively describe the degradation of stiffness and the variation of the hysteresis loop area.

Experimental verification

To accommodate the space and payload limitations of the shaking table and to make the seismic isolation design more reasonable and effective in this experimental study, the test structure model, as shown in Figure 1, was designed to be a 1/4-scale base-isolated three-story steel frame with single-bay widths of 3 m in the longitudinal direction (X direction) and 2 m in the transverse direction (Y direction).

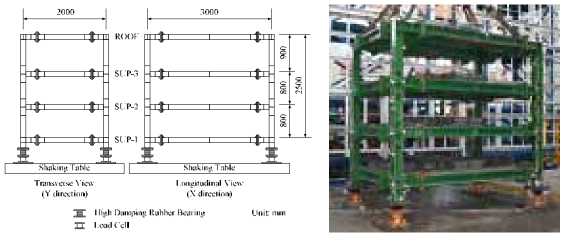

Figure 1. Design drawing and installation photo of the test structure model

The base isolation system was composed of four identical HDR bearings with diameter of 150 mm provided by Bridgestone Corporation. A single bearing comprised 25 HDR layers, each with a thickness of 1.97 mm. The shear modulus of the HDR layer was 0.62 N/mm^2. Steel shims bonded to each HDR layer were used to constrain the bulge behavior of HDR layers under vertical load. The thickness of each steel shim was 1.2 mm. The static axial load of a single HDR bearing was approximately equal to 41.7 kN. The superstructure was originally designed as a fixed-base structure according to the Taiwan seismic design code (MOI, Taiwan, 2011) without considering the reduction of force demand. Therefore, the superstructure was intended to remain elastic during the experiments. For simplicity, the story levels from the base slab to the superstructure are hereafter sequentially denoted as SUP-1, SUP-2, SUP-3 and ROOF. In addition to rigid diaphragms, supplemental mass blocks with a regular plane arrangement were attached to simulate the seismic reactive mass at each story. From SUP-1 to ROOF, the seismic reactive masses were respectively equal to 5, 4, 4 and 4 kN-sec^2/m. Assuming the superstructure was a rigid body (*i.e.*, a single degree-of-freedom system), and employing an equivalent bilinear model to represent the hysteretic behavior of the base isolation system, the effective period and the equivalent damping ratio subjected to design displacement of 55 mm were estimated to be 1.0 sec and 20%, respectively.

Three past earthquake records - the 1999 Chi-Chi earthquake (TCU047), the 1940 El Centro earthquake (ELC270), and the 1995 Kobe earthquake (KJM000) - were selected as input ground acceleration histories for both the unilateral and bilateral seismic simulation test schemes. Note that a time scale factor of 1/2 should be applied to satisfy the assumption of the test structure model as a 1/4-scale structure model.

Past research indicated that a larger shear strain (*e.g.*, larger than about 200%) will result in a greater coupling effect of HDR bearings under bilateral motion (Yamamoto *et al*., 2012). In other words, the smaller the shear strain, the less the coupling effect is observed. Therefore, to realize bilateral modeling of HDR bearings under moderate shear strain levels (*i.e.*, ignoring the coupling effect for simplicity), this study applied coefficients identified from unilateral tests to predict the bilateral seismic responses of the test structure model. Table 1 lists three sets of ten coefficients identified from each unilateral shaking table test. To further study the flexibility and limitations of the adopted mathematical model, the test results subjected to one of the three selected earthquake excitations are compared to the analytical predictions while considering the coefficients identified from the test results under the other selected earthquakes. In the state-space nonlinear dynamic analysis procedure, the inherent damping ratio of the superstructure was assumed to be 2%.

Table 1. The ten coefficients identified from each unilateral shaking table test

Test name	TCU047	ELC270	KJM000
a_1	3055.51	3121.88	2216.91
a_2	-139.55	-127.88	-28.09
a_3	2.52	1.87	0.61
a_4	2988.63	1474.36	193.51
a_5	0.10	0.08	0.09
a_6	2311.21	1719.44	2587.66
a_7	8.98	122.62	5.38
a_8	26.60	20.46	-30.39
a_9	-7.47E-06	-2.76E-06	9.18E-07
a_{10}	3.90E-07	-2.05E-06	-5.15E-07

The test results are shown in Figure 2. These include the hysteresis loops and displacement traces of the base isolation system, as well as the absolute acceleration and relative displacement responses at ROOF of the superstructure under bilateral ELC270. These are compared to the analytical predictions from the mathematical model with different sets of identified coefficients.

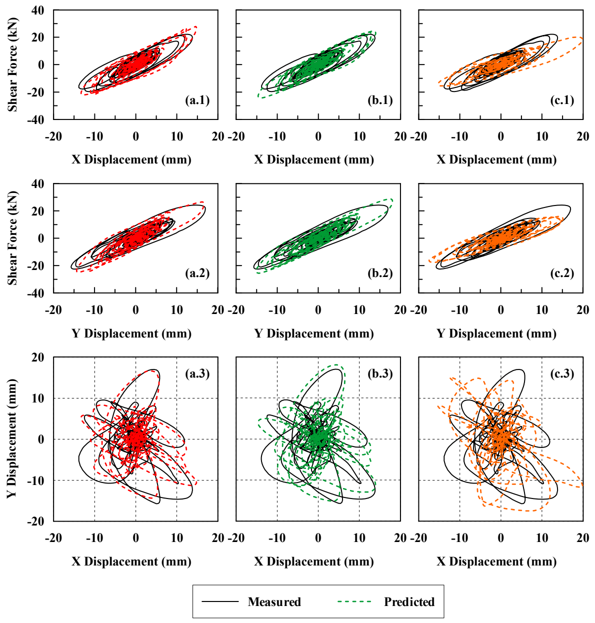

(I) Hysteresis loops and displacement traces of base isolation system

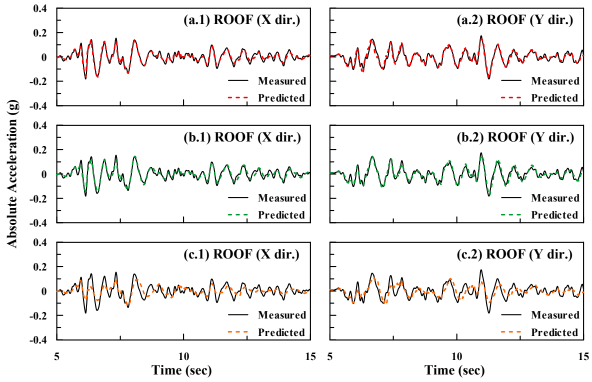

(II) Absolute acceleration response history at ROOF

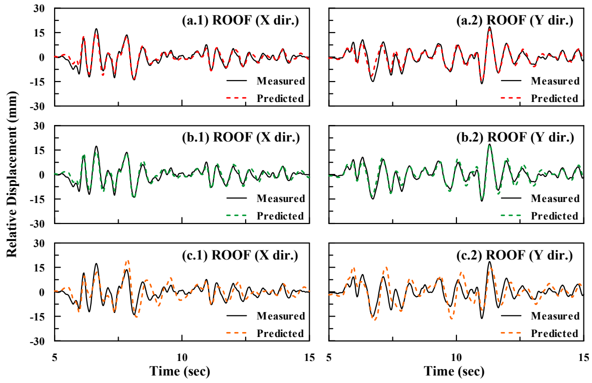

(III) Relative displacement response history at ROOF

Figure 2. Comparisons of test results and analytical predictions under bilateral ELC270 using ten coefficients identified from each unilateral test: (a) TCU047 (b) ELC270 (c) KJM000

As can be observed from these figures, an acceptable agreement between the experimental results and the analytical predictions in both orthogonally horizontal directions using the coefficients identified from the unilateral TCU047 and ELC270 tests demonstrates the applicability of the mathematical model in predicting the bilateral hysteretic behavior of HDR bearings under moderate shear strain levels. However, the accuracy is roughly acceptable while the analytical predictions using the coefficients identified from the unilateral KJM000 test.

Among the three selected earthquake records, the 1995 Kobe earthquake (KJM000) is known as a near-field ground motion, whereas the 1940 El Centro earthquake (ELC270) and the 1999 Chi-Chi earthquake (TCU047) are recognized as far-field ground motions. Near-field earthquakes in general have a noticeable velocity impulse and will cause a larger displacement demand for seismically isolated structures than far-field earthquakes do. It is obvious that the two nonlinear equations, Equations (2) and (3), of the mathematical model are highly dependent on the displacement and velocity experienced by the elastomeric bearings. As a result, the discrepancy discussed above is attributed to the difference in inherent earthquake characteristics between near-field and far-field earthquakes, that is, the dependence on the loading rates and load path histories of HDR bearings.

Furthermore, it is recognized from previous research that the coupling effect on the hysteretic behavior of laminated rubber bearings was of increasing significance, particularly for bearings such as HDR bearings, which possess viscous and/or plastic characteristics (Abe *et al.*, 2004a, 2004b; Grant *et al.*, 2004). The bilateral loading may cause twist deformation and then increase local shear strain in the HDR bearings, which results in the early failure of HDR bearings (Yamamoto *et al.*, 2012). Therefore, an improved and more robust bilateral mathematical model for HDR bearings under excessive shear strain levels (*e.g.*, larger than 200%) and its dependence on loading rates and load path histories should be further studied.

Conclusions

In this study, the mathematical hysteresis model identified from dynamic test results was adopted to simulate the highly nonlinear hysteretic behavior of high-damping rubber (HDR) bearings, and a state-space nonlinear dynamic analysis procedure was performed to predict the seismic responses of a test structure model isolated with HDR bearings. The comparison of experimental results and analytical predictions demonstrated in a preliminary manner whether the parameters identified from the unilateral tests can be applied to bilateral response prediction of a structure isolated with HDR bearings under moderate shear strain levels. It was revealed that the adopted mathematical model using coefficients identified from one earthquake can appropriately predict the seismic responses of an isolated structure subjected to another earthquake, if the two earthquakes do not possess significantly different kinematic characteristics such as those of near-field and far-field earthquakes. Therefore, it is suggested that for specific HDR bearings, two separate sets of coefficients of the mathematical model, corresponding to near-field and far-field earthquakes, should be identified so that the seismic responses of the isolation system and the isolated superstructure can be captured more exactly and conservatively.

References

Abe, M., J. Yoshida, and Y. Fujino. 2004a. "Multiaxial Behaviors of Laminated Rubber Bearings and Their Modeling. I: Experimental Study." J. Struct. Eng. 130 (8): 1119–1132.

Abe, M., J. Yoshida, and Y. Fujino. 2004b. "Multiaxial Behaviors of Laminated Rubber Bearings and Their Modeling. II: Modeling." J. Struct. Eng. 130 (8): 1133–1144.

Bouc, R. 1967. "Forced Vibration of Mechanical Systems with Hysteresis," In Proc. 4th Conf. on Nonlinear Oscillations, Prague, Czechoslovakia, 5-9 September 1967.

Clark, P. W., I. D. Aiken, and J. M. Kelly. 1997. "Experimental Studies of the Ultimate Behavior of Seismically-Isolated Structures." Report No. UCB/EERC-97/18, Earthquake Engineering Research Center.

Grant, D. N., G. L. Fenves, and A. S. Whittaker. 2004. "Bidirectional Modelling of High-Damping Rubber Bearings." J. Earthq. Eng. 8(1): 161-185.

Hwang, J.-S., J.-D. Wu, T.-C. Pan, and G. Yang. 2002. "A Mathematical Hysteresis Model for Elastomeric Isolation Bearings." Earthq. Eng. Struct. Dynam. 31 (4): 771-789.

Kikuchi, M., and I. D Aiken. 1997. "An Analytical Hysteresis Model for Elastomeric Seismic Isolation Bearings." Earthq. Eng. Struct. Dynam. 26 (2): 215-231.

Mullins, L. 1969. "Softening of Rubber by Deformation." Rubber Chem. Tech. 42 (1): 339-362.

Naeim, F., and J. M. Kelly. 1999. Design of Seismic Isolated Structures: From Theory to Practice. New York: John Wiley & Sons, Inc.

Özdemir, H. 1976. "Nonlinear Transient Dynamic Analysis of Yielding Structures." Doctoral dissertation, Department of Civil Engineering, University of California, Berkeley.

Pan, T.-C., and G. Yang. 1996. "Nonlinear Analysis of Base-Isolated MDOF Structures." In Proc. of the 11th World Conf. on Earthq. Eng., Acapulco, Mexico, 23-28 June 1996.

Seismic Design Specifications and Commentary of Buildings. 2011. Ministry of the Interior, Taipei, Taiwan.

Yamamoto, M., S. Minewaki, H. Yoneda, and M. Higashino. 2012. "Nonlinear Behavior of High-Damping Rubber Bearings under Horizontal Bidirectional Loading: Full-Scale Tests and Analytical Modeling." Earthq. Eng. Struct. Dynam. 41(13): 1845-1860.

Wen, Y. K. 1976. "Method for Random Vibration of Hysteretic Systems." J. the Eng. Mech. Div. 102 (2): 249-263.

Feasibility Study on Building Mass Damper for Seismic Design

Bo-Han Lee[1], Shiang-Jung Wang[2], Wei-Chu Chuang[3],

Kuo-Chun Chang[4] and Jenn-Shin Hwang[5]

李柏翰[1]、汪向榮[2]、莊幃竹[3]、張國鎮[4]、黃震興[5]

Abstract

A tuned mass damper (TMD) has been recognized as an effective energy absorbing device to reduce undesirable vibrations of an attached primary system subjected to harmonic excitations. Its design concept is to generate a phase lag attributed to resonance between the primary system and the TMD. In this study, the use of a partial structural mass, instead of an additional mass, to be an energy absorber, i.e. building mass damper (BMD), is discussed to seismically protect both the primary structure and building mass absorber. Taking appropriate mass ratios and objective functions into consideration, a simplified three-lumped-mass structure model, in which each of the three lumped masses is assigned to the building mass absorber, control layer and primary structure, is employed to derive the optimal design parameters for BMD. The practicability of BMD, as well as the effectiveness of the proposed optimal design method, is numerically verified using several recorded earthquakes that possess significantly different characteristics.

Keywords: building mass damper, tuned mass damper, objective function, optimum design, numerical analysis

Introduction

Various approaches for selecting optimum design parameters of tuned mass damper (TMD) have been developed in many studies. In addition, active and semi-active control devices have been gradually applied to a TMD to further enhance its control performance. In engineering practice, a TMD was first accepted to mitigate the wind-induced vibrations or to enhance the serviceability performance of high-rise buildings. Recently, the adoption of TMD to enhance the seismic capability of building structures has been attracting immense attention. Thus, a new design concept, namely a building mass damper (BMD), was proposed and numerically studied in some research. The use of a partial structural mass, instead of an additional mass, to act as an energy absorber in a BMD can overcome the drawback of limited response reduction due to insufficient tuned mass in a TMD. However, in these research studies, the control target is still focused on the primary structure performance rather than on either the building mass absorber performance or both. If the building mass absorber is intended to be used for occupancy as the primary structure, excessive dynamic responses are not acceptable. Under this circumstance, the seismic performance of both the primary structure and the building mass absorber should be emphasized. To achieve both seismic isolation performance and TMD effectiveness, the BMD system proposed in this study is composed of a building mass absorber, a control layer and a primary structure. Referring to Sadek's (1997) study and considering the flexibility of the building mass absorber in derivation, the optimum

[1] Assistant Researcher, National Center for Research on Earthquake Engineering, bhlee@ncree.narl.org.tw
[2] Associate Researcher, National Center for Research on Earthquake Engineering, sjwang@ncree.narl.org.tw
[3] Graduate student, Department of Civil Engineering, National Taiwan University, r01521215@ntu.edu.tw
[4] Professor, Department of Civil Engineering, National Taiwan University, ciekuo@ntu.edu.tw
[5] Professor, Department of Construction Engineering, National Taiwan University of Science and Technology JSH@mail.ntust.edu.tw

design parameters for a BMD, i.e. an optimum building mass damper (OBMD), to effectively protect both the primary structure and building mass absorber are discussed. A series of numerical analyses are conducted to verify the practicability of an OBMD for seismic design.

Optimal Design Parameters for a BMD

In a BMD, the building mass absorber may be designed to be a multi-story structure, which is very different from the conventional mass absorber in a TMD. In addition, the tuned absorber to primary structure mass ratio in a BMD is much larger than that in TMD. Therefore, a simplified three-lumped-mass structure model, in which three lumped masses are each assigned to the building mass absorber, control layer and the primary structure, is rationally assumed to represent a building structure with a BMD design, as shown in Figure 1. The reason for so doing is that, the inherent dynamic characteristics (i.e. the fundamental modal characteristics of vibration) of both the building mass absorber and the primary structure can be considered comprehensively in the simplified structure model. The motion equation of the simplified structure model can be further expressed in terms of the nominal frequency ω_1, frequency (or tuning) ratio f_i (i = 2, 3), mass ratio μ_i (i = 2, 3) and component damping ratio ξ_i (i = 1~3) as defined below:

$$f_i = \frac{\omega_i}{\omega_1},\ i = 2,\ 3 \tag{1}$$

$$\mu_i = \frac{m_i}{m_1},\ i = 2,\ 3 \tag{2}$$

$$\xi_i = \frac{c_i}{2\sum_{j=i}^{3} m_j \omega_i},\ i = 1\sim 3 \tag{3}$$

where i = 1, 2 and 3 denote the primary structure, control layer and building mass absorber, respectively; the nominal frequencies ω_1, ω_2 and ω_3 are defined as $\sqrt{k_1/m_1}$, $\sqrt{k_2/(m_2+m_3)}$ and $\sqrt{k_3/m_3}$, respectively; m_1, m_2 and m_3 are the generalized seismic reactive masses (for the fundamental mode of vibration computed with a unit modal participation factor) of the primary structure, control layer and building mass absorber, respectively; k_1 (c_1) and k_3 (c_3) are the elastic lateral stiffnesses (viscous damping coefficients) for the fundamental mode of vibration of the primary structure and building mass absorber; and k_2 (c_2) is the effective lateral stiffness (equivalent viscous damping coefficient) of the control layer. By means of the state space method under coupling approximation, the system matrix can be obtained in terms of ω_1, f_i (i = 2, 3), μ_i (i = 2, 3) and ξ_i (i = 1~3) as follows

$$\mathbf{A} = \begin{bmatrix} \mathbf{0} & \mathbf{I} \\ -\mathbf{M}^{-1}K & -\mathbf{M}^{-1}\mathbf{C} \end{bmatrix} \tag{4}$$

$$\mathbf{M}^{-1}K = \begin{bmatrix} -\omega_1^2\left[1+f_2^2(\mu_2+\mu_3)\right] & \omega_1^2 f_2^2(\mu_2+\mu_3) & 0 \\ \dfrac{\omega_1^2 f_2^2(\mu_2+\mu_3)}{\mu_2} & \dfrac{-\omega_1^2\left[f_2^2(\mu_2+\mu_3)+f_3^2\mu_3\right]}{\mu_2} & \dfrac{\omega_1^2 f_3^2 \mu_3}{\mu_2} \\ 0 & \omega_1^2 f_3^2 & -\omega_1^2 f_3^2 \end{bmatrix} \tag{5}$$

$$\mathbf{M}^{-1}C = \begin{bmatrix} -2\omega_1\left[(\xi_1+f_2\xi_2)(\mu_2+\mu_3)+\xi_1\right] & 2\omega_1 f_2\xi_2(\mu_2+\mu_3) & 0 \\ \dfrac{2\omega_1 f_2\xi_2(\mu_2+\mu_3)}{\mu_2} & \dfrac{-2\omega_1\left[f_2\xi_2(\mu_2+\mu_3)+f_3\xi_3\mu_3\right]}{\mu_2} & \dfrac{2\omega_1 f_3\xi_3\mu_3}{\mu_2} \\ 0 & 2\omega_1 f_3\xi_3 & -2\omega_1 f_3\xi_3 \end{bmatrix} \tag{6}$$

where **0** = the zero matrix; **I** = the identity matrix; and **M**, **K** and **C** are the generalized mass, stiffness and damping coefficient matrices, respectively;

The complex eigenvalues of Equation (4) can be determined in the form of conjugate pairs

$$\lambda'_{n,\,n+1} = \omega'_n \xi'_n \pm i\omega'_n\sqrt{1-\xi'^2_n},\ n = 1\sim 3 \tag{7}$$

where λ'_n is the n^{th} modal eigenvalue of the system; λ'_{n+1} is the conjugate of λ'_n; ω'_n and ξ'_n are the n^{th} modal natural frequency and the n^{th} modal damping ratio of the system, respectively; and i is the unit imaginary number (i.e. $i = \sqrt{-1}$). As illustrated in Figure 2, it is assumed that μ_2 and μ_3 vary within reasonable ranges from 0.1 (i.e. representing a high-rise primary structure) to 0.5 (i.e. representing a low-rise primary structure) and 0.1 (i.e. representing a low-rise building mass absorber) to 2 (i.e. the story number of the building mass absorber is twice that of the primary structure), respectively. In this study, the objective function is determined as such, the dominant modal damping ratios of the simplified structure model in the direction of interest are equally important and taken as an approximately equal value, i.e. $\xi'_1 \cong \xi'_2 \cong \xi'_3$. Based on the objective function with given (or assumed) parameters ω_1, μ_2, μ_3, ξ_1 and ξ_3, the optimum design parameters for BMD, including two frequency (or tuning) ratios f_2 and f_3 and one damping ratio ξ_2, can be determined.

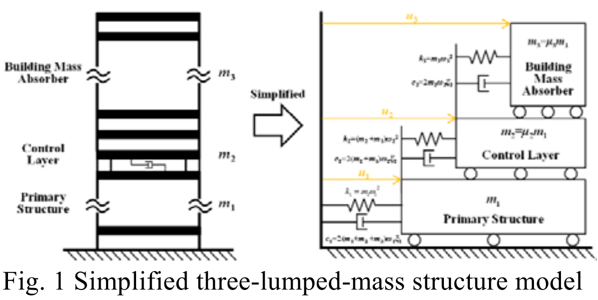

Fig. 1 Simplified three-lumped-mass structure model

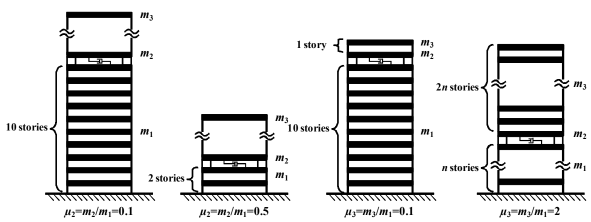

Fig. 2 Reasonable ranges of μ_2 and μ_3

Numerical Structure Models

The bare frame is designed to be an 8-story, 2-bay steel structure, as shown in Figure 3(a). The widths of each bay in the X and Y directions are 2250 mm and 2000 mm, respectively. The height of each story is 1250 mm. The sections of columns and beams are wide flanges with dimensions of 125×125×6.5×9 (mm) and 125×60×6×8 (mm), respectively. A uniform load of 0.5kN-sec^2/m is assigned at each floor.

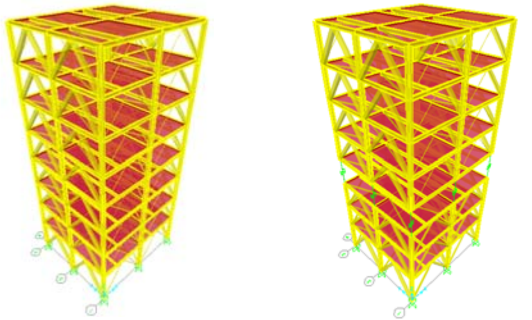

(a) Bare frame (b) OBMD design

Fig. 3 Numerical structure models

The numerical structure model with an OBMD design is shown in Figure 3(b). The upper four-story and lower three-story structures are intended to be the building mass absorber and the primary structure, respectively. The control layer between the building mass absorber and the primary structure is designed to be composed of natural rubber bearings (RBs) and linear viscous dampers (VDs). According to the proposed optimal design method, the OBMD design parameters can be calculated as ξ_2^{opt} =20%, f_2^{opt}=0.27 and f_3^{opt}=0.25. To achieve the OBMD design parameters, the primary structure and building mass absorber should be stiffened by angle braces with dimensions of 25×25×3 (mm) and 100×100×3 (mm), respectively. Analysis shows that the fundamental mode natural period is 0.42 seconds with a participation mass ratio of 63.4%. In addition, a noticeable participation mass ratio of 24.1% at 0.054 seconds is observed.

Input Ground Motions

Five real earthquake records, denoted as EL Centro, Kobe, TCU047, TCU072 and THU, are selected for the ground acceleration inputs along the X direction, as detailed in Table 1. The 5% damped response spectra of these input acceleration histories normalized to a peak ground acceleration (PGA) of 1g are illustrated in Figure 4.

Table 1 Input ground motions

Name	Earthquake Record	PGA
EL Centro	El Centro/I-ELC270, Imperial Valley, U.S., 1940/05/19	0.35g
Kobe	KJMA/KJM000, Kobe, Japan, 1995/01/16	0.59g
TCU047	Chi-Chi/TCU047, Chi-Chi, Taiwan, 1999/09/21	0.36g
TCU072	Chi-Chi/TCU072, Chi-Chi, Taiwan, 1999/09/21	0.47g
THU	Tohoku/THU, Tohoku, Japan, 2011/03/11	0.40g

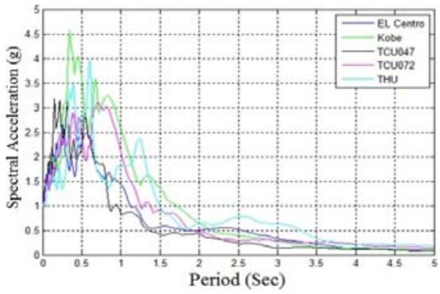

Fig. 4 Acceleration spectra of input ground motions (5% damping ratio)

Numerical Results

The maximum inter-story displacement and acceleration responses at each floor of the bare frame and the structure models with an arbitrary BMD design and OBMD design subjected to all the earthquake excitations are presented in Figures 5 and 6, respectively. With an arbitrary BMD design, the seismic responses at some stories may be enlarged compared to those of the bare frame, e.g. under TCU072. In contrast to the bare frame and the structure model with an arbitrary BMD design, it is obvious that the OBMD design has good potential in reducing the seismic responses of both the primary structure and the building mass absorber, which can demonstrate the effectiveness of the proposed optimal design method.

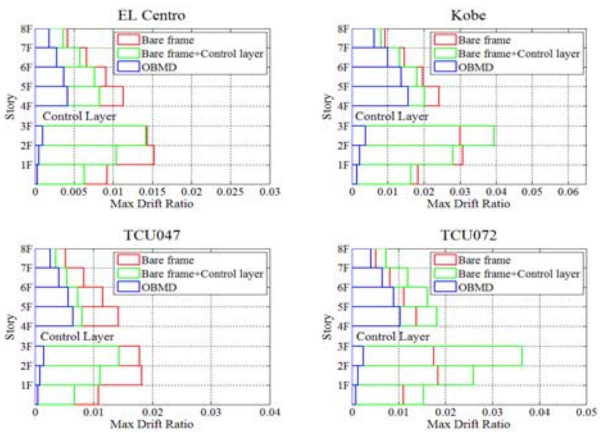

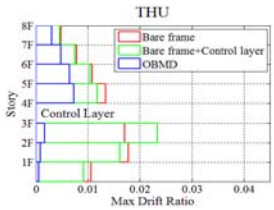

Fig. 5 Vertical distributions of maximum interstory displacement responses

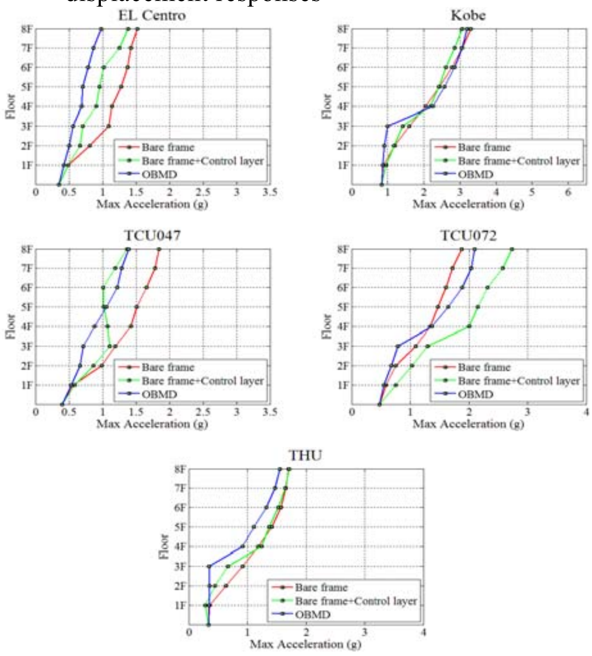

Fig. 6 Vertical distributions of maximum acceleration responses

Conclusions and Future Work

The most attractive feature of a BMD design is that the use of a partial structural mass as an energy absorber can overcome the drawback of insufficient tuned mass in a TMD design. In addition, with consideration of the flexibility of the building mass absorber, a reasonable optimal damping ratio demand will be obtained. In this study, an optimum design method for a BMD is proposed to seismically protect both a primary structure and a building mass absorber. The numerical results indicate that the proposed optimal design method is practicable and effective. In the future, different objective functions for the OBMD design, such as the optimal control of dynamic responses, will be further investigated. Furthermore, active and semi-active control devices will be applied to an OBMD to further enhance its control performance.

References

Hartog Den J P. (1956), *Mechanical Vibrations, 4th ed.*, McGraw-Hill, New York

Rahul Rana and T. T. Soong (1997), "Parametric study and simplified design of tuned mass dampers", Eng. Struct.

Sadek F, Mohraz B, Taylor AW and Chung RM (1997), "A Method of Estimating the Parameters of Tuned Mass Dampers for Seismic Applications", Earthq. Eng. Struct. Dyn., 26:617-635

Tsai HC and Lin GC (1993), "Optimum Tuned-Mass Dampers for Minimizing Steady-State Response of Support-Excited and Damped Systems", Earthq. Eng. Struct. Dyn., 23:957-973

Warburton GB and Ayorinde EO (1980), "Optimum Absorber Parameters for Simple Systems", Earthq. Eng. Struct. Dyn., 8:197-217

Warburton GB (1981), "Optimum Absorber Parameters for Minimizing Steady-State Response", Earthq. Eng. Struct. Dyn.

Seismic Design of Bottom Boundary Columns in Steel Plate Shear Walls

Keh-Chyuan Tsai [1], Chao-Hsien Li [2] and Hung-Chi Lee[3]

蔡克銓 [1]、李昭賢 [2]、李弘祺 [3]

Abstract

Steel plate shear walls (SPSWs) can effectively resist earthquake forces by the development of tension field action after infill steel plates buckle in shear and dissipate energy through cyclic tensile yielding of the infill plates. The tension field forces of the infill plates can cause some plastic hinges to form within the beam span or column height. During the past decade, many researchers have aimed to develop design methods to ensure that the boundary beams or columns have adequate strength to prevent the occurrence of in-span plastic hinges. However, limiting plastic hinges to concentrate at the column bases usually requires heavy bottom columns. In addition, past tests show that the formation of a plastic hinge within the height of the bottom columns would not deteriorate the seismic performance of the SPSWs. In order to achieve an economical design, this study proposes a series of less-stringent capacity design methods to determine the flexural or shear demands for the bottom boundary column in a SPSW. The proposed design requirements allow a plastic zone to form within the lower part of the bottom column but prevent the column top end from yielding. In this study, a series of capacity design methods is developed to control the location of the in-span plastic zone on the bottom column and prevent yielding of the column top end under two large deformation levels: State-UY and State-HD, which respectively correspond to the onset of the plastic mechanism and the maximum considered earthquake (MCE) hazard level.

Keywords: steel plate shear wall (SPSW), capacity design, seismic design, boundary column

Introduction

A steel plate shear wall (SPSW) is an emerging lateral force resisting structural system in North America and Japan. An SPSW consists of infill steel panels and a boundary frame. SPSWs can effectively resist horizontal earthquake forces by allowing the development of diagonal tension field action after the infill plates buckle in shear and dissipate energy through cyclic yielding of the infill in tension. In recent years, several researchers studied capacity design methods for the boundary beams or columns adjacent to the infill panels. Berman and Bruneau (2008) proposed a design method for calculating the axial and flexural demands for the columns in typical stories in SPSWs. Tsai *et al.* (2010) proposed a design method to limit the plastic hinge in the bottom boundary column at the bottom end and the effectiveness of this method has been experimentally verified. Li *et al.* (2012) developed a less-stringent design method to ensure that the plastic hinge forms within the bottom 1/4 height of the bottom column. This study aims at developing further cost-effective designs for the bottom boundary column and proposes a design requirement to prevent yielding of the column top end under various deformation levels. In order to verify the effectiveness of the proposed design methods, three full-scale two-story SPSW were cyclically tested up to a roof drift of 4.5% rad. at the Taiwan National Center for Research on Earthquake Engineering (NCREE).

[1] Professor, Department of Civil Engineering, National Taiwan University, kctsai@ntu.edu.tw.
[2] Assistant Researcher, National Center for Research on Earthquake Engineering, chli@ncree.narl.org.tw
[3] Former Graduate Student, Department of Civil Engineering, National Taiwan University, r98521206@ntu.edu.tw

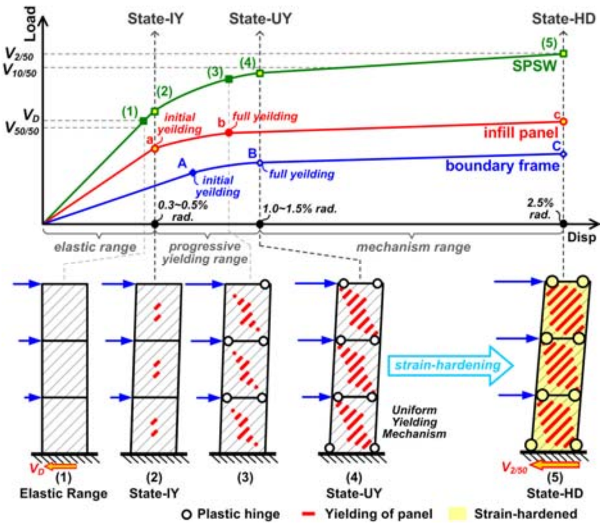

Fig. 1 Anticipated pushover responses of SPSWs.

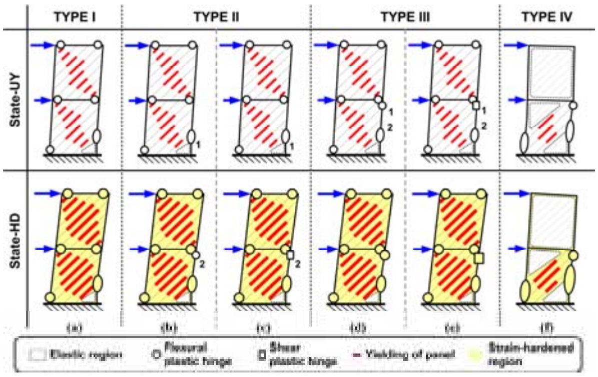

Fig. 2 Various inelastic responses of compressed bottom boundary columns in SPSWs

Capacity Design of Bottom Boundary Columns in SPSWs

Based on the observations from many past tests, this study proposes anticipated pushover responses for properly designed SPSWs. As illustrated in Fig. 1, the anticipated pushover responses can be delineated by four limit states:

(1) State-E (Elastic): The whole SPSW must remain elastic when the structure is subjected to the code-prescribed seismic forces.

(2) State-IY (Initial Yield): State-IY is defined as the state when the infill plates first experience yielding near the tensile diagonal region. In this state, the boundary elements remain elastic and the story drift is about 0.3~0.5% rad.

(3) State-UY (Uniform Yielding Mechanism): SPSW develops a uniform yielding mechanism when the story drift is around 1~1.5% rad. All the infill plates develop plastic tension field action and the plastic hinges form at the beam-ends and the column bases.

(4) State-HD (Target Hardening State): State-HD is the state when SPSWs reach the peak drift level under the maximum considered earthquake (MCE). Coinciding with the model building code, a MCE is defined as an earthquake that has a 2% probability of exceedance within 50 years. At this state, the plastic zones, which had fully developed at State-UY, have experienced strain hardening. The remaining parts except for those plastic zones should be designed to remain essentially elastic at this state in order to avoid the occurrence of any undesirable plastic mechanisms. A past pseudo-dynamic test (Lin *et al.*, 2010) suggests that the peak inter-story drift of a properly designed two-story SPSW during MCE ground motions would reach about 2.5% rad. Thus, this study proposes that the representative story drift for State-HD is 2.5% rad.

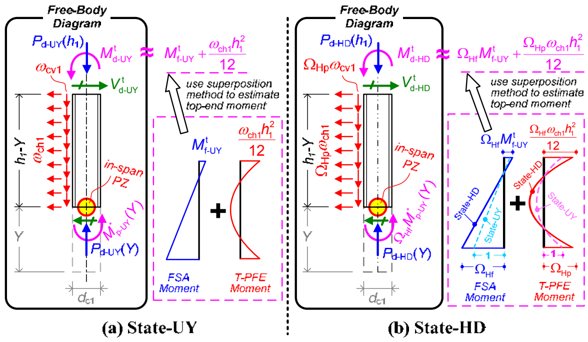

Fig. 3 Proposed methods to estimate shear forces and bending moments on the compressed bottom boundary column at State-UY and State-HD

When an SPSW is subjected to lateral forces, one side of the boundary columns will be tensioned while the other side will be compressed under the overturning action of the shear wall. For the tensioned bottom boundary column, the plastic hinge will only form at the bottom end. For the compressed one, except for an in-span plastic zone (PZ) which will inevitably form within the column height, there is a possibility that a plastic hinge (PH) will form at the top end.

Based on the occurrence and formation sequence of the plastic zones (Fig. 2), the inelastic responses of the compressed bottom boundary column can be classified into four main types:

(1) Type I: As shown in Fig. 2a, the in-span PZ forms during State-UY and the uniform yielding mechanism of the SPSW is fully developed. When the SPSW moves from State-UY to State-HD, no other plastic zone forms.

(2) Type II: As shown in Figs. 2b and 2c, the in-span PZ forms during State-UY and the uniform yielding mechanism of the SPSW is fully developed. In transitioning from State-UY to State-HD, the strain hardening effect causes a top-end PH (yielding in shear or moment) to form before entering State-HD.

(3) Type III: As shown in Figs. 2d and 2e, the top-end PH (yielding in shear or moment) forms before the formation of the in-span PZ. Afterwards, the bottom column behaves similar to a cantilever column subjected to lateral drift and panel forces. As the drift continues to increase, the in-span PZ forms soon after the hinging of the top end.

(4) Type IV: As shown in Fig. 2f, the top-end PH and in-span PZ forms prior to the completion of yielding of the infill panels and boundary beams in the upper stories. The soft-story mechanism takes place at the bottom of the SPSW.

This research proposed capacity design procedures to calculate the force demands on a compressed bottom boundary column in State-UY and State-HD. As illustrated in Fig. 3a, the superposition method is utilized to estimate the column bending moments in State-UY. The elevation ($y = y^*$) of the in-span plastic zone (PZ) can be estimated by solving the location at which the extreme State-UY moments occur in the lower half of the column. The shear force at the column top end in State-UY can be computed from the force balance of the free body diagram shown in Fig. 3a.

In order to determine the State-HD force demands, the factors Ω_{Hp} and Ω_{Hf} are introduced to estimate the strain-hardening effects on the member forces induced by panel forces and frame sway actions, respectively. The State-HD moment on the column can be estimated by the superposition method shown in Fig. 3b and the shear demand at the column top end can be calculated from the force balance of the free body diagram shown in Fig. 3b. The detailed procedures are presented in Tsai *et al*. (2014).

Experimental Program

There were three full-scale two-story SPSW specimens in this test program. All three specimens had the same center-to-center line dimensions. The wall span was 3420 mm and each story height was 3820 mm (as shown in Fig. 4a). All the infill plates had a thickness of 2.7 mm and were made of low yield strength (LYS) steel with a measured yield stress (F_{yp})of 220 MPa. All the specimens adopted identical top, middle, and bottom beams. The key differences among these specimens were the sizes of the boundary columns. All the boundary elements were made of A572 GR50 steel. The infill plates were welded at the edges to the boundary elements using 6 mm thick and 50 mm wide fishplate connection details. Details of reduced beam sections were adopted for the top and middle beams.

The three specimens were named NC (Normal Column), SC (Small Column), and WC (Weak Column). Fig. 5 shows the plastic mechanism of the three specimens predicted by the proposed design procedure. For Specimen NC, the top end of the bottom boundary column never yielded throughout the pushover responses. For Specimen SC, a top-end PH would occur after State-UY but before State-HD. For Specimen WC, the top end of the bottom column formed a plastic hinge before State-UY. The three specimens were designed to demonstrate three plastic behaviors in the bottom column. The details of specimen designs can be found in Li *et al*. (2014).

Fig. 4b shows the setup. A lateral support frame system was constructed in order to prevent the out-of-plane movement of the specimens. Cyclically increasing displacements were applied to the south column at the top beam elevation using two actuators. Both of these actuators were driven using the same displacement commands, each corresponding to two cycles of positive and negative roof drift ratios of 0.1%, 0.25%, 0.5%, 0.75%, 1%, 1.5%, 2%, 2.5%, 3%, 4%, and 4.5% rad. Before applying the cyclic lateral displacements, a vertical load of 10% of the column nominal axial yield capacity was applied at each column top using post-tension rods. These vertical column loads were maintained during the cyclic test.

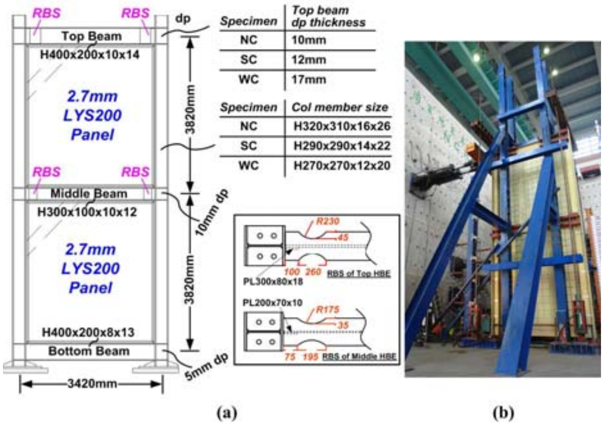

Fig. 4 (a) Test specimens and (b) test setup

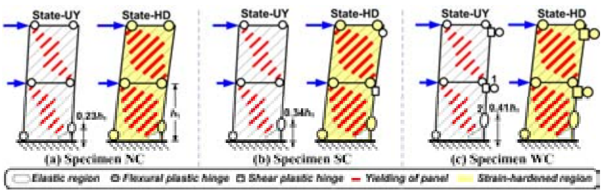

Fig. 5 Predicted plastic mechanism for specimens

Test Results and Design Implications

Fig. 6 shows the experimental cyclic force versus lateral drift relationships for the overall specimens and their second stories, and first stories. The peak experimental lateral forces were 1596, 1406, and 1327 kN for Specimens NC, SC, and WC, respectively. The test results show that the three specimens exhibited satisfactory ductile behaviors under cyclic loading, at least up to a roof drift of 4% rad. However, it should be noted that the first story (1F) columns in SC and WC developed lateral torsional buckling (LTB) at a roof drift of 3% and 2.5% rad., respectively. Nevertheless, the occurrence of LTB in the bottom column did not notably deteriorate the load carrying capacities of the specimens. Fig. 7 shows the conditions of the tested specimens. For SC and WC, the residual out-of-plane column deformations were evident.

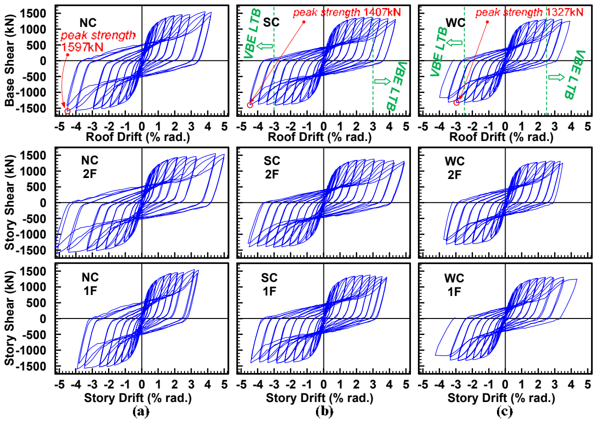

Fig. 6 Experimental cyclic force versus deformation for the three specimens

Fig. 7 Conditions of the tested specimens.

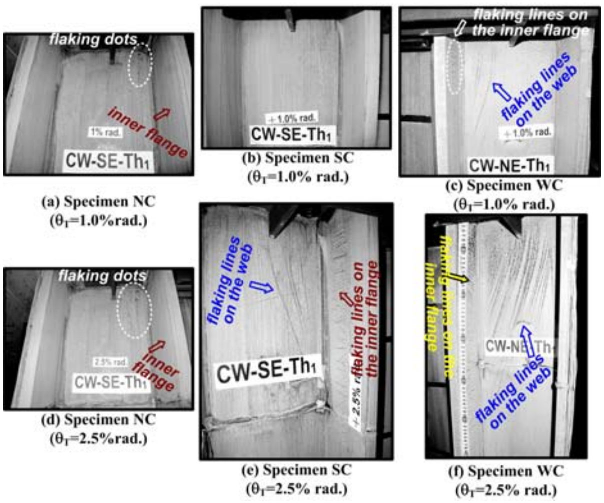

Fig. 8 Conditions of the top end of the bottom boundary columns for the three specimens at 1.0% and 2.5% rad. roof drift

Fig. 8 shows the conditions of whitewash flaking at the top end of the the bottom boundary columns of the specimens at different drift levels during the tests. At a roof drift θ_T = 1.0% rad., the top ends of the bottom boundary columns in Specimen NC (Fig. 8a) and SC (Fig. 8b) remained elastic while those in WC (Fig. 8c) slightly yielded. At θ_T = 2.5% rad., the bottom boundary columns' top ends in SC and WC developed slight yielding (Fig. 8e) and significant plastic hinges (Fig. 8f), respectively, whereas those in NC remained elastic. These responses show good agreement with the predictions made by the proposed design procedure. It can be found that the 1F story drifts in WC (Fig. 6c) were larger than those in SC (Fig. 6b) and NC (Fig. 6a) at each drift level, indicating that early yielding of bottom boundary columns' top ends would cause lateral deformation concentrated at the bottom of the SPSWs. Furthermore, in SC and WC, LTB of the bottom boundary columns was initiated after their top ends developed somewhat plastic rotations. This suggests that the formation of the top-end PH, which weakens the restraint at the column top end, could promote the development of LTB of the column.

Conclusions

This study proposed capacity design procedures for the bottom boundary column in SPSWs. Test results confirmed that the proposed method is effective in predicting yielding of the top end of a column. Test results also show that early yielding of the top end in the bottom column could result in a deformation concentration at the bottom of SPSWs and possibly promote lateral torsional buckling of the bottom boundary column.

References

Berman, J.W. and Bruneau, M., 2008. "Capacity Design of Vertical Boundary Elements in Steel Plate Shear Walls", *Engineering Journal (AISC)*, 15(1): 55-71.

Tsai, K.C., Li, C.H., Lin, C.H., Tsai, C.Y. and Yu, Y.J., 2010. "Cyclic Tests of Four Two-Story Narrow Steel Plate Shear Walls–Part 1: Analytical studies and specimen design". *Journal of Earthquake Engineering and Structural Dynamics (EESD)*, 39(7): 775-799.

Li, C.H., Tsai, K.C., Chang, J.T., Lin, C.H. Chen, J.C., Lin, T.H. and Chen, P.C., 2012. "Cyclic Test of a Coupled Steel Plate Shear Wall Substructure". *EESD*, 41(9):1277-1299.

Lin, C.H., Tsai, K.C., Qu, B., and Bruneau, M., 2010. "Sub-structural Pseudo-dynamic Performance of Two Full-scale Two-story Steel Plate Shear Walls". *Journal of Constructional Steel Research*, 66(12): 1467-1482.

Tsai, K.C., Li, C.H., and Lee, H.C., 2014. "Seismic Design and Tests of the Bottom Vertical Boundary Elements in the Steel Plate Shear Walls. Part 1: Design Methodology". *EESD*. (accepted)

Li, C.H., Tsai, K.C., and Lee, H.C., 2014. "Seismic Design and Tests of the Bottom Vertical Boundary Element in the Steel Plate Shear Walls. Part 2: Experimental Studies." *EESD*, (accepted)

NEESR-SG/NCREE International Collaborative Research on the Development of Self-Centering Steel Plate Shear Walls

Keh-Chyuan Tsai[1], Chao-Hsien Li[2], Kung-Juin Wang[3],
P. M. Clayton[4], D. M. Dowden[5], J. W. Berman[6], M. Bruneau[7]

蔡克銓[1]、李昭賢[2]、王孔君[3]、P. M. Clayton[4]、D. M. Dowden[5]、J. W. Berman[6]、M. Bruneau[7]

Abstract

An international collaborative research program between the Taiwan National Center for Research on Earthquake Engineering (NCREE) and a U.S. NEESR-SG team, composed of researchers from the University of Washington (UW) and University at Buffalo (UB), was conducted between 2012 and 2013 to develop a novel self-centering steel plate shear wall (SC-SPSW) system. This research leverages the strength and energy dissipating capabilities of steel plate shear walls (SPSWs) with self-centering technologies to reduce structural repair costs and loss of building functionality following an earthquake. Extensive experiments were conducted and consisted of three major components: (i) large-scale quasi-static testing of SC-SPSW subassemblies, (ii) quasi-static and shaking table testing of third-scale, three-story SC-SPSWs, and (iii) pseudo-dynamic testing of two full-scale, two-story SC-SPSWs at multiple seismic hazard levels. Major outcomes of these tests include: validation of the seismic performance of various SC-SPSW configurations, development of a new post-tensioned (PT) beam-to-column connection to eliminate frame expansion that is typical of self-centering systems, and recommendations for SC-SPSW design, detailing, and modeling.

Keywords: steel plate shear wall (SPSW), self-centering SPSW (SC-SPSW), seismic design, self-centering, post-tension (PT)

Introduction

In the past decade, many researchers have focused on developing a novel resilient lateral force resisting structural system. Significant advances have been made in research on steel plate shear wall (SPSW) lateral force-resisting systems as part of an awarded "George E. Brown, Jr. Network for Earthquake Engineering Simulation Research Small Group (NEESR-SG)" project entitled “Smart and Resilient Steel Walls for Reducing Earthquake Impacts”. This collaborative project comprised a team of researchers from the University of Washington (UW), University at Buffalo (UB), University of Illinois, and the Taiwan National Center for Research in Earthquake Engineering (NCREE). The primary goal of this research is to develop self-centering SPSWs (SC-SPSWs) for enhanced seismic performance.

The SC-SPSW system (Clayton *et al.*, 2012) combines the high strength, stiffness, and ductile energy dissipation of SPSW infill plates, with the recentering and damage-mitigating capabilities of post-tensioned (PT) rocking connections (Garlock *et al.*, 2007) as shown schematically in Fig. 1. The research on the new SC-SPSW system has included experiments on large-scale subassemblies, scaled

[1] Professor, Dept. of Civil Engineering, National Taiwan University, kctsai@ntu.edu.tw
[2] Assistant Researcher, National Center for Research on Earthquake Engineering, chli@ncree.narl.org.tw
[3] Technologist, National Center for Research on Earthquake Engineering, kjwang@ncree.narl.org.tw
[4] Assistant Professor, Dept. of Civil, Architectural and Environmental Engineering, Univ. of Texas at Austin
[5] Graduate Student Researcher, Dept. of Civil, Structural and Environmental Engineering, Univ. at Buffalo
[6] Associate Professor, Dept. of Civil and Environmental Engineering, Univ. of Washington
[7] Professor, Dept. of Civil, Structural and Environmental Engineering, Univ. at Buffalo

3-story systems, and a full-scale 2-story system.

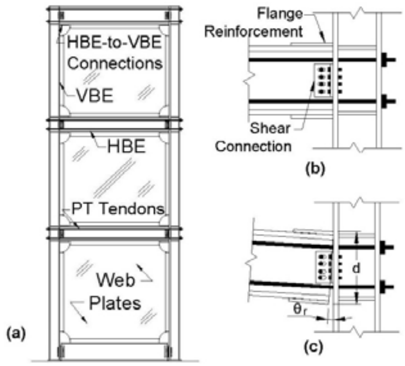

Fig. 1 Schematic of (a) a SC-SPSW and the flange rocking PT connection in its (b) undeformed and (c) deformed configuration

System Performance Objectives of SC-SPSW

The SC-SPSW system was developed to provide enhanced seismic performance. Performance objectives were proposed for earthquakes with a 50%, 10%, and 2% probability of exceedance in 50 years (denoted as 50/50, 10/50, 2/50 respectively). These performance objectives (POs) include:

1. *No connection decompression under wind or gravity loading.*
2. *System recenters and no repair required under frequent* (50/50) *earthquake demands.* Recentering is assessed using a residual drift limit of 0.2%, corresponding to out-of-plumb limits in construction. The no repair limit state requires that the web plate remains essentially elastic.
3. *System recenters and only web plate repair is required under design* (10/50) *earthquake demands.* The web plate may have significant yielding; however, the boundary frame and PT elements should remain elastic and the system should recenter. The damaged web plate can be replaced relatively quickly and simply, resulting in a rapid return to occupancy after an earthquake.
4. *Collapse prevention for the maximum credible earthquake* (2/50). Residual drifts and minor frame yielding may occur; however, soft-story mechanisms and significant PT and frame yielding should be avoided.

These performance objectives were incorporated into a performance-based seismic design (PBSD) procedure for the system. (Clayton *et al*., 2012)

Post-tensioned HBE-to-VBE Connections

In Fig. 1, the beams, also referred to as horizontal boundary elements (HBEs), and columns, also referred to as vertical boundary elements (VBEs), are connected via post-tensioning (PT) strands running horizontally from column to column, with horizontally slotted shear tabs to transfer shear forces. The PT HBE-to-VBE connection rocks open during lateral sway, as shown in Fig. 1(c), developing moment resistance as the PT strands elongate causing an increase in the compressive bearing flange force. If properly detailed, this rocking connection behavior eliminates the severe plastic deformation that occurs in the moment-resisting boundary frames of conventional SPSWs.

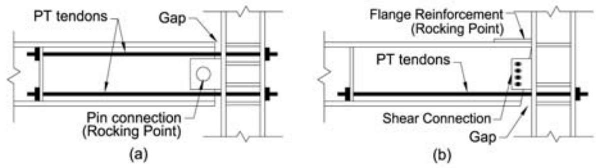

Fig. 2 (a) Centerline rocking and (b) NewZ-BREAKSS PT HBE-to-VBE connections

This PT connection, termed the flange-rocking (FR) connection, rocks about either the top or bottom flange depending on the direction of sway. The formation of gaps in the connections causes the columns to spread apart, which is termed frame expansion, and must be accommodated via special diaphragm detailing (Chou and Chen, 2011). As part of this research, two additional PT connections have been proposed to eliminate frame expansion while still providing recentering capabilities. These connections (shown schematically in Fig. 2) include one in which the beam rocks about its centerline via a pin, termed centerline (CL) connection, and one in which the beam rocks only about its top flange, termed NewZ-BREAKKS (NZ) connection (Dowden and Bruneau, 2011). In both of these connections, since frame expansion is not present, the PT strands must be terminated along the length of the beam to develop restoring forces during sway.

To ensure system recentering and elimination of damage in the boundary frame, the column base connection should also be detailed in such a way as to prevent axial-flexural hinging in the column. This can be accomplished with pin-clevis-type connections for smaller column demands (as shown later in Fig. 5 for the third-scale system test) or with FR-type PT rocking connections at the column base (as shown later in Fig. 6 for the full-scale pseudo-dynamic test).

Subassembly Testing in UW

The SC-SPSW subassembly tests (photo of a typical specimen shown in Fig. 3) were conducted at UW. These tests aimed at investigating the influence of various design parameters on intermediate HBE (the middle HBE in Fig. 3) and PT connection demands and global behavior. To simulate appropriate boundary conditions, an approximately half-scale, two-story specimen with FR-type PT beam-to-column connections was loaded with a single actuator at the top HBE. To accommodate frame expansion (as would be present in an intermediate story of a SC-SPSW with FR-type connections), a horizontal roller was provided at the base of the unloaded column (left column in Fig. 3), and a pin was provided at the base of the loaded column.

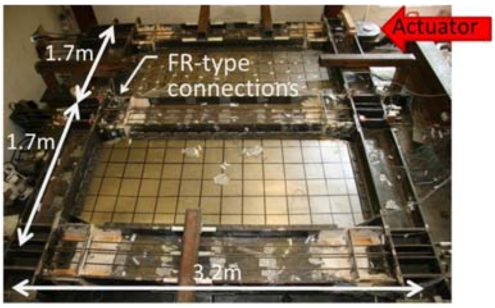

Fig. 3 Subassembly test set-up in UW

A total of 14 subassembly tests were conducted under quasi-static cyclic loading with increasing drift amplitudes of up to 5%. Parameters such as the web plate thickness, beam depth, number of PT strands per connection, initial PT force, methods of connecting web plate to boundary frame (welded versus bolted), and web plate-to-frame connection configuration (connected to beams and columns versus connected to beams only) were varied in these tests.

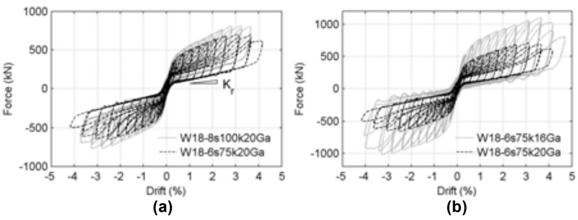

Fig. 4 Subassembly force versus drift responses comparing (a) number of PT strands and (b) web plate thickness.

Fig. 4 shows examples of specimen force versus drift responses comparing specimens with different numbers of PT strands (Fig. 4(a)) and different web plate thicknesses (Fig. 4(b)). The specimen naming scheme is as follows: beam depth (e.g. "W18" is a W18x106 wide-flange section), number of PT strands per connection (e.g. "6s" is six 13mm diameter Grade 270 seven-wire strands), initial PT force in units of kips (e.g. "100k" is equal to 445kN), followed by web plate gage thickness (e.g. "16Ga" is 1.52mm thick and "20Ga" is 0.91mm thick ASTM A1008 steel). These specimen response comparisons show that increasing the number of PT strands proportionally increases the unloading, or recentering stiffness, Kr, (Fig. 4(a)) and that increasing the web plate thickness increases the specimen strength and energy dissipation (Fig. 4(b)).

Third-scale System Testing in UB

Third-scale, three-story SC-SPSW specimens (Fig. 5) were tested under both cyclic (i.e. quasi-static) and shaking table (i.e. dynamic) loading at UB. A total of fifteen specimens were tested (nine cyclic tests, six shake table tests) with specimens having variations in type of PT HBE-to-VBE connection (e.g. FR, CL, and NZ types) and variations in web plate infill. The variations in web plate infill included specimens with no web plate (i.e. bare PT frame), full infill plate, and infill strips (i.e. diagonally-oriented strips of steel of the same thickness as the full infill plate). In each of these specimens, the column bases were connected to the foundation (e.g. strong floor or shaking table) via pin-clevis connections. Further details on this test program and results can be found in the reference (Dowden and Bruneau, 2014).

Fig. 5 Test set-up in UB for quasi-static third-scale system tests

Full-scale Pseudo-dynamic Testing at NCREE

Two full-scale, two-story SC-SPSW specimens (Fig. 6) were tested under pseudo-dynamic loading at NCREE. Both of the specimens utilized PT column base connections (FR-type connections) and had PT HBE-to-VBE connections at the middle and top beams, MB and TB respectively (the bottom beam, BB, used double-angle shear connections). The PT HBE-to-VBE connections were different for each specimen: Specimen FR used FR-type connections, while Specimen NZ used NZ-type connections. Other than the PT connection types, the specimens were physically identical. The specimens were loaded with two 1000 kN actuators at the top of the west column.

Both specimens were subjected to the same earthquake excitation representing seismic hazard levels with 50%, 10%, and 2% probability of exceedance in 50 years (50/50, 1050, and 2/50 respectively). The ground motions were selected from those developed for the SAC steel project (Somerville *et al.*, 1997) for the Los Angeles site.

The prototype building for the test specimens was a two-story adaptation of the three-story SAC building (Gupta and Krawinkler, 1999) in Los Angeles. The seismic mass for Specimen FR was taken as one quarter of the building's total seismic mass based on a reasonable yet less conservative design methodology (i.e. the specimen's design strength was estimated as the strength of the PT frame in addition to the strength of the web plate, whereas conventional SPSW and SC-SPSW design methodologies typically consider only the web plate lateral strength in design). The seismic mass of Specimen NZ was taken as 75% of that of Specimen FR due to the reduction in PT frame strength resulting from the initially decompressed NZ-type connections.

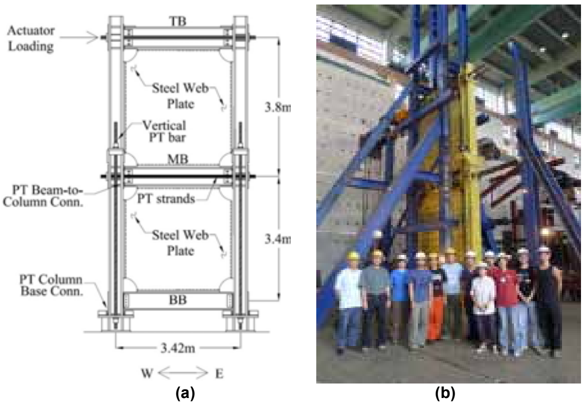

Fig. 6 (a) Specimen FR and (b) test setup at NCREE

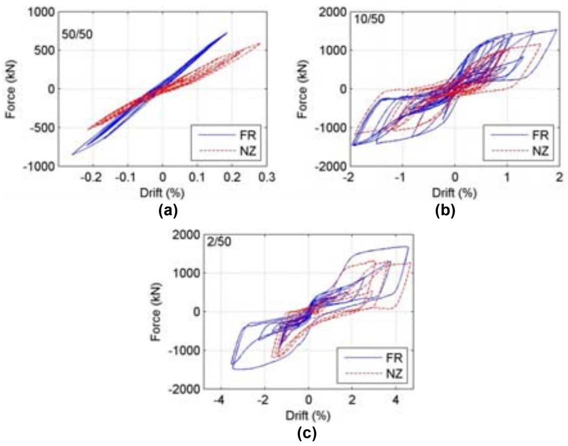

Fig.7 Force versus roof drift response for (a) 50/50, (b) 10/50, and (c) 2/50 tests

The force versus drift responses for Specimens FR and NZ during the 50/50, 10/50, and 2/50 pseudo-dynamic tests are shown in Fig. 7. Fig. 7(a) shows that during the 50/50 excitation, both specimens remained essentially elastic meeting the "no repair" performance objective (PO 2) described above. Fig. 7(b) shows that both specimens had peak drifts of less than the 2% code-based limit in the 10/50 event. During free vibration following the 10/50 excitation, the residual drifts of both specimens were less than 0.2%, indicating that each specimen was able to recenter and meet the "web plate repair only" performance objective (PO 3) described above.

During the 2/50 excitation shown in Fig. 7(c), both specimens had peak roof drifts of less than 4.7%. At the end of the 2/50 test for both specimens, only very minor localized yielding was found in the boundary frame near areas of stress concentration in the PT connections. Thus, both specimens were able to meet the "collapse prevention" performance objective (PO 4) at this hazard level. In this test, the web plates were not repaired or replaced following the 10/50 test prior to the 2/50 test; therefore, the drift demands in the 2/50 are more severe than would be expected in an actual 2/50 level earthquake where the SC-SPSW web plates would initially be undamaged and elastic.

Conclusions

Extensive experimental investigations have been conducted in multiple institutions in the US and in Taiwan to better understand the behavior and seismic performance of the SC-SPSW behavior. Subassembly cyclic tests investigated the impact of varying design parameters; third-scale cycle and dynamic system tests investigated the impact of different PT connect types and infill panel types; and full-scale pseudo-dynamic tests investigated seismic performance of SC-SPSWs utilizing two PT connection types that performed well in the previous scaled tests. A series of recommendations for SC-SPSW design, detailing, and modeling were developed based on the test results.

References

Clayton, P. M., Berman, J. W., and Lowes, L. N. (2012a). "Performance Based Design and Seismic Evaluation of Self-Centering Steel Plate Shear Walls". *Journal of Structural Engineering*. (*ASCE*), 138(1): 22-30.

Garlock, M. M., Sause, R., and Ricles, J. M. (2007). "Behavior and Design of Posttensioned Steel Frame Systems." *Journal of Structural Engineering*. (*ASCE*), 133(3): 389–399.

Chou, C.-C. and Chen, J.-H. (2011). "Seismic design and shake table tests of a steel post-tensioned self-centering moment frame with a slab accommodating frame expansion." *Earthquake Engineering and Structural Dynamics*. 40: 1240-1261.

Dowden, D., Bruneau, M., (2011) "NewZ-BREAKSS: Post-tensioned Rocking Connection Detail Free of Beam Growth." *AISC Engineering Journal*, 153-158.

Dowden, D., Bruneau, M., (2014) "Cyclic and Dynamic Testing of Self-Centering Steel Plate Shear Walls." *Proceedings of the 10th NCEE*, Anchorage, AK, USA.

Somerville, P., Smith, N., Punyamurthula, S., and Sun, J. (1997). "Development of ground motion time histories for phase 2 of the FEMA/SAC steel project." *SAC Background Document, Tech. Rep. SAC/BD-97/04*.

Gupta, A. and Krawinkler H. (1999). "Seismic demands for performance evaluation of steel moment resisting frame structures." *John A. Blume Earthquake Engineering Center, Stanford University, Stanford, CA, Tech. Rep. 132*.

Rapid Damage Assessment of Geotechnical Structures－Application of Close-Range Photogrammetry

Yung-Yen Ko[1] Jen-Yu Han[2] Jun-Yun Chou[3]

柯永彥[1]、韓仁毓[2]、周君芸[3]

Abstract

Regarding the fact that geotechnical structures tend to be damaged by natural disasters such as typhoons and earthquakes in Taiwan, this research aims to develop methods for rapid damage assessment of geotechnical structures. Because the failure sites of geotechnical structures are usually not easily accessible and direct measurements will be not possible in such situations, close-range photogrammetry, which gives accurate spatial information about an object at a certain distance, is utilized. For any object that is recorded in a pair of images from different viewpoints, its relative three-dimensional geometry can be reconstructed without ground control points using relative orientation between conjugate points in the image pair, along with a reference scale provided by any in situ object with a known length. Consequently, the local displacement and deformation of a geotechnical structure can be solved using this method and its damage state can be evaluated accordingly. A retaining wall, which was damaged in an ML = 6.5 earthquake in the middle of Taiwan, is chosen as a case study. Results show that the forward displacement on the top of the wall can be obtained using close-range photogrammetry based on the relative orientation between an image pair with good precision. Thus, the proposed method is verified to be applicable for the post-failure rapid reconnaissance of geotechnical structures.

Keywords: geotechnical structures, rapid damage assessment, close-range photogrammetry, image pair, relative orientation

Introduction

In Taiwan, typhoons and earthquakes are common natural disasters that tend to cause failures of geotechnical structures. This is because the heavy rainfalls brought by typhoons reduce the strength of soil material, and the inertial forces generated by earthquakes may damage structures. Consequently, there is much demand for rapid reconnaissance after these failures to assist in the emergency response.

The displacement and deformation of geotechnical structures are important for evaluating their damage state. However, it is sometimes difficult to approach the failure site of a geotechnical structure because there could have been no access originally or access could have been interrupted as failure occurred. In this case, the displacement and deformation cannot be closely observed and directly measured. Thus, indirect inspection techniques are required.

Close-range photogrammetry has been well developed over past years and is capable of giving useful spatial information about an object at a certain distance with satisfactory precision using a non-metric camera. Therefore, it can be applied in this situation.

In this research, close-range photogrammetry using the relative orientation technique was applied. This technique is designed to reconstruct the three-dimensional geometry of any object recorded in a pair of images from different viewpoints. Compared to classical photogrammetry based on the absolute orientation technique, this approach requires no ground control points and is particularly useful for rapid measurement of geotechnical structures in an inaccessible site. It requires a pair of partially

[1] Associate Researcher, National Center for Research on Earthquake Engineering, yyko@narlabs.org.tw
[2] Associate Professor, Department of Civil Engineering, National Taiwan University, jyhan@ntu.edu.tw
[3] PhD Student, Depart of Civil Engineering, National Taiwan University, d02521001@ntu.edu.tw

overlapping images taken from different exposure stations and a reference scale provided by any *in situ* object with a known length. Next, by identifying conjugate points in the image pair, their relative geometry in the object space can be uniquely solved.

In order to verify the feasibility of close-range photogrammetry using the relative orientation technique for the damage assessment of geotechnical structures, a retaining wall failure in an M_L = 6.5 earthquake in Nantou County in the middle of Taiwan was chosen for a case study. The wall and its backfill were separated as a result of shaking with a seismic intensity of up to CWB intensity V (80-250 gal) on the intensity scale of the Central Weather Bureau (CWB) of Taiwan. The forward displacement on the top of the wall was estimated using the proposed method with a pair of photographs that were taken on site and then compared to a direct tape measurement. The results will be presented later.

Close-Range Photogrammetry Using the Relative Orientation Technique

1. Concept of Relative Orientation:

By taking two photographs of the same scene from different viewpoints, a stereomodel can be created. To this end, the fact that the projected image rays through conjugate points (image points in an image pair that correspond to the same object point) will intersect in space is used to reconstruct the original epipolar geometry of the image pair. This procedure is known as relative orientation, and can be performed by adjusting the orientation elements of an analog stereoplotter, or by solving the orientation parameters by measuring corresponding image points.

Assuming that the interior orientation parameters of the images are known, each image still has six unknown exterior orientation parameters, which are three position parameters, (X_L, Y_L, Z_L), and three rotation parameters, (ω, ϕ, κ). Thus, for an image pair, there will be a total of twelve unknown parameters. These parameters can be solved by several approaches, such as dependent relative orientation and independent relative orientation.

As an example, in dependent relative orientation, six parameters of one image along with one position parameter of the second image are first fixed and then the remaining five parameters of the second image are still to be solved. As illustrated in Fig. 1, the six parameters of the first image are fixed if the model coordinate system is defined to be parallel to the coordinate system of the first image. The only fixed position parameter of the second image is used for the calculation of the model scale. Consequently, there will be two position parameters and three orientation parameters of the second image that remain to be determined (Mikhail *et al.*, 2001).

2. Coplanar Condition and Coplanarity Equation:

Fig. 2 illustrates a pair of partially overlapping images and a pair of conjugate image points. If the relative orientation of the two images has already been determined, then the two image rays defined by each image point and its corresponding perspective center will exactly intersect. The corresponding positions of these two image points in model space, which correlates to the object space but usually at a reduced scale, can be defined by this intersection (Mikhail *et al.*, 2001).

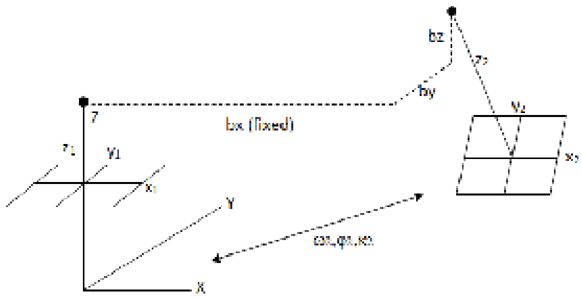

Fig. 1 Dependent relative orientation.

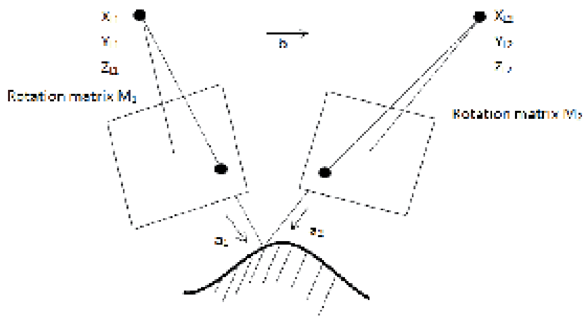

Fig. 2 Geometry of the coplanar condition.

The two image rays and the vector connecting the two perspective centers form a triangle, as shown in Fig. 2. The three sides of the triangle can be expressed as:

$$\bar{a}_1 = \begin{bmatrix} u_1 \\ v_1 \\ w_1 \end{bmatrix} = \frac{1}{k_1}\begin{bmatrix} X - X_{L1} \\ Y - Y_{L1} \\ Z - Z_{L1} \end{bmatrix} = \frac{1}{k_1} M_1^T \begin{bmatrix} x - x_0 \\ y - y_0 \\ -f \end{bmatrix} \quad (1)$$

$$\bar{a}_2 = \begin{bmatrix} u_2 \\ v_2 \\ w_2 \end{bmatrix} = \frac{1}{k_2}\begin{bmatrix} X - X_{L2} \\ Y - Y_{L2} \\ Z - Z_{L2} \end{bmatrix} = \frac{1}{k_2} M_2^T \begin{bmatrix} x - x_0 \\ y - y_0 \\ -f \end{bmatrix} \quad (2)$$

$$\bar{b} = \begin{bmatrix} b_X \\ b_Y \\ b_Z \end{bmatrix} = \begin{bmatrix} X_{L2} - X_{L1} \\ Y_{L2} - Y_{L1} \\ Z_{L2} - Z_{L1} \end{bmatrix} \quad (3)$$

where

$\vec{a}_1$ denotes the object space vector that forms the image point on the left image;

$\vec{a}_2$ denotes the object space vector that forms the image point on the right image;

$\vec{b}$ denotes the base vector, which is the displacement between the two perspective centers;

(X_{L1}, Y_{L1}, Z_{L1}) and (X_{L2}, Y_{L2}, Z_{L2}) are the position parameters of the left image and the right image, respectively;

(x_0, y_0, f) are the interior orientation parameters in the camera; and

M_1 and M_2 are the rotation matrices of the left image and the right image, respectively. For example, the elements of M_1 are functions of the rotation parameters (ω_1, ϕ_1, κ_1) and can be expressed as:

$m_{11} = \cos\phi_1 \cos\kappa_1$; $m_{12} = \cos\phi_1 \sin\kappa_1$; $m_{13} = -\sin\phi_1$;

$m_{21} = \sin\omega_1 \sin\phi_1 \cos\kappa_1 - \cos\omega_1 \sin\kappa_1$;

$m_{22} = \sin\omega_1 \sin\phi_1 \sin\kappa_1 + \cos\omega_1 \cos\kappa_1$;

$m_{23} = \sin\omega_1 \cos\phi_1$;

$m_{31} = \cos\omega_1 \sin\phi_1 \cos\kappa_1 + \sin\omega_1 \sin\kappa_1$;

$m_{32} = \cos\omega_1 \sin\phi_1 \sin\kappa_1 - \sin\omega_1 \cos\kappa_1$;

$m_{33} = \cos\omega_1 \cos\phi_1$

The triangle formed defines a unique plane and the relationship between the three vectors $\vec{a}_1$, $\vec{a}_2$, and $\vec{b}$ is called the coplanar condition:

$$\vec{b} \cdot (\vec{a}_1 \times \vec{a}_2) = 0 \tag{4}$$

This coplanarity equation can be used to determine the relative orientation between an image pair. As mentioned, this is usually achieved by fixing seven of the twelve orientation parameters and then solving for the remaining five.

3. Projective Geometry:

In dependent relative orientation, projective geometry can be used to reconstruct the original epipolar geometry of an image pair (Cheng, 2007). If a point m' is located on the right image, then its conjugate point m on the left image should be located on the epipolar line, of which the line equation can be expressed as:

$$l = Fm'^T = 0 \tag{5}$$

where F denotes the fundamental matrix (abbreviated as F-matrix hereafter) that describes the epipolar geometry of the image pair.

As $m \cdot l = 0$, the constraint of the epipolar geometry can be expressed as:

$$mFm'^T = 0 \tag{6}$$

If the interior parameters are known, a C-matrix containing the interior parameters can be defined as:

$$C = \begin{bmatrix} 1 & 0 & -x_0 \\ 0 & 1 & -y_0 \\ 0 & 0 & -f \end{bmatrix} \tag{7}$$

The F-matrix can be decomposed by the C-matrix and Eq. (6) can be rewritten as:

$$mFm'^T = mC^T ECm'^T = 0 \tag{8}$$

where E denotes the essential matrix (abbreviated as E-matrix hereafter).

If the vectors $\vec{a}_1$ and $\vec{a}_2$ in Eq. (1) and Eq. (2) are rewritten as:

$$\vec{a}_1 = \frac{1}{k_1} M_1^T \begin{bmatrix} 1 & 0 & -x_0 \\ 0 & 1 & -y_0 \\ 0 & 0 & -f \end{bmatrix} \begin{bmatrix} x \\ y \\ 1 \end{bmatrix} = \frac{1}{k_1} M_1^T C \begin{bmatrix} x \\ y \\ 1 \end{bmatrix} \tag{9}$$

$$\vec{a}_2 = \frac{1}{k_2} M_2^T \begin{bmatrix} 1 & 0 & -x_0 \\ 0 & 1 & -y_0 \\ 0 & 0 & -f \end{bmatrix} \begin{bmatrix} x \\ y \\ 1 \end{bmatrix} = \frac{1}{k_2} M_2^T C \begin{bmatrix} x \\ y \\ 1 \end{bmatrix} \tag{10}$$

$\vec{b}$ in Eq. (3) is modified into an skew-symmetric matrix K_b:

$$K_b = \begin{bmatrix} 0 & -b_Z & b_Y \\ b_Z & 0 & -b_X \\ -b_Y & b_X & 0 \end{bmatrix} \tag{11}$$

Thus, the coplanarity equation in Eq. (4) can be expressed as:

$$\begin{aligned} \vec{b} \cdot (\vec{a}_1 \times \vec{a}_2) &= \vec{a}_1 \cdot (\vec{b} \times \vec{a}_2) = \vec{a}_1^T K_b \vec{a}_2 \\ &= \begin{bmatrix} x_1 & y_1 & 1 \end{bmatrix} C^T M_1 K_b M_2^T C \begin{bmatrix} x_2 & y_2 & 1 \end{bmatrix}^T \end{aligned} \tag{12}$$

Upon comparison of Eq. (8) and Eq. (12), the E-matrix can be expressed as:

$$E = M_1 K_b M_2^T \tag{13}$$

The procedure for solving the relative orientation between a pair of images using projective geometry is as follows:

(a) According to dependent relative orientation, six orientation parameters of the left image, X_{L1}, Y_{L1}, Z_{L1}, ω_1, ϕ_1, and κ_1, and one orientation parameter of the right image, X_{L2}, are firstly fixed.

(b) Using Eq. (13) and the coordinates of the conjugate points in the image pair, the E-matrix can be obtained.

(c) Introducing the singular value decomposition technique (Faugeras and Luong, 2001) to decompose the E-matrix, the remaining five orientation parameters, Y_{L2}, Z_{L2}, ω_2, ϕ_2, and κ_2, can be determined, and the relative geometry between the two images can be solved.

(d) Using an object on the image pair with a known size in the object space and its observed size in the image space, the model scale from image space to object space can be computed, which can then be used to estimate the actual distance in the object space from the distance in the image space.

Case Study of a Retaining Wall Failure

On June 2, 2013, an M_L = 6.5 earthquake occurred in Nantou County, Taiwan. The seismic intensity in most areas of Nantou County reached CWB intensity V (80–250 gal) and a retaining wall at Lugu Junior High School was damaged as a result of this intense shaking. The retaining wall and its backfill were separated and a huge crack on its wing wall was induced, as shown in Fig. 3. If the top of the retaining wall had not accessible, then it would have been difficult to accurately estimate its forward displacement, which is important for the evaluation of the damage state of the retaining wall. Thus, this damage case was chosen to investigate the feasibility of the method proposed in the previous section for the damage assessment of geotechnical structures.

A pair of images as shown in Fig. 4 were first acquired in the field. A sufficient number of conjugate points (about twenty pairs) that were well distributed over the images were chosen to minimize the error. By applying the proposed procedure along with the minimum square method, all the relative coordinates of these conjugate points were solved. With the sizes of some of the objects in the images given (in this case, the height of the man and the depth of the unit segment of the wall), the displacement vector from point B to point A was calculated, and a 31.6-cm forward displacement was thus obtained. This value is close to the 30-cm tape measurement on the top of the retaining wall, as shown in Fig. 5.

Fig. 3 Retaining wall failure case in Lugu Junior High School (left: the crack on the wing wall; right: the separation of wall and backfill).

Fig. 4 Image pair for solving relative orientation of the retaining wall failure case.

Fig. 5 Tape measurement of forward displacement on the top of the retaining wall.

According to the results of the case study above, close-range photogrammetry using the relative orientation between an image pair has been demonstrated to be practical and gives a result that is accurate enough for the requirement of post-failure rapid reconnaissance.

References

Cheng, K.-W. (2007), Projective Geometry in Photogrammetry, MD Thesis, Department of Civil Engineering, National Taiwan University (in Chinese).

Faugeras, O.D. and Luong, Q.T. (2001), The geometry of multiple images, The MIT press, Cambridge, MA.

Mikhail, E.M., Bethel, J.S. and McGlone, J.C. (2001), Introduction to Modern Photogrammetry, John Wiley&Sons. Inc., New York.

Displacement Ductility Capacity of a Fixed-Head Pile in Cohesionless Soil

Jiunn-Shyang Chiou[1] and Yu-Ching Tsai[2]

邱俊翔[1]、蔡煜青[2]

Abstract

This study develops assessment formulas for the displacement ductility capacity of a fixed-head pile in cohesionless soil. The basic structure of these formulas is derived from an ideal model of a semi-infinite pile. This semi-infinite pile has bilinear moment-curvature properties in Winkler-type soils whose stiffness increases with depth (Gibson soil). In these formulas, the displacement ductility capacity of the fixed-head pile is explicitly expressed in terms of the pile-soil system parameters, which include the sectional over-strength ratio, curvature ductility capacity, and a modification factor for soil nonlinearity.

Keywords: Ductility capacity, piles, plastic hinge.

Introduction

Fixed-head piles usually experience a large flexural curvature demand at the pile head when subjected to large seismic loading since the pile head is restrained by a slab or a pile cap. In this case, it is more cost-effective to design piles as ductile structures that absorb earthquake energy instead of elastic structures, which are normally used in conventional design.

When the ductile behavior of a pile is considered in the design process, the displacement ductility capacity of the pile will be an important parameter. A strategy to prevent the piles from undergoing excessive plastic deformation during the maximum credible earthquake is to ensure that the displacement ductility capacity of the pile is sufficiently larger than the displacement ductility factor adopted in the ductility design. The displacement ductility capacity of a pile can be evaluated directly using a pushover analysis. However, this is burdensome in the preliminary design phase, since there are so many design parameters to be determined. Thus, simplified models and formulas have been developed for estimating the displacement ductility capacity more efficiently. Song et al. (2005) applied the concentrated plastic-hinge model to build an assessment model for the displacement ductility capacity of fixed-head piles. Budek and Benzoni (2008) simplified a fixed-head pile as a fixed-fixed column and apply the formula proposed by Priestley (1996) for the displacement ductility capacity of cantilever columns to precast, pre-stressed concrete piles.

In the above-mentioned studies, the curvature ductility capacity was considered a key parameter affecting the ductility capacity of a pile. However, Chiou et al. (2010, 2012) found that the over-strength ratio of a section (the ratio of ultimate moment to yield moment) is another important factor. In order to clearly identify the factors influencing the displacement ductility capacity of fixed-head piles, Chiou et al. (2011) adopted an ideal model of a semi-infinite nonlinear pile located in a soil having constant stiffness with depth in order to link the pile's displacement ductility capacity in cohesive soils to characteristics of the pile-soil system. For a pile in linear soil, the displacement ductility capacity is solely influenced by the curvature ductility capacity and the over-strength ratio of the pile section. A pile in nonlinear soil will have a larger displacement ductility capacity than a pile in linear soil because of the soil nonlinearity. There are large differences between the soil profiles of cohesive and cohesionless soil. This study aims to follow similar analysis procedures to derive assessment formulas for the displacement ductility capacity of a fixed-head pile in cohesionless soils and to compare them with those for cohesive

[1] Research Fellow, National Center for Research on Earthquake Engineering, jschiou@ncree.org.tw

[2] Head of Construction Section, Dept. of Transmission Line and Substation Projects, Taiwan Power Company

soils in order to investigate the influence of the soil profile.

Displacement Ductility capacity of a Long Pile

1. Pile in elastic soil

In order to derive the displacement ductility capacity of a pile, a simple ideal model is constructed as shown in Fig. 1(a). A semi-infinite pile with the fixed-head condition is embedded in a Winkler soil whose stiffness increases with depth. The sectional moment-curvature property of the pile is assumed to be a bilinear curve that is defined by a yield point (M_y, κ_y) and an ultimate point (M_u, κ_u), as shown in Fig. 1(c). The nonlinear sectional property of the pile can be characterized by its curvature ductility capacity μ_κ and over-strength ratio ω, which are defined as:

$$\mu_\kappa = \frac{\kappa_u}{\kappa_y} \tag{1}$$

$$\omega = \frac{M_u}{M_y} \tag{2}$$

Based on the model constructed above, the pile head, when subjected to lateral loading, will have the load-displacement response shape depicted in Fig. 1(c). Then, the displacement ductility capacity of the pile μ_Δ can be defined as

$$\mu_\Delta = \Delta_u / \Delta_y \tag{3}$$

where Δ_u is the ultimate displacement at the pile head when its moment reaches M_u and Δ_y is the yield displacement at the pile head when its moment reaches M_y.

Through theoretical derivation, the displacement ductility capacity can be expressed as

$$\mu_\Delta = \omega + 0.6825\frac{\eta}{\lambda}(1-\frac{1}{\omega})(\mu_\kappa - \omega) \tag{4}$$

where λ is the coefficient between the ultimate pile-head shear and moment, defined as $H_u/(1.088M_u)$, and η is the characteristic coefficient of the linear pile-soil system, which is defined as

$$\eta = \sqrt[5]{\frac{n_h}{EI}} \tag{5}$$

where E_s is the subgrade reaction modulus and EI is the elastic flexural rigidity of the pile.

From Eq. (4), it can be clearly seen that the ratio η/λ, the over-strength ratio ω, and the curvature ductility capacity μ_κ are the factors that influence the displacement ductility capacity of the pile. Since λ can be theoretically related to η, Eq. (5) is further reduced as

$$\mu_\Delta = \frac{-0.226\omega + \sqrt{\omega^2 + 1.057(\omega - 1)(\mu_\kappa - \omega)}}{0.774} \tag{6}$$

From Eq. (6), it is interesting to note that the ductility capacity of a pile in linear soil is purely related to the over-strength ratio and curvature ductility capacity of the pile section.

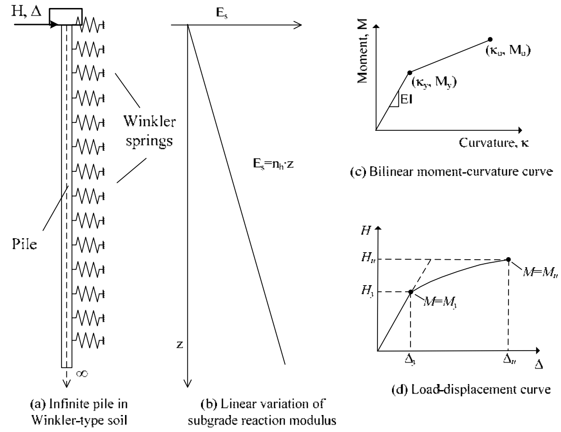

Fig. 1 Ideal model

2. Pile in Nonlinear Soil

When the pile is in the nonlinear soil, the soil may enter a nonlinear state during lateral loading. The degree of soil nonlinearity depends on the degree to which the pile displacement exceeds the soil yield displacement. Since Eq. (4) is derived for a pile embedded in linear soil, its formulation must be modified. Applying a modification approach similar to that of Chiou et al. (2011), a parameter α is introduced to modify Eq. (6) as follows.

$$\mu_\Delta = \omega + \alpha(-\omega + \sqrt{\omega + \mu_\kappa(\omega - 1)}) \tag{7}$$

where the parameter α is a modification factor that is displacement-dependent due to the degree of soil nonlinearity. Since it does not have a theoretical value, the following section will adopt a statistical approach to build an empirical relationship for α from a series of pushover analysis data.

Determination of α value

In this section, we will conduct a number of nonlinear pushover analyses based on full pile-soil models to determine the parameter α.

1. Analysis model and parameters

The analysis cases assume a fixed-head pile of length 25m embedded in cohesionless soil as shown in Fig. 2. The Winkler-beam model is applied to analyze the pushover curves for different specified parameters of the pile-soil system, while considering the nonlinearity of the pile and the soil. The Winkler-beam model uses the beam elements to simulate the pile and adopts a series of independent springs to model the soil reactions. As shown in Fig. 1(c), the moment-curvature response of the pile section is assumed to be a simplified bilinear curve. The nonlinear behavior of the pile is simulated by the distributed plastic hinge model. In this model, many plastic hinges are distributed along the pile shaft in order to simulate the plasticity propagation in the pile. For a detailed description of this model, one can refer to Chiou et al. (2009b). The American Petroleum Institute (API) sand model is adopted for the nonlinear *p-y* relationship for the cohesionless soil, as shown in Fig. 3.

Based on the above model, the analysis parameters for a pushover analysis include the pile diameter D, the axial load level $P/(f_c'A_g)$, the over-strength ratio ω, the curvature ductility capacity μ_κ, and the relative density D_r. Note that the axial load level $P/(f_c'A_g)$ is varied to change the flexural rigidity of the pile.

Based on the defined analysis parameters, the pushover analyses are performed to obtain the pile-head pushover curves. The displacement ductility capacities for all cases can be determined from the analyses accordingly.

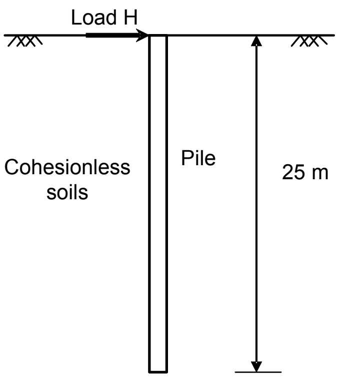

Fig. 2. Pile-soil model for case analyses

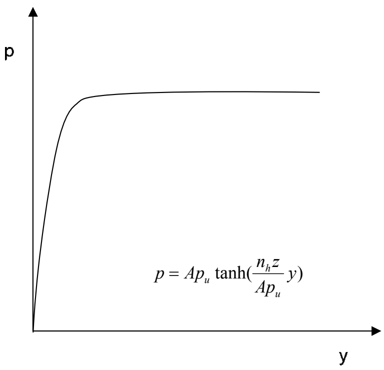

Fig. 3. *p-y* model for cohesionless soils

2. Empirical relationship of α

The displacement ductility capacity values from the pushover cases are substituted into Eq. (7) to compute the associated α values. A non-dimensional relationship of α versus Δ_u/y_y is constructed as shown in Fig. 4, in which Δ_u is the pile-head ultimate displacement and y_y is the soil effective yield displacement. Based on the *p-y* curve at a depth equal to one diameter, the parameter y_y is defined to be the *y*-coordinate of the intersection of the extension of the initial portion of the curve and its ultimate soil reaction, as shown in Fig. 5. A trend line as Eq. (8) is added to Fig. 4 to fit the data points.

$$\alpha = 1.05(\Delta_u / y_y)^{0.265} \tag{8}$$

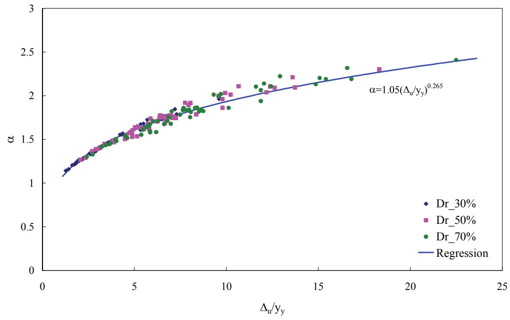

Fig. 4. α versus Δ_u/y_y

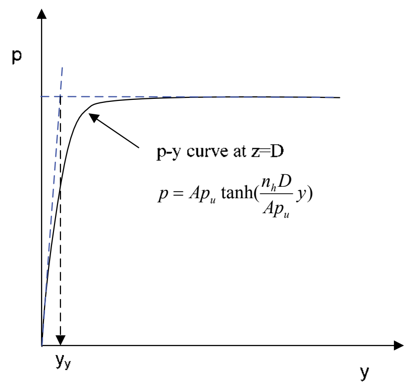

Fig. 5. Definition of effective yield displacement

Discussions

In this section, the formulas developed in this study are compared with those derived for a pile in cohesive soils. According to Chiou et al. (2011), for a pile in cohesive soils, the displacement ductility capacity for the case of a linear soil whose subgrade reaction modulus is constant with depth can be expressed as follows:

$$\mu_\Delta = \sqrt{\omega + \mu_\kappa(\omega - 1)} \tag{9}$$

Comparing Eqs. (6) and (9) shows that the displacement ductility capacity of the pile is independent of the soil stiffness, but is influenced significantly by the profile of soil stiffness with depth. Fig. 6 displays two relationships of μ_Δ versus ω, constructed based on Eqs. (6) and (9) for μ_κ=16. From this figure, it can be seen for linear soils a pile in cohesionless soil has a 1.1-1.2 times larger ductility capacity than a pile in cohesive soil does.

When the soil is nonlinear, the α values for cohesionless soils are between 1.2 and 2.5. According to Chiou et al. (2011), for cohesive soils, the values based on the Matlock clay model are, on average, between 1.8 and 2.5. The soil nonlinearity in cohesionless soils has less of an influence on the pile ductility capacity than in cohesive soils. However, as a whole, the pile in cohesionless soils has a slightly larger ductility capacity than in cohesive soils because it has a much larger pile ductility capacity in linear soil.

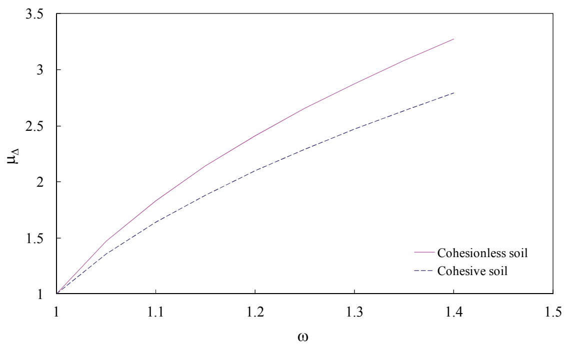

Fig. 6. Relationships of displacement ductility capacity vs. over-strength ratio for cohesionless and cohesive soils in the case of linear soil

Conclusions

The objective of this study was to derive simple formulas based on an ideal model of a semi-infinite nonlinear pile embedded in a Gibson soil in order to assess the displacement ductility capacity of a fixed-head pile in cohesionless soil. The structure of the formulas is similar to that of the formulas for cohesive soils. The parameters used in the formulas include the curvature ductility capacity and the over-strength ratio of the pile section, as well as a modification factor for the case of nonlinear soil. Since the formulas are dependent on the distribution of soil stiffness, it is useful for engineering practice to develop similar formulas for other types of soil stiffness distributions.

References

American Petroleum Institute (API). (2000). “API recommended practice for planning, design, and constructing fixed offshore platforms-working stress design.” Rep. RP-2A-WSD.

Budek, A.M., and Benzoni, G. (2008). “Rational seismic design of precast, prestressed concrete piles.” PCI Journal, 53(5), 40-53.

Chiou, J. S., and Chen, C. H. (2010). “Displacement ductility capacity of fixed-head piles.” Proc., 5th Int. Conf. on Recent Advance in Geotechnical Earthquake Engineering and Soil Dynamics, Paper No. 9-10.

Chiou, J.S., Tsai, Y.C., and Chen, C.H. (2011). “Simple estimation for ductility capacity of a fixed-head pile in cohesive soils.” Canadian Geotechnical Journal, 48(10), 1449–1460.

Chiou, J.S., Tsai, Y.C., and Chen, C.H. (2012). “Investigating influencing factors of the ductility capacity of a fixed-head reinforced concrete pile in homogeneous clay.” Journal of Mechanics, 28(3), 489–498.

Chiou, J.S., Yang, H.H., and Chen, C.H. (2009b). “Use of plastic hinge model in nonlinear pushover analysis of a pile,” Journal of Geotechnical and Geoenvironmental Engineeering, 135(9), 1341-1346.

Priestley, M.J.N., Seible, F., and Calvi, G.M. (1996). Seismic Design and Retrofit of Bridges, Wiley-Interscience, New York.

Song S.T., Chai, Y. H., and Hale, T. H. (2005). “Analytical model for ductility assessment of fixed-head concrete piles,” Journal of Structural Engineering, 131(7), 1051-1059.

Numerical Analysis of a Residual Heat Removal Piping System Subjected to Seismic Loading

Ming-Yi Shen[1], Zih-Yu Lai[2], Juin-Fu Chai[3], Fan-Ru Lin[2], Yin-Nan Huang[4], Wen-Fang Wu[5], Ching-Ching Yu[6] and Yan-Fang Liu[7]

沈明毅 [1]、賴姿妤 [2]、柴駿甫 [3]、林凡茹 [2]、黃尹男 [4]、吳文方 [5]、游青青 [6]、劉嚴方 [7]

Abstract

The objectives of this study are to build a credible numerical model using SAP2000 for fragility analysis of a Residual Heat Removal (RHR) piping system, and to establish the load pattern of a cyclic loading test to identify the seismic vulnerability of the system. The RHR piping system selected for testing and numerical analysis was duplicated from a part of the RHR system in a nuclear power plant (NPP) in Taiwan, and this part is distributed between the floor of the reactor building (RB) and the wall of the reinforced concrete containment vessel (RCCV) of the sample NPP.

The numerical model for the sample RHR piping system was developed, and a nonlinear time series analysis was conducted using input motions compatible with the floor response spectrum at the anchor points of the sample piping system subjected to a Safe Shutdown Earthquake (SSE). Based on the distribution of resultant inertial forces and the responses at critical locations of the piping system under an SSE, the magnitudes and locations of the equivalent concentrated static loads were determined and used in the pushover analysis to estimate the capacity of the RHR piping system. The numerical results will be verified by the aforementioned cyclic loading test. More studies are under way including shaking table tests and fragility analyses for the sample piping system to identify the seismic performance and risks associated with the system further.

Keywords: RHR piping system, numerical analysis, time series analysis

Introduction

The main functions of residual heat removal (RHR) system include providing cooling water to the reactor core if a loss of coolant accident (LOCA) happens, spraying water into the containment, removing heat from the core, reducing the temperature of the suppression pool, and cooling typical components of the core after shutdown. These functions are based on a multiple use system of a RHR system with modes of operation for low-pressure flooder (LPFL), containment spray (CS), suppression pool cooling (SPC), shutdown cooling (SDC), and AC independent water addition (ACIWA). An ACIWA system has to provide a long-term water feed to reactors during a station blackout out (SBO) condition until power recover. The failure of the ACIWA system would cause core damage in some accident sequences and to avoid this situation, the piping system has to remain functional and integrated as seismic events occur.

This study aims at determining a load pattern acting on the selected RHR piping system which has been designed to comply with the ASCE code for a quasi-static cyclic loading test to reflect the response of pipelines and their components. This study also aims to estimate the seismic capacity of the RHR piping system under strong ground motion. The design

[1] Research Assistant, National Center for Research on Earthquake Engineering
[2] Assistant Researcher, National Center for Research on Earthquake Engineering
[3] Researcher, National Center for Research on Earthquake Engineering, chai@narlabs.ort.tw
[4] Assistant Professor, Department of Civil Engineering, National Taiwan University
[5] Professor, Department of Mechanical Engineering, National Taiwan University
[6] Graduated Student, Department of Civil Engineering, National Taiwan University
[7] Graduated Student, Department of Mechanical Engineering, National Taiwan University

of a RHR piping system should meet the requirements of the ASME boiler and Pressure Vessel Code, Section III, Division 1, Subsection NB/NC/ND [1] limits. The service limits of the piping system are defined in the subsection NCA-2000 [1] under four expected performance level. The level A service limits are that the component or support remains performance of its specified service function when subjected to level A service loadings. Under the level B service limits, the component or support must withstand the level B service loadings (ex: operating basis earthquake, OBE) with no damage. The level C service limits subjected to level C service loadings permit large deformations in areas of structural discontinuity to prevent the significant loss of structural integrity and it is necessary that the component or support has to remove for inspection or repair. The level D service limits permit gross general deformations with some consequent loss of dimensional stability and damage requiring repair under the level D service loadings (ex: safe shutdown earthquake, SSE).

The Selected RHR Piping System

The RHR piping system selected for the test and numerical analysis is based on the accident sequence presented in Fig. 1 [2]. Under the SBO condition, the RCIC provides core cooling for 8 hours as designed. Subsequently, the reactor is depressurized to permit the ACIWA to inject water supplied by cooling pond and water tanks into the reactor. According to the aforementioned sequence, the ACIWA which is a mode of the RHR system fails which consequently results in core damage.

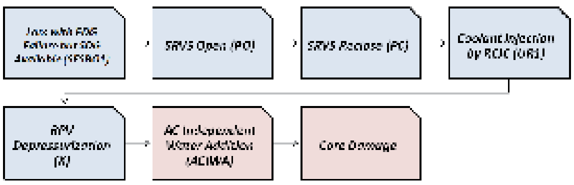

Fig. 1 Accident Sequence [2]

In this paper, the sample piping system as shown in Fig.2 is duplicated from a part of the RHR system and this part is distributed from the attachment on the floor of the reactor building (RB) to the penetration through the wall of the reinforced concrete containment vessel (RCCV).

Ideal piping analysis models should run from one structural anchor to the next, but it is quite difficult to achieve this in application. In general, instead of a real anchorage point, the boundary of an established model has to include at least three changes of direction and two seismic supports in each of the three orthogonal directions. The isometric drawing of the sample piping system is shown in Fig. 3. In addition to the straight pipeline, the selected part consists of elbows, a reducer and a flange, a motor operated valve (MOV), and a spring hanger. The Nodes 15, 17, 18 and 21 are supported by adjustable pipe saddle supports with U-bolts and the Node 13 is supported by the pipe saddle with a strap.

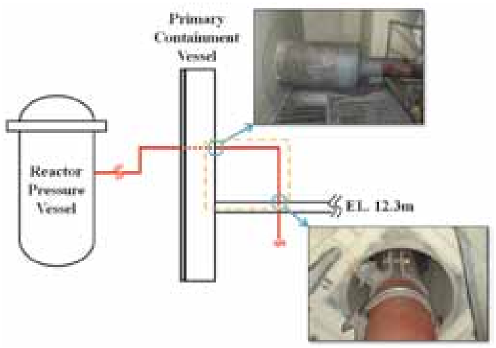

Fig. 2 Location of the sample piping system

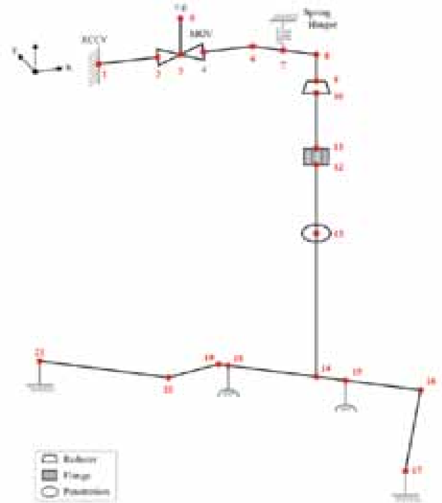

Fig. 3 Isometric drawing of the piping system

Input Motions

The input motions (named #82 and #1726) for a nonlinear time series analysis were derived for the node located on the floor of the RB using a lumped mass model of the sample NPP subjected to an SSE [2]. Fig. 4(a) and 4(b) are the time series of the input motions, and both are compatible with the required floor response spectrum (FRS) as shown in Fig. 4(c).

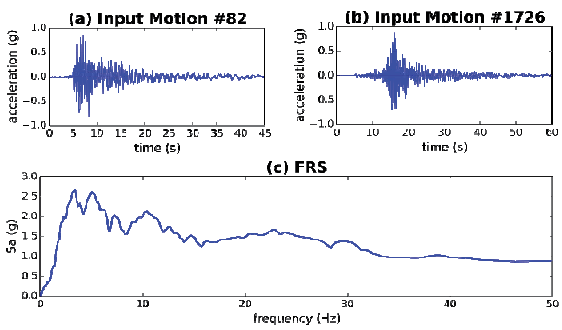

Fig. 4 (a) Input motion #82 (b) Input motion #1726 (c) FRS

Numerical Models and Their Boundary Conditions

The 3D finite element models of the piping system were developed by SAP2000 [3] to preliminary simulate the nonlinear response of the piping system subjected to strong ground motion. The numerical model for elbows, a reducer, a flange, and a spring hanger for the sample piping system were properly simplified. The elbows were modeled using two straight continuous elements with specified pipe sections. For SAP2000, the reducer connecting two pipe sections was modeled by the non-prismatic frame section with properties varying along the section axis, and the properties were determined from component test results [4]. The flange was modeled by a link element with self-weight and its stiffness ($k_{bending}$ = 40000 KN/m) determined from the strong cyclic loading test results [4]. The axial stiffness of the spring hanger modeled by a link element was found to be 531.32 KN/m. The MOV was modeled by rigid link element with self-weight (W_{MOV} = 15.93 KN) applied on the center of mass due to the much larger stiffness of MOV body compared to that of the pipes.

Fig. 5(a) is the finite element model of the sample piping system that is developed based on the aforementioned details and the original drawing. The response of the sample piping system can be simulated well by this model. However, the complexity of the piping geometry may cause difficulties in the following cyclic loading test and shaking table test. Therefore, a simplified model as shown in Fig. 5(b) was built to decrease the complexity of the piping system and to predict the seismic weakness of the selected part of the piping system.

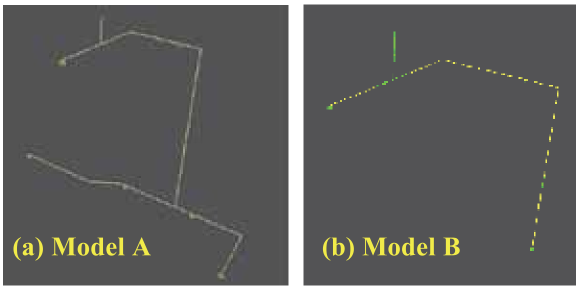

Fig. 5 Numerical models. (a) Model A (Original) (b) Model B (Simplified).

Seismic Analysis of the Piping System

Fig. 6 shows the distribution of the internal shear force and moment of the simplified model under 2D input motions at the time step as when the maximum shear/moment occurred. Due to the large mass and the associated inertia force of the MOV, the straight pipe connecting to the shield wall of the RCCV suffered larger shear forces and moments, and Node 1 is the most critical location in the sample piping system. It can be observed in Table 1 that the member that suffered maximum shear/moment of the piping system still remained elastic under the SSE.

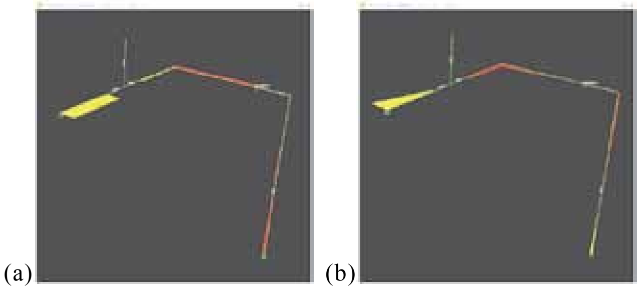

Fig. 6 Maximum internal force and moment diagram during input motion #82. (a) shear force V3, (b) moment M2.

Table 1 The maximum shear force, moment, and torsion in the piping system

Shear force in the straight pipe (KN)		
V_{max}	V_n	V_{max} / V_n
27.38	1201.97	0.02
Moment in the straight pipe (KN-m)		
M_{max}	M_n	M_{max} / M_n
33.30	328.65	0.10
Torsion in the straight pipe (KN-m)		
T_{max}	T_n	T_{max} / T_n
15.22	489.04	0.03

Static Load Pattern and Pushover Analysis

Based on the distribution of resultant inertial forces and the responses at critical locations of the piping system under SSE (as shown in Fig. 6), four equivalent concentrated static loads were determined. As shown in Fig. 7, the concentrated loads were applied on the MOV with a magnitude of 1562.5 kgf (15.33 KN) and 2500 kgf (24.53 KN) in the global *X*- and *Y*- directions, respectively, on the elbow with a magnitude of 500 kgf (4.91 KN) in the axial direction of the pipe, and on upper part of the flange with a magnitude of 400 kgf (3.92 KN) in the global-*Y* direction.

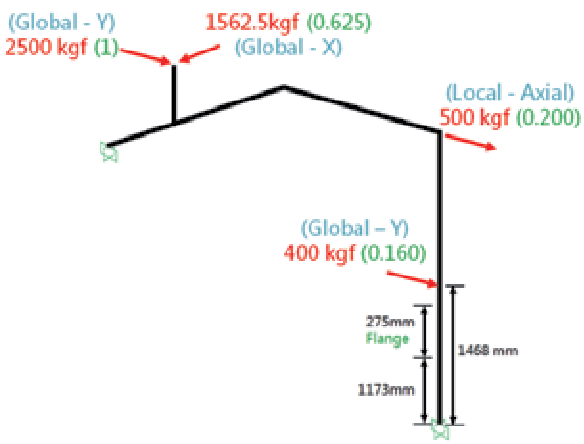

Fig. 7 The load pattern for the cyclic loading test

Fig. 8 depicts the comparison of the distribution of shear/moment responses under concentrated static loads and the time series analysis results under input motion #82. It can be seen that the internal force and moment distributions under static loads are quite similar to those under dynamic loading.

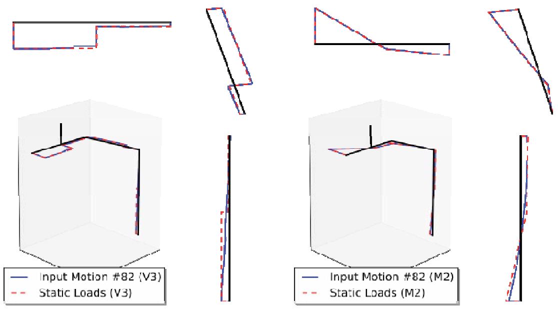

Fig. 8 The comparison of (a) shear and (b) moment distribution under static loads and input motion #82

Fig. 8 shows that the load pattern acting on the simplified model can simulate the dynamic response under the SSE well. Thus, it implies that the pushover analysis with the proposed load pattern can estimate the seismic capacity of the piping system with high reliability. Fig. 9 shows the performance curve corresponding to the pushover analysis, where the vertical axis is the total sum of reaction forces at Nodes 1, 7 and 13, and the horizontal axis is the displacement at the MOV. It can be observed that the first yielding point occurs as the straight pipe connecting to the shield wall yields, and the next yielding is caused by the elbow connecting two horizontal pipelines (i.e. Node 6). The performance point for the SSE is still in the elastic range with a ductility ratio of only 0.15.

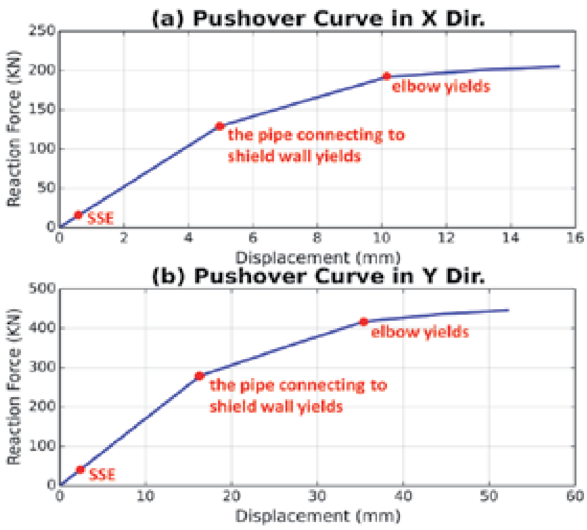

Fig. 9 The pushover curves of the simplified model (a) in the x direction and (b) in the y direction.

Conclusions

Based on the numerical analysis in this study, the member that suffers maximum shear/moment of the sample piping system is the straight pipe section between the MOV and the fixed end anchored at the shield wall of the RCCV, and it continues to remain elastic under an SSE. The magnitudes and applied locations of the equivalent concentrated static loads were determined based on the distribution of resultant inertial forces and the responses at critical locations of the sample piping system under an SSE. The seismic capacity of the piping system is adequate to resist an SSE within an acceptable margin.

In recent research progress, an actual test setup is established for the following cyclic loading tests as shown in Fig. 10. In addition, more studies are under way including shaking table tests and fragility analysis for the sample piping system to identify the seismic performance and risks associated with the system further. Moreover, the results of the numerical analysis and the cyclic loading test will be compared with the shaking table test in the future.

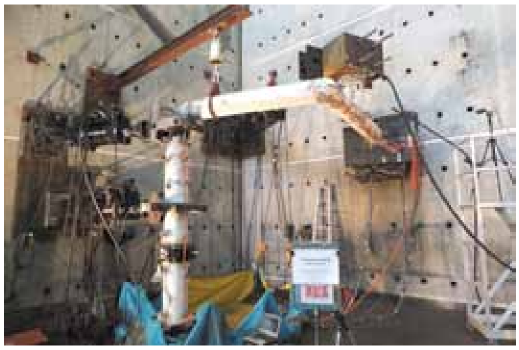

Fig. 10 Actual test setup of the cyclic loading test

References

1. ASME Boiler & Pressure Vessel Code, (2007). Rules for Construction of Nuclear Facility Components. Section III.
2. Shen, Y.-H., Chang, C.-C., & Huang, Y.-N. (2013). Seismic Probabilistic Risk Assessment of Nuclear Power Plants Using Response-Based Fragility Curves. Conference on Structural Mechanics in Reactor Technology, Division VII, San Francisco, California, USA.
3. SAP2000 (2004). Linear and Nonlinear Static and Dynamic Analysis and Design of Three-Dimensional Structure. v9, Computers and Structures, Inc. Berkeley, California, USA.
4. Lai, Z. Y., Chai, J. F., Lin, F. R., Huang Y. N., Wu, W. F., Liu, Y. F., Yu, C. C., & Shen, M. Y. (2014). Cyclic Loading Test and Numerical Analysis of Flange Joint and Reducer of RHR Piping Systems. Pressure Vessel and Piping Conference, ASME, PVP2014-29112, Anaheim, California, USA.

Seismic Probabilistic Risk Assessment of Nuclear Power Plants Using Response-Based Fragility Data

Yin-Nan Huang [1], Ying-Hsiu Shen [2], and Chang-Ching Chang [3]

黃尹男 [1]、沈盈琇 [2]、張長菁 [3]

Abstract

Seismic probabilistic risk assessment (SPRA) has been widely used to compute the frequencies of core damage and release of radiation of nuclear power plants (NPPs). In 2011, Huang et al. published a SPRA methodology with the following characteristics that are different from the widely used Zion method: (a) seismic fragility curves are defined as a function of structural response parameters, such as floor spectral acceleration and story drift; (b) nonlinear response-history analysis is used to estimate statistical distributions of seismic demands for structural and non-structural components of NPPs; and (c) Monte Carlo simulation is used to determine damage states of structural and non-structural components. In the study, the seismic risk of a sample NPP was evaluated using the methodology proposed by Huang et al. (2011a, 2011b). The seismic risk was quantified using the annual frequency of unacceptable performance defined by a sample accident sequence for a sample NPP. The values of seismic risk computed using the methodology proposed by Huang et al. (2011a, 2011b) and Boolean algebra were compared to evaluate the accuracy and efficiency of the methodology of Huang et al. The two procedures generated similar risk values and the methodology stated by Huang et al. was found to be more efficient than the procedure that uses Boolean algebra.

Keywords: Seismic probabilistic risk assessment, seismic fragility curves, seismic hazard curves, Monte Carlo simulation

Introduction

In 1991, the United States Nuclear Regulatory Commission (USNRC) issued Supplement 4 to Generic Letter No. 88-20 (USNRC, 1991) requiring nuclear power plant (NPP) utilities to perform an Individual Plant Examination of External Events (IPEEE) and also issued NUREG-1407 (Chen et al., 1991) to help guide the IPEEE. For an Individual Plant Examination (IPE) of seismic events, NUREG-1407 identified Seismic Probabilistic Risk Assessment (SPRA) as an acceptable methodology for the examination of earthquake-induced risks. SPRA provides a formal process in which the randomness and uncertainty in seismic input, structure response and material capacity are considered in the computation of risk. NUREG/CR-2300 (USNRC, 1983) provides general guidance for performing SPRA for NPPs. The guideline describes two SPRA methods: (1) Zion and (2) the Seismic Safety Margin (SSM). Recently, Huang et al. (2011a, 2011b) proposed a new SPRA methodology, which is based on the conventional methods described above and the new tools developed for the next-generation performance-based earthquake engineering (ATC, 2012, Yang, 2009). The method proposed by Huang et al. (2011a, 2011b) differs in many regards from methods used to date for the probabilistic risk assessment of NPPs. Key differences include 1) the use of component fragility curves that are expressed in terms of structural responses (e.g., story drift and peak floor acceleration) and not on ground-motion intensity (e.g., peak ground acceleration (PGA)), 2) the characterization of earthquake shaking using seismic hazard curves, and 3) procedures for both scaling earthquake ground motions and assessment of component damage.

In the study presented herein, the seismic risk of a sample NPP was evaluated using the methodology

[1] Assistant Professor, Department of Civil Engineering, National Taiwan University, ynhuang@ntu.edu.tw
[2] Research Assistant, National Center for Research on Earthquake Engineering, yhshen @narlabs.org.tw
[3] Assistant Researcher, National Center for Research on Earthquake Engineering, ching@narlabs.org.tw

proposed by Huang et al. (2011a, 2011b). The seismic risk was defined as the annual frequency of the event represented by the sample accident sequence. The risk was also computed using conventional Boolean algebra and compared with the results using the proposed methodology. The advantages and disadvantages of these procedures are also discussed.

SPRA Methodology Proposed by Huang et al. (2011a, 2011b)

The SPRA methodology proposed by Huang et al. (2011a, 2011b) includes five steps. Step 1 of the methodology performs a plant system analysis of a NPP to establish the accident sequences that could result in target unacceptable performance, such as core damage and large early release of radiation. The event trees and fault trees associated with the identified accident sequences are developed. The fragility curves for structural and non-structural components included in the identified accident sequences are developed in terms of structural response parameters. Step 2 develops the mean seismic hazard curve for the NPP site and divides the curve into 8 equal intervals. Acceleration histories of ground motions are selected and scaled for each intensity level. Step 3 performs a nonlinear response-history analysis at each intensity level and identifies the distributions and correlation of all structural response parameters used to express the fragility curves of Step 1. Step 4 uses the Monte Carlo method to generate a significant number of response data that are statistically consistent with those of Step 3 and to identify the possible distribution of damage to structural and non-structural components of the NPP at each intensity level. Step 5 computes the probability of target unacceptable performance at each intensity level using the event and fault trees of Step 1 and calculates the annual frequency of target unacceptable performance of the NPP.

Sample Nuclear Power Plant

The sample nuclear power plant hosts boiling water reactors. Figure 1 presents the lumped mass-beam 3D models for the reactor building (RB) subjected to horizontal (panel a) and vertical shaking (panel b). In each panel, the model is composed of four sticks representing the external containment structure (R/B), the reinforced concrete containment vessel (RCCV), the reactor shield wall (RSW) and the reactor pressure vessel (RPV). The lumped mass-beam 3D models were developed for the RB using the computer code SAP2000. The first mode periods in the two horizontal and the vertical directions computed based on best-estimate values for the stiffness and mass of the buildings are 0.197s, 0.214s and 0.094s.

To directly include in the analysis the variations in 1) structural damping, 2) strength of the sticks, 3) damping and 4) stiffness of the soil springs for the RB, we developed 30 numerical models for each sample building. Each of the four mechanical properties was assumed to be distributed lognormally with a median equal to its best-estimate value and a logarithmic standard deviation recommended by Reed and Kennedy (1994). A set of 30 realizations was generated to fit each lognormal distribution. The Latin Hypercube Sampling procedure was used to select a realization from each set. A total of 30 combinations of mechanical properties mentioned above were established and each combination determined a numerical model for the sample RB.

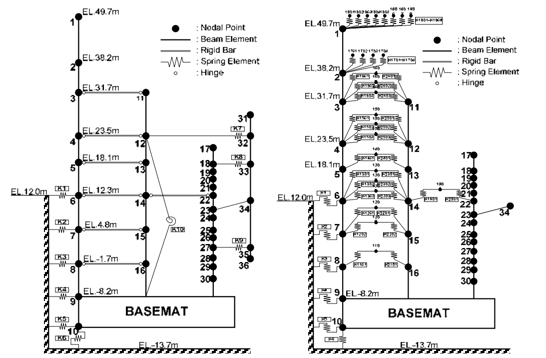

(a) (b)

Figure 1. Stick models for the sample reactor building for (a) horizontal shaking and (b) vertical shaking.

Step 1: Plant System Analysis and Fragility Curves

Figure 2 presents the seismic event trees for the core damage event of the sample NPP. The seismic risk assessments performed in this study focus on the core damage frequency caused by a specific accident sequences, which are numbered #2 in Figure 2. Sequences #2 starts from a seismic event (SE), end at core damage and consist a series of safety functions (SFs) in between. The failures of the related SFs in sequence #2 are the off-site power (LOP), the service water (SW) and the AC independent water addition (ACIWA) systems. In SFs, the emergency diesel generators (EDG) cannot function without SW and is not considered in sequence #2 since the probability of failure of the system in the sequence is 1.

A fault tree identifies the various combinations and sequences of the failure of NPP components which lead to the failure of a given SF. Figure 3 presents the fault tree for the ACIWA system in the sample NPP. The SFs that fail to operate in sequence #2 are involved with 29 basic components at the lowest level of their fault trees. Structural-response-based fragility curves were developed for these basic components. Fragility curves used in this study are the cumulative distribution functions of logarithmic normal distributions, as presented in the following equation:

$$G_C\left(a\right)=\Phi\left[\frac{\ln\left(a/\hat{a}\right)}{\beta_C}\right] \tag{1}$$

where $G_C\left(a\right)$ is the probability of failure of a NPP component at a given value a of a structural response parameter critical for the functionality of the component and $\hat{a}$ is the median capacity of the component. Parameter β_C is the composite logarithmic standard deviation in the capacity of the component, including both aleatory variability and epistemic uncertainty.

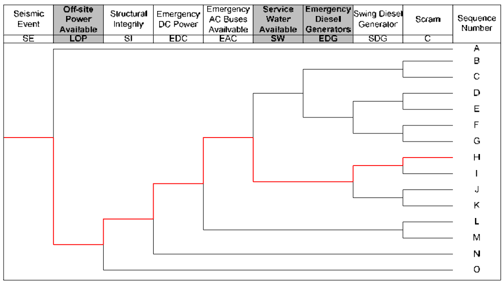

(a) Main seismic event tree of the sample NPP

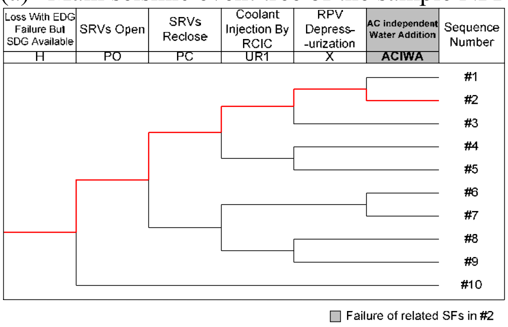

(b) Seismic event tree following Accident Sequence H

Figure 2. Seismic event trees of the sample NPP.

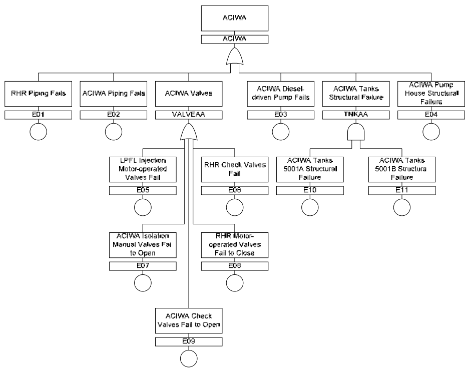

Figure 3. Fault tree for the ACIWA system

Step 2: Seismic Hazard

The sample NPP is assumed to be located close to Taipei, Taiwan. The seismic hazard for the sample NPP site, as shown in Figure 4, was developed as a function of spectral acceleration (S_a) at the fundamental period of the RB, which is 0.2 second in this case. The range of spectral acceleration was split into 8 equal intervals (termed Δe_i, $i = 1-8$ in Figure 5) representing 8 ground-motion intensity levels (termed $S_{a,i}$, $i = 1-8$) Each intensity level of the seismic hazard is associated with a mean annual frequency of occurrence, termed $\Delta\lambda_{H,i}$. The fourth column of Table 1 presents the value of $\Delta\lambda_{H,i}$ for each $S_{a,i}$.

For each $S_{a,i}$, the modal magnitude-distance pair was identified using the de-aggregation data for the sample NPP site and a conditional mean spectrum (Baker and Cornell 2006) anchored to the given $S_{a,i}$ was developed and used as the target spectrum for scaling of ground motions for the response-history analysis of the sample NPP. In this study, 20 sets of ground motions from the PEER ground-motion database were selected and scaled for each intensity level. Each set of ground motions was scaled by a single factor determined using the greedy optimization procedure of Jayaram et al. (2011). Both the median and dispersion in the spectral ordinates of the selected ground motions were considered in the optimization process. The scaled ground motions are used in the response-history analysis for the sample NPP.

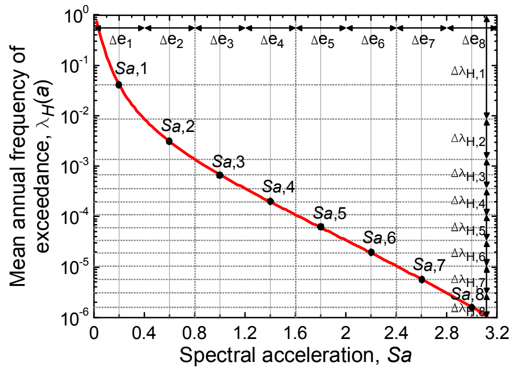

Figure 4. Seismic hazard curve for the site of the sample NPP.

Step 3: Structural Response

A total of 4,800 tri-directional response-history analyses (30 numerical models and 20 sets of ground motions for each $S_{a,i}$) were conducted for the sample RB. As described earlier, 29 structural response parameters were used to develop the fragility curves for the 29 basic components. The values of the 29 response parameters were recorded in each nonlinear response-history analysis and a total of 8 demand-parameter matrices were developed for the 8 intensity levels. The size of the demand-parameter matrices is 20×29, where the number of row vectors is determined by the number of ground motions for a given shaking intensity and the number of columns is determined by the number of structural response.

The procedure of the ATC-58 Guidelines and Yang et al. (2009) was used in this study to increase the number of row vectors in the demand-parameter matrix from 20 to 50,000. The mean vector and covariance matrix of the natural logarithm of the new demand-parameter matrix were the same as those of the underlying matrix from the results of the response-history analysis.

Step 4: Damage Assessment

The Monte Carlo procedure was used to determine the damage status (i.e., success or failure) of NPP components subjected to ground shaking. For a given row vector in a $50{,}000 \times 29$ demand-parameter matrix for the sample NPP, the procedure was performed for all basic components to determine the damage status of each component and, based on the distribution of damage (safe or failure) in all basic components, the fault and event trees for the accident sequence #2 of Figure 1 were then used to determine whether the target unacceptable performance occurred or not. This procedure was repeated for each row vector in the 50,000 × 29 demand-parameter matrix and the probability of unacceptable performance for accident sequence #2 at the associated with the demand-parameter matrix can be determined by the ratio of the number of row vectors with occurrence of unacceptable performance to 50,000. The third column of Table 1 presents the probabilities of unacceptable performance ($P_{UP}(S_{a,i})$) caused by accident sequence #2.

Table 1. Seismic risk of the sample NPP for accident sequence #2 at each ground-motion intensity level.

Ground-motion intensity level, $S_{a,i}$		Probability of unacceptable performance, $P_{UP}(S_{a,i})$	Mean annual frequency of occurrence, $\Delta\lambda_{H,i}$	Annual frequency of unacceptable performance, $P_{UP}(S_{a,i})\times\Delta\lambda_{H,i}$
$S_{a,1}$	0.2g	0.000	7.36×10^{-1}	0.000
$S_{a,2}$	0.6g	6.86×10^{-3}	7.20×10^{-3}	4.94×10^{-5}
$S_{a,3}$	1.0g	4.77×10^{-2}	1.00×10^{-3}	4.79×10^{-5}
$S_{a,4}$	1.4g	1.05×10^{-1}	2.49×10^{-4}	2.62×10^{-5}
$S_{a,5}$	1.8g	2.56×10^{-1}	7.43×10^{-5}	1.91×10^{-5}
$S_{a,6}$	2.2g	3.20×10^{-1}	2.35×10^{-5}	7.51×10^{-6}
$S_{a,7}$	2.6g	4.50×10^{-1}	7.40×10^{-6}	3.33×10^{-6}
$S_{a,8}$	3.0g	6.15×10^{-1}	2.25×10^{-6}	1.39×10^{-6}

Step 5: Seismic Risk Computation

The annual frequency of target unacceptable performance, λ_{UP} , is the sum of the products of $P_{UP}(S_{a,i})$ and $\Delta\lambda_{H,i}$:

$$\lambda_{UP} = \sum_{i=1}^{8} P_{UP}\left(S_{a,i}\right)\cdot\Delta\lambda_{H,i} \quad (2)$$

Table 1 presents the annual frequency of unacceptable performance caused by the accident sequence #2, which for the sample NPP, is 1.55×10^{-4}. Note that this number should be interpreted with care and only three SFs in accident sequence #2 were considered in this study to simplify the analysis. This simplification will lead to a conservative estimate of the risk. In addition, the values of seismic risk computed using the methodology proposed by Huang et al.. and Boolean algebra were compared to evaluate the accuracy and efficiency of the proposed methodology. The two approaches generated similar results, and the resultant annual frequencies of unacceptable performance were both 1.55×10^{-4}. The methodology proposed by Huang et al. is more efficient than the procedure that uses Boolean algebra.

Conclusions

In this study, we demonstrate the procedures of SPRA for a sample NPP using the methodology proposed by Huang et al. (2011a, 2011b). The procedures enable the use of structural-response-based fragility curves and directly consider the correlation in the responses of NPP components in the risk computation. The uncertainties in soil properties of the sample NPP site and the mechanical properties of structural components of the sample NPP were included in this study. We note that a simplified accident sequence was used in this study. The simplification will result in a conservative estimate on the seismic risk of the sample NPP.

References

Applied Technology Council (ATC). (2012). “Seismic performance assessment of buildings. Volume 1 – Methodology”, *FEMA P-58* pre-release version, Federal Emergency Management Agency. Washington, D.C.

Baker, J. W., and Cornell, C. A. (2006). “Spectral shape, epsilon and record selection”, Earthquake *Engineering and Structural Dynamics*, 35(9), 1077-1095.

Chen, J.T., Chokshi, N.C., Kenneally, R.M., Kelly, G.B., Beckner, W.D., McCracken, C., Murphy, A.J., Reiter, L., Jeng, D., (1991). “Procedural and Submittal Guidance of Individual Plant Examination of External Events (IPEEE) for Severe Accident Vulnerabilities”, *NUREG-1407*. USNRC. Washington, DC.

Huang, Y.-N., Whittaker, A. S. and Luco, N. (2011a). “A Probabilistic Seismic Risk Assessment Procedure for Nuclear Power Plants: (I) Methodology”, *Nuclear Engineering and Design*, 241(2011), 3996-4003.

Huang, Y.-N., Whittaker, A. S. and Luco, N. (2011b). “A Probabilistic Seismic Risk Assessment Procedure for Nuclear Power Plants: (II) Application”, *Nuclear Engineering and Design*, 241(2011), 3985-3995.

Jayaram, N., Lin, T., and Baker, J. W. (2011). “A Computationally Efficient Ground-Motion Selection Algorithm for Matching a Target Response Spectrum Mean and Variance”, *Earthquake Spectra*, 27(3), 797-815.

Reed, J. W. and Kennedy, R. P., (1994). *Methodology for Developing Seismic Fragilities*. TR-103959. Electric Power Research Institute, Palo Alto, California, USA.

U.S. Nuclear Regulatory Commission, (1991). “Individual Plant Examination of External Events (IPEEE) for Severe Accident Vulnerabilities. *Generic Letter No. 88-20*, Supplement 4”, USNRC, Washington, DC.

U.S. Nuclear Regulatory Commission, (1983). “PRA Procedures Guide”, *NUREG/CR-2300*. USNRC, Washington, DC.

Yang, T.Y., Moehle, J., Stojadinovic, B., Der Kiureghian, A. (2009). “Performance Evaluation of Structural Systems: Theory and Implementation”, *Journal of Structural Engineering*. 135(10), 1146-1154.

Study of Seismic Anomalies in Crust from Observed Waveform Analysis

Yi-Zeng Chang [1] and Strong Wen [2] and Chau-Huei Chen [3] and Kou-Liang Wen [4]

張議仁 [1]、溫士忠 [2]、陳朝輝 [3]、溫國樑 [4]

Abstract

In this study, we use P-wave dispersion and attenuation properties and the shear-wave splitting technique to detect seismic anomalies prior to an earthquake. The results show that P-wave dispersion of attenuation factor dQ (Q value will be at the epicenter of the linear regression to remove the effect) will be relatively high before an earthquake, the fast-shear-wave polarization angle of the S-wave changes after the earthquake, and the delay time will be increased. This study also discusses the 2012 M_L=5.28 event that occurred in the Chiayi area near station CHN5 and the Meishan fault. Form analysis of the case study and the high seismic potential areas, we expect to identify the anomalies prior to a strong earthquake.

Keywords: Dispersive attenuation, shear-wave splitting, polarization angle, delay time

Introduction

This project utilized the characteristics of seismic wave propagation to observe abnormal changes in the crust before an earthquake. There are two main methods for this; the first is the application of P -wave attenuation of dispersion characteristics. As the crust exhibits non-homogeneous, non-uniform, and non-elastic properties, when a seismic wave propagates, geometrical spreading and inelastic absorption cause the attenuation of seismic waves. Hence, in this research, we analyzed the observed natural seismic waveform to identify anomalies before an earthquake resulting from changes in the crust material. The second method is the application of shear-wave splitting, for observation of earthquake precursors (Crampin, 2004). The main characteristics of shear-wave splitting can reflect the size of cracks, the orientation of cracks in the crust, the rock foliation, and other behaviors that can indicate tectonic stress, the crystal arrangement, or fault shear stress. The effective range of this method is about 30 km from the station.

We expect to apply the two methods to detect these anomalies before an earthquake, and to monitor high seismic potential areas to verify the above techniques, in order to obtain relevant information before an earthquake. In this paper, we only describe the principles of the shear-wave splitting method, not P-wave attenuation of dispersion aspect. A case study from the end of 2012 and related preliminary observations from July 2013 also will be described in the "Results and Discussion" section.

Methodology

Shear-Wave Splitting

Anisotropy describes how different properties of an object can vary with direction. When a seismic wave passes through an anisotropic material, the shear-wave will be split. This phenomenon is known as shear-wave splitting, in which the polarization direction of the fast-shear-wave will run parallel to the direction of the rupture surface, and the slow shear wave will be directed perpendicular to the fracture plane.

[1] Assistant Researcher, National Center for Research on Earthquake Engineering, yzchang@ncree.narl.org.tw
[2] Associate Researcher, National Center for Research on Earthquake Engineering, scwen@ncree.narl.org.tw
[3] Professor, Dept. of Earth and Environment Sciences, National Chung Cheng Univ., seichen@eq.ccu.edu.tw
[4] Professor, Dept. of Earth Science, National Central Univ.,wenkl@ncree.narl.org.tw

Waveform Calculation

We adopted the method used by Liang (1990) to calculate the waveform correlation coefficient and extract the first cycle of the S-wave to be identified. We define two horizontal components in increments of 1-degree rotation and 1-millisecond shift for the calculation of the cross-correlation coefficient. When the maximum correlation coefficient is found, the fast and slow shear waves can be identified, hence, the delay time and fast-shear-wave polarization angle can be found. These reflect the range of crust fracture density or size, the geological structural trends, rock foliation, and so on.

Correction coefficient and confidence interval

The correlation coefficient is calculated with confidence intervals (Kreyszig, 1970). We computed the correlation coefficient of the wave polarization angle and its confidence intervals using the two horizontal components as the sample space, for every 1-degree rotation or 1-millisecond latency. When the 95% confidence interval and the correlation coefficient reach their maximum values, the delay time and the fast-shear-wave polarization angle are obtained.

Data processing

Data selection

We used waveform data from the Central Weather Bureau short-period network with a local magnitude less than 3 and an epicenter distance less than 30 km. If the distance were too far away from the epicenter, this would lead to poor data quality. Furthermore, a big earthquake has high low-frequency energy, and this is not suitable for measuring the attenuation of dispersion, and increases the signal complexity owing to the large dislocation momentum from the earthquake. Therefore, the scale of the earthquake was set at $M_L \leqq 3.0$. The study area contains the CHN5, CHN2, and CHY stations, but CHY and CHN2 produced poor data quality with fewer waveforms available. Hence, this report adopts station CHN5 as an example.

Waveform processing

In order to remove the tidal effect, the velocity waveform data was integrated to displacement with baseline correction. According to the spectrum analysis by Chen (2006), the frequency range of the shear wave was roughly concentrated at 2-6 Hz in the Taiwan area. Therefore, we adopted a band-pass filter within this range.

Extracting the first cycle of the S wave

In this section, we capture the first cycle of the S-wave, in order to analyze the signals, through the use of the technique to obtain the waveform correlation coefficient (Liang, 1990), detailed in Section 2.2. The calculated parameters include delay time (expressed by δt) and the fast-shear-wave polarization angle (expressed by ψ). As delay time reflects the crust fracture density, it is increased as the range of crustal fracture density is increased. Conversely, when the delay time is decreased, it may be closed when cracks in the crust are generated. The fast-shear-wave polarization angle reflects the arrangement of the fractured crust, leading to rock foliation and other, phenomena. The results indicate the tectonic stress, the crystal arrangement, the fault shear stress, *etc*. As a result, this study adopted rose diagrams as shown in Figure 6.

Table 1. A list of earthquakes near CHN5 in 2012

No	Date	Epicenter		Depth (km)	M_L
01	**10/24**	**23.67°**	**120.91°**	**13.18**	**3.63**
02	**10/24**	**23.56°**	**120.53°**	**5.46**	**3.49**
03	**11/29**	**23.39°**	**120.64°**	**11.41**	**4.00**
04	**12/08**	**23.58°**	**120.82°**	**17.13**	**3.25**
05	**12/31**	**23.46°**	**120.90°**	**4.41**	**5.28**

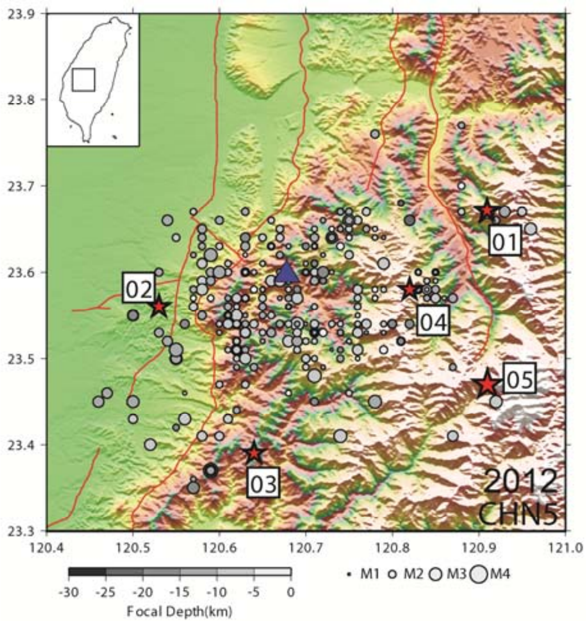

Figure 1. The selected events near CHN5 in 2012. The blue triangle indicates the station, and the red stars indicate the earthquakes, numbered as in Table 1.

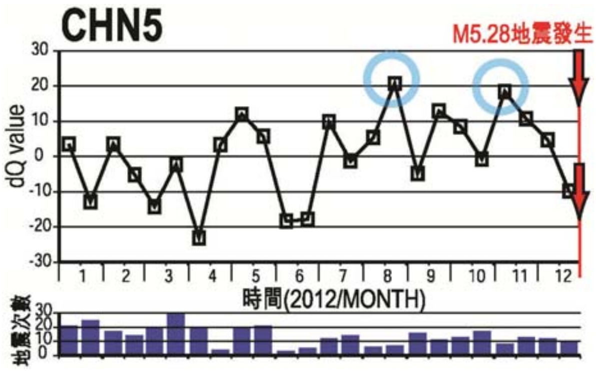

Figure 2. The distribution of dQ for station CHN5 in 2012. The red arrow indicates the M_L=5.28 event that occurred in the Chiayi area. The lower panel is a histogram of the seismic events for each month.

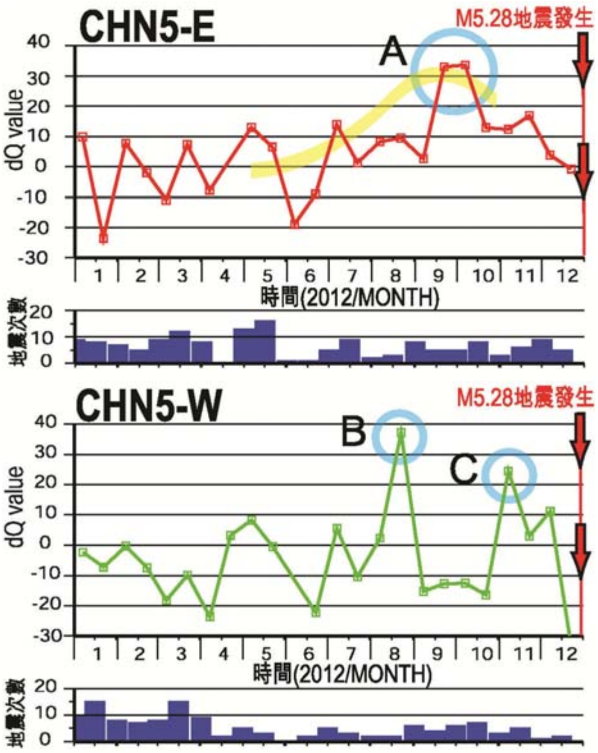

Figure 3. The variation of dQ at CHN5 in 2012. It is divided into two sides (east and west) to identify the anomalies

Results and discussion

In order to understand P-wave attenuation of dispersion prior to an earthquake, we selected a relatively large-scale earthquake to analyze and discuss, which occurred in December 2012 with M_L=5.28(shown in Figure 1 with red star no. 05). Figure 2 shows the seismicity (for magnitudes lower than 3) within 30 km of the epicenter near station CHN5 for the whole of the year 2012. In Figure 2, two relatively high values appear, with dQ values of around 20. The dQ value is unlikely to increase as a result of seismic energy attenuation, but the area may be experiencing increased stress, density, or other physical and chemical changes, while earthquakes can occur after high dQ values. We further used station CHN5 as a center-point to divide the study area into east and west sides, as shown in Figure 3. In this figure, the symbols A, B and C indicate dQ values that were higher than 20.

Table 2. A list of earthquakes near CHN5 in 2013

No.	Date	Epicenter		Depth (km)	M_L
01	**10/25**	**23.36°**	**120.63°**	**12.60**	**3.16**
02	**11/21**	**23.50°**	**120.68°**	**12.21**	**3.02**
03	**12/01**	**23.45°**	**120.63°**	**9.75**	**3.29**
04	**12/03**	**23.59°**	**120.70°**	**14.43**	**3.44**
05	**12/07**	**23.52°**	**120.48°**	**12.98**	**3.42**

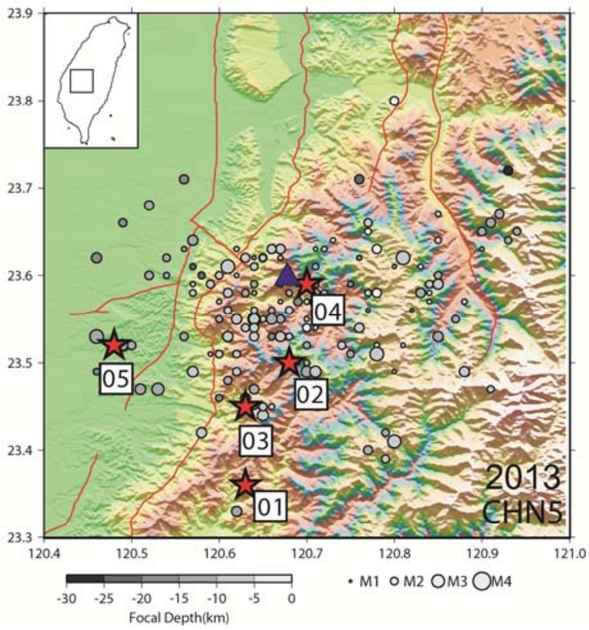

Figure 4. The selected events near CHN5 in 2013. The red stars indicate the earthquakes corresponding to Table 2

In order to facilitate discussion of events in the second half of 2012, we list the seismic events with magnitudes greater than 3.0 in Table 1. In Figure 3, point A east of CHN5 (CHN5-E) exhibits high values that may relate to the No. 05 earthquake, as both readings are on the east side of the station. In Figure 3, points B, and C west of CHN5 (CHN5-W) have high values that may relate to the No. 02 and 03 earthquakes in Table 1. The epicenters are plotted as red stars in Figure 1, where events 02 and 03 are on the west side of the station.

For the smaller earthquakes, the question of whether more observations are required for this study needs to be verified in future research. Because the data used in this method involves the collection of the direct P-wave, it carries information about when the wave propagated through the disturbed crust. Indeed, the waveform would exhibit some unusual characteristics and the P-wave attenuation of dispersion is more sensitive to these variations. Another major factor influencing dQ is whether the earthquakes are evenly distributed in the study area. For example, the lower seismicity near No. 05 earthquake shows that seismic waves pass poorly through the seismogenic zone. Another factor is the epicenter distance, as a longer distance would diminish the effectiveness of dQ.

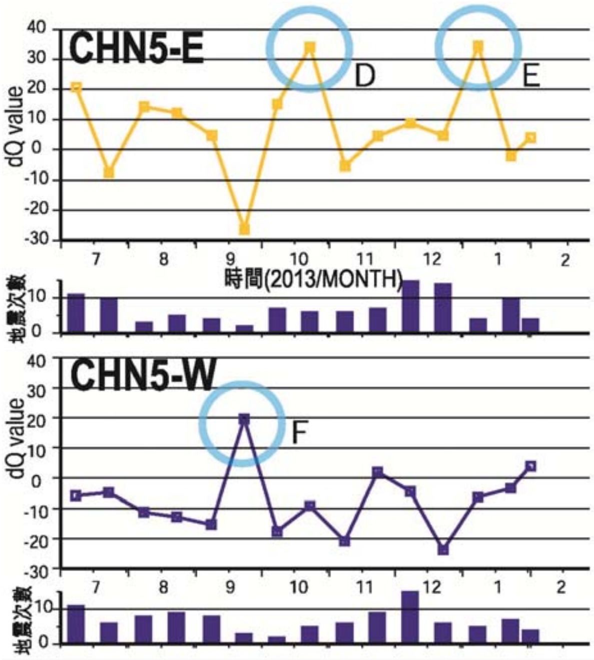

Figure 5. The variation of dQ at CHN5 in 2013, divided into east and west sides to identify the anomalies.

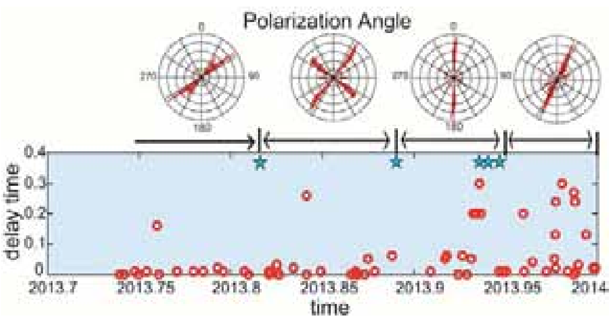

Figure 6. The distribution of fast-shear-wave polarization angle and delay time. The blue stars indicate the earthquakes shown in Table 2.

In order to verify the methods described above, we made actual observations at the end of 2013. In Figure 5, the results for the second half of 2013 are shown, where points D, E, and F indicate relatively high dQ values. As point B is in 2014, we neglect it here. In order to discuss the high values of D and F, we list the locations of seismicity with magnitudes lower than 3 and the times that occurred in the second half of 2013 in Table 2 and plot them in Figure 4 at the same time. Meanwhile, Figure 6 shows the results of both the fast-shear-wave polarization angle and delay time. In Table 2, the locations of earthquakes Nos. 02–05 may be similar for the same earthquake sequence. In Figure 5, the high values marked by D and F appear in September and October, and therefore may have been affected by the earthquake sequence of Nos. 02–05 in Table 2. Point F in CHN5-W in Figure 5 first appeared with a high value, which may indicate geological differences with crustal movement. In Figure 6, the visible changes in the angle of polarization after each earthquake reflect the change in stress in the local area, and the delay time increases after each earthquake.

Conclusions

Real-time data is currently available to analyze seismic anomalies through the above two methods for magnitudes greater than 5. Fortunately, the results appear to show that the attenuation dispersion anomalies occurred one month ago, making the present real-time observations still applicable. The sizes of only five or more previously selected earthquakes were analyzed, but the magnitudes 3-5 of these earthquakes in the observation period also apparently support this point but more observational data is required to confirm this. For the dQ values, more observations of weak and hard geological conditions and the relationship between magnitude and epicenter distance, need to be assessed. In addition, after an earthquake, the polarization angle and delay time exhibit variations that can be important factors for verifying whether the stress in a region returns to its original state before the earthquake.

References

Correig, A. M. (1991). On the measurement of body wave dispersion, J. Geophys. Res. 96, 16,525-16,528.

Crampin, S., S. Peacock, Y. Gao, and S. Chastin(2004). The scatter of time-delays in shear-wave splitting above small earthquakes ,Geophys. J. Int. 156, 39–44.

Kreyszig, Erwin, (1970).Introductory Mathematical Statistics : Principles and methods.

梁文宗(1990)，利用地震 S 波的分離作用探討臺灣北部地殼之非均向性，國立臺灣大學海洋研究所碩士論文。

陳美瑜(2006)，利用地震剪力波的分離性質探討台灣西部變形前緣地殼變形機制，國立臺灣海洋大學應用地球科學研究所碩士論文。

Complex Tomography of Structures beneath the Yun-Chia-Nan Area, Taiwan

Strong Wen [1] Yi-Zen Chang [2] Che-Min Lin [3] and Kuo-Liang Wen [4]

溫士忠 [1]、張議仁 [2]、林哲民 [3]、溫國樑 [4]

Abstract

In this study, we adopt the damping least-square inversion method to investigate the Vp structures and Vp/Vs ratios of the crust beneath the Yun-Chia-Nan area, Taiwan. Previous studies have shown that velocity structure can be used as an indicator of the geometry of a fault and general aspects of the area's tectonics. Therefore, the goal of this research is to analyze the degree of correlation between the velocity structure and the seismic characteristics with respect to the tectonic implications of the area. Finally, the distribution of Vp/Vs ratios and its association with fault activities is also investigated. Our results indicate that the variations in velocity structure beneath the Yun-Chia-Nan area are caused by local geological structures, such as fault crossing. We also find that most earthquakes occur in areas that have Vp/Vs gradients that vary greatly. In addition, according to the distribution of the earthquakes, there appears to be a west-dipping fault west of the Chukou fault; however, this needs to be investigated further in a future study.

Keywords: Vp、Vp/Vs、complex structure、tomography method

Introduction

In recent years, several major communications and transportation systems have been built in the Yun-Chia-Nan area (see Figure 1) to improve its economic development. As such, it is extremely important to analyze the accumulation of seismic energy in the upper crust and seismic potential in this area. In this study, we investigate the variations in velocity structure beneath the Yun-Chia-Nan area and their tectonic implications. We expect to provide useful information about the occurrence of hazardous earthquakes in the region.

The National Center for Research on Earthquake Engineering (NCREE) and the Central Weather Bureau Seismic Network (CWBSN) of Taiwan have set up seismic monitoring systems around Taiwan and its outlying islands. This dense seismic network and high precision "three-components" seismometers provided us with the high-quality travel time records for P and S waves required for this study. Not only have we been able to analyze this data to precisely determine earthquake locations, but we have also been able to obtain 3-D tomographic velocity structures beneath this area. In addition to the Vp and Vs structures, we are also interested in studying the Vp/Vs ratio. The ratio of Vp/Vs reflects the rock porosity, the degree of fracture in the rock, and the fluid pressure of the rock. Therefore, the Vp/Vs ratio is a key parameter for understanding the properties of crustal rocks (Walck, 1988; Chen et. al., 2001). Furthermore, recent studies have shown that the Vp/Vs ratio can also provide useful information about geological evolution and tectonic variations .

Geological Setting

The Yun-Chia-Nan area can be divided into two main areas: the Western Foothills (WF) and the Western Coastal Plain (WCP). The WF are mainly composed of Neogene clastic sediments and partly of Oligocene strata. The dominant rock types are an

[1] Associate Researcher, National Center for Research on Earthquake Engineering, scwen@narlabs.org.tw.

[2] Assistant Researcher, National Center for Research on Earthquake Engineering, yzchang@narlabs.org.tw

[3] Associate Researcher, National Center for Research on Earthquake Engineering, cmlin@narlabs.org.tw

[4] Professor, Dept. of Earth Science, National Central Univ., wenkl@narlabs.org.tw

interlamination of sandstone and shale and the thickness of the shale and mudstone layers increases from north to south. This main tectonic structure of the WF is a standard type of fold thrust belt, an obvious imbricate system composed of dense, unbalanced folds and low-angle thrust faults dipping toward the southeast. The WCP is covered with diverse Quaternary alluvial sediments that consist of marine sands and reworked beach materials. The alluvial deposits indicate tectonic uplift and denudation of the Central Mountain Range (CMR) as well as the occurrence of erosion. The surface of the system is about 10 km thick and is covered with alluvium or laterite gravel. The deposition on the system is flatter than that in the eastern area nearer to the CMR (Ho, 1986). The outcrops of the WF possess very complex folding structures, which consist of synclines, anticlines and three major fault systems. Geologically, the properties of the rock formation from north to south and from east to west change from rigid to loose, and this could affect the velocity structure (Ho, 1986). It is one of our more important goals to investigate the possibilities of this effect.

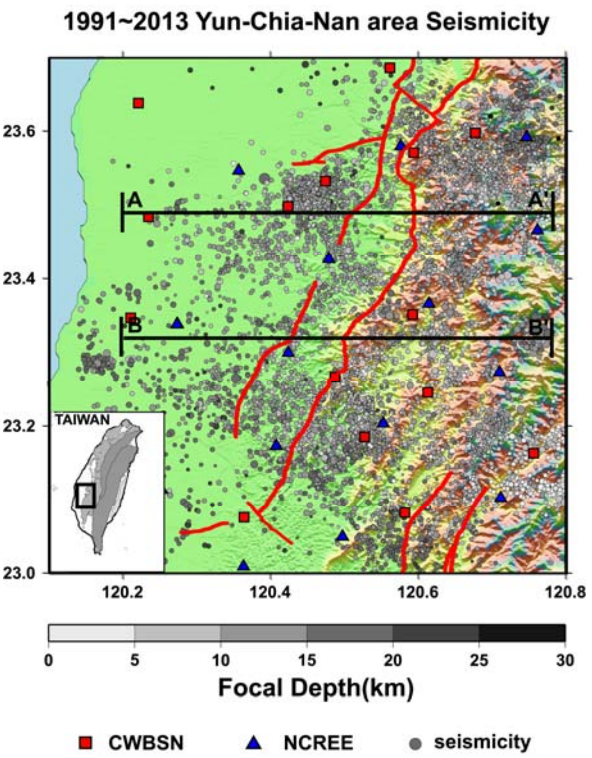

Figure 1. The locations of the faults and the stations of the CWBSN in our research area. The two lines represent the profiles AA' and BB' used in this study

Data Processing

This study uses the travel time data of P and S waves from the period 1991 to 2013 recorded by the CWBSN and NCREE. A damping least-square inversion method was used to determine the Vp structure and Vp/Vs ratio in the crust and upper mantle of the region. The programs and routines used to perform the 3-D inversion were originally developed by Thurber (1983) and Eberhart-Phillips and Michael (1998), and have since been modified by others to obtain both the Vp and the Vp/Vs ratio. The latitude and longitude ranges of our study area were 22.9°N - 23.8°N and 120.1°E - 121.°E. Many seismic events have occurred in the region of interest. In order to improve the resolution of the tomographic inversion and achieve uniform ray distribution around the volume source, we chose events with epicenter location errors of less than 5 km and events with more than six readings of the P and S waves. To ensure the quality of the seismic data, the ERH (error in horizontal components) and ERZ (error in vertical component) were set at less than 5km and 10 km respectively. Under the above conditions, we were able to select 7,591 events with 67,793 P-wave and 60,513 S-wave arrival times for use in this study. We chose an *a priori* 1-D P-velocity model parameterized by horizontal layers of constant velocities that could roughly reproduce the main features of the known velocity structure obtained by Yeh *et al.*, (2013). An uneven 3-D grid formed through a trial-and-error process parameterized the 3-D structure. Several other were also taken into account during the process: station spacing, estimated resolution, and the desired spatial resolution around the fault plane. Table 1 lists the one-dimensional initial velocity model(Yeh et al., 2013) that couples with the grid node from the top surface to a depth into the inversion of more than 75km. The effect of station elevation on the 3-D tomographic inversion was also considered in our calculations.

Table 1 The 1-D initial velocity model (Yeh, et. al., 2013)

Depth(km)	P wave(km/s)	Vp/Vs
0~3	4.08	1.78
3~7	5.07	1.79
7~12	5.11	1.78
12~17	5.76	1.83
17~22	6.21	1.74
>22	7.15	1.78

Results and Discussions

In this section, we discuss our results in two parts. The first part discusses the results in terms of how the velocity structures and Vp/Vs ratios were derived and is accompanied by an examination of the checkerboard test. Here, the epicenters are relocated and the velocity structures are calculated through an iterative process. The second part of our discussion involves examining velocity structures in profile. In order to do this velocity structures beneath the Yun-Chia-Nan area, have been examined in two profiles across this area (see Figure 1). These profiles are almost perpendicular to the Chukou fault. Thus we can outline the relationship among the velocity structures, fault zones and seismicity.

As the distributions of the seismic events were observed uniformly, the results show good resolution at the selected zones including the Chukou fault and in a band roughly 15 km wide running along the sides of the fault (see Figure 2). However, the resolution at depth from 0 to 3 km and from 22 to 35 km is relatively poor. At depth between 0 and 3 km, this problem may be due to the incident angles being almost perpendicular to the surface, meaning that the lateral resolutions of velocity are lower. At depth between 22 and 35 km, a reasonable explanation may be that only a few of selected events actually occurred at such a depth. The high resolution indicates that the seismic rays crossed most of the area, and ought be reliable in helping determine the geology structures more precisely beneath the Yun- Chia-Nan area.

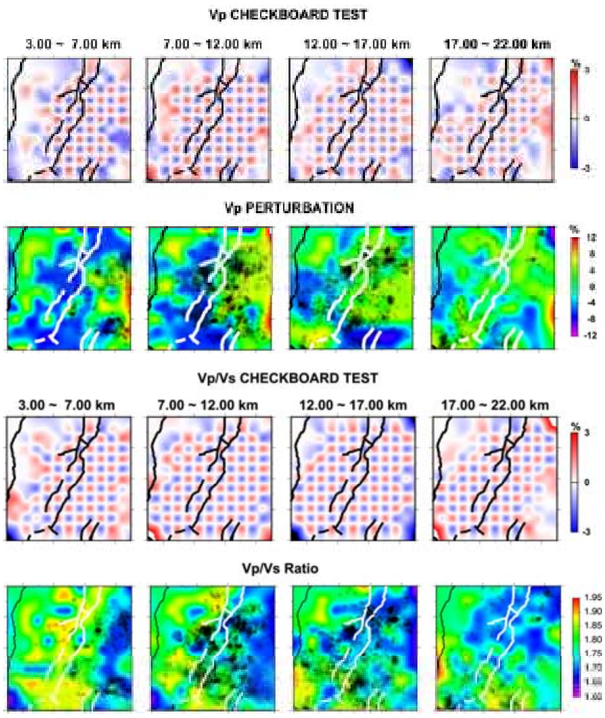

Figure 2. The checkerboard tests and 3-D tomographic Vp and Vp/Vs structures at four depth ranges (3-7km, 7-12km, 12-17km, 17-22km). The black and white lines represent the locations of the main faults in the research area and the small circles indicate the seismicity

In Figure 2, the seismic events in each layer are numerous; however, most are located in the shallow layers at depths from 3 to 22 km. Therefore in our inversion process, it is not possible to avoid the case where seismicity is not uniform. At a depth of 0 to 7km, the high and low values of Vp have a dispersed distribution. We also observed that there exist low Vp anomalies scattered within the vicinity of the fault zone. At a depth of 7 to 17 km, we found that the low Vp anomalies increase with depth and expand in a southwesterly direction. This may be related to the existence of shallow sediment structures beneath this area (Ho, 1986). There are several cluster events existing in each layer and most lie within the low Vp anomalies. In the vicinity of the fault zones, a high Vp/Vs ratio anomaly is due to increases in pore pressure and therefore decreases in the S wave velocity. We also observed that a high Vp/Vs ratio anomaly broadened from the WF to the WCP between 3 to 17 km and that the low Vp/Vs ratio zone extends to the CMR with increasing depth (see Figure 2). The likely reason for this is that rock formations are older and denser beneath the CMR, and so contain less fluid or SiO_2, and this leads to the lower Vp/Vs ratio. Our results indicate that most seismic events are located in areas with Vp/Vs gradients that vary greatly or that have a high Vp/Vs ratio.

In Figure 3, two profiles AA ' and BB' show that the anomalies exist in the Vp and Vp/Vs cross section, and also potentially indicate an eastward leaning fault geometry beneath the Chukou fault zone, which implies the fault should be the Chukou fault. On the west side of the fault, there is also a low Vp, high Vp/Vs anomaly area, and this abnormal area tends to dip toward the west and exhibits an earthquake cluster. The west side of Chukou fault zone exhibits anomalous activity, possibly owing to the high pore pressure, which can reduce the pressure to rupture. Therefore, the abnormal area can be interpreted as an oversaturated pore pressure zone. We conclude that high seismicity exists in zones that exhibit a low P wave velocity and where the gradients of the Vp/Vs ratio vary greatly in each profile. Hence, we can observe a seismic zone dipping toward the west and believe that this lies around a blind fault zone. The geological implications of this phenomenon with regard to the Yun-Chia-Nan area are worth further investigation.

Conclusions

In this study, we applied a damping least-square inversion method to investigate, via 3-D tomographic inversion, the Vp structures and Vp/Vs ratios of the crust and upper mantle beneath the Yun-Chia-Nan area of Taiwan using body waves travel time data. By using the time difference between the observed P and S waves, we were able to invert the Vp/Vs ratios. Our results indicate that we are able to not only locate earthquakes, but also deduce the relationship between the seismicity and the regional geological structures. An additional finding was that most earthquakes occurred in areas that have Vp/Vs gradients that vary greatly. From our study, we inferred that there might exist a west-dipping fault in the western Chukou fault region; however, this inference needs further study.

Due to the 1022 Chiayi earthquake sequence that occurred in this area, the focal mechanism solution of the main shock is also speculated to be the westward tilt of a reverse fault (Wen et al., 2008), suggesting that this is a blind fault. Therefore, the results are consistent with the focal mechanism of the bigger earthquake. As such, it is difficult to outline the variability of the velocity structure beneath the surface from the P wave velocity, and thus the Vp/Vs ratios were used to improve our understanding of the tectonic evolution. The 3-D numerical model from this study are helpful in improving the accuracy of earthquake location, and are also an important factor in estimating strong motion. Therefore, for the Yun-Chia-Nan area, the results are also of great significance in earthquake prevention and mitigation.

References

Chen, C.H.,W.H. Wang, and T. L. Teng (2001). 3-D Velocity Structure Around the Source Area of The Chi-Chi Earthquake,1999,Taiwan： Before and After Mainshock , *Bull. Seismol. Soc. Am.*, **91**, 1010-1027

Eberhart-Phillips, D., and A. Michael (1998). Seismotectonics of the Loma Prieta, California, region determined from three-dimensional Vp, Vp/Vs, and seismicity, *J. Geophys. Res.*,**103**, 21,099-21,120.

Ho, C.S. (1986). A synthesis of the geologic evolution of Taiwan, *Tectonophysics* 125, 1-16.

Thurber,C. H.(1983). Earthquake locations and three-dimension crustal structure in the Coyote Lake area,central California, *J. Geophys. Res.*, **88**,8226-8236.

Walck, M. C. (1988). Three-Dimensional Vp/Vs Variation for the Coso Region,California, *J. Geophys. Res.*, **93**, 2047-2052.

Wen S., C. H. Chen, and T. L. Teng (2008) Ruptures in a Highly Fractured Upper Crust, *Pure and Applied Geophysics*, **165**, 201-213.

Yeh, Y-L., Wen, S., Lee, K-J., Chen, C-H. (2013), Shear-wave velocity model of the Chukuo Fault Zone, Southwest Taiwan, from Cross Correlation of Seismic Ambient Noise, Journal of Asian Earth Sciences, doi: http : // dx.doi.org /10.1016/ j.jseaes. 2013.07.023.

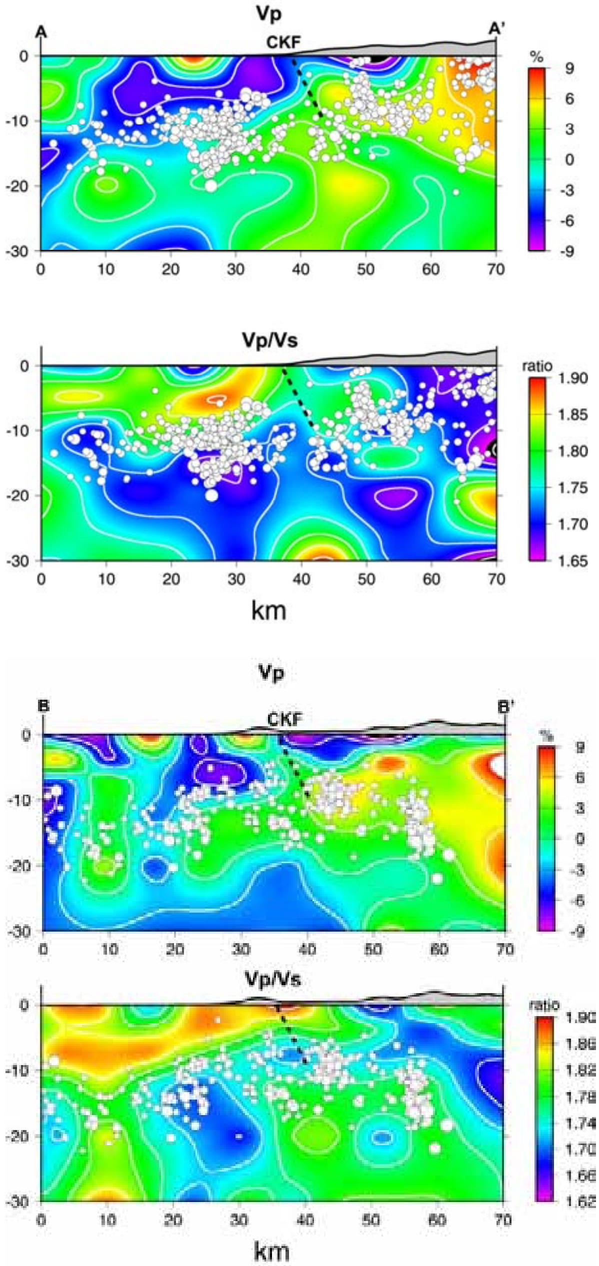

Figure 3. Tomographic Vp structure along the profiles AA' and BB'. Circles represent event used in inversion for this profile. CKF indicates the location of Chukou fault. Note: the Vp values are shown by percentages of the differences with respect to the 1-D model. Tomographic Vp/Vs ratio structure also along the profiles AA' and BB'. Circles represent event used in inversion for this profile.

Geochemical Monitoring: Real-Time Database for Earthquake Precursory Research

Vivek Walia [1], Hsiao-Hsien Chang [2], Shih-Jung Lin [3], Arvind Kumar [4], Tsanyao Frank Yang [5] and Kuo-Liang Wen [6]

Abstract

The present investigations aims at devlop effective earthquake precursory model from the long term soil-gas data obtained from a network of soil-gas monitoring covering NW, SW and eastern Taiwan. As per the present practice, the data from various stations are examined synoptically to evaluate earthquake precursory signals against the backdrop of rainfall and other environmental factors. The present study is also aimed at the appraisal and filtrations of these environmental/meteorological parameters and to create real-time database for earthquake precursory study. In recent years manually operating real-time database had been developed and efforts were made to improve data processing system for earthquake precursory studies by changing the operating system from manual to automatical. We tried to replace the business package software "Visual Signal" to an open source programming language "R" for the data computing work. "R" is a free software programming language and software environment for statistical computing and graphics. To upgrade our working procedure to integrate our data with the popular and famous open source web application solution stack "AMP" (Apache, MySQL, and PHP) has been used.

Keywords: Soil-gas, Earthquake, Radon, AMP, Real-time, Database

Introduction

Earthquakes are one of the most devastating natural hazards, and for the reason, earthquake prediction studies are continuously growing, especially in countries which have relatively greater risk. Despite the fact that countries such as the USA, China, Italy, Japan, Taiwan and Russia have been conducting research on long-term reliable and frequent enough hydrologic–hydrogeologic data for earthquake prediction with a number of changes pertaining to earthquakes have been recorded and discussed by various researchers. However, only a few studies have discussed any tectonic relationship between earthquake producing faults and the location monitoring sites. These studies indiacte that soil gas monitoring located in areas close to seismogenic faults are more sensitive to deformation and can be suitable for earthquake precusrory studies.

Gases like radon, helium and carrier gases like carbon dioxide, nitrogen, methane etc. with different origins in soil have been used to trace various fault systems (Fu et al., 2005; Walia et al, 2009a, 2010) and in earthquake precursory studies (Kumar et al., 2009; Walia et al., 2005; Yang et al., 2006). The continuous monitoring of changes in the daily variation of soil-gas composition along some active faults are demonstrated to be a good investigating tool to monitor the tectonic activities in the region (Walia et. al, 2009a; Walia et al., 2005; Fu et al., 2005; Yang et al., 2006). Studies on diffuse degassing from sub-surface carried out have clearly shown that gases can escape towards the surface by diffusion and by advection and dispersion as they are transported by rising hot fluids and migrate along preferential pathways such as fractures and faults (Yang et al., 2003). To explain the radon migration over large distances, several models have been elaborated and it has been established that radon can be monitored using soil gas method (Etiope and Martinelli, 2002).

In the last few years, we focused on the temporal variations of soil-gas composition at established geochemical observatories along the Hsincheng fault (HC) in Hsinchu area, Hsinhua fault (HH) in Tainan and at Jaosi (JS) in Ilan areas of Taiwan, respectively,

[1] Research Fellow, National Center for Research on Earthquake Engineering, walia@ncree.narl.org.tw
[2] Assistant Researcher, National Center for Research on Earthquake Engineering, seanchang@ncree.narl.org.tw
[3] Assistant Researcher, National Center for Research on Earthquake Engineering, sjlin@ncree.narl.org.tw
[4] Associate Researcher, National Center for Research on Earthquake Engineering, kumar@ncree.narl.org.tw
[5] Professor, Department of Geosciences, National Taiwan University, tyyang@ntu.edu.tw
[6] Professor, National Center for Research on Earthquake Engineering, wenkl@ncree.narl.org.tw

to determine the influence of enhanced concentrations of soil gases to monitor the tectonic activity in the region and to test the previously proposed tectonic setting based model (Walia et al, 2009b, Walia et al, 2012) from data generated at earthquake monitoring stations during observation period. The stress-induced variations due to impending earthquakes in radon are contaminated by meteorological changes (i.e. Atmospheric temperature, pressure, precipitation, etc.) and, hence assessment and quantification of these influences are a major prerequisite in the isolation of precursory signals. Long term time series data are fundamental to try various numerical tools to quantify the influences of meteorological parameters as well as critical to re-validate the developed methodology using some recent segments of the data. As per the present practice, the data from various stations are examined synoptically to evaluate earthquake precursory signals against the backdrop of rainfall and other environmental factors. The present study is aimed at the appraisal and filtrations of these environmental/ meteorological parameters and to create real-time database for earthquake precursory study.

Methodology

Temporal soil-gases compositional variations were measured regularly at continuous earthquake monitoring stations using RTM2100 (SARAD) for radon and thoron measurement following the procedure as described in Walia et al, 2009b. Seismic parameters (viz. earthquake parameters, intensity at a monitoring station, etc.) and meteorological parameter data were obtained from Central Weather Bureau of Taiwan (www.cwb.gov.tw).

To carry out the present investigation, temporal soil-gases compositions variations were measured regularly at continuous earthquake monitoring stations using RTM2100 (SARAD) for radon and thoron measurement (for details see previous reports).

Results and Discussions

Taiwan is one of the most active seismic regions of the world with an average of about 20,000 earthquakes occurring every year in or around as reported by the Central Weather Bureau of Taiwan (www.cwb.gov.tw). In earthquake prediction research it is extremely important to estimate the size and shape of the earthquake preparation zone. Based on previous year's long term geochemical monitoring results at the established earthquake monitoring stations HC, HH and JS. We proposed and published a tectonic based model (Walia et al., 2009b). According to that proposed model HC and HH monitoring stations give precursory signals for impending earthquake that happened in different tectonic settings/zones of Taiwan (see previous reports). It has been found that variations in soil gas at HC are disturbed by the stress variation due to tectonic activities along Okinawa Trough and Ryukyu Trough, which are located in north and central eastern part of Taiwan, respectively, in addition to local earthquakes within the periphery of about 50kms from the monitoring station. Whereas, in the case of HH, soil-gas variations are observed to be due to tectonic activities along the Luzon Arc and subduction of the Eurasian plate in the southern part of Taiwan. Hence, it implies that HH monitoring station shows precursory signals for earthquakes occurring south or southeastern part of Taiwan, whereas, for HC most of soil-gas variation precursory signals are recorded for the earthquakes that occurre north or northeastern part of Taiwan. However, both the monitoring stations have a common overlapping zone, indicative of the fact that the earthquakes that happen to be in this region might have precursory signals in both the monitoring stations. In addition to that, it is essential to define some selection criteria to identify threshold earthquakes for this study. Based on the anomalous signatures from particular monitoring stations we are in a state to identify the area for impending earthquakes of magnitude ≥ 5. For selection criteria, earthquakes having local intensity ≥ 1 at the monitoring stations with epicentral distance (R) < 150 kms having D/R ratio ≥ 1 with focal depth < 40 kms are considered.

Despite some success stories for each class of precursors, no individual is considered diagnostic for application in real-time forecasting of earthquakes. Characterisation of true time-evolution of precursory signatures, their identification in tectonic settings and cross-validation among different classes is the road map to advance the science of earthquake precursory research, especially for their prognostic implementation. Such goals and growth of earthquake precursory research can be achieved by real-time database with multiple data sets of various parameters, e.g. all the monitoring stations, seismic parameters and meteorological parameters.

As per the present practice, the data from various stations are examined synoptically to evaluate earthquake precursory signals against the backdrop of rainfall and other environmental factors (see the previous reports). Various guidelines are developed to identify the nature of precursory signals almost in real-time. Time to time real-time base has been developed, modified and used. In recent years manually operating real-time base had been developed and efforts were made to improve it. During the last year, to increase the efficiency of real-time base and to improve data processing system for earthquake precursory studies. Efforts were made to change the real-time database from manually to automatically operating system. For the earthquake prediction the efficiency of an operation system depends not only upon its logical correctness, but also upon the response time . So, it's very important to work on reducing the "response time" effectively, which it can be achieved by using with some information technology techinques.

For creating a real-time geochemical database, for quantitative/qualitative analysis of the gentrated data. Hence, we can ehance the information integration system for earthquake prediction studies. Firstly, we tried to replace the business package software "Visual Signal" to an open source programming language "R" for the data computing work. “R” is a free software programming language and software environment for statistical computing and graphics. The R language is widely used among statisticians and data miners for developing statistical software and data analysis. R provides a wide variety of statistical and graphical techniques, including linear and nonlinear modeling, classical statistical tests, time-series analysis, classification, clustering, and others. Polls and surveys of data miners are showing R's popularity has increased substantially in recent years. R is highly extensible through the use of user-submitted packages for specific functions or specific areas of study. Another strength of R is static graphics, which can produce publication-quality graphs, including mathematical symbols.

The data processing flow also includes a low-pass filter to reduce the noise level. It will filter out the high frequency noise and daily variation caused by different parameters like measurement uncertainty, background noise, environmental parameters and earth tides (Fig.1).

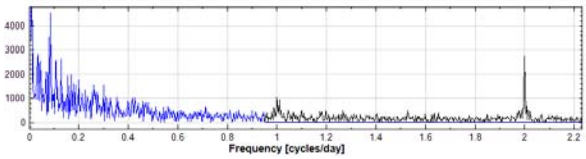

Fig.1.The blue line is filtered FFT result computed from the R script to compare with the original signal (black line).

The rolling average and normalization were used to quantify the probability distribution of variation in the data (Fig.2). In the fig.2 blue line recipients are the final processed result computed from the R script. Comparing the results computed from business package software "Visual Signal"(black line) it has been found the result from both the techniques almost similar. From the residual plot it can be seen that the difference is less than 0.2 (Fig.3). So it can successfully replace "Visual Signal" for our study.

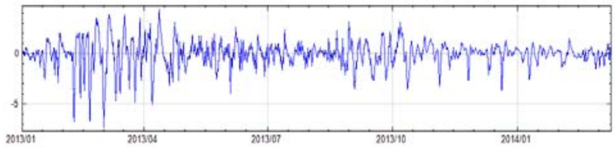

Fig. 2. Final processed plot computed from the R after rolling average and normalization distribution.

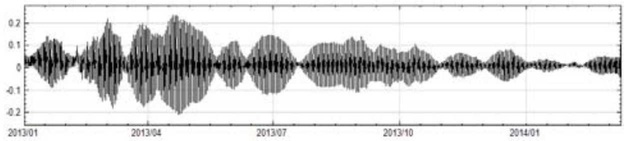

Fig. 3. Residual plot shows the difference is less than 0.2.

We upgraded our working procedure to "programmed data operation and visualization", which not only helps to have the ability to achieve real-time, but also help in batch processing to reduce the response time. It also helps to move a step forward to integrate our data with the popular and famous open source web application solution stack "AMP" (Apache, MySQL, and PHP). The Apache HTTP Server, commonly referred to as Apache, is a web server application notable for playing a key role in the initial growth of the World Wide Web. MySQL "My S-Q-L"officially, but also called "My Sequel" is the world's second most widely used open-source relational database management system.Whereas, PHP is a server-side scripting language designed for web development but is also used as a general-purpose programming language. Above said methodology was adopted to process the data from the monitoring stations (run by NCREE and NTU in collaboration) and automatically uploaded to the web service which provides the data management/exhibition with less response time database. In addition to monitoring station data seismic parameters (i.e. magnitude/location/depth of event, intensity/epicentral distance at monitoring station etc.) and meteorological parameter data are also uploaded from Central Weather Bureau of Taiwan (www.cwb.gov.tw) simultaneously (Fig.4). It would be helpful in increasing efficiency of earthquake prediction studies.

During the observation period of 2013, about 33 earthquakes of magnitude ≥ 5 were recorded in and around Taiwan. However, out of these, 14 earthquakes fell under the defined selection criteria and were tested for the proposed model. Out of these 14 earthqaukes 9 have shown precursory signals.

References

Etiope G., Calcara, M., Quattrocchi, F. (1997). “Seismogeochemical algorithms for earthquake prediction: an overview”. *Annali Di Geofisica*, 40(6), 1483-1492.

Dobrovolsky, I.P., Zubkov, S.I. and Miachkin, V.I. (1979). “Estimation of the size of earthquake preparation zones”. *Pure and Appl. Geophys*., 117, 1025-1044.

Kumar, A., Singh, S., Mahajan, S., Bajwa, B.S., Kalia, R., Dhar, S., (2009). “Earthquake precursory studies in Kangra valley of North West Himalayas, India, with special emphasis on radon emission”. Appl. Radiat. Isot. 67, 1904-1911.

Fu, C.C., Yang, T.F., Walia, V., Chen, C.H. (2005). “Reconnaissance of soil gas composition over the buried fault and fracture zone in southern Taiwan”. *Geochemical Journal*, 39,427-439.

Walia, V., Yang, T.F., Lin, S.J., Hong, WL., Fu, C.C., Wen, K-L.,Chen, C-H. (2009a). “Geochemical variation of soil-gas composition for fault and earthquake precursory studies along Hsincheng fault in NW Taiwan”. *Appl. Radiat. Isotopes, 67, 1855- 1863*.

Walia, V., Yang, T.F., Lin, S.J., Hong, W.L., Fu, C.C., Wen, K.L.,Chen, C.H. (2009b). “Continuous temporal soil.gas composition variations for earthquake precursory studies along Hsincheng and Hsinhua faults in Taiwan”. *Radiat. Meas.,* 44, 934.939.

Walia, V., Virk, H.S., Yang, T. F., Mahajan, S., Walia, M. and Bajwa, B.S. (2005). “Earthquake prediction studies using radon as a precursor in N.W Himalayas, India: a case study”. *TAO*, 16(4), 775.804.

Walia, V., Lin, S-J.,Yang, T.F., Fu, C-C., Hong, W-L., Wen, K-L.,Chen, C-H. (2010). “Soil-gas monitoring: A tool for fault delineation studies along Hsinhua Fault (Tainan) Southern Taiwan.” *Applied Geochemistry, 25,* 602-607.

Walia, V., Yang, T.F., Lin, S-J., Kumar, A., Fu, C-C., Chiu, J-M., Chang, H-H., Wen, K-L.,Chen, C-H. (2012). “Temporal variation of soil gas compositions for earthquake surveillance in Taiwan.” *Radiat. Meas.,* http://dx.doi.org/10.1016/j.radmeas.2012.11.007.

Yang, T.F., Chou, C.Y., Chen, C.H, Chyi, L.L., Jiang, J.H. (2003). “Exhalation of radon and its carrier gases in SW Taiwan”. *Radiat. Meas.* 36, 425.429.

Yang, T.F., Fu, C.C., Walia, V., Chen, C.H., Chyi, L.L., Liu, T.K., Song, S.R., Lee, M., Lin, C.W., Lin, C.C., (2006). Seismo-geochemical variations in SW Taiwan: multi.parameter automatic gas monitoring results, *Pure Appl. Geophys.*, 163, 693.709.

Yang, T.F., Wen, H.-Y., Fu, C.-C., Lee, H.-F., Lan, T.F., Chen, A.-T., Hong, W.-L., Lin, S.-J., Walia, V., (2011). “Soil radon flux and concentrations in hydrothermal area of the Tatun Volcano Group, Northern Taiwan”. *Geochem. J.*, 45, 483-490.

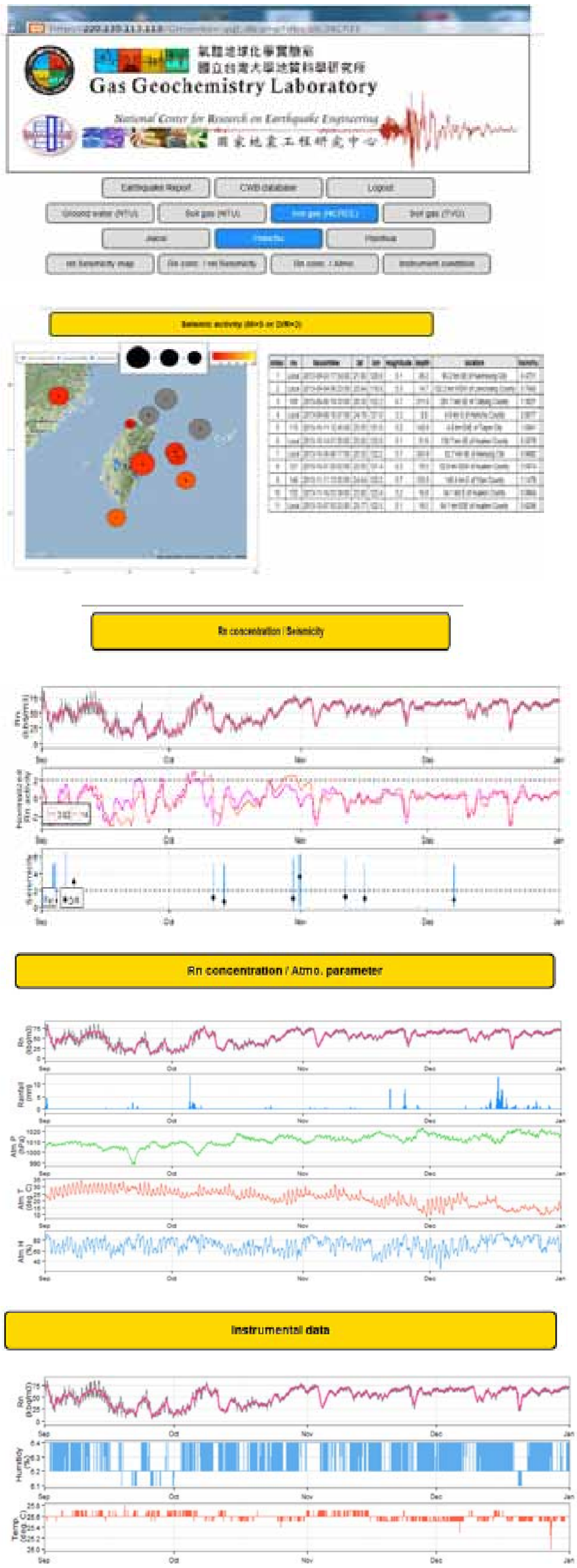

Fig. 4. Real-time database for all the monitoring station data (e.g. HC monitoring station) with seismic parameters and meteorological parameters.

Analysis of Site Effects using Microtremors and Velocity Measurements

Chun-Hsiang Kuo[1], Hung-Hao Hsieh[2], Che-Min Lin[1], and Kuo-Liang Wen[3]

郭俊翔 [1]、謝宏灝 [2]、林哲民 [1]、溫國樑 [3]

Abstract

In order to develop a new microtremor technique, this study conducts microtremor measurements at free-field strong motion stations in Ilan, Taiwan. The Engineering Geological Database for TSMIP in this area, which contains 48 stations, is also used to analyze the properties of microtremors as well as site effects. In addition, we installed a downhole array of accelerometers at the National Center for Research on Earthquake Engineering (NCREE). The preparations for microtremor analysis, geological drilling, and PS-logging velocity measurements are introduced in this report. The dominant frequencies of the Horizontal-to-Vertical Spectral Ratio (HVSR) of microtremors are proportional to the average shear-wave velocity in the first 30 m of the subsoil (Vs30) in the Ilan area. The dominant frequency increases with the increase in Vs30. However, for stations belonging to classes D and E with a sediment thickness of more than 30 meters, the Vs30 value can indicate the difference in velocity between the two classes. HVSRs reflect the sedimentary depth, and therefore, it is not easy to define the difference between two classes. We found similar situations in Taipei, Kaohsiung, and Pintong. Most of the strong motion stations are located in plain areas and are classified as class D, showing no significant variations in the shear-wave velocity (Vs) with depths. Stations of class C are mainly distributed at the edge of the Ilan plain and show a larger variation in their Vs values with depth. Four class-B stations are distributed from the northeastern corner, along the north of the Ilan plain to the southwestern cornor. The shear-wave velocity of the bedrock is more than 1,000 m/s. There are only three class E stations in the area. The dominant frequencies are less than 2 Hz in the plain area and greater than 3 Hz in the mountainous area. According to drilling results of the borehole at NCREE, the sedimentary depth is 57.7 m, which covers weathering bedrock. A clear velocity increase occurs at a depth of 58 m from the velocity measurement. The estimated depth of the sediment layer is 50.1 m, which is underestimated by the microtremor technique.

Keywords: microtremor, HVSR, free-field strong motion stations, site classification

Introduction

The so-called site effect is the study of seismic wave amplification by local unconsolidated sediments at specific frequencies during strong ground motions. It is an important consideration in both seismology and earthquake engineering. The fact that different seismic site conditions are able to cause varied site effects was first recognized in the 19th century. Site effects can be evident at two nearby stations, and this indicates the importance of site effects in strong ground motions.

Microtremors are caused by various natural (such as wind, tide, and rain) and artificial (such as traffics and industrial) vibration signals. These signals occur continually and thus the time of measurements can be

[1] Associate Researcher, National Center for Research on Earthquake Engineering, chkuo@ncree.narl.org.tw; cmlin@ncree.narl.org.tw

[2] Assistant Researcher, National Center for Research on Earthquake Engineering, hhhsieh@ncree.narl.org.tw

[3] Professor, Dep. of Earth Science, National Central University and Division Manager, National Center for Research on Earthquake Engineering, wenkl@ncree.narl.org.tw

very short in comparison with that for earthquakes. After Nakamura (1989) proposed the Horizontal-to-Vertical Spectral Ratio (HVSR) method, microtremors became a popular tool to assess site responses to ground motions, *i.e.*, the resonance frequency and amplification factor at a specific site. The Engineering Geological Database for TSMIP (EGDT) was constructed by the NCREE and Central Weather Bureau (CWB), and includes logging data at over 400 stations. Data on the Vs30 and site classification of drilled stations has also been accomplished (Kuo *et al.*, 2011; 2012) according to the criteria of the Building Seismic Safety Council (2001). Site classification is a prerequisite for the present study of developing HVSR models for different seismic site conditions in this study. 48 stations were characterized in EGDT for Ilan.

In this study, microtremors were measured at 43 free-field TSMIP stations in Ilan (Fig. 1) containing two stations of class B, eleven stations of class C, 28 stations of class D, and two stations of class E. The data were used to analyze the properties of microtremors in different site conditions.

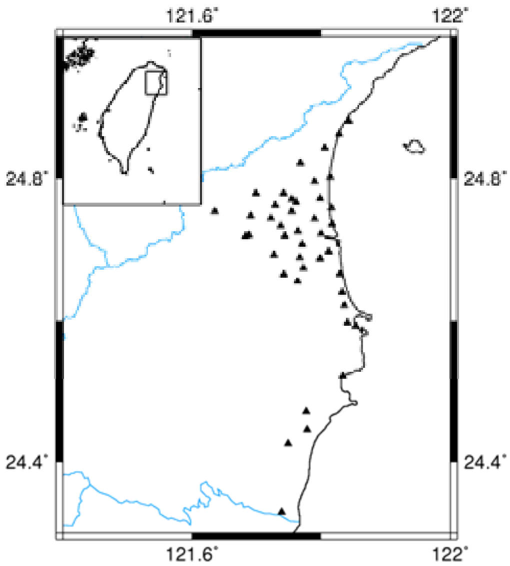

Fig. 1 Distribution of the measured stations (black triangles) in Ilan.

Fig. 2 The locations of the three boreholes at NCREE.

Two engineering boreholes (BH1 and BH2) were drilled at the location shown in Fig.2 when the NCREE extended its laboratory. For the installation of a downhole array of accelerometers at the NCREE, borehole drilling (AH4) as well as PS-logging measurements were implemented. The result can be used to test the accuracy of the approach for estimating sedimentary depth and Vs30 using HVSRs. Otherwise, the Vs empirical equations proposed by Kuo *et al.* (2012) can also be examined.

Microtremor measurements and data processing

A SAMTAC-801B recorder and a VSE311C sensor manufactured by Tokyo Sokushin as well as a K2 recorder with an EpiSensor manufactured by Kinemetrics were the instruments used in the study. The sampling rate was 200 points per second and the recording period was 18 minutes for each measurement. The microtremor measurements were located at the sides of each station to ensure that the geological conditions were identical. The instrumental response was eliminated in the HVSR procedure. Multi-windows with a length of 8192 points were utilized to partition the microtremor recordings, and a 6% cosine taper was implemented at both ends of each window. The recordings were checked so that windows contaminated by unusual noise could be deleted in advance; however, the number of selected windows was maintained at more than 20 to ensure that the averaged result was stable. A geometric mean of the horizontal Fourier spectra was calculated, smoothed five times, and then divided by the smoothed vertical Fourier spectrum to derive a single HVSR. After averaging the single HVSR of each window, the mean HVSR at a station was finally derived.

Properties of microtremors

The HVSRs of microtremors at the 43 strong motion stations were derived following the standard data processing steps introduced in the previous section. The HVSRs were plotted using different colors according to the Vs30 values from the logging data (Fig. 3). From this figure, it can be seen that the dominant frequencies increased with Vs30. Roughly speaking, the colors of class D and E stations are yellow, that of class C stations are green, and that of class B stations are blue in this figure. Most of the stations were classified into classes C and D as can be seen in this figure.

Moreover, these HVSRs were categorized into classes B, C, D, and E and further averaged in each class (Fig. 4) according to the site classification of Kuo *et al.* (2012). Accordingly, the differences in HVSRs in each class are very evident, with dominant frequency gradually moving to the higher frequencies with an increase in Vs30. Therefore, it is believed that HVSR are can distinguish among site classes (or indicate the hardness of a certain site). The deamplification at higher frequency HVSRs is obvious at the sites of classes D and E and this is also consistent with the results in Taipei. Generally speaking, for class B, the dominant frequency of the averaged HVSR is over 10 Hz, while that for class C is at 4~9 Hz. Meanwhile, there are two dominant frequencies of the averaged HVSR for classes D and E at 1-2 Hz and 0.4-0.6 Hz, respectively. This phenomenon may indicate the variation of the sedimentary depth or imply that two velocity interfaces exist in the subsurface of the plain.

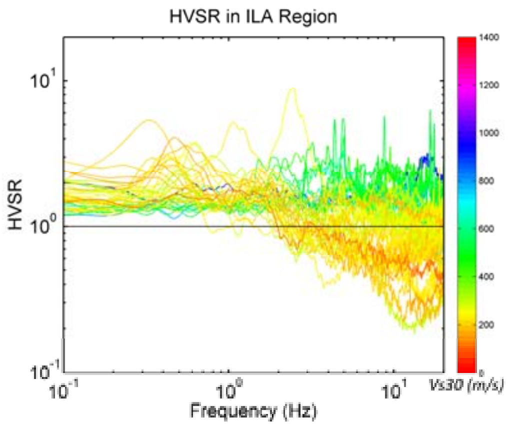

Fig. 3 HVSRs of the 43 measured stations at different seismic site conditions with different colors corresponding to Vs30 values.

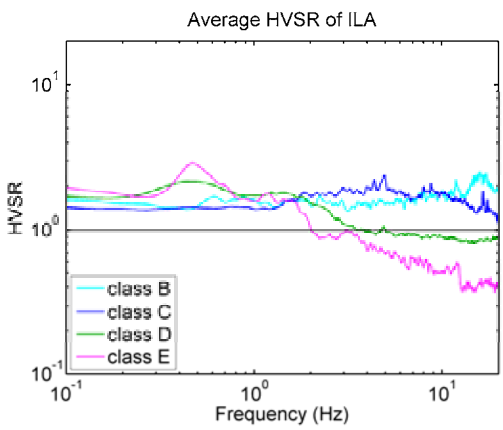

Fig. 4 Averaged HVSRs of class B, C, D, and E in Ilan.

Site characteristics at NCREE

A downhole array of accelerometers was installed behind the laboratory at the NCREE to observe and analyze the propagation and amplifications of seismic waves in the shallow subsurface of the Taipei Basin. The preparations consisted of microtremor measurements and analysis, geological drilling, and suspension PS-logging measurements. We conducted a survey of microtremors at the selected site. The observed HVSR is shown in Fig. 5. The analysis demonstrates that the site should be class D with a Vs30 of 207.2 m/s, and a sedimentary depth of approximately 50.1 m. Meanwhile, according to the drilling results, the depth of the bedrock is 57.7 m.

According to the report of the extension of the laboratory of NCREE, the two engineering boreholes, BH1 and BH2, were drilled and the depths of the bedrock are 42.3 and 48.8 meters, respectively. This result implies that the bedrock underlying the NCREE is on a slope. The shear-wave velocity profiles were calculated from the N-values using the empirical Vs equations for the Ilan region that were proposed by Kuo *et al.* (2012). The profiles are shown in Fig. 6. The values of Vs30 are 223.3 m/s at BH1, 224.8 m/s at BH2, and 213.9 m/s at AH4.

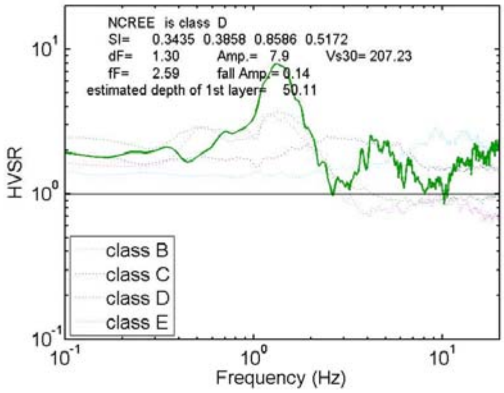

Fig. 5 The HVSR of microtremors and the estimated results at site AH4.

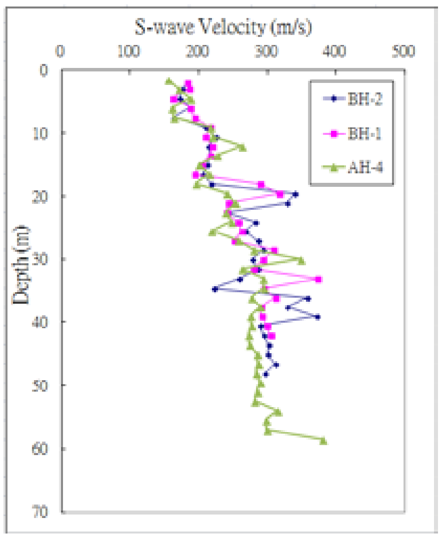

Fig. 6 The estimated Vs profiles calculated by empirical equations using N-values.

Thereafter, we used a suspension PS-logging system to measure the P-wave and S-wave velocities at AH4. The frequency of the velocity measurement is every 0.5 m, and thus we can obtain one P-wave and two S-wave seismograms from every measurement. The depth sequences are composed of P-wave and S-wave seismograms, as shown in Fig. 7. A clear time shift of P-wave and S-wave arrivals can be found at a depth of approximately 58 m. This indicates a clear velocity change at this depth.

After we determined the P-wave and S-wave arrival times of each depth, the velocity profiles of the P-wave and S-wave were plotted, as shown in Fig. 8. The S-wave velocity increases from approximately 150 m/s to approximately 300 m/s at a depth of 30 m, and then no obvious changes occur at the greater depths until the depth of the bedrock reaches 58 m. The S-wave velocity increases to more than 1,000 m/s in the bedrock and the calculated Vs30 is 236.7 m/s. The values and variations of the shallow part of the S-wave velocity profile are very similar to those estimated from the N-values in Fig. 6.

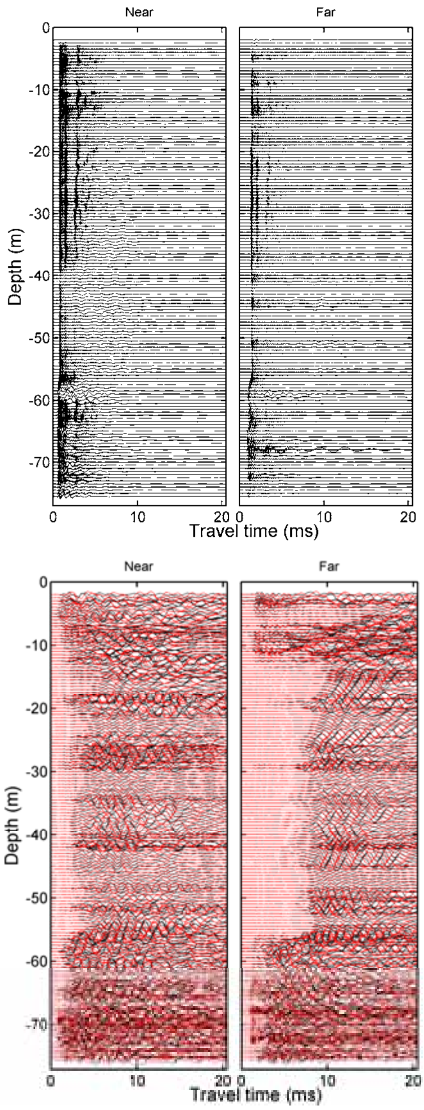

Fig. 7 The depth sequences of the PS-logging measurement at AH4. The upper plot is for the P-wave and the lower plot is for the S-wave.

Conclusions

There were two parts to this report. One is the analysis of the microtremor HVSRs at the free-field strong motion stations in Ilan and the other is the site characterization at the NCREE. In the Ilan area, the dominant frequency at stations of class B is higher than 10 Hz while that at stations of class C is between 4 to 9 Hz. Two dominant frequencies exist at stations of classes E and D, which are between 1 to 2 Hz and 0.4 to 0.6 Hz, respectively. This either indicates variations of the sedimentary depth or implies two possible interfaces in the subsurface. The HVSRs and drilling results show a sloped bedrock underlying the NCREE with a depth variation of around 40 to 60 meters. The estimated bedrock depth and Vs30 values using microtremors are underestimated; however, the deviations are acceptable. The comparison between the estimated and observed S-wave velocity profiles at the NCREE (Fig.6 and Fig.8) shows the accuracy and reliability of the proposed empirical equations for the S-wave velocity (Kuo *et al.*, 2012).

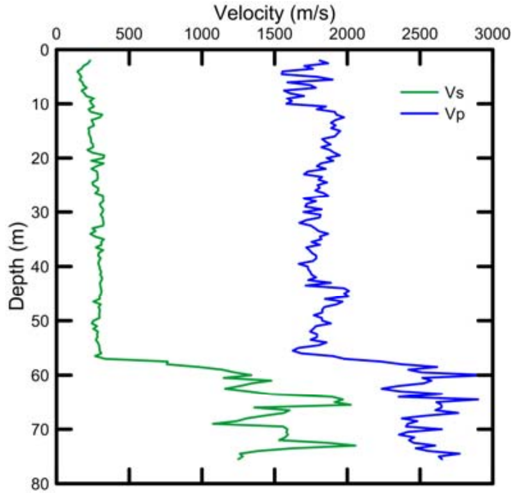

Fig. 8 The observed P-wave and S-wave velocity profiles at AH4.

References

Building Seismic Safety Council, BSSC (2001), “NEHRP Recommended Provisions for Seismic Regulations for New Buildings and Other Structures”, Washington, DC.

Kuo, C. H., K. L. Wen, H. H. Hsieh, C. M. Lin, and T. M. Chang (2011), “Characteristics of Near-Surface S-wave Velocity”, National Center for Research on Earthquake Engineering, NCREE-11-022, 82 p. (In Chinese)

Kuo, C.H., Wen, K.L., Hsieh, H.H., Lin, C.M., Chang, T.M., and Kuo, K.W. (2012), “Site Classification and Vs30 estimation of free-field TSMIP stations using the logging data of EGDT”, *Engineering Geology*.

Nakamura, Y. (1989), “A method for dynamic characteristics estimation of subsurface using microtremor on the ground surface”, *Quarterly Report of Railway Technical Research Institute*, 30 (1), 25-33.

Earthquake Source Parameters of Active Faults for Seismic Potential Assessment in the Chianan Region of Taiwan

Che-Min Lin[1], Hung-Hao Hsieh[2], Yi-Zen Chang[3], Chun-Hsiang Kuo[4], and Kuo-Liang Wen[5]

林哲民 [1]、謝宏灝 [2]、張議仁 [3]、郭俊翔 [4]、溫國樑 [5]

Abstract

The Chiayi and Tainan (Chianan) regions in southwestern Taiwan are scattered with several active faults that have induced massive earthquakes. The seismicity is generally quite high and widespread in this region. The potential for disastrous earthquakes is expected to be high in the near future. Therefore, the present study aims to monitor micro-earthquake activity in the Chianan region over three years. The acquired monitoring data will provide important information about recent seismicity and the source parameters of active faults, which are indispensable in assessing the seismic potential of the Chianan region. Over 2100 earthquakes were observed using a broad-band micro-earthquake network. The data are processed and analyzed periodically to evaluate the seismicity of the Chianan region. Earthquake relocations and focal mechanism solutions were also studied to understand the probable seismogenic structures and source ruptures. Several earthquake clusters induced by the activities of faults are identified in this study. The rupture planes and seismicities of some active faults are confirmed.

Keywords: earthquake monitoring, active fault, earthquake location, focal mechanism

Introduction

Over the last century, the Chiayi and Tainan (Chianan) region in southwestern Taiwan has experienced numerous serious disasters caused by massive earthquakes, including the Meishan earthquake in 1906, the Chungpu earthquake in 1941, the Hsinhua earthquake in 1946, the Paiho earthquake in 1964, the Rueyli earthquake in 1998, and the Chiayi earthquake in 1999. More recently, the Jiasian earthquake occurred in Kaohsiung with a magnitude of M_L = 6.7 and also caused damage to some buildings in the Chianan region. According to the paleoseismological research of the National Science Council, the Meishan Fault in Chiayi has the highest short-term probability of experiencing a characteristic earthquake amongst all active faults of the first catagory in Taiwan. The probabilities of earthquakes from these faults with magnitudes of 7 or more within 10 and75% a 50 years are 9.nd 45%, respectively. Additionally, there are still four other active faults of the first category and four faults of the second category rooted in the Chianan region. Since there is the potential for disastrous earthquakes in the Chianan region in the near future, it is imperative to understand the characteristics of the active faults in this region.

Therefore, this study monitored the micro-earthquakes to understand the seismicity of active faults in the Chianan region over three years. The fault planes and rupture mechanisms of the faults were also studied to estimate the source parameters of characteristic earthquakes for assessing the seismic potential of the Chianan region.

Micro-Earthquake Monitoring Network in the Chianan Region

The development and planning of the micro-earthquake monitoring network in the Chianan

[1] Associate Researcher, National Center for Research on Earthquake Engineering, cmlin@ncree.narl.org.tw
[2] Assistant Researcher, National Center for Research on Earthquake Engineering, hhhsieh@ncree.narl.org.tw
[3] Assistant Researcher, National Center for Research on Earthquake Engineering, yzchang@ncree.narl.org.tw
[4] Associate Researcher, National Center for Research on Earthquake Engineering, chkuo@ncree.narl.org.tw
[5] Professor, Dep. of Earth Science, National Central University and Division Director, National Center for Research on Earthquake Engineering, wenkl@ncree.narl.org.tw

region was based on the distributions of historical earthquakes and major fault lines. Twenty-one stations were installed to develop the network in the second half of 2011. In addition, several real-time stations were also installed in the Chianan region. Each real-time station was equipped with a broadband velocimeter and an accelerometer. The combined monitoring data provides complete ground motion information for the region.

Figure 1 shows the distribution of all seismic stations of the micro-earthquake network installed in this study. Because the seismicity was widely distributed over the Chianan region, the integrated network covered Chiayi County and City, Tainan City, and the adjacent foothills over which the faults were spread. The network provides the complete ability to monitor the seismicity of the Chianan region.

High-sensitivity broadband seismometers (CMG-6TD, Guralp Systems Ltd) were used in the micro-earthquake network to detect weak seismic waves. Recording was conducted continuously with a sampling rate of 100 points per second to avoid missing any micro-earthquakes. A set of solar energy equipment and a GPS antenna were installed at each station to supply electricity and correct the internal clock of the seismometer. In the real-time strong motion stations, a broadband seismometer and an additional accelerometer (Etna, Kinemetrics) were set up together.

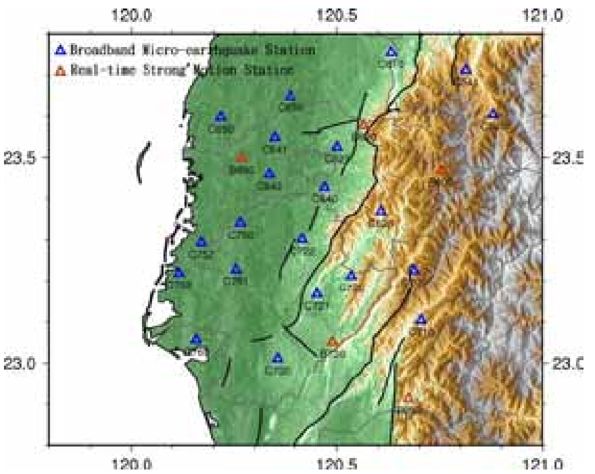

Fig. 1 The distribution of the monitoring network in the Chianan region.

Data Processing

Data processing was based on a program developed by the National Center for Research on Earthquake Engineering (NCREE) for the micro-earthquake monitoring network (Chang, 2009). Data conversion, earthquake selection, arrival time selection, and earthquake location techniques are all included in the program. The preliminary location for each earthquake was determined using the program HYPO 71 to estimate the origin time, epicenter location, focal depth, and duration magnitudes (M_d) based on the arrival times of the P- and S-waves.

Figure 2 shows the distribution of over 2100 micro-earthquakes located by the Chianan network between October 2011 and November 2013. As expected, the micro-earthquakes exhibited a widespread and frequent distribution within the monitoring scope of the network. In the northern part of the monitoring region, the Chiayi region, the earthquakes were concentrated at the eastern side of the Tachienshan and Chukou Faults. Some earthquakes also took place east of Chiayi City. Meanwhile, the seismicity was lower near the Meishan and Hsinhua Faults, which are dislocated and have induced destructive earthquakes in the past. In Tainan City, in the southern part of the monitoring region, high seismicity was highly concentrated along the Chukou, Muchiliao, and Liuchia Faults and extended to the southeast of the northern Chishan Fault. Earthquakes occurred on both sides of these faults and were uniformly concentrated along the fault traces to form a wide NW–SE trending seismic zone. The seismic zone extends to the border between Kaohsiung and Taitung. The high seismicity may result from a broken local structure.

Furthermore, the mainshock region of the Jiasian earthquake, which occurred on 3rd March 2010, in the south of the network continued to induce small earthquakes. This indicates that the seismogenic structure of the Jiasian earthquake is still active in order to release the associated tectonic stress.

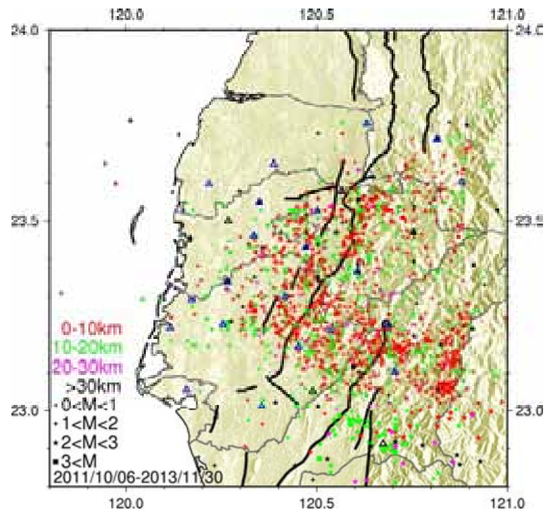

Fig. 2 The earthquakes located by the Chianan micro-earthquake monitoring network in this study.

To reduce location errors, a double-difference hypocenter location program, called hypoDD (Waldhauser and Ellsworth, 2000) was used to relocate the earthquakes observed by the network. This program incorporates ordinary absolute travel-time measurements and cross-correlation of P- and S-wave differential travel-time measurements to determine high-resolution hypocenter locations for an earthquake sequence. The location method collapses diffuse locations into sharp images of seismicity and reveals seismogenic structures. Some 703 earthquakes were relocated by hypoDD and are shown in Fig. 3.

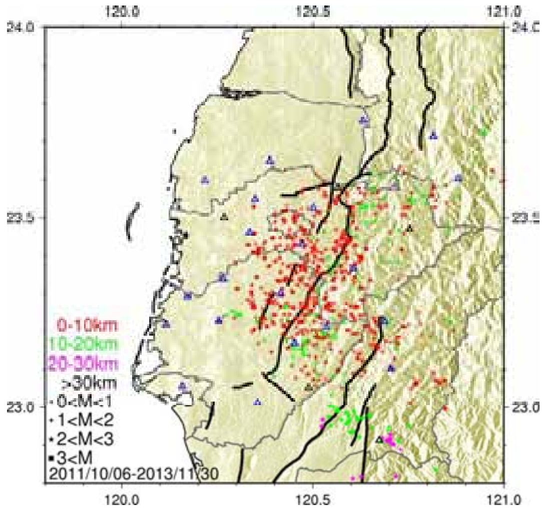

Fig. 3 Double-difference locations of earthquakes

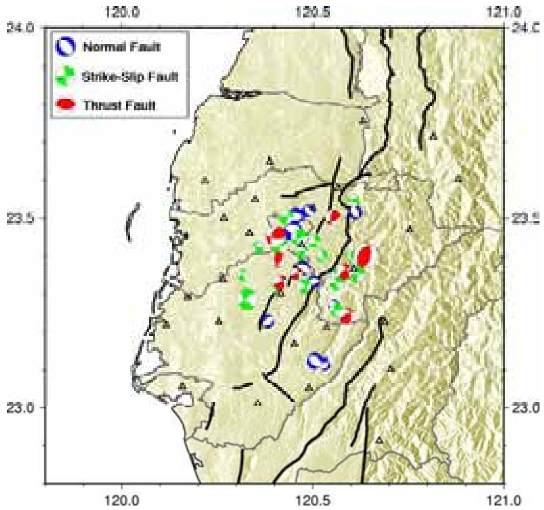

Fig. 4 Focal mechanisms of earthquakes solved by this study

The program HASH, developed by the United States Geological Survey (USGS) (Hardebeck and Shearer, 2002, 2003), was utilized in solving the focal mechanisms of the observed earthquakes. However, the effective first-motion polarities are limited owing to the weak waveforms; therefore, just 52 focal mechanisms were solved and classified (Fig. 4). Most of the solved sources belonged to the strike-slip fault mechanism. The normal fault mechanism was the second most common type of source, but in these cases the magnitudes were mostly smaller than 2. The number of thrust faults, mostly with magnitudes over 3, was the least common source. The active faults spread across the Chianan region mostly belong to the thrust fault mechanism. On the contrary, the frequent micro-earthquakes that were detected exhibited strike-slip or normal mechanism types. The mechanism of these micro-earthquakes may be caused by the repeated accumulation, release, and recovery of tectonic stress in the ruptured zones.

Fault Activities

The catalog of this micro-earthquake monitoring network was compared with that of the Taiwan Strong Motion Instrumentation Program (TSMIP), and all of the clusters of intensive events were checked. Some fault activities have been identified.

Chukou Fault is a thrust fault and has been gauged as an active fault of the first category. The northern end of the fault joins the Tachienshan Fault. On the 18th January 2012, a M_L = 4.2 earthquake occurred at the eastern side of the northern end of the Chukou Fault. The Chianan micro-earthquake monitoring network observed some aftershocks over the next few days. The mainshock focal mechanism and the double-difference hypocenter relocations of the aftershocks along with the cross-section are both shown in Fig. 5. The relocated aftershocks indicate an E–W-striking source rupture plane dipping toward the east with a high angle of 60° according to the cross-section (Fig. 5). The rupture plane agrees with the mainshock focal mechanism. The upward extension of the plane is close to the fault trace of the Chukou Fault on the surface. These results verify that the M_L = 4.2 earthquake and its aftershocks were induced by the partial activity of the Chukou Fault.

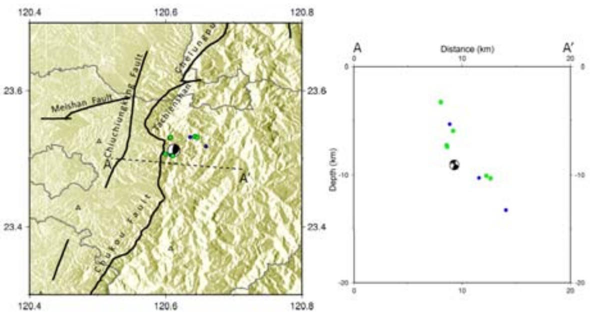

Fig. 5 The CWB mainshock focal mechanism and aftershocks of the 18th January 2012 M_L = 4.2 earthquake relocated by this study. The cross-section of the dashed line is shown on the right-hand side.

During August 2013, a cluster of about a dozen earthquakes (Fig. 6), with magnitudes lower than 2.5, occurred along the eastern side of the middle part of the Chukou Fault. The cross-section view of the cluster also indicates a source rupture plane dipping toward the east, but it shows a gentler dipping angle of 45°. The Chukou fault turns its strike from E–W of the northern part to NE–SW of the middle part at Chukou Village, Chiayi. The tectonic transition of the fault may cause different dipping angles of the rupture plane between the two parts of the Chukou Fault. The Central Geological Survey (CGS) inferred that the dipping angle of the Chukou Fault is about 60°, based on drilling near Chukou Village. This dipping angle is between the two angles exhibited in this monitoring research.

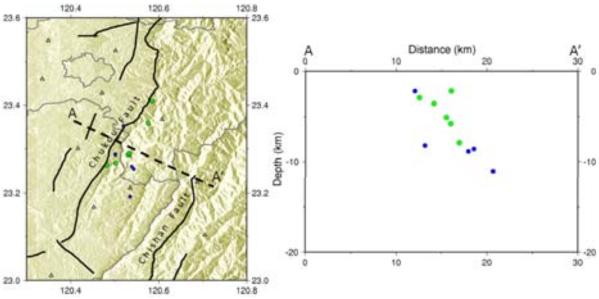

Fig. 6 The micro-earthquake cluster along the middle of the Chukou Fault during August 2013. The cross-section of the dashed line is shown on the right-hand side.

Another cluster of about a dozen earthquakes (Fig. 7), with magnitudes lower than 2, were observed near the Tachienshan Fault between March and April 2013. The cross-section of the cluster shows two rupture planes both dipping toward the east with different angles. The upper one is at a depth of 6 km to 10 km with a gentle slope of 12°, and extends to the underneath of the Chiuchiungkeng Fault. The lower one is at a depth of 8 km to 20 km with a sharper slope of 55°, and occurred at the eastern side of the Tachienshan Fault. Although the local tectonics that include several faults are too complex to be described, the observation still agrees with the difference between the dipping angles of the Chiuchiungkeng (35°) and Tachienshan (72°) Faults, that are both inferred by the CGS.

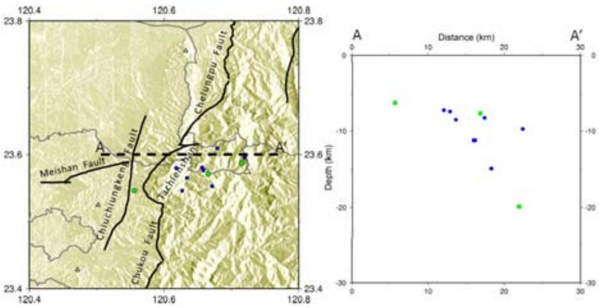

Fig. 7 The micro-earthquake cluster of the Tachienshan Fault between March and April 2013. The cross-section of the dashed line is shown on the right-hand side.

It should be noted that the northern part of the Chishan Fault was gauged as an inactive fault by the CGS. However, the observations made in this research have shown the opposite. On the 6th November 2013, a $M_L = 3.3$ earthquake occurred near the northern part of the Chishan Fault. Some linear foreshocks and aftershocks were located by the micro-earthquake monitoring network (Fig. 8). All the depths of the foreshocks and aftershocks are much shallower than the mainshock, but the downward extension of the southeast dipping plane with a high angle is directed to the mainshock. In addition, an $M_L = 5.2$ earthquake occurred at the northern end of the Chishan Fault on the 5th March 2008. More than 200 foreshocks and aftershocks were observed around the mainshock (Fig. 8). The focal mechanism of the mainshock in 2008 and the spread of the adjoining earthquakes conform to the thrust-type movement on the Chishan Fault. The magnitude of the mainshock in 2013 was much smaller than that of 2008. The location of the earthquake sequence in 2013 was south of that in 2008. The cross-section map in Fig. 8 shows both sequences in 2008 and 2013. The two sequences both dip toward the southeast with a high angle of approximately 70 degrees, and almost overlap each other. It is concluded that the north end of the Chishan Fault ruptured to induce the $M_L = 5.2$ earthquake sequence in 2008. Following this event, the fault remained active and then induced the $M_L = 3.3$ earthquake sequence in 2013. Therefore, the northern part of the Chishan Fault has undoubtedly been active recently.

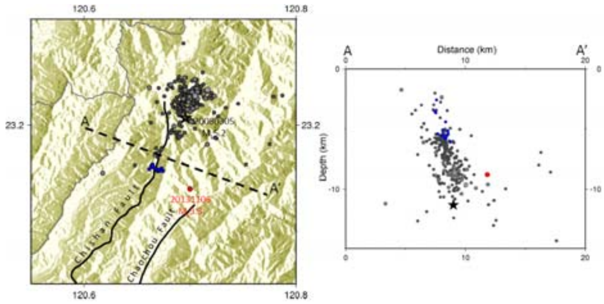

Fig. 8 The mainshock (black stars) and aftershocks (black circles) of the 5th March 2008 M_L 5.2 earthquake, and those (red and blue circles respectively) of the 6th November 2013 $M_L = 3.3$ earthquake. The cross-section of the dashed line is shown on the right-hand side.

References

Chang, T. M. (2009), “Earthquake data processing system installation and using guide”, NCREE Rep., NCREE-09-066. (In Chinese)

Hardebeck, J. L. and Shearer, P. M. (2002), “A new method for determining first motion focal mechanisms”, Bull. Seism. Soc. Am., 92, 2264-2276.

Hardebeck, J. L. and Shearer, P. M. (2003), “Using S/P amplitude ratios to constrain the focal mechanisms of small earthquakes”, Bull. Seism. Soc. Am., 93, 2434-2444.

Waldhauser, F. and Ellsworth, W. L. (2000), "A double-difference earthquake location Algorithm: method and application to the northern Hayward fault, California", Bull. Seism. Soc. Am., 90, 1353-1368.

Tests with Water Pressure and Nonlinear Pushover Analysis under Faulting for Water Pipeline

Lap-Loi Chung[1], Gee-Yu Liu[2], Po-Yu Uang[3], Yu-Hsuan Chiu[4], Chiung-Shiann Huang[5] and Chein-Shan Liu[6]

鍾立來[1]、劉季宇[2]、汪渤喻[3]、邱于軒[4]、黃炯憲[5]、劉進賢[6]、

Abstract

This study has conducted seismic testing of ductile iron pipes with K-type joints, which are a commonly used type of water pipeline in Taiwan. Full and pressurized pipe specimens are tested separately under tension, compression, and bending loads. The capacity of deformation and the failure mechanism of the pipe specimens are investigated experimentally. Before performing a nonlinear pushover analysis of the pipelines, nonlinear plastic hinges for K-type joints are set. In this study, the axial and moment plastic hinges of the pipe with K-type joints are determined by the results of the tests and analyses. According to the results of the nonlinear pushover analysis, the allowable fault displacement and failure modes of pipes under a strike-slip fault are investigated. If the failure mode is a tension failure of the joint, then the allowable fault displacement tends to decrease when compared to a continuous pipeline without joints.

Keywords: water pipelines, pushover, analysis, plastic hinges, DIP, K-type-joint, local buckle

Introduction

The seismic safety of a water system is critical to people's welfare. The pipeline network for a public water supply may be damaged or broken by earthquake-induced ground faulting and vibrations. Evidence from the 1999 Chi-Chi earthquake indicated that ductile iron pipes (DIP)—one of the major pipe materials—were mostly damaged at their joints. The vulnerability of DIPs is highly dependent on the pipe size as well as the joint type. Although the allowable deformation of a pipeline joint is already stated in the manual, seismic forces may induce additional lateral and axial displacements causing pipeline joint failure.

Wang and Yeh (1985) investigated the behavior of a continuous pipe under a strike-slip fault with a Winkler beam and large-deformation analysis. They assumed that the pipe was antisymmetric so that the model could be simplified to consider only half of the model. The model was divided into two sections: one that uses a small element near the fault and another that uses a large element far away from the fault. Hence, a pipe far from a fault has no relative displacements between soil and the pipe and it will be a straight line. After integration of related papers, the National Center for Research on Earthquake Engineering (NCREE, 2012) used the material characteristics of DIPs and ABAQUS to find nonlinear plastic hinges, which are used in the nonlinear pushover analysis of a DIP without joints.

Test and Nonlinear Plastic Hinges

Before carrying out a nonlinear pushover analysis of the pipelines, the nonlinear plastic hinges must be set. A report by the NCREE in 2011 used the material characteristics of DIPs and ABAQUS to find the nonlinear plastic hinges. Figure 1 shows the plastic hinge of a pipeline under a moment, which was set by the relationship of moment-curvature analyzed from ABAQUS. Figure 2 shows the plastic hinge of a pipeline under tension. The yielding force was calculated from the material characteristics of the DIP, and the critical displacement was defined as 10% of the total specimen length. Finally, the behavior of a DIP under compression was analyzed using ABAQUS

[1] Research Fellow and Professor

[2] Associate Research Fellow

[34] Graduate Student

[56] Professor

to establish the plastic hinge, which is shown in Figure 3.

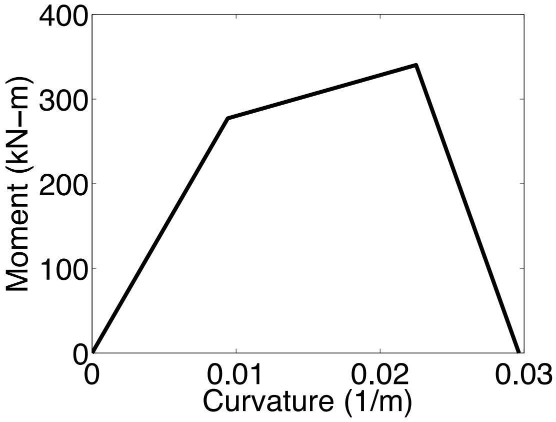

Fig. 1 Plastic hinge of a pipeline under moment

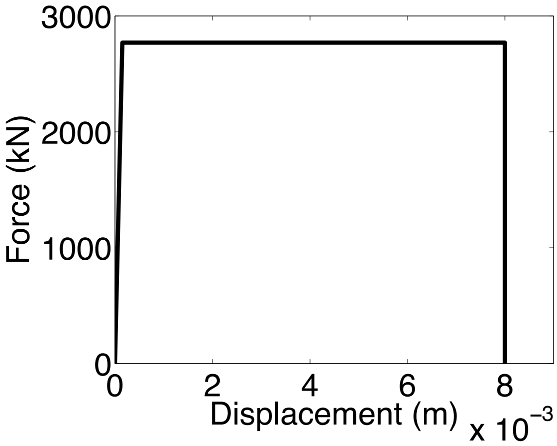

Fig. 2 Plastic hinge of a pipeline under tension

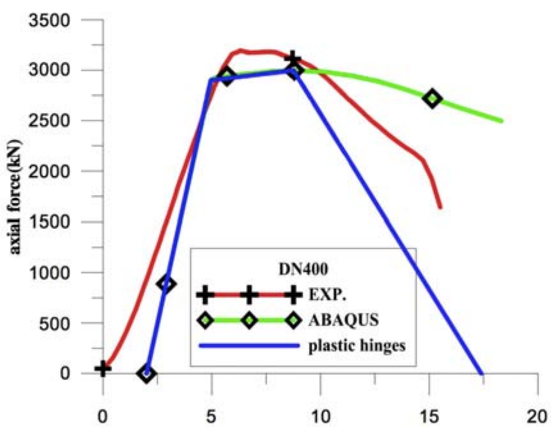

Fig. 3 Plastic hinge of a pipeline under compression

Because the structure of a joint is complex, it is hard to analyze the force–displacement curve using a computer. Thus, we conducted a test for a DIP with a K-type joint to explore mechanical behaviors such as tension, compression, and bending. As the specimen is an underground water pipeline, it was filled with water and the pressure was kept under control. Failure was defined as when the water pressure decreased. Figure 4 shows a K-type joint.

Fig. 4 Clamping ring, rubber ring, T-bolt, and a K-type-joint

Following the tests, we investigated the force–displacement curve of a K-type joint subjected to tension, compression, and bending. After obtaining the force–displacement curve, we found the corresponding nonlinear plastic hinges. Figure 5 shows a force–displacement curve and a nonlinear plastic hinge under bending, and Figure 6 shows those under tension.

In the tensile test, the displacement of a joint was almost the same as the displacement of a specimen. That is, it was completely displaced from the joint. We disassembled the specimen after the test and damage was only observed on the rubber ring. The tension force was completely created from the friction of the rubber ring.

Due to the complicated behavior of compression, the force–displacement curve of compression was analyzed using the commercial code ABAQUS (the procedure is similar to the previous study). Figure 7 shows the force–displacement curve of compression. In this figure, we can see three curves; the unlabeled curve was obtained from testing, that the curve with the plus sign was obtained from ABAQUS. According to these curves, we investigated the nonlinear plastic hinge under compression, which is as shown in Figure 7. The capacities of tensile displacement and rotation are good, but the forces are small, so the displacement cannot be distributed to other sections of the pipeline.

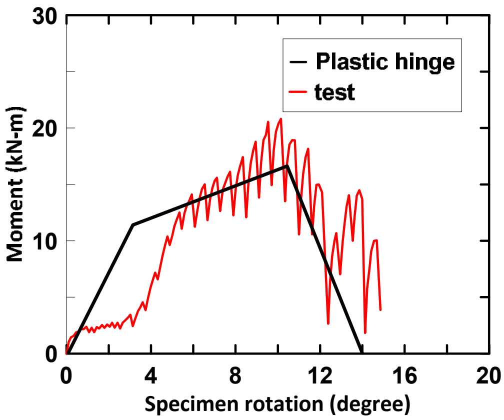

Fig. 5 Moment-rotation under bending

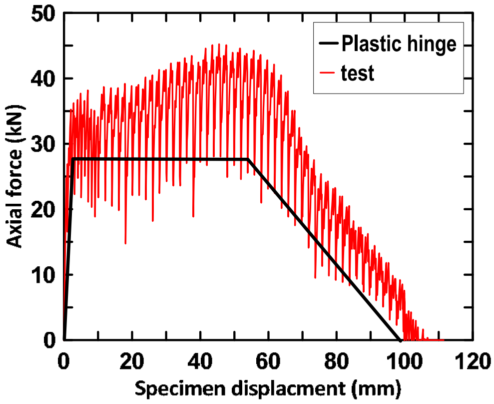

Fig. 6 Force-displacement under tension

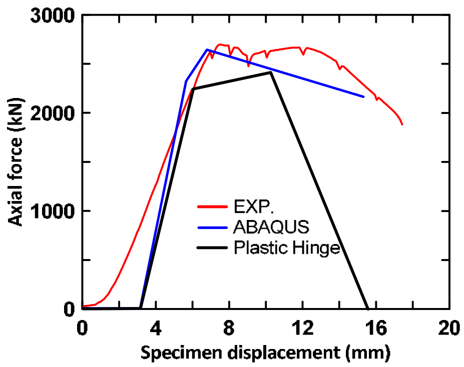

Fig.7 Force-displacement under compression.

Pushover Analysis

Model in SAP2000

The original model was a 372-meter-long DIP with an outside diameter of 0.4 meters, a thickness of 0.007 meters, and a fault in the middle. Due to the assumption of antisymmetric deformation, the model was halved to 186 meters, and a joint was set every 6 meters. In the initial 15 meters, we meshed it to an element with a length of 0.08 meters. The others were 0.04 meters. In this study, only a strike-slip fault took place. Hence, the plane coordinate system (a horizontal surface) was considered, and so did the soil springs (Figure 8). Then nonlinear springs were used to simulate soil and a pushover analysis was performed. The angle of the strike-slip fault varied with an increment of 15 degrees from 0 to 180 degrees (Figure 9).

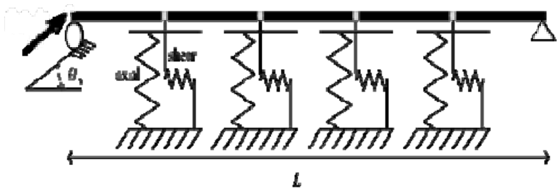

Fig.8 Simplified model of the pushover analysis

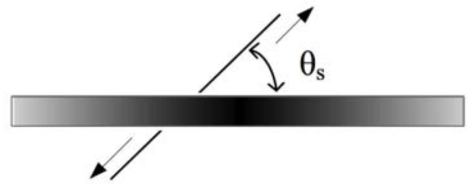

Fig.9 Angle of the fault

Analysis result

From the results, we can observe that as the fault angle varied from 0 to 90 degrees, the axial force on the elements was tension, and, as the fault angle increased from 105 to 180 degrees, the axial force was compression.

Tension failure

Although the whole model was 186 meters long, the failure was concentrated at a location within 3 meters of the fault. Similarly, the moment and axial force approached zero at 40 meters away from the fault in every case. That is, the length of the model was sufficient. Now we can discuss the failure modes in different cases. Due to the small strength of the allowable tension force, the cases from 0 to 90 degrees all failed under tension, and the cases of 75 and 90 degrees underwent yielding due to a moment. We note that the axial force increased and the shear force decreased as the angle between the fault and the pipeline decreased. The pipe itself did not fail or yield under tension, compression, or a bending moment.

Compression or moment failure

Cases with fault angles of 105 and 120 degrees both underwent failure due to the bending moment, and cases with fault angles from 135 to 180 degrees underwent failure due to compression. Similarly, there was also yielding due to the moment for the case with a fault angle of 135 degrees.

Allowable fault displacements

Figure 10 shows a diagram of allowable fault displacements. We note that the curve is not symmetric. The allowable fault displacement when the fault angle was 75 degrees was not equal to that when the fault angle was 105 degrees, and the allowable fault displacement under the compression failure mode was larger than that under the tension failure mode. The reason is that the allowable tension force is small. Because of this, failure under tension at the joints occurred earlier. This figure also shows the allowable fault displacements of a pipeline without joints. Owing to the small amount of allowable tension force of a joint, the allowable fault displacements of the pipeline without joints are always larger than those with joints for the cases from 0 to 75 degrees. Because the joint can carry more curvature, the allowable fault displacement of the pipeline with joints was larger than that for the cases from 90 to 135 degrees. As we set the allowable force and displacements of plastic hinges of joints under compression to be 80 percent of the pipe, the allowable fault displacements of the pipeline with and without joints for the cases from 150 to 180 degrees appears to be in a ratio of 0.8.

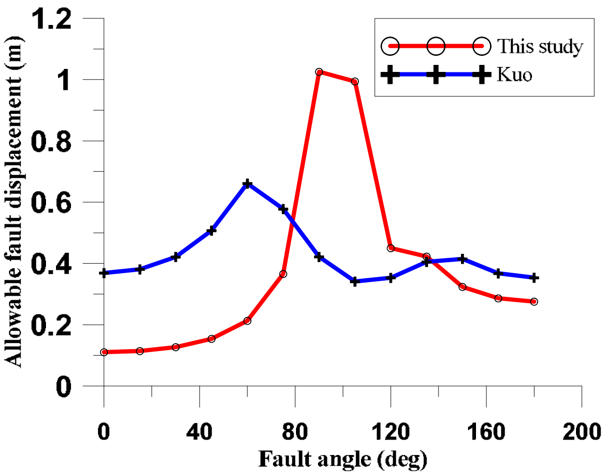

Fig.10 Allowable fault displacements

Conclusion

According to the results of the nonlinear pushover analysis, the main conclusions of this study are summarized as follows:

K-type-joint

A K-type joint is effective at resisting water, but is easy to be separated. It is not as effective in places where large displacements or rotations may occur.

Plastic hinges of a K-type-joint

In this study, we first conducted tests on ductile iron pipes with K-type joints under water pressure, including axial tension, axial compression, and bending. According to the tests, we obtained the force–displacement curve of a K-type joint (compression was analyzed using a commercial code called ABAQUS). Finally, the nonlinear plastic hinges were built.

Allowable fault displacement

Owing to the small amount of allowable tension force, cases with fault angles from 0 to 90 degrees all failed under tension, and cases with fault angles of 75 and 90 degrees underwent yielding due to the moment. Cases with fault angles of 105 and 120 degrees both failed under a bending moment, and cases with fault angles from 135 to 180 degrees all failed under compression. The features of the nonlinear plastic hinges apparently responded to the allowable displacements. According to the previous comparison of allowable fault displacements, the influence of a joint in a pipeline network cannot be neglected, and it can be concluded that joint failure is of a higher proportion than pipe failure.

Reference

Chen, Z. H., Chung, L. L., Wu, L. Y., Liu, G. Y., Hung, K. L. (2012), "Application of Nonlinear Pushover Analysis on Buried Water Pipelines under Faulting", *National Center for Research on Earthquake Engineering*, Research Paper, NCREE-11-026.

Kuo, C. W., Chung, L. L., Wu, L. Y., Chen, Z. H., Liu, G. Y. (2012), "Tests and Nonlinear Pushover Analysis of Water Pipeline", *National Center for Research on Earthquake Engineering*, Research Paper, NCREE-12-010.

Wang, L.R.L., Yeh, Y.H. (1985), "A refined seismic analysis and design of buried pipeline for fault movement" International Journal on Earthquake Engineering and Structural Dynamics, 13(1), pp. 75-96.

Scenario-based Probabilistic Seismic Hazard Analysis of Soil Liquefaction

Chin-Hsun Yeh[1] and Gee-Yu Liu[2]

葉錦勳 [1]、劉季宇 [2]

Abstract

Both severe ground shaking and ground deformation may cause damage to civil infrastructures. Soil liquefaction is one of the well-known seismic hazards in soft soil regions caused by long-duration cyclic shaking. Therefore, it is helpful to have a quick method to assess the soil liquefaction potential, the associated permanent ground deformation (PGD), and the induced damage and losses in a large study region, immediately after a severe earthquake. Since both the duration and intensity of ground shaking may significantly influence the soil liquefaction potential and severity, it is more realistic to estimate the soil liquefaction potential through a scenario-based approach. This paper first proposes a classification scheme for soil liquefaction susceptibility categories (LSC). The exact definition and the assignment of a LSC at a specific site can be obtained from engineering borehole data at a site. To facilitate the estimation of the soil liquefaction potential and the associated PGD based only on the LSC, semi-empirical formulas have been derived for each LSC, considering the magnitude of the earthquake scenario, the peak ground acceleration, and ground-water depth at the site. Combining the estimates of ground shaking and deformation, the results can be applied to estimate the probable damage to buildings, bridges, and buried pipelines in a large area. Furthermore, in view of the large uncertainty associated with seismic activities and the consequences, the proposed soil liquefaction assessment model may be integrated with a probabilistic seismic source model to study the liquefaction potential in a probabilistic sense. In other words, a hazard curve of liquefaction potential at a specific site or a hazard map of liquefaction corresponding to specific return periods is studied through a scenario simulation approach.

Keywords: soil liquefaction, liquefaction susceptibility category, seismic scenario simulation, probabilistic seismic source model

Estimation of Liquefaction Potential

According to the earthquake loss estimation methodology of HAZUS, the soil liquefaction susceptibility in a study region is classified into six categories: "very high", "high", "moderate", "low", "very low" and "none". The liquefaction susceptibility categories (LSC) were defined qualitatively in HAZUS, however, HAZUS does not provide any quantitative way to classify soil LSC from engineering borehole data [1]. To overcome this shortcoming and to obtain the LSC map of Taiwan, Yeh et al. [2] proposed a classification scheme for LSC using engineering borehole data, which was collected by NCREE and the joint researchers. Several years later, in order to improve the quality of borehole data and the number of boreholes, the borehole database used to create the LSC map of Taiwan includes those from the Central Geologic Survey Bureau (CGSB). The semi-empirical formulas for estimating the liquefaction probability and the amount of induced PGD were also derived by Yeh et al. [4] who considered the earthquake magnitude, the peak ground acceleration, and the ground water depth of the site.

In the previous study, a modified Seed method [5] was employed to estimate the liquefaction potential at each depth of a site. This method includes the estimation of soil resistance and excitation intensity at each depth of the site, respectively. The

[1] Research Fellow, National Center for Research on Earthquake Engineering, National Applied Research Laboratories

[2] Associate Researcher, National Center for Research on Earthquake Engineering, National Applied Research Laboratories

ratio of soil resistance and excitation intensity is the safety factor which indicates the liquefaction potential at each depth, but not the site as a whole. Considering the effect of depth and using depth as the parameter for a weighting function, Iwasaki et al. [3] developed a soil liquefaction potential index (P_L), which was used to estimate the liquefaction potential and severity at a site. Comparing many liquefied and non-liquefied cases after strong earthquakes, Iwasaki et al. found that P_L could be used as an indicator of liquefied or non-liquefied regions. For $P_L \geq 15$, the liquefaction probability is high and the sites may be severely liquefied. For $P_L \leq 5$, the liquefaction probability is low and the sites may not be liquefied at all.

Using this concept and by varying the levels of peak ground acceleration, boreholes belonging to each susceptibility category, from "very high" to "none" can be identified sequentially, as shown in Yeh et al. [2]. According to Yeh et al. [2], in order to simplify the analysis model and to reduce the number of susceptibility categories, boreholes with $P_L \geq 15$, when the peak ground accelerations are 0.15g, 0.2g, 0.25g, 0.35g and 0.45g, belong to "very high", "high", "moderate", "low" and "very low" susceptibility categories, respectively. Other boreholes with $P_L < 15$ when the peak ground acceleration reaches 0.45g, are classified as "none" with regard to their sensitivity to soil liquefaction. The earthquake magnitude and the ground water depth are assumed to be 7.5 and 1.5 meters, respectively, in the LSC classification scheme.

Using the definitions for each LSC and the borehole database, the influences of PGA, earthquake magnitude, and ground water depth in the estimation of liquefaction potential can be studied in detail. From the figure of P_L versus PGA for different susceptibility categories and under various earthquake magnitude and ground water depths, it is noted that the relationships between P_L and PGA are almost linear within the range $5 \leq P_L \leq 20$. Thus, for simplicity, the liquefaction potential index for different LSC can be expressed as follows:

$$P_{L,i} = \alpha_i f(M) g(d_w) \cdot \mathrm{PGA} + \beta_i \tag{1}$$

where

$$f(M) = 0.0353M^2 - 0.1855M + 0.4069$$

$$g(d_w) = 0.0002{d_w}^4 - 0.0051{d_w}^3 + 0.0535{d_w}^2 - 0.2758d_w + 1.3105$$

and the values of α_i and β_i are shown in Table 1.

Table 1 Values of α_i and β_i in Eq. (1).

Category	α_i	β_i
Very High	227.52	-13.63
High	188.30	-18.45
Moderate	157.35	-20.51
Low	103.02	-14.95
Very Low	66.95	-10.64

Probabilistic Seismic Source Model and Hazard Anaylsis

It is well known that there are large uncertainties in earthquake occurrences and the induced consequences. Hence, seismic hazard analysis at a specific site is often carried out through a probabilistic approach. Traditionally, probabilistic seismic hazard analysis (PSHA) considers only ground-motion estimates and involves four steps. The first step is to identify and characterize all the probable seismic sources, including the known active faults and the area-sources with unknown fault locations or rupture directions, in the neighborhood of the study region. The second step is to characterize the temporal distribution of earthquake recurrence with respect to different magnitudes, such as the Gutenberg-Richter relationship, to determine the probable ultimate magnitude for each seismic source, and to specify the scaling law of earthquake magnitude with respect to fault rupture length, area, and dislocation. The third step is to select an appropriate ground-motion prediction model. The last step is the summation of individual effects due to different seismic sources. The uncertainties in the earthquake location, fault rupture direction, and ground-motion prediction model should be taken into consideration to obtain the probability that the ground motion parameter will be exceeded during a particular time period.

The seismic source model in PSHA is a description of the spatial and the temporal distribution of earthquakes with various magnitudes and focal depths. Referring to the fault-rupture model proposed by Der Kiureghian et al [4], the known active faults were classified as Type 1 sources. The remaining seismic sources with unknown fault locations or rupture directions were classified as either Type 2 or Type 3 and they are referred to as area sources in this study. The area sources are often classified by focal depth (denoted as shallow or deep sources) and are divided into several zones according to historical seismicity and tectonic conditions so that the seismic source characteristics may be assumed to be similar in each zone. The seismic source zones are further divided into smaller grids in the calculation of hazard curves or risk estimates. The annual earthquake occurrence rate in each grid can be assumed to be uniform within each zone or proportional to the number of historical earthquakes that occurred within the grid. In view of the uncertainty of future earthquakes and the tendency for earthquakes to occur in particular regions, it is most likely that the true annual earthquake occurrence rate in each grid lies within the previous bounds.

Representative Scenario Earthquakes

In order to carry out a scenario-based probabilistic seismic risk assessment, the first step is to select or to define a set of representative scenario earthquakes. The set of representative scenario earthquakes should represent all of the possible cases that may occur in the future around the study region. As is mentioned in the previous section, all of the possible seismic sources are divided into two types: known active faults and area-sources with unknown fault trace and rupture direction. As the name implies, the known active faults refer to the active faults whose geographic properties, such as the surface trace and the dip angle of the fault plane, have been found. The characteristic earthquake magnitude, average annual slip rate, etc. of each active fault in Taiwan have been investigated by CGSB. The representative scenario earthquakes due to known active faults are modeled as plane-sources so that effects of hanging-wall versus foot-wall sides may be observed in the simulation results.

Since the fault trace and rupture direction of area-sources are not known for certain, it is best to model the representative scenario earthquakes due to area-sources as line-sources. In view of the huge number of possible combinations, it is not practical to model them as plane-sources. In order to include all of the possible cases, the surrounding rectangular region of Taiwan is divided into grids. Six focal depths, which are 5, 15, 25, 35, 45 and 55 km, are chosen to represent the possible focal depths. In each grid and at each focal depth, various earthquake magnitudes from 5.1 to 7.5 with 0.2 increments are defined. The fault rupture length and the number of rupture directions in the set of representative scenario earthquakes are functions of earthquake magnitude.

Seismic Event Loss Table and Risk Estimates

From the analysis of the probabilistic seismic source model, the recurrence rate of each representative scenario earthquake with specific earthquake magnitude, epicenter location, focal depth, and fault rupture direction can be determined either from regression analysis of the historical earthquake catalog or the investigation results of known active faults. On the other hand, the expected consequences of each representative scenario earthquake can be obtained through seismic disaster simulation technology. A seismic event loss table can be calculated by combining these two sets of information [5]. A schematic of this is shown in Table 2; the content of a seismic event loss table includes information such as the scenario ID, annual occurrence rate of the scenario (ν_k), expected loss due to that scenario (L_k), standard deviation of loss given the scenario (σ_k), and the total exposure to the scenario (X_k). Setting the total exposure to the scenario is solely intended to limit the maximum probable value of L_k when it is treated as a random variable.

Table 2 Schematic description of the contents of the seismic event loss table

Scenario ID	Annual Occurrence Rate	Expected Loss	Standard Deviation of Loss	Total Exposure
1	ν_1	L_1	σ_1	X_1
2	ν_2	L_2	σ_2	X_2
…	…	…	…	…
k	ν_k	L_k	σ_k	X_k
…	…	…	…	…
J	ν_J	L_J	σ_J	X_J

The measures of seismic risk are diversified to answer different questions and may include the number of damaged buildings, number of casualties, amount of losses, and so on, which can be obtained as the results of seismic disaster simulations. One seismic event loss table may be virtually established for each type of damage, casualty, and loss for each target (either in a study region or for any specific critical facility).

Once the seismic event loss tables have been obtained, various kinds of risk estimates can be calculated. For example, let L_j denote the expected loss due to scenario earthquake, j , with an annual occurrence rate, ν_j . The average annual loss and the standard deviation of the loss (denoted μ_L and σ_L , respectively) can be expressed as:

$$\mu_L = \sum_j \left(L_j \cdot \nu_j \right)$$

$$\sigma_L = \sqrt{\sum_j \left[\left(L_j^{\,2} + \sigma_j^{\,2} \right) \cdot \nu_j \right]}$$

Case Studies of Soil Liquefaction Hazard Map

If the soil liquefaction susceptibility category (LSC) is assumed to be "very low" everywhere, the hazard map in terms of liquefaction potential index in a 100-year return period is shown in Figure 1. The regions in yellow color correspond to areas where the liquefaction potential index is greater than 15 and indicates large liquefaction potential in the specified return period. On the other hand, the liquefaction potential index is smaller than 10 in regions with a green color. That is, the liquefaction potential is low in these regions.

Concluding Remarks

The methodology may be applied to evaluate various kinds of risk estimates such as insurance premiums, the exceedance probability curve of insurance losses, and so on. The inherent event and loss uncertainties can be considered through Monte Carlo simulations. As a simple example, the methodology was applied to evaluate the soil liquefaction hazard map if a liquefaction susceptibility category map was given.

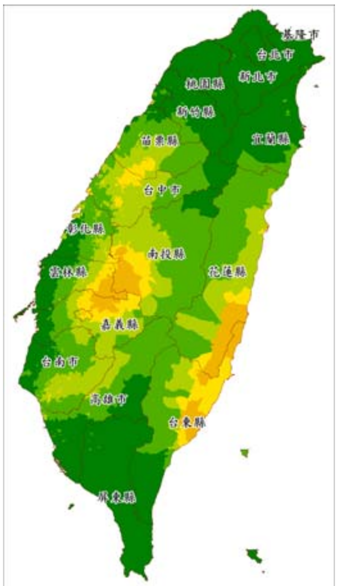

Figure 1 Soil liquefaction hazard map corresponding to 100-year return period in terms of liquefaction potential index in Taiwan if LSC is assumed to be all "very low".

References

Risk Management Solutions, 1997. Earthquake Loss Estimation Method – HAZUS97 Technical Manual, National Institute of Building Sciences, Washington, D.C.

Yeh, C. H., M. Y. Hsieh and C. H. Loh, 2002. "Estimations of Soil Liquefaction Potential and Settlement in Scenario Earthquakes," Proceedings of the Canada-Taiwan Natural Hazards Mitigation Workshop, July 17-19, Ottawa, Canada.

Iwasaki, T., Arakawa, T. and Tokida, K., 1982. "Simplified Procedures for Assessing Soil Liquefaction During Earthquake," Proceedings of the Conference on Soil Dynamics & Earthquake Engineering, Volume II, pp. 925-939.

Der Kiureghian, A. and H. S. Ang, 1977. "A Fault-Rupture Model for Seismic Risk Analysis," Bulletin of the Seismo-logical Society of America, 67 (4), 1173-1194.

Dong, W., 2001. Building a More Profitable Portfolio – Modern Portfolio Theory with Application to Catastrophe Insurance, Reactions Publishing Group.

Yeh, C. H., W. Y. Jean, C. C. Lin, W. C. Chen and Y. W. Chang, 2010. Taiwan Residential Earthquake Insurance Fund – Earthquake Risk Assessment Scheme (TREIF-ERA), Technical Manual.

Mobile Application Development for Seismic Disaster Precaution: The Android APP Prototype

Kuang-Wu Chou [1], Shih-Liang Chen [2], Chih-Hsin Chen[3], Gee-Yu Liu[4], and Chin-Hsun Yeh[5]

周光武[1]、陳世良[2]、陳志欣[3]、劉季宇[4]、葉錦勳[5]

Abstract

This study develops a mobile application (APP) that supports seismic disaster precaution. The APP is designed to offer the mobile interface of the early seismic loss estimation (ESLE) module of Taiwan Earthquake Loss Estimation System (TELES). Considering Google's Android is the most popular mobile platform, the APP will be developed for Android mobile devices so that most people may exploit its services. In 2013, we carried out a requirement analysis that helped us determine what functions the APP should offer. An APP prototype was then created to discover the difficulties we will encounter in the APP development, deployment, and user-application.

Keywords: seismic disaster precaution, TELES, APP, Android, Push technology, Google Cloud Messaging, Google Map

Introduction

In the past, people use mobile phones to talk with others. In addition, mobile phones helped people send and receive text messages. Recently, more advanced mobile devices such as smart phones and tablets are pervasive. So many people use mobile devices not only for daily talking, but also for surfing the internet. In particular, people can find information through mobile devices' applications, the so-called APPs, instead of internet browsers. An APP can offer a more sophisticated interface to interact with the user than what a browser can offer. Any APP, as a native application of mobile devices, allows the user to exploit more services from mobile devices, such as location services, photographing, videoing, and community services. Besides, APPs are supported by the push technology. This technology enables an APP to timely and effortlessly receive the latest information from the APP service provider.

This study focuses on developing an APP that can notify people of new seismic events as soon as possible. In 2013, we carried out a requirement analysis that helped us determine what functions the APP should offer. An APP prototype was then created to discover the difficulties we will encounter in the APP development, deployment, and user-application.

The Choice of Mobile Platform

According to what International Data Corporation surveyed in 2012, Android took the lead in all smartphone operating systems, with a 68.3% market share (See Fig. 1). Though taking the second lead with an 18.8% market share, Apple's iOS considerably led the rest. Blackberry is at 4.7%, Microsoft's Windows Phone 2.6%, and Linux 2.0%. Android and iOS still remains the market leaders. While iOS is proprietary software that Apple owns exclusively, many smart phone manufacturers opt for Android because it is free and open-source. This is one of the reasons why Android keeps the lead in the mobile device market. Thus, to promote our APP, we choose Android as the mobile platform where the APP works.

[1] Associate Researcher, National Center for Research on Earthquake Engineering, kwchou@narlabs.org.tw
[2] Assistant Technologist, National Center for Research on Earthquake Engineering, slchen@narlabs.org.tw
[3] Assistant Technologist, National Center for Research on Earthquake Engineering, chhschen@narlabs.org.tw
[4] Associate Researcher, National Center for Research on Earthquake Engineering, karl@narlabs.org.tw
[5] Research Fellow and Division Director, National Center for Research on Earthquake Engineering, chyeh@narlabs.org.tw

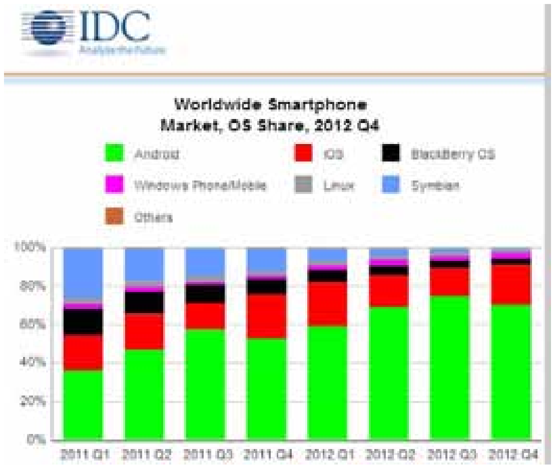

Fig. 1 IDC worldwide smartphone operating system market share 2012

APP System Architecture and Functions

Fig. 2 shows the system architecture of the APP, which offers a mobile interface for TELES's early seismic loss estimation (ESLE). Right after an earthquake, the ESLE module will receive from the Central Weather Bureau an email that describes the earthquake. According to that description, the ESLE module estimates seismic loss of buildings. The estimation outcome is then translated by The Taiwan Early Seismic Loss Estimation (TESLE) website, into what people can comprehend. Meanwhile, the APP server brings the same estimation outcome to all mobile devices that subscribe the APP service. Under such an information-transferring mechanism, APP service subscribers do not need to visit the TESLE website for querying loss estimation of an earthquake. The APP service will notify them of the loss estimation outcome right after the earthquake. Despite being passive, APP subscribers can get seismic information quickly and effortlessly.

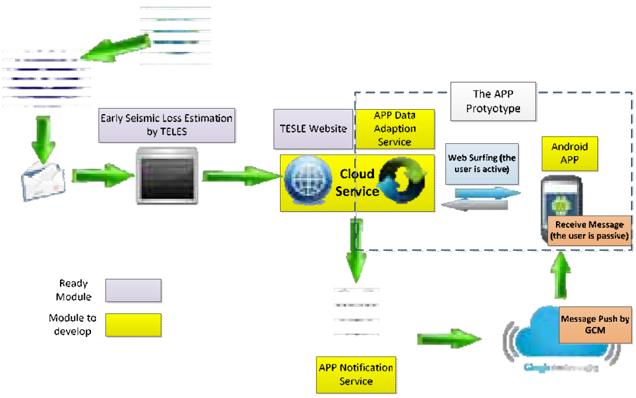

Fig. 2 The system architecture of the APP service

Fig. 3 shows the functions of the APP service. These are the earthquake event list, earthquake event map, push notification record, and settings. The earthquake event list shows all earthquake events in a list view. The earthquake event map shows the same events on the Taiwan map. The user may select an event in the list or on the map to view the description of the epicenter and seismic loss estimation of buildings. The push notification record stores every push notification by the APP service. A notification carries the loss estimation outcome of an earthquake. The setting function allows the user to specify the conditions to filter the earthquake events and the options to update the event list.

The APP will classify people and government officials into different roles and offer them different services. Because the user needs to pass authentication of the APP service before using it, the APP will be able to know to which role the user belongs, and thus will give him or her the optimal service.

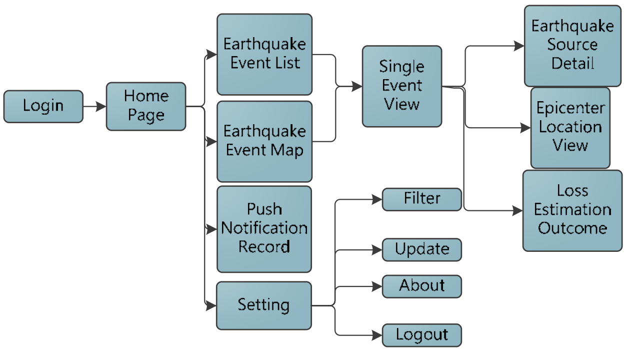

Fig. 3 The functional architecture of the APP service

Android Overview

At the top of the Android software architecture is the layer of applications, offering APPs that the user needs, such as Browser and Phone (See Fig. 4). At the bottom is the base layer of the architecture, the Linux kernel, which manages all the device drivers.

The middle layer includes the application framework, libraries, and the Android runtime. The application framework offers all components required for APP development. By writing Java or C++ codes, any APP developer can exploit the framework components to integrate Android system functions into their APPs.

Android provides a software development kit (SDK) to help developers build, test, and debug their APPs. Android SDK offers application programming interface (API) libraries. APPs can invoke the API libraries to use Android system services, including Activity Manager, Window Manager, Content Provider, View System, Package Manager, Telephony Manager, Resource Manager, Location Manager, and Notification Manager.

We believe that Android SDK suffices to develop an APP that satisfies our requirements. The requirements are to show the outcome of seismic loss estimation and to manage user privileges. To show the outcome, the APP should be able to read the loss estimation database and then show the event list as well as texts and pictures that describe the outcome. To better visualize the outcome, and to wield mobile device features, the APP should be able to show an event on a map, offer location services, and actively notify the user of seismic events. Such a map service may work by invoking Google Map Android API. The active notification service could be realized with the help of Google Cloud Messaging (GCM) for Android.

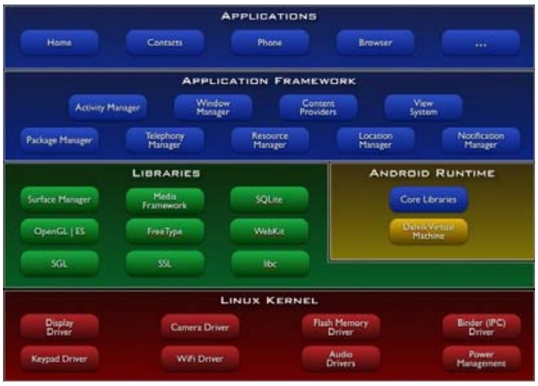

Fig. 4 Android software architecture diagram created by elinux.org

The Prototype

Fig. 5 shows the functions of our APP prototype. The prototype cooperates with a server. The prototype exploits the server's data interchange service to help users browse earthquake events in Taiwan. In addition, the prototype applies Android's Google Map technology, visually displaying earthquake events on the Taiwan map. The design of the prototype is illustrated in the following:

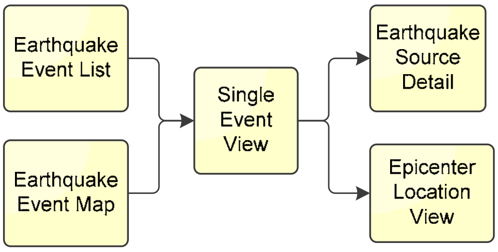

Fig. 5 The functional architecture of the Android APP prototype

1. The APP interface layout: the interface comprises a menu bar and a display area (See Fig. 6). The menu bar contains a title and four menu items.

Fig. 6 The APP interface layout

2. The earthquake event list: after startup, the APP reads all earthquake events from the server, and shows those events in a list view from new to old (See Fig. 7). Fig. 8 shows how the APP displays the detail for an event item in the list. The alert state of the event is shown in the lower right corner of the event item. The numeric range of an event's magnitude is represented by color. For example, red denotes that the magnitude is equal to or greater than 7 (See Fig. 9). Besides, the user may click on an event, and then a single-event view (See the point 4) will show to replace the list view on the screen.

Fig. 7 The earthquake event list

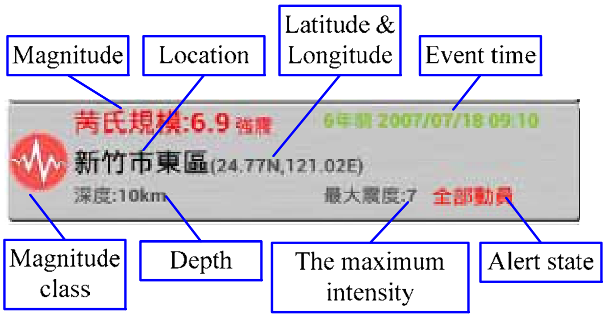

Fig. 8 Detail of an event item in the earthquake event list

Magnitude (Richter)	Class Icon
0 – 3.9	
4 – 4.9	
5 – 5.9	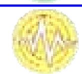
6 – 6.9	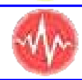
7 or more	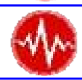

Fig. 9 Magnitude classes

3. The earthquake event map: such a map view applies Google Map Android Technology to show earthquake events on the Taiwan map (See Fig. 10). The icon of an event in the map has the same color as in the event list. The color expresses the numeric range of the event's magnitude. The shape and the size of the icon express the period in which the event occurs. Fig. 11 shows the icons for different periods. The bigger the icon appears, the more recent the event. By clicking on an event icon, we can view the detail of that event.

4. The single-event map view (See Fig. 12): only an event with its detail is shown in such a map view. To help people learn more about a seismic event, we will improve the single-event map so that it can display the loss estimation outcome.

Conclusions

With help of the Android Application Framework and Android SDK, this study has successfully created the prototype of a mobile APP for seismic precaution. The people responding to seismic disaster can use the prototype to learn about seismic events, which the prototype shows with an event list or on the Taiwan map. Based on the prototype, the study will realize all required functions of the APP. Besides, Push technology will be applied to enable the APP server to send seismic information to mobile devices of the user as soon as possible.

Fig. 10 The earthquake event map

Time	Icon
In 3 months	ballon
In 4-12 months	circle
Before 1 year	star

Fig. 11 Period classes

Fig. 12 The single-event map view

A Study of Experimental Control Methods for Real-time Hybrid Simulation

Pei-Ching Chen [1] and Keh-Chyuan Tsai [2]

陳沛清 [1]、蔡克銓 [2]

Abstract

Real-time hybrid simulation (RTHS) is an innovative experimental technology for evaluating the dynamic responses of structural systems under seismic loading. It requires high quality measurements, accurate control of actuators, and refined signal processing to perform versatile and reliable experiments. In this research, a second order discrete adaptive phase lead compensator (PLC) and a restoring force compensator (RFC) have been proposed to enhance the experimental accuracy of RTHS containing rate-independent specimens. In addition, RTHS of a smart base-isolation system with a semi-actively controlled magneto-rheological (MR) damper was physically tested. Experimental results demonstrated that the adaptive second-order PLC can lead to fair test results for rate-dependent components. Finally, RTHS of a nine-story shear building controlled by MR dampers was conducted. Experimental results showed that the adaptive model-based feedforward-feedback control method achieves excellent displacement tracking for RTHS.

Keywords: real-time hybrid simulation, actuator compensation, model-based control, adaptive control, MR damper

Introduction

Real-time hybrid simulation (RTHS), combining numerical simulation with experimental testing, is an efficient and cost-effective method for evaluating the seismic performance of structural systems. Unlike conventional testing methods, the computed command displacements in RTHS are imposed by hydraulic actuators in real-time (Nakashima *et al.*, 1992). There is a small but inevitable time delay between the command and the achieved displacements due to the dynamics of the servo-hydraulic actuators. This time delay generates negative damping, and therefore can result in inaccuracies or even destabilize the overall structural system. Consequently, accurate tracking control for servo-hydraulic actuators and signal correction for RTHS have attracted the interest of researchers.

RTHS of Rate-dependent Specimens

The servo-hydraulic actuators used to impose desired displacements on the test specimens for RTHS are mainly controlled by a digital PID controller. In order to improve actuator performance, an outer-loop controller is employed around the existing servo-hydraulic system, and thus the dynamics of the overall test system can be changed. This research begins by employing a dual delay compensation strategy that combines a phase lead compensator (PLC) and a restoring force compensator (RFC). Figure 1 illustrates the block diagram of the proposed dual-compensation strategy. An outer-loop adaptive feedforward PLC is derived by introducing the inverse model and adaptive law, and the RFC is adopted to improve the accuracy of the experimental results, especially when the structure is subjected to high frequency excitations.

Recently, advanced digital controllers with a Shared Common Random Access Memory Network (SCRAMNet) interface have been equipped to control the servo-hydraulic actuators at NCREE. With SCRAMNet, the data written to the replicated shared memory at one machine can be instantly sent to all the other replicated shared memories. In addition,

[1] Assistant Researcher, National Center for Research on Earthquake Engineering, pcchen@ncree.narl.org.tw
[2] Professor, Department of Civil Engineering, National Taiwan University, kctsai@ntu.edu.tw

MATLAB/Simulink is collocated to provide a general purpose programming environment to build the outer-loop control system for the servo-hydraulic system. With Real-Time Workshop and C compiler, executable codes can be created and downloaded to the xPC target. The target application can be run in real time with the SCRAMNet card embedded to connect to the digital controller. The block diagram of the high-tech test layout is illustrated in Fig. 2. The dual compensation method can be implemented using this high-tech facility.

The SDOF structure used to verify the dual compensation method can be divided into two parts: (a) the experimental substructure, consisting of a spring represented by a steel plate anchored between a shaking table and a rigid frame, and (b) the numerical model, consisting of the damper and the mass. The overall test setup is shown in Fig. 3. In this test, the stiffness term in the equation of motion is completely determined from the test specimen. This configuration is considered to be one of the most challenging cases for the conduction of a real-time hybrid test because the accuracy of the test is highly dependent on the accuracy of the imposed displacement and the restoring force measurement. Figure 4 shows the time histories of the RTHS and the assumed exact response of the SDOF structure subjected to a 30-second El Centro Earthquake with a normalized PGA of 0.04g. It is evident that all the test responses are close to the exact solution.

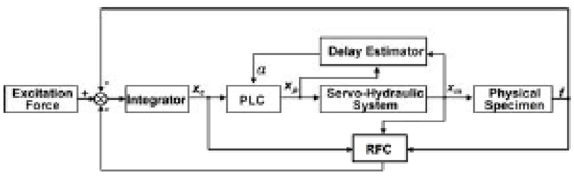

Fig. 1 Block diagram of the dual-compensation strategy

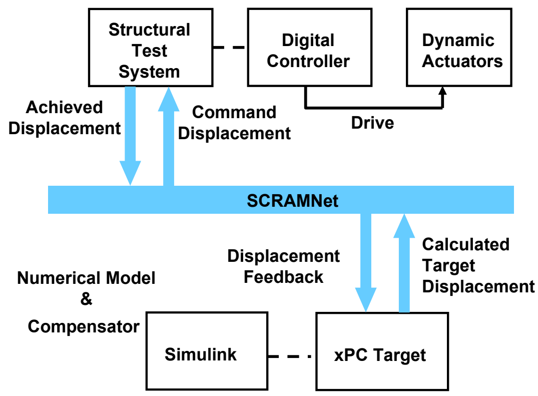

Fig. 2 Hardware layout of the control system

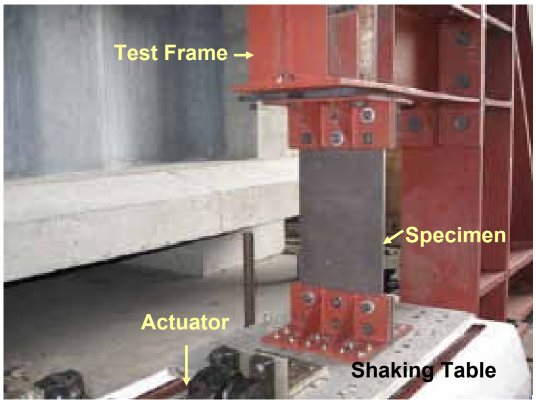

Fig. 3 Experimental setup for the SDOF RTHS

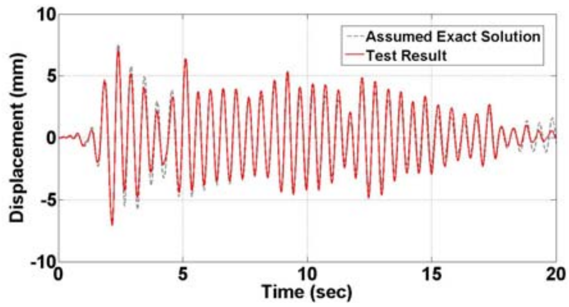

Fig. 4 Experimental and analytical results

RTHS of a Smart Base Isolation System

A smart base isolation system is a combination of low-damping elastomeric bearings and controllable dampers (Ramallo *et al.*, 2002). The dampers (normally MR dampers) provide additional damping to the structure in order to satisfy the structural control requirements. In this research, RTHS of a smart base isolation system is carried out. The numerical model contains the superstructure, low-damping base isolator, and MR damper control algorithm. The control current computed by the control algorithm is sent to the MR damper, which is physically tested in real-time. The experimental setup is illustrated in Fig. 5. The adaptive PLC is used to compensate for the actuator delay in order to increase accuracy during the test. The block diagram of the RTHS is illustrated in Fig. 6 where x_c and x_m are the command and measured displacements, respectively.

The responses of the MR damper are highly dependent on its velocity and the control current; however, during the test, the servo-hydraulic actuator was displacement-controlled instead of velocity-controlled. If the differences between the desired and the achieved velocities are significant, the responses of the MR damper may not be accurate enough and could even lead to a meaningless test result. Figure 7 illustrates the desired and the achieved velocity time histories for the test in which the MR damper was controlled by a linear-quadratic regulator (LQR). It appears that the difference between the achieved and desired velocities is less than 10%, which is acceptable for the RTHS.

The MR damper has been demonstrated to be able to reduce base drifts without increasing acceleration in the RTHS. Experimental results indicate that different control algorithms for the MR damper can be implemented and verified through RTHS without constructing a physical superstructure specimen. Meanwhile, the advantage of semi-active controlled devices is clearly observed in the RTHS. This suggests that simultaneous-control techniques for servo-hydraulic actuators and MR dampers can be used for the performance evaluation of a smart base isolation system without conducting a shaking table test.

Fig. 5 Experimental setup for the RTHS of a smart base isolation system

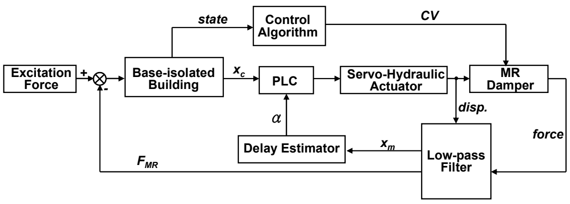

Fig. 6 Block diagram of the RTHS of a smart base isolation system

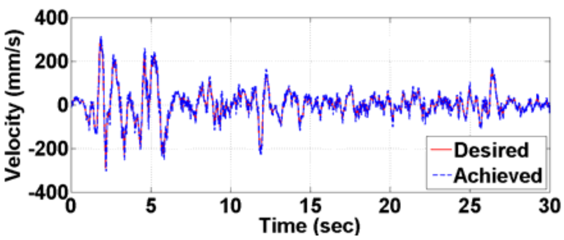

Fig. 7 Time histories of the desired and achieved velocities

Adaptive Model-based Feedforward and Feedback Control for RTHS

Model-based feedforward and feedback tracking control has been shown to be one of the most effective methods for RTHS (Carrion and Spencer, 2007). The feedforward control is used to cancel the dynamics of the servo-hydraulic system whereas the feedback controller is designed to minimize the errors between the command and measurement. This approach is based on a time-invariant linear model representing the servo-hydraulic system; however, the dynamics of the servo-hydraulic system may vary during a hybrid test due to the nonlinearity of the test specimen. In this research, an adaptive model-based feedforward and feedback controller is proposed to further improve the tracking performance of the actuator. This adaptive strategy is used to estimate the system parameters for the feedforward controller online during a test. The robust stability of this adaptive controller is achieved by introducing Routh's stability criteria and applying a parameter projection algorithm (Ioannou and Fidan, 2006). Figure 8 shows the block diagram for the proposed control framework in which the LQG represents the linear-quadratic Gaussian controller that combines the LQR state feedback gain with the Kalman observer.

A nine-story steel frame benchmark shear building (Ohtori *et al.*, 1994) was selected to verify the performance of the adaptive model-based control strategy for RTHS. All modal damping ratios were assumed to be 2%. The 1940 El Centro and 1995 Kobe earthquake records were selected to evaluate the seismic performance of the building. The intensity of the records was adjusted by a factor in order to investigate the robustness of the proposed adaptive model-based control scheme. This RTHS was conducted using the facility at the University of Illinois. In the test setup, a second generation, large-scale 200 kN MR damper was attached to a 556 kN hydraulic actuator as shown in Fig. 9. The MR damper had a stroke of ±292 mm. The input currents were limited to between 0 and 2.5 Amps. Both the passive-mode and semi-active control strategies were evaluated. The input current for the MR damper in the passive mode was kept constant at 2.5 Amps. The semi-active control utilizes the clipped-optimal control algorithm (Dyke *et al.*, 1996). In this validation, the maximum damper force was assumed to be 10% of the building weight, indicating a total number of 18 MR dampers that were placed in parallel. These dampers were installed on the first floor.

In this RTHS, dSPACE was adopted as it directly interfaces with MATLAB/Simulink running on a host computer. The DS1103 controller board, which is a system with a real-time processor, provides fast I/O for applications. By using Real-Time Interface (RTI), the proposed control scheme can be fully synthesized by the Simulink block diagram environment, and all the I/O can be configured as Simulink blocks. After completing the controller design, the Simulink based diagram can be then converted to real-time C code and downloaded to the DS1103 controller board. The graphical user interface software ControlDesk allows the adjustment of parameters, the collection of data, and the display of results during the tests. The entire dSPACE system was capable of handling all I/O channels in this study with a sampling rate of 2000 Hz.

The experimental results demonstrate that this adaptive control scheme improves the tracking performance of the actuator. The discrepancies between the desired and achieved displacements were effectively reduced by the adaptive tracking control; therefore, the semi-active control implementation subsequently showed a more representative structural response. The semi-active control strategy can surpass the passive-on case in structural response reductions. For example, the semi-active control strategy meets the design control objective that all floor accelerations can be effectively mitigated. Consequently, the proposed adaptive control scheme provides an effective means for conducting RTHS for complex engineering structures.

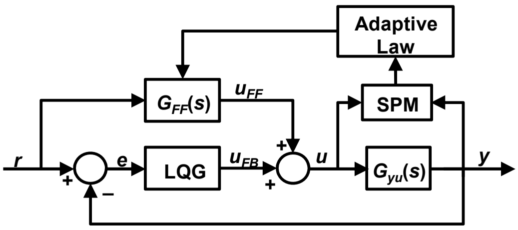

Fig. 8 Adaptive model-based feedforward and feedback control scheme

Fig. 9 RTHS experimental setup at the University of Illinois

Summary and Conclusions

In order to investigate and evaluate the seismic responses of structures, an advanced real-time experimental technology was developed and validated at NCREE. Unlike the conventional test methods such as quasi-static cyclic loading tests and pseudo-dynamic testing, the servo-hydraulic actuators act at a real-time rate. As a result, the stability and accuracy of a test become the most critical issues. In this study, an outer-loop control was adopted to externally improve the tracking accuracy of the servo-hydraulic actuator and stabilize the system. The designed outer-loop controllers were implemented in the original servo-hydraulic control loop directly by using Matlab/Simulink compatible hardware such as xPC target and dSPACE.

The dual-compensation strategy can be applied for rate-independent specimens. The experimental results demonstrated that the accumulated displacement error of the dual-compensation method can be significantly reduced. In addition, a smart base-isolation system was used to verify the RTHS control method where the isolation layer and the superstructure were numerically simulated and the MR damper was physically tested. Experimental results indicated that the compensation strategy can also be successfully applied to rate-dependent components. Finally, an adaptive model-based feedforward and feedback control scheme for RTHS was proposed using a semi-actively controlled nine-story shear building. This adaptive control method can be applied to verify semi-active control strategies in which the input currents to the MR damper change over time.

Future Works

Further study of multi-degree-of-freedom (MDOF) RTHS is indispensable in order to meet the test requirements of researchers. The coupling of the various degrees-of-freedom of the physical specimen is the most challenging part of such research. In addition, nonlinear numerical elements for the analytically modeled substructure are required for RTHS in which the inelastic responses of the emulated structure are to be investigated.

References

Carrion, J. E. and Spencer, Jr. B. F. (2007), "Model-based strategies for real-time hybrid testing", Newmark Structural Engineering Laboratory Report Series, University of Illinois at Urbana-Champaign, Urbana, IL, No. 6.

Dyke, S. J., Spencer, Jr. B. F., Sain, M. K. and Carlson, J. D. (1996), "Modeling and control of magnetorheological dampers for seismic response reduction", *Smart Materials and Structures*; 5(5), 565-575.

Ioannou, P. A. and Fidan, B. (2006), "Adaptive control tutorial", Society for Industrial and Applied Mathematics: Philadelphia.

Nakashima, M., Kato, H. and Takaoka, E. (1992), "Development of real-time pseudo dynamic testing", *Earthquake Engineering and Structural Dynamics*; 21, 79-92.

Ohtori, Y., Christenson, R. E. and Spencer, Jr. B. F. (1994), "Benchmark control problems for seismically excited nonlinear buildings", *Journal of Engineering Mechanics*; 130(4), 366-385.

Ramallo, J. C., Johnson, E. A. and Spencer, Jr. B. F. (2002), "Smart base isolation systems", *Journal of Engineering Mechanics, ASCE*; 128 (10), 1088-1099.

Design of a Versatile Engineering Simulation Environment for Coupled Continuous-Discontinuous Simulation

Wei-Tze Chang[1], Shang-Hsien Hsieh[2], Ren-Zuo Wang[3], and Kuo-Chun Chang[4]

張慰慈 [1]、謝尚賢 [2]、王仁佐 [3]、張國鎮 [4]

Abstract

To address the complexity of integrating continuous/discontinuous numerical methods into a software but retain its flexibility at the same time, National Center for Research on Earthquake Engineering (NCREE) under National Applied Research Laboratories (NARLabs) in Taiwan has developed a Versatile Engineering Simulation ENvironment (named VESEN), which is a coupled continuous-discontinuous simulation platform based on integration of Vector Form Intrinsic Finite Element (VFIFE) method and Discrete Element Method (DEM). Object-Oriented Programming (OOP) technology and design patterns in software engineering are used to facilitate VESEN's software usability and extensibility for adapting future requirement changes involving various constitutive laws, contact detection algorithms, geometric shapes of elements, interaction solvers between elements, failure criteria, control points, relations between element and control points, and member sections. This paper presents the software framework of VESEN with a concept of "solver pool". It can be expected that VESEN can simulate large-scale deformation and collapse of buildings and soil-structure interaction problems in the future.

Keywords: Vector Form Intrinsic Finite Element Method, Discrete Element Method, coupled continuous-discontinuous simulation, Object-Oriented Programing, design patterns

Background

Coupled continuous-discontinuous simulation can be applied in studying complex engineering problems such as solid-liquid interaction, estimate the impact on structure caused by earthquake, debris flow, and tsunami. National Center for Research on Earthquake Engineering (NCREE) under National Applied Research Laboratories (NARLabs) in Taiwan has integrated two numerical methods, Vector Form Intrinsic Finite Element (VFIFE) method (Shih, *et al.*, 2004; Ting, *et al.*, 2004a and 2004b) and Discrete Element Method (DEM) (Cundall, 1971; Williams, *et al.*, 1985), to design a Versatile Engineering Simulation ENvironment (named VESEN, a Norwegian word in a spiritual way meaning "being"), for the purpose of modelling multi-hazard phenomenon.

Software Framework

After analyzing the concepts from VFIFE's and DEM's research (Chang and Hsieh, 2009; Wang, 2005), this study identified eight major types of concepts for designing VESEN framework: (1) constitutive law, (2) contact detection algorithm, (3) element, (4) failure criterion, (5) geometric shape for illustrating boundary of element, (6) points, (7) interaction solvers, and (8) cross section of structure member. This study modifies and extends VErsatile Discrete Objects (VEDO) framework (Yang and Hsieh, 2005; Chang and Hsieh, 2009) to develop VESEN's object-oriented framework (see Fig. 1) that includes all of the above concepts in classes. For fulfilling the physical meaning of a coupled continuous-discontinuous simulation environment,

[1] Assistant Researcher, National Center for Research on Earthquake Engineering

[2] Professor, National Taiwan University

[3] Associate Researcher, National Center for Research on Earthquake Engineering

[4] Professor, Department of Civil Engineering, National Taiwan University

some classes from the VEDO framework were renamed, as shown in Table 1.

Solver Pool — Decoupling of Data and Solver in Numerical Models

An object with physical meaning in VESEN is divided into two parts, data (classes with symbol "#") and solver (classes in gray). This design uses the "bridge pattern" in software engineering (Gamma, *et al.*, 1995) to decouple the data from the implementation of solution methods and reduce the complexity of adding new models (see Table 2).

Table 1 Class table of VEDO and VESEN (abstract classes are in *italics*)

Issue	Class of VEDO	Class of VESEN
Interaction between elements	Interaction	Interaction
	ImpactSolver	*InteractionSolver*
	ContactDetecor	Contact & *ContactSolver*
	DiscreteObject	*VESENOvject* & its subclasses
Data structure & simulation procedure control	DOWorld	VESENWorld
	Consultant	*Consultant*
	SimMediator	SimMediator
	DOContainer	ElementContainer, PointContainer, & InteractionContainer

Table 2 The classes in VESEN using the design of "bridge pattern"

Physical meaning	Data class	Solver class
● Constitutive law	ConstitutiveLaw	*ConstitutiveLawSolver*
● Contact detection algorithm	Contact	*ContactSolver*
● Element	Element	*ElementSolver*
● Failure criterion	FailureCriterion	*FailureSolver*
● Geometric shape	GeometricShape	*GeometricShapeSolver*
● Point	Point	*PointSolver*
● Interaction	Interaction	*InteractionSolver*
● Section	Section	*SectionSolver*

To make things easier for model designers in adding and testing their new models without the need to touch the core of VESEN, we design a "solver pool" (i.e. the "SolverPool" class) for managing these models. At the beginning, the main program imports all solvers into the "solver pool" as candidates for simulation. The name of a solver (reported by the class itself) is the index for searching the solver in the pool (see Fig. 2a). After that, VESEN gets the parameters (data) and the name of solver from the input file (see Fig. 2b). At this step, the relationship between element and the designated element solver is built. With the help of the "bridge pattern" as mentioned above, the function of "*ElementSolver*" is independent of the data in "Element" (see Fig. 2c). Only two lines of codes need to be added into the main function and all other existing codes would remain untouched when importing a new solver into VESEN (bold words in Fig. 2a). Not only for the convenience for the designer of new models, but also the knowhow of individual models can be protected with this design.

Current State and Future Work

Currently the prototype of VESEN has been developed with 25 numerical models in 8 types and used to study large-scale deformation of a truss system. Once necessary implementation for modelling building structure (such as VFIFE frame elements) is completed, VESEN will be used to study seismic performance of bridges with functional bearing systems and collapse behavior of structures. The simulated results will be verified using experimental data obtained at NCREE.

Acknowledgement

The authors would like to thank Prof. Chung-Yue Wang of National Central University (NCU), for his helpful discussions and suggestions on the VFIFE theory.

References

Chang, W.-T. and Hsieh, S.-H. (2009). "Parallelization of Discrete Element Simulation," *Journal of the Chinese Institute of Engineers*, 32(6), 825-841.

Cundall, P.-A. (1971). "A Computer Model for Simulating Progressive, Large Scale Movement in Blocky Rock System," Proceeding of ISRM Symposium on Rock Fracture, Nancy, France, 129-136.

Gamma, E., Helm, R., Johnson, R. and Vlissides, J.-M. (1995). *Design Patterns: Elements of Reusable Object-Oriented Software*, Addison-Wesley Longman, Boston, USA, 416 pages.

Munjiza, A. (2004). *The Combined Finite-Discrete Element Method*, Wiley, 352 pages.

Shih, C., Wang, Y.-K. and Ting, E.-C. (2004). "Fundamentals of A Vector Form Intrinsic Finite Element: Part III. Convected Material Frame and Examples," *Journal of Mechanics*, 20(2), 133-143.

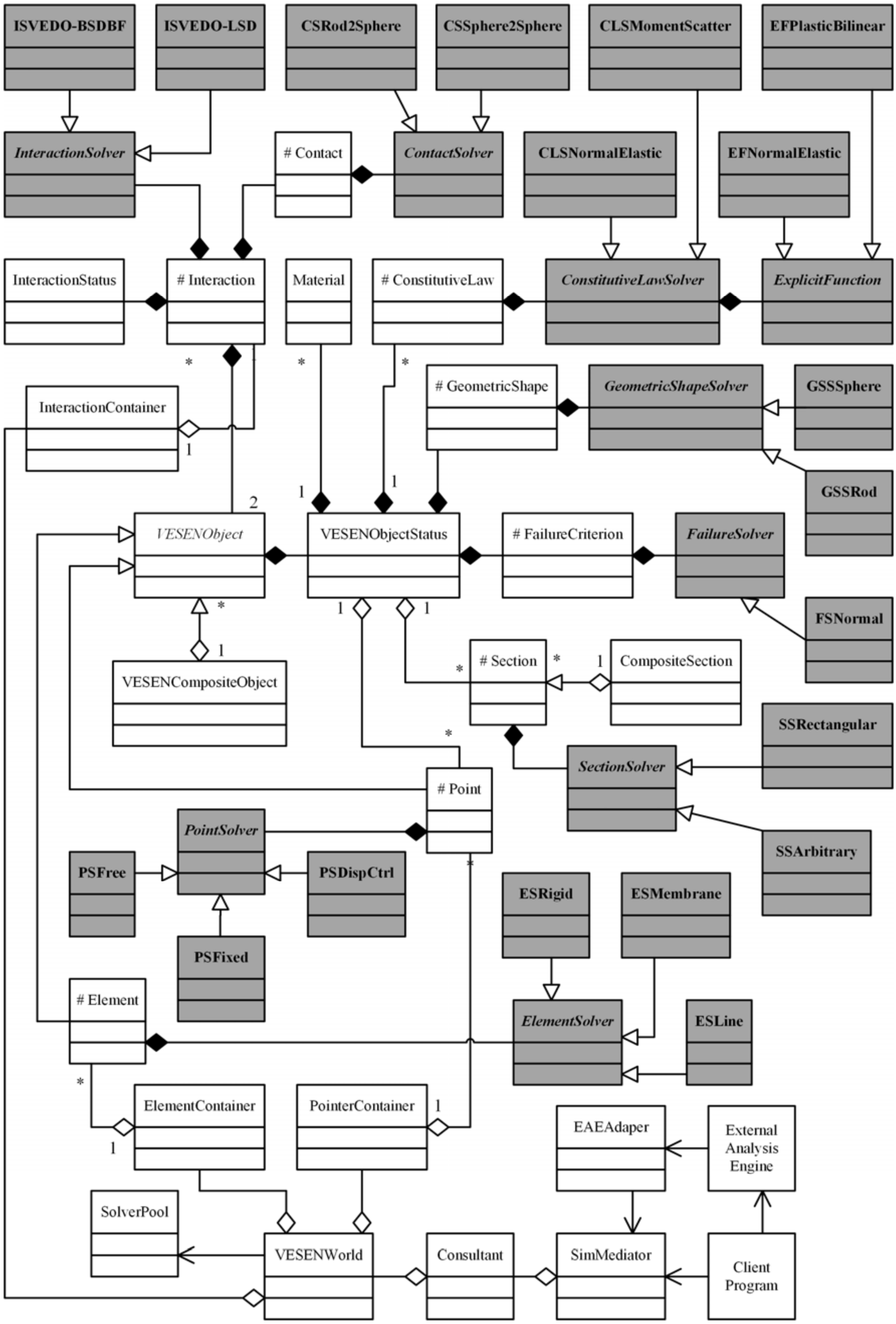

Fig. 1 VESEN framework in class diagram. Names of classes in italics indicate abstract classes. Names with symbol "#" and in gray color indicate "data" and "solver", respectively

Ting, E.-C., Shih, C. and Wang, Y.-K. (2004a). "Fundamentals of A Vector Form Intrinsic Finite Element: Part I. Basic Procedure and A Plane Frame Element," *Journal of Mechanics*, 20(2), 113-122.

Ting, E.-C., Shih, C. and Wang, Y.-K. (2004b). "Fundamentals of a Vector Form Intrinsic Finite Element: Part II. Plane Solid Elements," *Journal of Mechanics*, 20(2), 123-132.

Wang, R.-Z. (2005). "Vector Form Motion Anylysis of Structure," Ph.D. Dissertation, National Central University, 294 pages (in Chinese).

Williams, J.-R., Hocking, G., and Mustoe, G.-G.-W. (1985) "The Theoretical Basis of the Discrete Element Method," in Proceeding of the International Conference on Numerical Methods in Engineering: Theory and Applications, NUMETA 85, Balkema, A.-A. ed., Rotterdam, 897-906.

Yang, C.-T. and Hsieh, S.-H. (2005). "An Object-Oriented Framework for VEsatile Discrete Objects Simulation Using Design Patterns," *Computational Mechanics*, 36(2), 85-99.

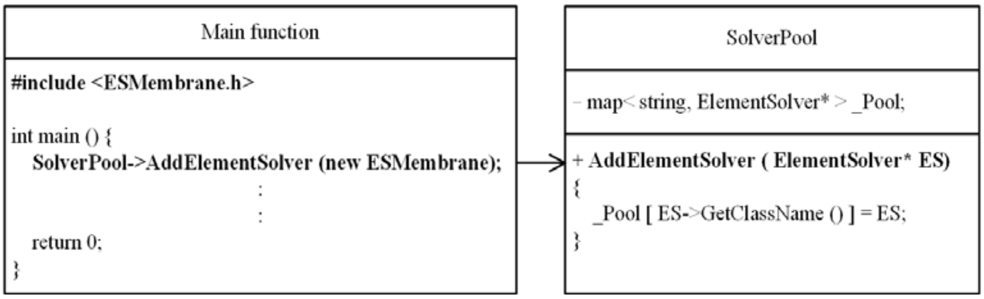

(a) Main function imports an element solver with only two lines of codes (words in **bold**)

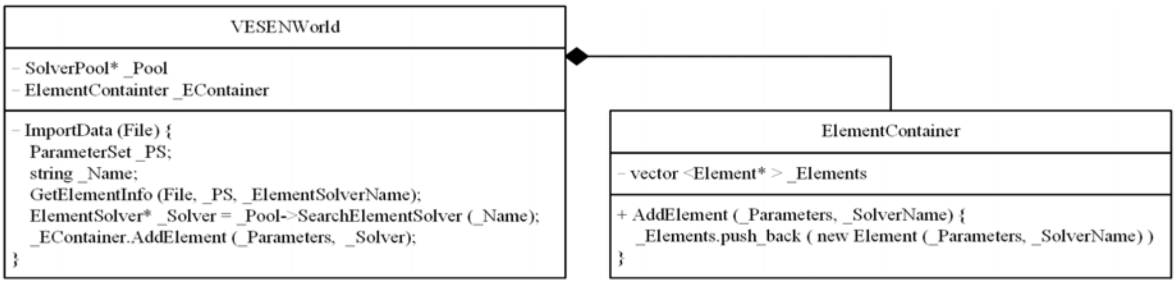

(b) "VESENWorld" gets parameters and the name of element solver from the input file

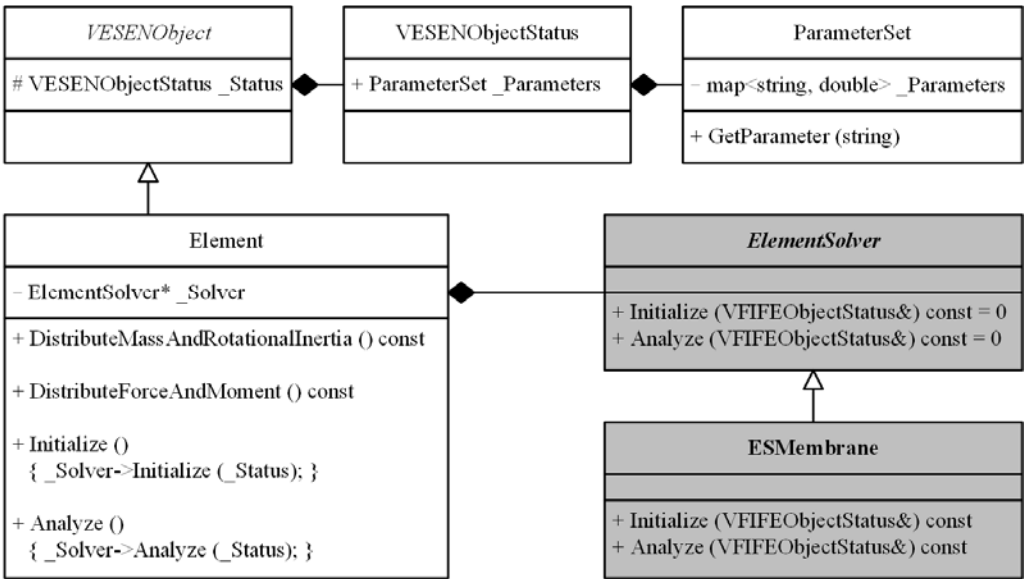

(c) Design of "Element" and "*ElementSolver*" classes using "bridge pattern"

Fig. 2 It is easy to add a new element solver in VESEN with the design of solver pool

Study on Deterioration of Seismic Capacity for RC Bridges Attacked by Corrosion

Chia-Chuan Hsu [1]

許家銓 [1]

Abstract

The structural performance of existing reinforced concrete (RC) bridges is highly dependent on the changing properties of the concrete and reinforcing steel caused by neutralization or chloride-induced corrosion. This study utilized previous regression analyses to predict the effect of neutralization and chloride-induced corrosion on bridges in Taiwan in order to define the properties of the deteriorated plastic hinge of a neutralized RC bridge column. Based on the defined plastic hinge, and considering neutralization and chloride-induced corrosion, decayed seismic capacity curves can be obtained from a pushover analysis. As a result, the performance regression curve of the whole structure can also be determined quantitatively via structural analysis. The results obtained can not only systematically describe the life cycle of the existing RC bridges, but also reveal the critical time at which repair or retrofit of the neutralized bridges is necessary to prevent sub-standard performance. This study can improve maintenance and minimize life cycle costs (LCC) of the relevant bridges.

Keywords: Neutralization, Salt attack, Life cycle

Introduction

The seismic retrofitting of bridges that have insufficient structural integrity is an important subject for countries located in earthquake-prone regions. Detrimental environmental factors may gradually result in the degradation of structural members in existing bridges; a deterioration in material strength; and also affect various fundamental parameters relating to structural capacity, including the cross-section of the still functional area (Kong and Frangopol 2003, Akgül and Frangopol 2005a b). As a result, structural capacity decreases with time, and the extent or severity of the problem (which has the potential to breach specifications) tends to increase the required retrofitting costs over the life cycle of a bridge (Frangopol et al. 1997, Frangopol and Liu 2007, Furuta 2008). In order to evaluate these cost implications, the establishment of time-dependent seismic fragility curves that consider material degradation is necessary.

The neutralization or salt attack of concrete may cause the RC member to receive less protection from corrosion. As time goes on, the regression of the structural performance, particularly in a polluted environment, will accordingly become increasingly significant. If the digression can be predicted with acceptable precision, a durability assessment of the existing RC bridge can be carried out, which greatly helps bridge management and is an important consideration for developed countries. The still functional cross-sectional areas of both the reinforcements and the concrete components during the neutralization process have been estimated in a previous study by Sung and Su (2011), where the expressions were presented in terms of service time. In addition, the corrosion process of salt attacked reinforcements has also been defined by Siao et al. (2012). Based on these studies, the plastic hinge properties of an RC bridge column were determined based on its functional section at a given time, and a sequential pushover analysis of the bridge was carried out. As a result, the performance regression curve of the whole structure could also be determined quantitatively via structural analysis. The results obtained can not only systematically describe the life cycle of existing RC bridges, but also reveal the critical time for necessary repairs or retrofitting to

[1] Assistant Researcher, National Center for Research on Earthquake Engineering, chiachuan@narlabs.org.tw.

prevent the unacceptable performance of neutralized bridges. This study may improve maintenance and minimize the life cycle cost (LCC) of the bridges.

Sectional properties of a corrosion RC member

The neutralization of an RC structure can be described as occurring in four stages, as indicated in Figure 1 (Niu 2003). In the initial incubation stage ($t \leqq t_i$), the neutralization depth of the concrete has not reached the critical threshold. In Figure 1, t_i is the critical time at which reinforcements are required in the neutralized concrete during the period of initial corrosion. It can be defined as:

$$t_i = \left(\frac{c - D_0}{K} \right)^2 \tag{1}$$

Where K (mm/year$^{0.5}$) is the diffusive coefficient, c (mm) is the thickness of the covering concrete and D_0(mm) is the partial neutralization depth from the measured neutralized depth, $D_C = K\sqrt{t}$ (mm), to the outer surface of the reinforcements during initial corrosion, $D_0 = c - D_C$.

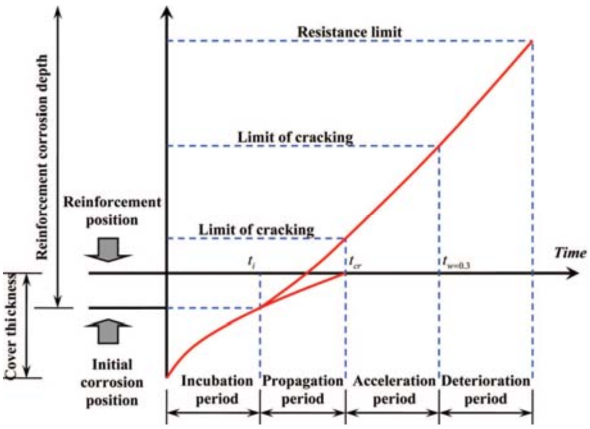

Fig. 1 Neutralization processes in concrete

The corrosion of salt attacked reinforcements has been categorized into four stages, the initiation stage, the propagation stage, the former period of the acceleration stage, and the latter period of the acceleration stage, by Siao et al. (2012), as shown in Figure 2.

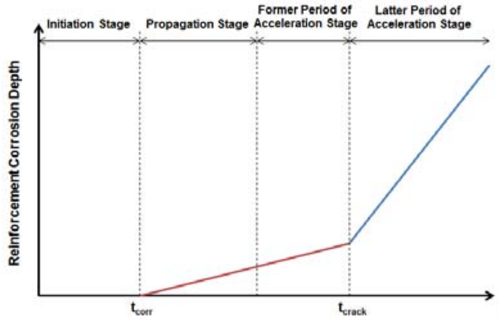

Fig. 2 Corrosion stage of salt attacked reinforcement

Seismic capacity of a corroded RC bridge

For a given RC member, its plastic hinge property values can be adequately defined in accordance with the design details of the member (Sung et al. 2005) and thus pushover analysis can be performed by employing available software packages such as SAP 2000. The seismic capacity curve, represented by the relation of lateral force versus lateral displacement, can be obtained via this pushover analysis and then sequentially converted into the ADRS format. This enables the spectral capacity to be determined in terms of spectral acceleration and displacement (ATC-40 1995). By superposing the capacity spectrum with the demand spectrum, the performance point where capacity is equal to demand can be found. Sung et al. (2006) proposed a modified seismic evaluation method by revising the ATC-40 approach. In this approach, the PGA corresponding to each specific structural displacement can be used to express seismic capacity through a diagram of the PGA as a function of displacement. For the corroded RC column, the still functional cross sectional area elements and their service time can be employed to ascertain seismic capacity as a time-dependent characteristic.

Based on the analysis results of several representative bridges located in different regions of Taiwan, the database of the time-dependent seismic capacity of corroded RC bridges in Taiwan can be established. These data not only relate to bridge type, soil conditions, and bridge site; but also to environmental parameters, such as humidity, temperature, and salinity level. Using this database, the time-dependent durability prediction model for bridges in Taiwan under different conditions can be established through the nonlinear regression approach, and consequently the time-dependent seismic capacity as a function of PGA for all the bridges in Taiwan can be obtained.

Time-dependent seismic fragility curve and retrofitting cost evaluation for the life cycle of a corroded RC bridge

The fragility functions explicitly express the probability of meeting or exceeding the damage limit stages for a given intensity of seismic excitation. In this study, the fragility curves are developed analytically with respect to the PGA for seismic damage assessment of bridges. The seismic capacity of a bridge is determined using a bilinear diagram, plotting PGA against structural displacement (Sung et al. 2007). Four performance objectives (POi, I = 1~4) have been carefully defined: (1) structural performance below 80% of yielding (PO_1); (2) structural performance at the yielding point (PO_2); (3) structural displacement at two-thirds of the ductile capacity (PO_3); and (4) the structural displacement at the limit of ductile capacity, as shown in Figure 3. In this study, the fragility curves are constructed assuming a normal distribution. An expression exists for the cumulative probability P_i (≧R_i) of damage occurring at a level equal to or greater than the designated level PO_i:

$$P_i(\geq PO_i) = \Phi\left(\frac{X-\mu_{X_i}}{\sigma_{X_i}}\right) \tag{2}$$

Where Φ is the log-normal cumulative distribution function, μ_{Xi} is the mean, σ_{Xi} is the standard deviation of *i*-th damage level, and R_i is represented by the PGA, X_i. The evolved probabilities $P_r(R_i)$ thus correspond to five damage limit stages comprising: (1) no damage R_1, (2) slight damage R_2, (3) moderate damage R_3, (4) extensive damage R_4, and (5) catastrophic structural failure R_5. Each of these cases is presented in Figure 4 along with the following equations:

$$\begin{aligned} &P_r(R_1) = 1 - P_1 \\ &P_r(R_i) = P_{i-1} - P_i \, , i = 2 \sim 4 \\ &P_r(R_5) = P_4 \end{aligned} \tag{3}$$

Both Equation (3) and Figure 4 represent the seismic fragility curve of a neutralized RC bridge with a given seismic capacity at a specific service time. Based on the time-dependent seismic capacities obtained, this preliminary outcome can be successfully extended to obtain corresponding time-dependent seismic fragility curves.

If the direct costs corresponding to each damage limit stage are expressed by *Cost_R*$_i$(*t*), *i* = 1~5, the total direct cost for retrofitting the bridge subject to a specific PGA may be expressed as a function of service time:

$$\begin{aligned} &TOTAL\_DIRECT\_COST(t) \\ &= \sum_{i=1}^{5} COST\_R_i(t) \times P_r(R_i) \end{aligned} \tag{4}$$

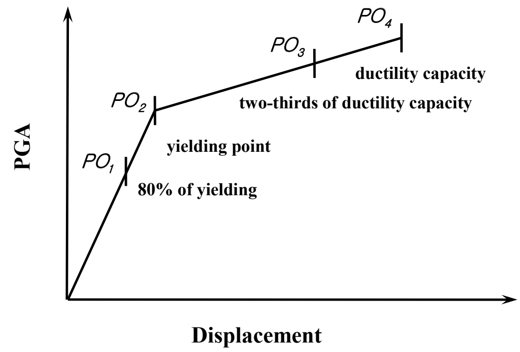

Fig. 3 Various performance objective levels for a neutralized RC bridge at a specific service time

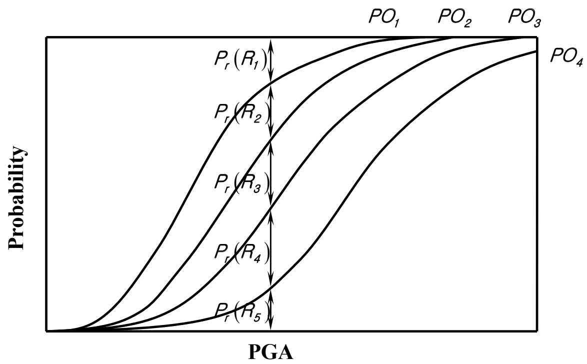

Fig. 4 Seismic fragility curve of a neutralized RC bridge at a specific service time

Conclusions

A realistic method is established in this study to evaluate the influence of concrete corrosion on existing RC bridges. The methodology is developed by establishing the digression curve of structural performance, which improves the assessment of the life cycle of the bridge structure. Finally, the strategy of bridge management can also be improved through this method, thereby minimizing life cycle cost.

References

Akgül, F. and Frangopol, D.M., 2005a. Lifetime performance analysis of existing reinforced concrete bridges. I: theory. Journal of Infrastructure Systems, 11 (2), 122–128.

Akgül, F. and Frangopol, D.M., 2005b. Lifetime performance analysis of existing reinforced concrete bridges. II: application. Journal of Infrastructure Systems, 11 (2), 129–141.

Applied Technology Council, 1996. Seismic Evaluation and Retrofit of Concrete Building (ATC-40), Redwood City, California.

Chinese National Standards (CNS), 1998. Ready-mixed con-crete, CNS-3090 A2042, Taipei, Taiwan. (in Chinese)

Chiu, C. A., Lin, P. H., 2004. Spatial Interpolation of Air Tem-perature and Precipitation from Meteorological Stations at Taiwan, Atmospheric Sciences. 32(4), 329-350. (in Chinese)

Directorate General of Highways (DGH), 2008. Report on Seismic Evaluation and Feasibility of Retrofitting for Highway Bridges, Taipei, Taiwan. (in Chinese)

Frangopol, D.M. and Liu, M., 2007. Maintenance and management of civil infrastructure based on condition, safety, optimization, and life-cycle cost. Structure and Infrastructure Engineering, 3 (1), 29–41.

Frangopol, D.M., Lin, K.Y., and Estes, A.C., 1997. Lifecycle cost design of deteriorating structures. Journal of Structural Engineering, 123 (10), 1390–1401.

Furuta, H., 2008. Life-cycle cost and bridge management. In: Proceedings of international workshop on frontier technologies for infrastructures engineering, 277–294.

Kong, J.S. and Frangopol, D.M., 2003. Evaluation of expected life-cycle maintenance cost of deteriorating structures. Journal of Structure Engineering, 129 (5), 682–691.

Niu, D.T., 2003. Durability and Life Forecast of Reinforced Concrete Structure, Science Press: Beijing. (in Chinese)

Siao, F.P., Chiu, C.K., Tu, F.J., 2012. Seismic performance evaluation for deteriorating and earthquake-damaged RC school buildings (NCREE-12-018). Taipei: National Center for Research on Earthquake Engineering (in Chinese).

Sung, Y.C., Liu K.Y., Su, C.K., Tsai, I.C. and Chang, K.C., 2005. A Study on Pushover Analyses of Reinforced Concrete Columns, Journal of Structural Engineering and Mechanics. 21(1), 35-52.

Sung, Y.C., et al., 2006. Performance-based damage assessment of low-rise reinforced concrete buildings. Journal of the Chinese Institute of Engineers, 29 (1), 51–62.

Sung, Y.C., Lin, T.W., Tsai, I.C., Chang, S.Y. and Lai, M.C., 2007. Application of Normalized Spectral Acceleration- Displacement (NSAD) Format on Performance-Based Seismic Design of Bridge Structures, Journal of Mechanics, 23(2), 86-93.

Sung, Y.C., and Su, C.K., 2011. Time-dependent seismic fragility curves on optimal retrofitting of neutralized rein-forced concrete bridges. Structure and Infrastructure Engineering, 7 (10), 797–805.